INFORMATION TO USERS

This manuscript has been reproduced from the microfilm master. UMI films the text directly from the original or copy submitted. Thus, some thesis and dissertation copies are in typewriter face, while others may be from any type of computer printer.

The quality of this reproduction is dependent upon the quality of the copy submitted. Broken or indistinct print, colored or poor quality illustrations and photographs, print bleedthrough, substandard margins, and improper alignment can adversely affect reproduction.

In the unlikely event that the author did not send UMI a complete manuscript and there are missing pages, these will be noted. Also, if unauthorized copyright material had to be removed, a note will indicate the deletion.

Oversize materials (e.g., maps, drawings, charts) are reproduced by sectioning the original, beginning at the upper left-hand corner and continuing from left to right in equal sections with small overlaps.

Photographs included in the original manuscript have been reproduced xerographically in this copy. Higher quality 6" x 9" black and white photographic prints are available for any photographs or illustrations appearing in this copy for an additional charge. Contact UMI directly to order.

UMI®

ANISOTROPY OF ICE I_h: DEVELOPMENT OF FABRIC AND EFFECTS OF ANISOTROPY ON DEFORMATION

Throstur Thorsteinsson

A dissertation submitted in partial fulfillment of

the requirements for the degree of

Doctor of Philosophy

University of Washington

2000

Program Authorized to Offer Degree: Geophysics Program

UMI Number: 9995444

UMI®

In presenting this dissertation in partial fulfillment of the requirements for the Doctorial degree at the University of Washington, I agree that the Library shall make its copies freely available for inspection. I further agree that extensive copying of this thesis is allowable only for scholarly purposes, consistent with "fair use" as prescribed in the U.S. Copyright Law. Requests for copying or reproduction of this dissertation may be referred to University Microfilms, 1490 Eisenhower Place, P.O. Box 975, Ann Arbor, MI 48106, to whom the author has granted "the right to reproduce and sell (a) copies of the manuscript in microform and/or (b) printed copies of the manuscript made from microform."
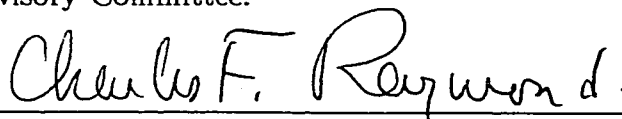
Signature

Date December 8, 2000

University of Washington

Graduate School

This is to certify that I have examined this copy of a doctoral dissertation by
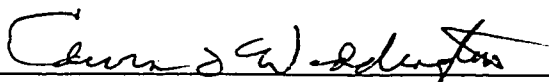
Throstur Thorsteinsson

and have found that it is complete and satisfactory in all respects,
and that any and all revisions required by the final
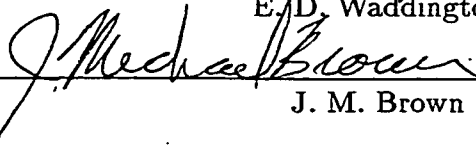examining committee have been made.
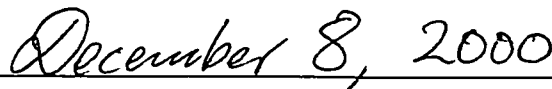
Chair of Supervisory Committee:

Charles F. Raymond (signature)

Charles F. Raymond

Reading Committee:

E. D. Waddington (signature)

E. D. Waddington

J. M. Brown (signature)

J. M. Brown

Date: _December 8, 2000_

University of Washington

Abstract

ANISOTROPY OF ICE I_h: DEVELOPMENT OF FABRIC AND EFFECTS OF ANISOTROPY ON DEFORMATION

by Throstur Thorsteinsson

Chair of Supervisory Committee

Professor Charles F. Raymond
Geophysics Program

The anisotropy arising from preferred crystal orientation of ice I_h is examined. To understand plastic anisotropy of polycrystalline materials it is necessary to examine the behavior at the single crystal level. Ice crystals have extremely strong plastic anisotropy that strongly influences the bulk behavior. There are several ways to relate single crystal deformation to the bulk behavior. Two approaches are used here. The first one is to assume a homogeneous stress throughout the bulk, which allows us to derive analytical relations between stress and strain rate. The anisotropy affects the strain rate-stress relationship significantly. For example strongly anisotropic ice, with a vertically symmetric fabric, can deform transversely to the applied stress in pure shear, be nearly undeformable in vertical compression, and shear easily in simple shear. The second approach takes the interaction between neighboring crystals into account, and recrystallization processes are also considered. Comparison of fabric evolution using the model and fabric from the GRIP ice core indicates that nearest neighbor interaction is necessary to explain observations. Quantification of the interaction is complicated by recrystallization processes.

A consistent method of characterizing measured fabric is needed to verify models of fabric development. Here the elastic anisotropy of ice plays a central role, and relations between fabric and elastic wave velocities are used to characterize fabric. As always, several other

methods are possible, but comparison indicates that sonic measurements give an accurate estimate for deformation effects from vertically symmetric fabric, especially in simple shear.

The deformation of the borehole at Dye 3, Greenland, has been measured with borehole inclinometry. Sonic velocity measurements done in the borehole allow us to model the deformation using an anisotropic flow law. Anisotropy alone cannot explain all the deformation. The additional processes responsible for the extra deformation are still unknown.

The anisotropy effects the deformation of polycrystalline ice, and therefore the flow of ice sheets. Criteria for folding is modified by the anisotropy. Anisotropy of polycrystalline ice must be taken into account when modeling the flow of ice sheets and interpreting ice core records.

TABLE OF CONTENTS

LIST OF FIGURES

LIST OF TABLES

ACKNOWLEDGMENTS

Chapter 1

INTRODUCTION

1.1 BACKGROUND

Water, H_2O, in its many forms, is probably one of the materials most studied throughout human history (*Ball*, 2000). There are at least 12 known solid forms of water. But, only one of these, ice I_h, forms naturally under Earth-like conditions. Of all the water on Earth, 97% resides in the world's oceans, and 2.4% as ice. The remainder is in rivers, groundwater and the atmosphere (*Wallace and Hobbs*, 1977).

The two large ice sheets, Greenland and Antarctica, account for over 98% of all the ice on Earth (*van der Veen*, 1991). Interest in the behavior of these ice sheets is great, particularly in light of the potential sea level rise should they melt. Total melting of Greenland could raise sea level by 7.5 m, West Antarctica by 6.0 m, and East Antarctica by 60 m (*van der Veen*, 1991). The exploration of past climate variations relies heavily on our ability to model the flow of ice, as do predictions of future behavior of ice sheets in response to climate forcing.

The flow of ice has traditionally been described by Glen's flow law (*Glen*, 1958)

$$\dot{\varepsilon}_{ij} = A(T)\sigma_e^{n-1}\sigma_{ij}, \qquad (1.1)$$

where $A(T) = A_0 \exp(-Q/(RT))$, and A_0 is a constant with a slight dependence on pressure, Q is the thermal activation energy for creep, R is the gas constant, T is the temperature, σ is the deviatoric stress and $2\sigma_e^2 = \sigma_{kl}\sigma_{kl}$ and I will assume that $n = 3$. Glen's flow law has been used with great success to model the flow of ice sheets. However, as data quality and measurement technique have advanced, important deviations from Glen's flow law have emerged.

This is not surprising; *Glen* (1958, 1963) warned that the non-random crystal orientation of crystals (anisotropy) of polycrystalline ice would invalidate some of the assumptions made in deriving the flow law.

In recent years, each factor in Glen's flow law has been questioned. The stress exponent n is generally taken to be 3, but that seems to be valid only at high stresses (>0.1 bar), and even under those conditions values of $n = 4$ have been suggested (*Durham et al.*, 1997; *Goldsby and Kohlstedt*, 1997). Values closer to 1 have been suggested at lower stresses, but it is difficult to get accurate measurements at low stresses, since the strain rate is so low, which makes experimental evidence inconclusive. The A_0 constant has often been modified to fit deformation rate data. These "corrections" or enhancement factors have often been attributed to softening effects of impurities and/or other potential softening mechanisms (crystal size, anisotropy) as needed. Especially intriguing is the possibility of relating dislocation densities to impurity content and to the possible grain size dependent mechanism, but these concepts are not pursued here. The activation energy Q is fairly well known, but some questions still linger (*Goldsby and Kohlstedt*, 1997). The proportionality between strain rate and stress components $\dot{\varepsilon}_{ij} \propto \sigma_{ij}$ does not hold when anisotropy is taken into account.

Ice I_h has extreme plastic anisotropy, with glide in the basal plane being 60 times easier than other slip systems (*Duval et al.*, 1983). The strong anisotropy represents a major complication when modeling the deformation of single crystals and their interactions in polycrystalline ice. The distribution of stress and strain between crystals in an aggregate has no analytical solution (*Wenk and Christie*, 1991). Assuming homogeneous stress or strain for all the crystals in an aggregate defines two end member cases; the "true" behavior is most likely somewhere in between. In glaciology, Glen's flow law (*Glen*, 1958) has been used with great success since its introduction. This thesis examines the effects of anisotropy on the bulk deformation, the evolution of fabric, and measurements of anisotropy.

1.2   MOTIVATION AND GOALS

Large gaps still exist in our understanding of the flow law for ice. The effects of fabric, impurities, and crystal size, for example, on the deformation of ice are poorly understood. The goal here is to examine the effects that the strong plastic anisotropy of single ice I_h crystals has on the bulk deformation. I also want to calculate how the fabric evolves as the ice strains, since fabric evolution leads to the anisotropy at depths in ice sheets. To measure fabric for use in a flow law for the instantaneous deformation, I want to use sonic wave velocities. Then the anisotropic elastic properties of ice also become important in order to relate the velocity to the degree of anisotropy. The effects of impurities and crystal size on strain rate are briefly examined in order to explain bore hole deformation. The deformation of ice is likely to involve several processes acting in parallel. However, deformation mechanisms, other than dislocation glide, will, most likely, have an isotropic contribution and the formulation of the anisotropic response would still remain valid.

1.3   SYNOPSIS

The underlying physics of ice flow lies in part in the deformation mechanisms of ice crystals. A short overview is given in Chapter 2. This is not meant to be an exhaustive summary of the possible deformation processes, nor a complete review of the processes covered. The idea is first and foremost to introduce dislocation glide and slip systems. With some background information about how crystals deform, one can better appreciate all the complications that arise when constructing a flow law. The emphasis in that chapter is on evidence of deformation mechanisms and anisotropy from seismology and solid earth physics. This highlights the close relation between the deformation of ice, other rocks and even metals.

The main challenge when studying deformation of polycrystalline natural ice is to relate the single crystal properties to the bulk behavior. This question is examined in Chapter 3. The basic assumption is that the stress is homogeneous at the single crystal level. This assumption is often attributed to *Sachs* (1928), as discussed by *Tomé* (1998). The derived equations for the strain rate are analytical and are formulated in a way that resembles Glen's flow law. There are, however, many differences between the resulting strain rate obtained

using the anisotropic formulation and Glen's flow law (isotropic). These differences are highlighted with examples in that chapter.

The deformation of the bore hole at Dye 3, Greenland, is examined in Chapter 4. Previously, enhancement factors correlated to impurities, fabric, and crystal size had been used to describe the deformation. I had hoped, with new measurements of anisotropy (sonic log) and an anisotropic flow law, to show that anisotropy would explain all the deformation not explained by Glen's flow law. It turned out that anisotropy alone cannot do that; some other process is occurring simultaneously. Chronologically this work preceded the full development of the analytical relations for anisotropy.

In Chapter 5 I develop a new method for modeling fabric evolution. Nearest neighbor interaction is included explicitly. The interaction significantly changes the rate and style of the fabric evolution. Dynamic recrystallization is also included, by considering the energy associated with evolving dislocation density and grain boundary energy. The results are compared to other models (without recrystallization) and data from ice cores. The fabric determined from the model matches the fabric in the GRIP ice core very well. The results are similar to those calculated using VPSC models (*Castelnau et al.*, 1996b), and they are more realistic than fabric evolution modeled using the homogeneous stress (no nearest neighbor interaction) and strain rate assumptions.

To verify models of fabric evolution and strain rates as a function of fabric, it becomes extremely important to have a consistent and accurate method of measuring and characterizing fabric. Thin section data provide information about the crystal orientation of single crystals, but the measurements are time consuming and give the orientation of only a few hundred crystals. Sonic logging, the little used but extremely useful method of measuring fabric is the subject of Chapter 6. Here the elastic anisotropy of ice is utilized to relate fabric and wave velocity anisotropy (*Bennett*, 1968). The fabric is then characterized using cone angles, inferred from wave velocity measurements and thin section data. I then compare the different estimates of cone angles obtained from wave velocities, thin section statistics (R/N) and cone angle fit from thin sections. The sonic velocities give the "best" estimate of fabric for predicting deformation.

Chapter 7 addresses folding in an anisotropic medium. The conditions for passive folding

of a layer disturbance in a steady state flow field are examined using the anisotropic flow relations derived in Chapter 3. The source of layer disturbances is also examined, especially in relation to changes in stress and/or orientation of the symmetry axis for the fabric.

Each chapter has been written as a stand-alone section. Chapter 4 has already been published as a paper, and Chapters 3 and 5 have been submitted to refereed journals. Chapters 6 and 7 have a complete description of the ideas presented within them, but await further input from potential co-authors.

6

Chapter 2

DEFORMATION MECHANISMS

2.1 SUMMARY

Defects in the crystal structure play a crucial role in deformation of crystalline materials. Diffusion creep, which involves the motion of vacancies, is expected to dominate at low stress. Dislocation glide, the motion of linear defects, occurs at higher stresses. Defects are almost always present in the crystal structure, either because they lower the free energy of the crystal, or they are grown into the material or induced by strain. Deformation of polycrystalline materials, such as rock and ice, by dislocation glide gives rise to a non-random orientation distribution of the constituent crystals (*Ribe and Yu*, 1991) due to intra-crystalline deformation. Ice I_h crystals deform mainly by dislocation glide on the basal plane, other systems being at least 60 times harder. Deformation of a polycrystalline materials by diffusion does not lead to preferred orientation of crystals, and neither does grain boundary sliding (*Goldsby and Kohlstedt*, 1997), although the evidence is still rather sparse.

2.2 INTRODUCTION

The origin and development of anisotropy have been the subject of intense investigations in Earth science ever since Hess in 1964 and Francis in 1969 pointed out that deformation during convection flow was the cause of lattice preferred orientation (LPO, fabric) of olivine and of seismic anisotropy near ocean ridges (*Chastel et al.*, 1993). Evidence for anisotropy of the upper mantle comes from numerous direct measurements of ophiolite and xenolith samples (*Ribe and Yu*, 1991) and also from seismology, where shear wave splitting gives the strongest evidence (*Savage*, 1999). Analysis of seismological data has revealed an azimuthal anisotropy of P and S-wave velocities and a polarization anisotropy of shear waves. Surface

wave dispersion provides additional evidence of the anisotropy of the mantle, down to 450 km depth. P-wave anisotropy can reach 10%, but is typically 3-6% (*Nicolas and Christensen*, 1987). The wave speed (P and S) is faster in the horizontal direction in the asthenosphere; this is seen from Love and Rayleigh surface-wave dispersion data (*Nicolas and Christensen*, 1987).

Generally it is assumed that 80% to 95% of the upper mantle is made up of a mixture of olivine and ortho-pyroxene (*Nicolas and Christensen*, 1987), of which olivine is about 70% (*Ringwood*, 1979). These numbers are also approximately correct for the volume ratios of these minerals. Minerals like olivine and ortho-pyroxene contribute much to the seismic anisotropy, whereas clino-pyroxene and garnet do not (*Nicolas and Christensen*, 1987). Although clino-pyroxene has a high seismic anisotropy, as does olivine and to smaller extend ortho-pyroxene, it does not form strong LPO in the mantle. Garnet on the other hand does not have large seismic anisotropy and is thus not important in this content. Olivine (Ferromagnesium olivine $(Mg, Fe)_2SiO_4$) is the dominant and least viscous mineral in the upper mantle and as such it is expected to be the controlling factor in the rheological behavior of the upper mantle (*Bai et al.*, 1991). Modeling of fabric evolution in a convection cell, with olivine as the anisotropic mineral, shows broad agreement with the anisotropy inferred from seismology (*Dawson and Wenk*, 2000).

The first observations of anisotropy in ice sheets arose in seismic work in Antarctica and *Bennett* (1968) probably did the first theoretical studies in the 1960's. Sonic velocity measurements in bore holes are the first direct observations of the development of anisotropy in ice sheets (*Bennett*, 1972; *Bentley*, 1972; *Kohnen and Gow*, 1979). The interpretation of sonic velocities was based on the theory of *Bennett* (1968). Since then numerous thin section studies have confirmed that fabric does develop at depths in the ice sheets.

There are several possible modes of non-elastic deformation of polycrystalline ice I_h: i) diffusion flow, ii) power law creep, iii) cleavage fracture (*Duval et al.*, 1983), and iv) grain boundary processes. Diffusion flow should be dominant at low stresses, high homologous temperature (T/T_m, where T_m is the melting temperature) and small ($\sim$ 1 mm) grain size (*Duval et al.*, 1983). Power law creep is dominant for higher stresses and high homologous temperature. Cleavage fracturing happens only when deviatoric stresses are high and the

confining pressure low, a situation that does not apply at depths in real ice sheets. Grain boundary migration is believed to be active in accommodating large deformations (*Duval et al.*, 1983). Grain boundary sliding is inferred for very small grain sizes (a few to tens of μm) (*Goldsby and Kohlstedt*, 1997). Whether grain boundary sliding occurs seems to depend on the relative orientation of crystals (*Ignat and Frost*, 1987). Motion of grain boundary dislocations seems to be the main mechanism of grain boundary sliding (*Pshenichnyuk et al.*, 1998; *Weiss and Schulson*, 2000). Laboratory experiments on ice, using >0.1 mm crystal sizes, have not shown any significant dependence of secondary and tertiary creep rate on crystal size (*Duval and LeGac*, 1980; *Jacka*, 1984).

In the absence of recrystallization, it is necessary to activate some other slip systems in addition to the basal slip to develop large strains in polycrystalline ice. Self-consistent modeling shows that at least 4 independent slip systems are needed. If homogeneous strain is assumed, 5 independent slip systems would be needed. But deformation on other slip systems of ice crystals requires stresses that are at least 60 times larger than that for basal slip at the same strain rate. Since the basal slip system only contributes two independent slip systems, non-basal slip or climb of dislocations must play a major role in the macroscopic behavior of polycrystalline ice.

Laboratory experiments on ice are usually done at high deviatoric stresses and temperature. Experiment have spanned a temperature range of 0°C to -50°C and octahedral stress (Eq. 2.30) range from 0.02 to 2.5 MPa. But due to the temperature dependence and slowness of ice flow, lower temperature usually must be accompanied by high stress to get measurable deformation. In natural ice masses the temperatures can get even colder, but deviatoric stress is generally no larger than about 200 kPa.

Single ice crystals shear about 2 orders of magnitude more rapidly, on their basal planes, than does polycrystalline isotropic ice (*Budd and Jacka*, 1989) and 3 orders of magnitude according to *Duval et al.* (1983).

In this Chapter I explore deformation processes, beginning at the atomic scale with diffusion and dislocation glide, and show how these microscopic processes lead to large scale deformation. Recrystallization is also introduced. Chapter 5 "Fabric Development with Nearest Neighbor Interaction and Dynamic Recrystallization" addresses many of the

details.

2.3 DEFORMATION PROCESSES

At high temperature $(T > \frac{1}{2}T_m)$ creep at significant strain rate occurs in response to deviatoric stress. At low stress levels, Newtonian flow results from stress-directed bulk vacancy diffusion; grain boundaries act as sources and sinks of vacancies. Vacancies are created at faces under tension and migrate either through the lattice (*Naborro-Herring creep*) or along the grain boundaries (*Coble creep*). At intermediate to high stress levels, dislocation glide or climb controls the mechanical behavior (*Tsenn and Carter*, 1987).

Experiments on ductile flow of polycrystalline olivine show that dislocation glide dominates at high stress and large grain size. Whereas, at low stress and small grain size, diffusion dominates (*Chastel et al.*, 1993). Diffusion depends on crystal size, but dislocation creep does not (*Chastel et al.*, 1993). At depths below a few kilometers, most rocks flowing in steady-state deform pre-dominantly by diffusion-assisted dislocation creep (*Tsenn and Carter*, 1987). Diffusion does not produce fabric, and can even destroy preexisting fabric (*Karato*, 1993), but dislocation glide does produce fabric (*Nicolas and Christensen*, 1987).

Evidence about dislocation glide comes from direct observations of xenoliths brought to the surface. *Green and Radcliffe* (1972) used transmission electron microscopy (TEM) to elucidate the dislocation flow mechanism of two of the major phases of the upper mantle, olivine and orthorhombic pyroxene (enstatite). They concluded that flow in the upper mantle is dominated by dislocation movement and that such flow processes are rate controlled by dislocation climb. Deformation tests on single crystals of olivine show that they deform exclusively by dislocation glide. Tests done on both dry and wet (water in the structure) samples, found that a factor of 2 higher stresses were needed for the dry samples relative to the wet ones at constant strain rate. The deformational weakening in olivine is considered to be the result of hydrolysis of Si-O-Mg bridges adjacent to slip dislocations (*Blacic*, 1972).

Observations of dislocations in ice are numerous (*Baker*, 1997). They show that basal screw and 60° dislocations do not cross-slip and glide on non basal planes. This is strong evidence that they are widely dissociated on the basal plane (partial dislocations) and that

slip occurs on planes of the glide set (*Baker*, 1997), rather than on the shuffle set (*Petrenko and Whitworth*, 1994a).

2.3.1 Diffusion Creep

Diffusion here refers to the movement of point defects in the crystal lattice. The point defects can be vacancies, interstitials, impurity atoms, bivacancies, Schottky and Frenkel pairs, and some others. Common to them all are the relationships between concentration, formation energy, jump rates, diffusion coefficient and mobility (*Petrenko and Whitworth*, 1994b). Diffusion of these point defects can also affect dislocation motion, which is discussed below.

At constant temperature and volume, thermal equilibrium is attained at minimum free energy F rather than minimum internal energy U,

$$F = U - TS, \tag{2.1}$$

where T is temperature and S the entropy. Defects increase the internal energy U, but the entropy S increases more rapidly, so a minimum F is attained at some finite concentration of defects. To examine this a little further, consider a lattice of N identical points (atoms, molecules). Formation of n defects (each has energy of formation E_f) with equal probability of forming at any one point in the lattice has a free energy

$$F = E_f n - TS_c, \tag{2.2}$$

where S_c is the configurational entropy $S_c = k_B \ln W$, and W is the number of possible arrangements of n defects over N sites

$$W = \frac{N!}{n!(N-n)!}. \tag{2.3}$$

At equilibrium, $\delta F/\delta n = 0$, using the Stirling formula $\ln N! = N \ln N - N$ for $N >> 1$, we get using Equation (2.2)

$$\frac{n}{N-n} = \exp\left(-\frac{E_f}{k_B T}\right). \tag{2.4}$$

Assuming that $E_f >> k_B T$, we get $n \simeq N \exp\left(-\frac{E_f}{k_B T}\right)$. Typical values for ice are $E_f \sim 0.5eV$ and $k_B T \sim 0.023eV$ at $-10°C$ (*Petrenko and Whitworth*, 1994b). To be very careful

one must account for changes in vibrational entropy S_f, because of a slight change in the elastic lattice vibration spectrum, which gives

$$n \simeq N \exp\left(\frac{S_f}{k_B}\right) \exp\left(-\frac{E_f}{k_B T}\right). \tag{2.5}$$

The equilibrium positions of point defects in the lattice are separated by potential barriers of height U_m, and motion occurs by thermally activated hops over these barriers (*Petrenko and Whitworth*, 1994b).

Now consider the motion of an electrically charged defect, of charge q, that will be called an ion in the following. To move an inter-atomic distance a in the direction of the field E, a positive ion would need an activation energy $U_m - qEa/2$, and against the field, $U_m + qaE/2$. The frequency of jumps along the field is

$$f_1 = \nu \exp\left(-\frac{U_m - qaE/2}{k_B T}\right), \tag{2.6}$$

and similarly for jumps against the field f_2, but with a change in sign for the charge term. ν is related to the frequency of oscillations of the ion in its potential well. The mean drift velocity is

$$\bar{v}_d = a(f_1 - f_2) = 2\nu a \exp\left(-\frac{U_m}{k_B T}\right) \sinh\left(\frac{qEa}{2k_B T}\right). \tag{2.7}$$

Since usually $qEa << 2k_B T$ one finds

$$\bar{v}_d = \left(\frac{\nu q a^2}{k_B T}\right) \exp\left(-\frac{U_m}{k_B T}\right) E. \tag{2.8}$$

The probability of jumping, or the mean number of jumps in a given direction per second, is then

$$\nu_h = \frac{1}{2}\nu \exp\left(-\frac{U_m}{k_B T}\right), \tag{2.9}$$

and the diffusion coefficient of the ion is $D = \nu_h a^2$. For chaotic thermal motion of this kind, the ion mobility $\mu \equiv \frac{\bar{v}_d}{E}$ and the diffusion coefficient D are always related by the Einstein relation

$$\frac{\mu}{D} = \frac{|q|}{k_B T}$$

so that (*Petrenko and Whitworth*, 1994b)

$$D = \nu_h a^2 = \nu a^2 \exp\left(-\frac{U_m}{k_B T}\right). \tag{2.10}$$
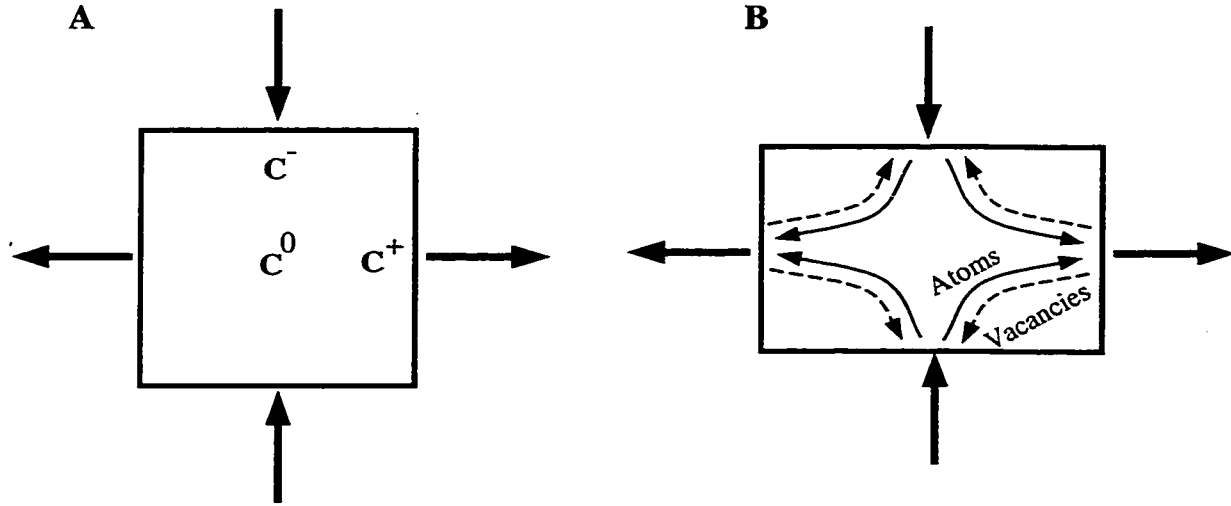
Figure 2.1: Principle of diffusion creep (Nabarro-Herring). Vacancies flow from the faces in tension (concentration C^+) to the faces in compression (concentration $C^- < C^+$) and matter (atoms) flows in the opposite direction.

This relation holds for neutral as well as charged defects since neither q nor E appears in Equation (2.10).

Now consider a cube, with sides of length d, subjected to a normal compressive stress on a pair of faces and to normal tensile stresses on the four other faces, as shown in Figure 2.1. The compressive normal stress hinders the formation of vacancies while the tensile stress facilitates it. The formation energy of vacancies is therefore increased by $\sigma V / kT$ on the faces in compression and decreased by the same amount on the faces in tension, where V is the atomic volume (*Poirier*, 1991). The equilibrium concentrations of vacancies on the faces in compression and tension are,

$$C^{\mp} = C_0 \exp\left(\frac{\mp \sigma V}{RT}\right). \tag{2.11}$$

There is a flow of atoms from the tensile to the compressed faces, and an opposite flow of vacancies. The flux of atoms is given by

$$\vec{J} = -D_v \nabla C = -\frac{\alpha D_v (C^+ - C^-)}{d}, \tag{2.12}$$

where D_v is the diffusion coefficient of vacancies and α is a geometrical factor. In a unit time Jd^2 atoms leave the faces in compression and are added to the faces in tension; thus

the crystal shortens by Δd and widens by the same amount. Since $\Delta d = (Jd^2)V/d^2 = JV$, the strain rate is $\dot{\varepsilon} = \Delta d/d = JV/d$. Taking everything together we get

$$\dot{\varepsilon} = \alpha D_v C_0 V d^{-2} \sinh\left(\frac{\sigma V}{k_B T}\right). \tag{2.13}$$

Using the coefficient of self diffusion $D_{sd} = D_v N_v = D_v C_0 V$ and assuming that $\sigma V << k_B T$

$$\dot{\varepsilon} = \frac{\alpha D_{sd} V}{d^2 k_B T}\sigma. \tag{2.14}$$

For ice the diffusion of molecules through the crystal or along its boundaries causes a strain rate that can be expressed as

$$\dot{\varepsilon} = \frac{20\bar{\sigma}\Omega}{kTd^2}\left(D_v + \frac{\pi\delta}{d}D_b\right), \tag{2.15}$$

where Ω is the molecular volume, δ is the boundary thickness, d is the crystal size and D_v and D_b are the lattice and boundary diffusion coefficients respectively (*Duval et al.*, 1983). This can be simplified by writing the diffusion coefficients as

$$D = D_0 \exp\left(-\frac{Q}{RT}\right), \tag{2.16}$$

where Q is the activation energy for diffusion. At temperatures $T > 0.8T_M$, lattice diffusion dominates, while boundary diffusion is more important at lower temperatures (*Duval et al.*, 1983). The activation energy Q for lattice diffusion in ice is large compared to most other materials. This results in slower diffusion processes in ice, at a given fraction of the melting point, than in other materials. According to *Duval and LeGac* (1982) diffusion flow (Nabarro–Herring or Coble creep) seems to dominate the creep for the upper 905 m near Dome C.

2.3.2 Dislocation Glide

Dislocations are line defects, bounding an area within the crystal where slip by an inter atomic distance $|\mathbf{b}|$, where $\mathbf{b}$ is the Burgers vector, has taken place (*Poirier*, 1991). The case when the Burgers vector is parallel to the dislocation is called a *screw dislocation*, and when $\mathbf{b}$ is perpendicular to the dislocation is called an *edge dislocation* (*Lliboutry*, 1987,
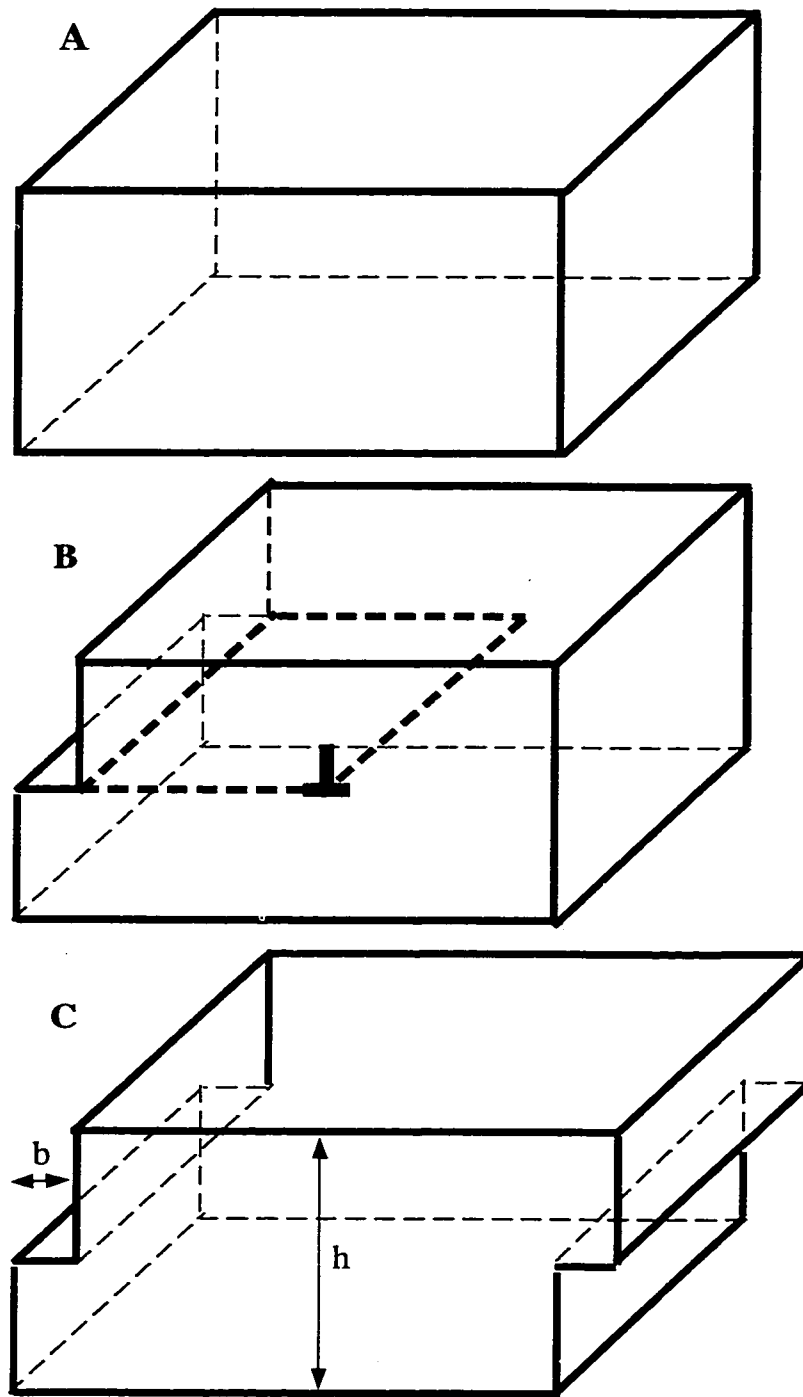
Figure 2.2: Slip by dislocation motion. (A) An undeformed crystal. (B) A dislocation line created on the left side has moved inside the crystal and caused a slip by b behind it. The up-side-down T indicates the dislocation. (C) The dislocation has swept the whole length of the crystal and left a step, length b, at the surface. The shear strain is $\varepsilon = b/h$ (*Poirier*, 1991).

p. 69). The motion of dislocations on a slip plane is called glide (*Petrenko and Whitworth*, 1994a). Figure 2.2 illustrates slip by dislocation glide, modified from *Poirier* (1991).

The density of mobile dislocation is given by $\rho =$ (length of dislocation lines)/(volume) which has units of 1/(area). When the dislocations move an average distance ΔL, the shear strain is $\varepsilon = \rho b \Delta L$ and the strain rate is

$$\dot{\varepsilon} = \rho b \bar{v}, \tag{2.17}$$

where $\bar{v}$ is the average dislocation velocity. Equation (2.17) is called *Orowan's equation*.

The mean velocity is controlled by the nature and distribution of obstacles. The principal obstacle lies in the intrinsic difficulty in breaking atomic bonds (*Poirier*, 1991) and is called lattice friction. If there are only discrete obstacles, with spacing ΔL, then the average velocity will be given by

$$\bar{v} = \frac{\Delta L}{t_g + t_o}, \tag{2.18}$$

where t_g is the average time gliding over distance ΔL between obstacles and t_0 is the time overcoming the obstacles. If $t_g \ll t_o$ then $\bar{v} = \Delta L / t_o$. Edge dislocations can overcome obstacles by moving out of their glide plane by diffusion-controlled climb, called *Weertman creep*. The strain rate in Weertman creep is

$$\dot{\varepsilon} = \frac{\rho b \Delta L v_c}{\delta}, \tag{2.19}$$

where δ is the distance to climb to escape obstacle, v_c is the climb velocity. Thus we get, with $\rho \propto \sigma^2$ and $v_c \propto \sigma$

$$\dot{\varepsilon} = A \exp\left(-\frac{Q}{RT}\right)\sigma^3, \tag{2.20}$$

where Q is the activation energy for creep (*Tsenn and Carter*, 1987). For ice, the stress exponent is approximately 3, at least over the deviatoric stress range 0.1 MPa $< \tau < 0.5$ MPa in ice (*Duval et al.*, 1983). The lower bound is poorly constrained since experiments at such low stress are subject to great uncertainty.

2.4 DYNAMIC RECRYSTALLIZATION

Dynamic recrystallization can be defined as a solid-state process leading to the creation of a new (and usually different) grain structure in the course of plastic deformation of crystalline

solids. The differences between the initial and re-crystallized structures can reside in one or several of the following features: preferred orientations of the grains (petrofabric), misorientation between adjacent grains, and grain size and shape. Dynamic recrystallization, as opposed to static (annealing) recrystallization, occurs simultaneously with deformation under certain conditions of stress, strain, temperature, and purity, and the same microscopic processes that cause or control deformation are also responsible for dynamic recrystallization (*Guillope and Poirier*, 1979).

Recrystallization in materials involves the growth of new, relatively strain-free grains (neoblasts) from old strained grains, thereby lowering the strain energy of the aggregate (*Ross et al.*, 1980).

At least two possible mechanisms are known for dynamic recrystallization. One is the grain-boundary and sub-boundary bulge nucleation type. The other, progressive sub-grain rotation may be important in relatively low stress and low temperature regimes.

Polygonization results when a pre-existing grain is split into two or more new grains with similar orientations through the alignment of dislocations into low-angle grain boundaries (*Alley et al.*, 1995b).

Dynamic recrystallization and deformation appear to produce qualitatively similar textures in olivine, although there are some differences (*Chastel et al.*, 1993). In experiments on single-crystalline halite (temperature range 250 to 790°C and stress 0.15 to 12 MPa), *Guillope and Poirier* (1979) found that recrystallization occurs by two different mechanisms. At lower temperatures and stresses the new grains result from the rotation of sub-grains, without grain boundary migration (rotation recrystallization or polygonization), and at higher temperatures and stresses the final texture results from the migration of the high-angle grain boundaries of the rotated sub-grains (migration recrystallization or just recrystallization (*Alley*, 1992)).

If different parts of a grain are subjected to different stress states (almost always the case), then the grain can become bent or twisted. Dislocations tend to organize between relatively undeformed regions called sub-grains to form sub-grain boundaries that relieve this bending or twisting and lower the energy of the system. If a sub-grain boundary becomes sufficiently strong, or a sub-grain becomes sufficiently rotated, then the boundary

becomes a full grain boundary (*Alley*, 1992). Recrystallization is the production of new grains at high angles to their neighbors. The new grains typically nucleate from existing grain or sub-grain boundaries separating regions with different stored strain energy, with the boundary bowing out toward the more strained side. The stored strain energy in the region ahead of the migrating boundary must be large enough to overcome the increase in grain-boundary energy caused by this bowing out of the boundary (*Alley*, 1992). This is discussed in more detail in Chapter 5.

The free energy difference ΔP_n, associated with the boundary energy is

$$\Delta P_n = \frac{2\gamma_{gb}}{r},\tag{2.21}$$

where r is the radius of the bulge and γ_{gb} is the grain boundary energy. If $r = 100$ μm and $\gamma_{gb} = 0.06$ J m^{-2}, then $\Delta P_n = 10^3$ J m^{-3}. This much energy can be available only if there are peaks in the internal stress distribution, as discussed below.

The elastic energy per unit volume is

$$P_{el} = \frac{1}{2}\frac{\sigma^2}{E},\tag{2.22}$$

where E is Young's modulus. With $\sigma = 0.5$ MPa and $E = 9$ GPa, the elastic energy is about 1 J m^{-3}. This is approximately 0.1% of the energy needed to drive recrystallization. The energy associated with a steady state dislocation density $\rho = 9\sigma_s^2(Gb)^{-2}$, where G is the shear modulus, σ_s is shear stress, and b is the magnitude of the Burgers vector is

$$P_{dis} = \frac{\rho G b^2}{2} = \frac{9}{2}\frac{\sigma_s^2}{G} \simeq 4\frac{\sigma_s^2}{E} = 8\frac{1}{2}\frac{\sigma_s^2}{E}.\tag{2.23}$$

This is 8 times the elastic energy, that is only about 1% of what is needed to drive dynamic recrystallization (*De La Chapelle et al.*, 1998). In Chapter 5, I show that, with non-homogeneous distribution of stress and strain, the dislocation density in the fastest deforming crystals increases very rapidly, so that the energy needed for recrystallization is obtained at a small bulk strain.

2.5 ICE DEFORMATION

2.5.1 Single Crystals of Ice

At temperatures below 263K, the constitutive relation for single ice crystals has a different stress sensitivity exponent, $n = 2$, than the $n = 3$ for polycrystals. The activation energy is also smaller, $E_c = 63$ kJ mol^{-1}, compared to $E_c = 80$ kJ mol^{-1} for polycrystals. Non-basal slip is extremely difficult to measure. In experiments where stress on non-basal planes is up to 60 times larger than on the basal plane, all the deformation still happens by glide/slip on the basal plane (Duval et al., 1983).

2.5.2 Polycrystalline Ice

To deform polycrystalline ice to large strains, slip systems other than the basal plane, (0001) $< 11\bar{2}0 >$, where (0001) denotes the basal plane using Miller indices and $< 11\bar{2}0 >$ the direction (Hook and Hall, 1991), must be activated because at least 4 independent slip systems are required. Glide on the basal plane gives two independent slip systems. Other possible slip systems could in principle be the prismatic (10$\bar{1}$0) $<11\bar{2}0>$, witch adds two independent slip systems, and the pyramidal (11$\bar{2}$2) $< \bar{1}\bar{1}23 >$, which adds one new independent slip system. Slip on the pyramidal slip system is not observed (Fukuda et al., 1987) and the prismatic slip system is at least 60 times harder than the basal slip (Duval et al., 1983).

Another possibility is that shear on the basal plane generates dislocations which then climb on planes perpendicular to the basal plane, giving two more independent systems, to give polycrystalline plasticity (Duval et al., 1983). Climb of [0001] or $\frac{1}{3} <11\bar{2}3>$ dislocations on the basal plane, is in fact what (Fukuda et al., 1987) propose as the third deformation mechanism for ice, in addition to basal slip and climb of dislocations on prism planes. By this mechanism, the ice crystals deform under uniaxial loading parallel to c-axis at a low rate limited by diffusion processes, but about million times faster than by Nabarro–Herring diffusion creep (Fukuda et al., 1987). Liu et al. (2000) conclude that all dislocations have Burgers vectors in the basal plane, and that loops expanding on this plane take up a hexagonal form made up of screw and 60° segments. They also concluded that screw segments

cannot cross-glide on non-basal planes, but edge dislocations can glide easily on non-basal planes containing their Burgers vector. That plays an important role in deformation of ice since it provides the principal mechanism for the generation and multiplication of the dislocation which subsequently move on the basal planes and produce macroscopic basal slip (*Baker*, 1997). Using in situ synchrotron X-ray topography *Liu et al.* (1995) propose that grain boundaries are the dominant mechanism for dislocation nucleation, and that internal stresses result in basal plane glide deformation of crystals with no resolved shear stress on the basal plane.

Perfect dislocations on the basal plane can be dissociated to partial dislocations by $\frac{1}{3}[11\bar{2}0] \rightarrow \frac{1}{3}[10\bar{1}0] + \frac{1}{3}[01\bar{1}0]$. Figure 2.3 shows how a dislocation with Burgers vector $\mathbf{b} = \mathbf{b}_1 + \mathbf{b}_2$ along a crystal axis can dissociate into two partials. The leading partial dislocation $\mathbf{b}_1$ is not a lattice vector, and therefore places the atoms behind it in positions not allowed by the crystal structure. A planar defect, called a stacking fault, is thus created behind it. But the fault ends at the trailing partial dislocation $\mathbf{b}_2$, which restores the atoms to normal lattice positions. Because stacking faults are regions of atomic mismatch, they have an energy per unit area, the stacking fault energy, that effectively binds the partial dislocations together (*Barber*, 1985).

The total energy of a dislocation per unit length can be approximated by

$$E = \frac{Kb^2}{4\pi} \ln\left(\frac{r}{r_0}\right), \qquad (2.24)$$

where K is a constant involving the rigidity and Poisson's ratio, b is the length of the Burgers vector, r_0 is the dislocation core cutoff radius and r is the average distance between dislocations (*Fukuda et al.*, 1987). It can then be shown that the dissociation of dislocations in the basal plane, into partial dislocations p_1 and p_2, lowers the energy of the dislocation structure, that is $E > E_{p_1} + E_{p_2}$.

In order to glide, dislocations must overcome the barriers presented by proton disorder. For basal slip it is already known that proton disorder will prevent dislocation motion on planes of the shuffle set (*Whitworth*, 1983). The rate controlling process for basal glide is considered to be proton rearrangement, as first pointed out by Glen in 1968 (*Fukuda et al.*, 1987).
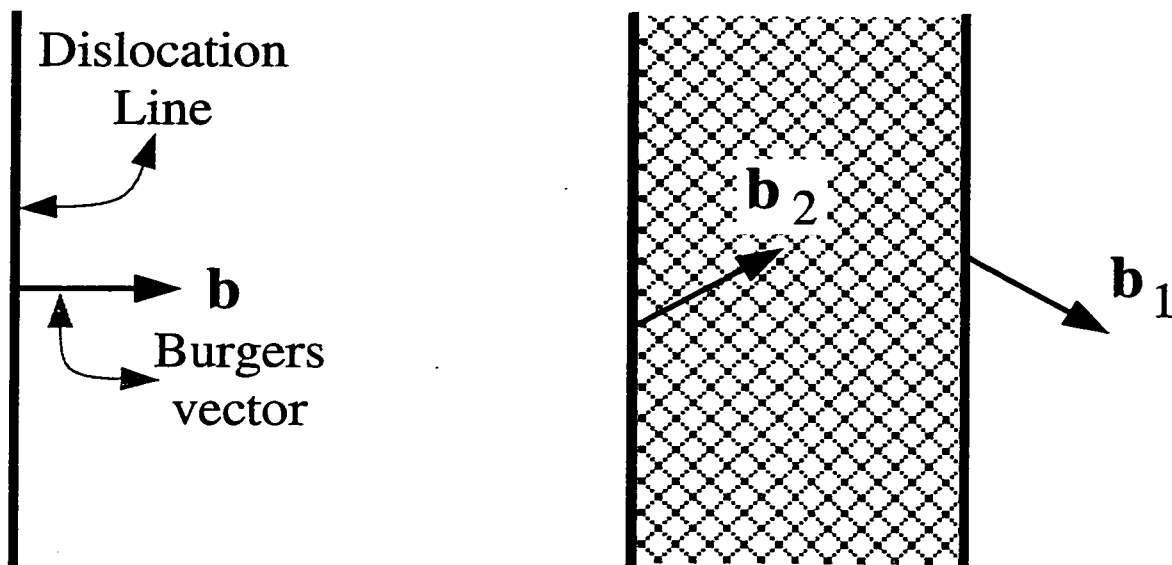
Figure 2.3: Slip by motion of partial dislocations. Shown is the dissociation of a unit dislocation **b** into two partial dislocations **b**$_1$ and **b**$_2$ (called Shockley pair), separated by a region of stacking fault.

2.5.3 The Creep Curve of Polycrystalline Ice I_h

The creep curve of ice has four distinct regimes. Following loading, first there is initial instantaneous elastic impulse strain, which is fully recoverable. Then there is primary creep, with decreasing strain rate that occurs up to strains of about 1%. The primary creep is largely anelastic; it has time dependent recoverable strain if the load is removed. When the strain reaches about 10% ice is in the tertiary creep regime, which is irrecoverable viscous creep (*Budd and Jacka*, 1989). In fact, almost all the creep beyond 1% is irrecoverable. Between primary and tertiary creep there is secondary creep, where ice reaches a minimum strain rate. The minimum strain rate $\dot{\varepsilon}_{min}$ is achieved at octahedral strains of 0.5% to 2%, usually close to 1% (*Hooke et al.*, 1980). The exact value may depend on the stress applied, although the experiments are inconclusive.

In constant stress experiments, the initial instantaneous elastic impulse strain increases approximately linearly with stress from strain of 0.024% at 0.2 MPa to 0.3% at 2.5 MPa (*Budd and Jacka*, 1989). Secondary creep is not truly a steady state, but rather a transition from strain hardening to strain softening.

The secondary creep constant, B, depends on temperature with an activation energy E_c which is slightly larger than the activation energy for self-diffusion. B can be written as

$$B = B_0 \exp\left[-\frac{E_c}{kT}\right], \qquad (2.25)$$

where B_0 is a constant.

There is some evidence that the rate controlling process during secondary creep is the diffusion-controlled climb of dislocations on planes normal to the basal plane. Then the slow creep of ice could have its origin in the unusually, compared to most other materials, slow rates of diffusion, discussed above.

At temperatures larger than -10°C the activation energy, E_c, changes. The reason for this change is not known, but the grain boundary mobility also increases at this temperature. A possible explanation for both may be grain boundary melting (*Duval et al.*, 1983).

After the minimum strain rate is reached at about 1% strain, the creep accelerates to tertiary creep. The acceleration is often thought to be due to changes in fabrics (*van der Veen and Whillans*, 1994), but others believe that 1% strain is far too small for significant

changes to occur (*Duval et al.*, 1983). Intrinsic softening of the individual crystals by dislocation multiplication has also often been suggested (*Hooke et al.*, 1980). An alternative explanation is that internal cracks nucleate, increasing the stress on uncracked grains thus accelerating the creep rate (*Duval et al.*, 1983). This has been seen in some experiments. However, careful tests at different stress levels (in uni-axial compression) suggest that this may not be the complete explanation, because some samples are crack free, while others crack at very low strains, $\varepsilon \sim 10^{-2}\%$, even though all tests show a minimum creep rate at 1% strain. Thus cracking cannot be the sole explanation. One possible mechanism to avoid this controversy is dynamic recrystallization, if it causes a major reorientation of certain grains. Dynamic recrystallization is known to happen at $\varepsilon < 1\%$, even in single crystals of ice, because dynamic recrystallization induces the development of preferred c-axis orientation, thus it can explain the acceleration of creep.

2.5.4 Flow Law for Ice

Glen's flow law

An isotropic relationship between two second order tensors can generally be written in the form

$$\dot{\varepsilon}_{ij} = A(\Sigma_1, \Sigma_2, \Sigma_3)\delta_{ij} + B(\Sigma_1, \Sigma_2, \Sigma_3)\sigma_{ij} + C(\Sigma_1, \Sigma_2, \Sigma_3)\sigma_{ik}\sigma_{kj}, \qquad (2.26)$$

where $\dot{\varepsilon}_{ij}$ is strain rate, σ_{ij} stress and the Σ_i's and E_i's are the invariants of the stress and strain rate tensors (see Section 2.6). In order to simplify this expression for use in an ice flow law it is assumed that density does not vary (the material is incompressible), that is $E_1 = \dot{\varepsilon}_{ii} = 0$. Also because the material is not affected by hydrostatic pressure, it is standard to use the stress deviator (' denotes deviatoric stress), $\sigma'_{ij} = \sigma_{ij} - \frac{1}{3}\Sigma_1$. This assumption means that $\Sigma'_1 = 0$.

Then we can write

$$\dot{\varepsilon}_{ij} = -\frac{2}{3}\Sigma'_2 C(\Sigma'_2, \Sigma'_3)\delta_{ij} + B(\Sigma'_2, \Sigma'_3)\sigma'_{ij} + C(\Sigma'_2, \Sigma'_3)\sigma'_{ik}\sigma'_{kj}, \qquad (2.27)$$

Further simplifications follows from the assumption (*Nye*, 1957) of proportionality of strain rate components and stress deviator components, and the assumption that the second

invariant of the strain rate tensor is a function of Σ'_2 only. If this is so, the equation reduces to

$$\dot{\varepsilon}_{ij} = B(\Sigma'_2)\sigma'_{ij}, \qquad (2.28)$$

which is Glen's flow law.

Anisotropic flow laws

There are two extreme assumptions that can be made when modeling the deformation of anisotropic aggregates. One is to assume homogeneous strain, the other is to assume homogeneous stress. The former ensures strain compatibility, but stresses are discontinuous, while the latter ensures stress continuity, but overlaps and voids can form. The homogeneous strain assumption demands at least 4 active slip systems (from Visco Plastic Self Consistent modeling, von Mieses criterion requires 5), but ice has only two. Modeling shows that fabric evolution using the homogeneous strain assumption is much slower than observed, while the homogeneous stress assumption leads to unrealistically rapid fabric evolution. The homogeneous stress assumption is more plausible for ice, since grain boundary migration is expected to relieve much of the incompatibilities and ice has very few slip systems. These approaches are discussed in Chapter 5.

2.6 DEFINITIONS

There are several definitions for the invariants of stress and strain. The invariants of the stress tensor, and similar ones for strain, are

$$
\begin{aligned}
\Sigma_1 &= \sigma_{ii}, \\
\Sigma_2 &= \tfrac{1}{2}\sigma_{ij}\sigma_{ij}, \\
\Sigma_3 &= \tfrac{1}{3}\sigma_{ij}\sigma_{jk}\sigma_{ki}.
\end{aligned}
\qquad (2.29)
$$

In laboratory experiments octahedral strain and stress are often used. Octahedral strain rate and stress are defined as

$$
\begin{aligned}
\dot{\varepsilon}_o^2 &= \tfrac{1}{3}\dot{\varepsilon}_{ij}\dot{\varepsilon}_{ij}, \\
\tau_o^2 &= \tfrac{1}{3}\sigma_{ij}\sigma_{ij}.
\end{aligned}
\qquad (2.30)
$$

Equivalent stress and strain rate is also commonly used

$$\begin{aligned}
\sigma_{eq}^2 &= \tfrac{3}{2}\sigma_{ij}\sigma_{ij}, \\
\dot{\varepsilon}_{eq}^2 &= \tfrac{2}{3}\dot{\varepsilon}_{kl}\dot{\varepsilon}_{kl}.
\end{aligned}$$

(2.31)

There is also effective stress and strain

$$\begin{aligned}
\sigma_e^2 &= \tfrac{1}{2}\sigma_{kl}\sigma_{kl}, \\
\dot{\varepsilon}_e^2 &= \tfrac{1}{2}\dot{\varepsilon}_{kl}\dot{\varepsilon}_{kl}.
\end{aligned}$$

(2.32)

Chapter 3

DEFORMATION OF STRONGLY ANISOTROPIC MATERIALS

3.1 SUMMARY

Deformation rates of single crystals, deforming by glide on the basal plane, as a function of stress state and orientation, are used to infer the deformation rate of aggregates with arbitrary c-axis orientations assuming that the stress distribution within the crystal aggregate is homogeneous. Analytical equations for the deformation rate of anisotropic ice aggregates are derived for vertically symmetric cone angle fabric. These equations can easily be incorporated into existing models that are based on Glen's flow law. Even with this simple characterization of fabric, several interesting features arise. In a pure shear stress state, there is a non-zero transverse strain rate, except in the limiting cases of either perfect vertical alignment of crystals, or isotropic fabric. In simple shear there is a slight de-enhancement for cone angles between 60° - 90°. In uniaxial compression the maximum enhancement occurs when the cone angle is 57°. In combined uniaxial compression and simple shear stress, the vertical strain rate is very sensitive to the degree of anisotropy at small cone angles. Even if the fabric and the compressive stress at two sites in an ice sheet are the same, but one has an added simple shear stress, the vertical strain rates measured will be very different.

3.2 INTRODUCTION

For more than 40 years, ice deformation has generally been modeled using Glen's flow law (*Glen*, 1958). Due to its success in explaining both early field observations and laboratory tests, combined with its simple analytical formulation, only minor adjustments have been

made to it since its introduction. Recently, as measurement techniques and data quality have improved, important discrepancies have emerged. The deformation rate of bore-holes (*Gundestrup and Hansen*, 1984; *Dahl-Jensen and Gundestrup*, 1987; *Thorsteinsson et al.*, 1999) for instance, is often very different from what Glen's flow law would predict (*Paterson*, 1991). This has lead to a commonly used correction to Glen's law in terms of "enhancement factors" that are empirical constants used to make the ice "softer". The discrepancy between measured and predicted deformation rates is, at least partly, due to effects of impurities (which we will not consider here) and the non-random alignment of crystals, which makes the ice anisotropic. *Glen* (1958) noted that anisotropy would render the existing theories approximate.

It is well established that crystal fabric does strongly affect the plastic deformation of polycrystalline ice (*Steinemann*, 1958; *Russell-Head and Budd*, 1979; *Duval*, 1981; *Duval and LeGac*, 1982; *Budd and Jacka*, 1989; *van der Veen and Whillans*, 1990; *Alley*, 1992; *Anandakrishnan et al.*, 1994; *Azuma*, 1994, 1995; *Azuma and Goto-Azuma*, 1996; *Castelnau et al.*, 1996a). A strongly anisotropic aggregate of ice is much softer in simple shear applied normal to the mean c-axis direction than is isotropic ice under the same stress condition. From thin section measurements and sonic logging in Greenland and Antarctica (*Kohnen and Gow*, 1979; *Herron et al.*, 1985; *Taylor*, 1982; *Thorsteinsson et al.*, 1997; *Gow et al.*, 1997; *Thorsteinsson et al.*, 1999), it is known that ice develops an increasingly aligned fabric with depth as it strains. If the temperature of the ice rises above about −12°C, recrystallization will alter the fabric (*Duval and Castelnau*, 1995).

An initially isotropic polycrystalline ice aggregate undergoing ductile deformation will develop lattice-preferred orientation (anisotropy) as a result of intra-crystalline slip. To relate the deformation of single crystals to the bulk deformation, assumptions about the distribution of stress and strain within the aggregate are needed. There are two well known extremes: homogeneous stress and homogeneous strain. The homogeneous strain model is not well adapted to strongly anisotropic materials, since activation of up to five independent slip systems is necessary to produce arbitrary strain (*Castelnau et al.*, 1996a). Single crystals of ice deform almost entirely by slip on the basal plane (*Duval et al.*, 1983), which provides only two slip systems. It is also observed in experiments that crystal strain is not

homogeneous throughout an ice aggregate (*Azuma and Higashi*, 1985); that argues against the homogeneous strain assumption. Experimental data indicates that the homogeneous stress assumption is closer to reality (*Azuma*, 1995, cf. Figure 4), although interaction with surrounding crystals modifies the stress to some extent (*Azuma*, 1995; *Sarma and Dawson*, 1996; *Castelnau et al.*, 1996a; *Thorsteinsson*, 2000b). Incompatibilities arising at grain boundaries caused by the homogeneous stress assumption can be relieved by grain boundary migration (*Means and Jessell*, 1986; *van der Veen and Whillans*, 1994; *Lliboutry and Duval*, 1995). The "true" behavior of ice is somewhere between these two extremes, and is probably closer to the homogeneous stress.

In this paper I examine in some detail the deformation rate of single ice crystals deforming by glide on the basal plane. The characteristics of the deformation rate are independent of the assumptions made about the bulk properties, but yields useful information about the bulk deformation. The rotation rate of single crystals is derived, and the implications for fabric evolution examined briefly; the emphasis here is on the instantaneous deformation.

Then I use the homogeneous stress assumption (often referred to as "lower bound" or *Sachs* (1928) model) to formulate a flow law that accounts for the effects of fabric on the instantaneous deformation of polycrystalline ice. Several previous studies have accounted for the anisotropy of ice using similar assumptions (*Lliboutry*, 1993; *Lliboutry and Duval*, 1995) and even attacked the evolution of fabric (*Gödert and Hutter*, 1998; *Morland and Staroszczyk*, 1998; *Staroszczyk and Gagliardini*, 1999). However, describing the evolution of fabric is not a goal of this paper.

To derive analytical equations for the deformation, I describe the fabric using a single parameter, the cone angle (two parameters if the fabric is a girdle). The cone angle is a half-apex angle of a cone within which all the crystals are uniformly distributed, while a girdle angle describes the angle of a smaller cone within which all the crystals have been removed (see Figure 3.1). I chose to derive the equations for the bulk deformation as a function of a vertical cone or girdle fabric; this fabric has a transversely isotropic fabric symmetry. It is a useful case to examine since: a) a vertically symmetric fabric is commonly observed in ice sheets, b) analytical solutions for strain rate as a function of cone angle (and stress) are relatively easy to calculate, c) it is about the simplest type of anisotropy imaginable. Other

fabric symmetries could also be formulated.

Several commonly encountered stress states are examined, and relatively simple analytical equations for the deformation are derived. The formalism needed to derive analytical equations for other stress states is provided. Examples of how the anisotropy affects the flow are used to point out differences between anisotropic and isotropic materials, and highlight the importance of accounting for the anisotropy.

The formulation presented here can be incorporated into existing ice flow models without a major increase in the computational time required to run the models, when the fabric can be specified a priori. Although a complete model should include the fabric development, many of the important effects of anisotropy can be explored with this kind of formulation. The focus here is on the properties of ice (I_h) crystals, but the formulation is general enough to apply to other anisotropic materials.

3.3 SINGLE CRYSTAL DEFORMATION

Hexagonal ice crystals (ice I_h) show very strong plastic anisotropy. Ice (I_h) deforms almost entirely by dislocation glide on the basal plane, other slip systems being ~ 100 times harder (*Duval et al.*, 1983). A slip system is defined by a normal vector, n and the slip direction, b (the Burgers vector). Dislocations are line defects bounding an area within the crystal where slip by an interatomic distance $|b|$ has taken place (*Poirier*, 1991). Using three vectors in the basal plane, it is possible to describe all glide directions within the basal plane. The Burgers vectors are perpendicular to n (the c-axis in ice), and in ice they are at $120°$ angles to each other (the a-axes).

In the following a subscript or superscript in parentheses will refer to the slip system s in question, and superscript c refers to a single crystal. Vectors are denoted by v with components v_i, and second-rank tensors as A (also $\dot{\varepsilon}$ and σ) with components A_{ij} where

$i, j = 1, 2, 3$. The following notation is used for tensor operations,

$$
\begin{aligned}
a = \mathbf{A} : \mathbf{B} &\quad \Leftrightarrow \quad a = A_{mn} B_{mn}, \\
\mathbf{A} = \mathbf{n} \otimes \mathbf{b} &\quad \Leftrightarrow \quad A_{ij} = n_i b_j, \\
\mathbf{v} = \mathbf{A} \cdot \mathbf{n} &\quad \Leftrightarrow \quad v_i = A_{ij} n_j, \\
a = \mathbf{n} \cdot \mathbf{k} &\quad \Leftrightarrow \quad a = n_i k_i.
\end{aligned}
\tag{3.1}
$$

The normal to the basal plane is described by

$$
n_i = [\sin\theta\cos\phi, \sin\theta\sin\phi, \cos\theta],
\tag{3.2}
$$

where θ is the zenith angle and ϕ the azimuth in the external reference frame. In the case of ice, $\mathbf{n} = \mathbf{c}$, where $\mathbf{c}$ is the crystallographic c-axis, but for generality I will retain $\mathbf{n}$ until modeling ice exclusively. The three Burgers vectors perpendicular to $\mathbf{n}$ can be specified as

$$
\begin{aligned}
b_i^{(1)} = &\quad \tfrac{1}{3}[\cos\theta\cos\phi, \cos\theta\sin\phi, -\sin\theta], \\
b_i^{(2)} = - &\quad \tfrac{1}{6}[(\cos\theta\cos\phi + \sqrt{3}\sin\phi), \\
&\quad (\cos\theta\sin\phi - \sqrt{3}\cos\phi), -\sin\theta], \\
b_i^{(3)} = - &\quad \tfrac{1}{6}[(\cos\theta\cos\phi - \sqrt{3}\sin\phi), \\
&\quad (\cos\theta\sin\phi + \sqrt{3}\cos\phi), -\sin\theta].
\end{aligned}
\tag{3.3}
$$

The shearing on each slip system is driven by the resolved shear stress (RSS) on the basal plane in the direction of $\mathbf{b}$. To calculate the RSS, the first step is to find the traction, $\mathbf{T} = \boldsymbol{\sigma} \cdot \mathbf{n}$ on the basal plane, where $\boldsymbol{\sigma}$ is the stress tensor acting in the crystal. The next step is to find the component of the traction in the basal plane aligned along $\mathbf{b}$, $\tau = \mathbf{b} \cdot \mathbf{T} = \mathbf{b} \cdot \boldsymbol{\sigma} \cdot \mathbf{n}$. The Schmid-tensor for each slip system is defined as

$$
\mathbf{S} = \mathbf{b} \otimes \mathbf{n}.
\tag{3.4}
$$

Then the RSS on a given slip system is

$$
\tau = \mathbf{S} : \boldsymbol{\sigma} = \mathbf{S} : \boldsymbol{\sigma}',
\tag{3.5}
$$

where $\boldsymbol{\sigma}' = \boldsymbol{\sigma} + p\mathbf{I}$, and $p = -\sigma_{ii}/3$. We can use either the full or the deviatoric part of the Cauchy stress tensor, because $\mathbf{S} : \mathbf{I} = \mathbf{n} \cdot \mathbf{b} = 0$.

The rate of shearing on a slip system is given by

$$\frac{\dot{\gamma}}{\dot{\gamma}_0} = \left|\frac{\tau}{\tau_0}\right|^{n-1}\frac{\tau}{\tau_0},\tag{3.6}$$

where $\dot{\gamma}_0$ and τ_0 are the reference shear strain rate and reference resolved stress respectively, and the exponent n is typically 3 when modeling polycrystalline ice.

The total velocity gradient tensor, $\mathbf{L}^c$, for the crystal is then given by

$$\mathbf{L}^c = \sum_s \mathbf{S}^{(s)}\dot{\gamma}^{(s)}.\tag{3.7}$$

The strain rate is $\dot{\varepsilon} = (\mathbf{L} + \mathbf{L}^T)/2$ and the rotation rate $\dot{\Omega} = (\mathbf{L} - \mathbf{L}^T)/2$. The single crystal strain rate is $\dot{\varepsilon}^c = \sum_s \mathbf{R}^{(s)}\dot{\gamma}^{(s)}$, where $\mathbf{R} = (\mathbf{S} + \mathbf{S}^T)/2$ is the symmetric part of the Schmid-tensor. Thus, the strain rate is

$$\dot{\varepsilon}^c = \sum_s \dot{\gamma}_0^{(s)}\mathbf{R}^{(s)}\left|\frac{\mathbf{R}^{(s)} : \boldsymbol{\sigma}}{\tau_0^{(s)}}\right|^{n-1}\frac{\mathbf{R}^{(s)} : \boldsymbol{\sigma}}{\tau_0^{(s)}}.\tag{3.8}$$

3.4 BULK PROPERTIES AND FABRIC DEVELOPMENT

Different formulations of anisotropic flow (TBH (*Bishop and Hill*, 1951), Sachs (*Sachs*, 1928), VPSC (*Molinary et al.*, 1987), *Azuma* (1994)) use different methods to calculate the bulk response from the single crystal properties. The TBH method assumes homogenous strain of all the crystals. Sachs assumes homogeneous stress. The VPSC method represents a compromise between the homogeneous stress and homogeneous strain bounds (*Castelnau et al.*, 1996a). Azuma effectively assumes that the slip on the basal plane is the same for all crystals. Below I use the homogeneous stress assumption to calculate the bulk deformation rate.

The bulk deformation rate of the crystal aggregate is calculated as the mean deformation rate of single crystals. The resulting velocity gradient for the bulk calculated from the model, $\mathbf{L}^m$, is

$$\mathbf{L}^m = \frac{1}{N}\sum_{c=1}^{N}\mathbf{L}^c,\tag{3.9}$$

where N is the number of crystals and $\mathbf{L}^c$ is the velocity gradient of a single crystal. This could also be written in terms of volume fractions.

3.4.1 Strain Rates for Specified Fabric

Since the reference strain rate, $\dot{\gamma}_0$, and reference shear stress, τ_0, are the same for all three slip systems in the basal plane, we can write $\dot{\gamma}_0/\tau_0^n = \beta A(T)$, for all the slip systems ($s = 1,2,3$). Here β is a constant, and $A(T)$ accounts for the temperature dependence, and other isotropic effects (softening due to impurities, etc.). By introducing β the $A(T)$ function is the same as in Glen's flow law for isotropic ice (*Paterson*, 1994, p. 97). I will assume throughout that $n = 3$ (*Budd and Jacka*, 1989). The strain rate for a single crystal (Eq. 3.8) is then given by

$$\dot{\varepsilon}^c = \beta A(T)[\mathbf{R}^{(1)}\tau_{(1)}^3 + \mathbf{R}^{(2)}\tau_{(2)}^3 + \mathbf{R}^{(3)}\tau_{(3)}^3]. \tag{3.10}$$

The resolved shear stress, strain rate tensor and rotation tensor for each slip system are written out explicitly in Appendix A.1.

To calculate the bulk properties, we first define a c-axis orientation distribution function (ODF) $F(\theta, \phi)$ such that

$$\int \int F(\theta, \phi)d\theta d\phi = 1. \tag{3.11}$$

The bulk strain rate is then obtained from the integral

$$\dot{\varepsilon} = \int \int \dot{\varepsilon}^c(\theta, \phi)F(\theta, \phi)d\theta d\phi. \tag{3.12}$$

3.4.2 Fabric Development

Fabric development (texture evolution in metallurgy) refers to the rotation of the c-axis of single crystals in an external reference frame. The deformation $\mathbf{L}^m$ does not by itself specify the bulk rotation, since it is derived from the stress state, which is a symmetric second order tensor. The velocity gradient for an isotropic material will thus have the same symmetry as the applied stress, that is $\mathbf{L}^m \propto \sigma$, where $\mathbf{L}^m$ is the velocity gradient of the aggregate calculated from the model (Eq. 3.9). This means that for isotropic fabric in simple shear, for example, no bulk rotation $\dot{\Omega}^m$ is predicted according to the model, since $\mathbf{L}^m = (\mathbf{L}^m)^T$. Kinematic boundary conditions are required to determine the bulk rotation rate, $\dot{\Omega}^b$, as

$$\dot{\Omega}^b = \dot{\Omega}^m + \dot{\Omega}^d,$$

where $\dot{\Omega}^d$ is the rotation rate necessary to satisfy those boundary conditions (*Castelnau and Duval*, 1994). The velocity gradient $\mathbf{L}$ of the bulk is then defined as

$$\mathbf{L} = \mathbf{L}^m + \dot{\Omega}^d, \tag{3.13}$$

and the bulk strain rate is $\dot{\varepsilon} = (\mathbf{L}^m + (\mathbf{L}^m)^T)/2$. (Note that when dealing with strain rates we do not have to consider $\dot{\Omega}^d$ since it is anti-symmetric.) The rotation rate $\dot{\Omega}^d$ necessary to add to the velocity gradient is calculated from

$$\dot{\Omega}^d = \dot{\Omega}^b - \dot{\Omega}^m, \tag{3.14}$$

where $\dot{\Omega}^m$ is the mean rotation rate from the model

$$\dot{\Omega}^m_{ij} = \frac{1}{2}(L^m_{ij} - L^m_{ji}). \tag{3.15}$$

In simple shear, for example, $\dot{\Omega}^b$ would be defined as $\dot{\Omega}^b_{13} = \dot{\varepsilon}_{13} = -\dot{\Omega}^b_{31}$. Thus by introducing the boundary conditions $\dot{\Omega}^b$, we can calculate $\dot{\Omega}^d$.

Fabric development refers to the rotation of $\mathbf{n}$ in the external reference frame. This rotation of the lattice results from the constraints of neighbors during deformation (one can think of the lattice rotation rate $\dot{\Omega}^*$ below as $\dot{\Omega}^d$). The lattice rotation rate $\dot{\Omega}^*$ is the difference between the bulk rotation rate $\dot{\Omega}^b$ and the plastic rotation rate $\dot{\Omega}^p$ of the crystal itself,

$$\dot{\Omega}^* = \dot{\Omega}^b - \dot{\Omega}^p. \tag{3.16}$$

The plastic rotation of a crystal is given by

$$\begin{aligned}
\dot{\Omega}^p_{ij} &= \sum_s \frac{1}{2}(S^{(s)}_{ij} - S^{(s)}_{ji})\dot{\gamma}^{(s)} \\
&= \Omega^{(1)}_{ij}\dot{\gamma}^{(1)} + \Omega^{(2)}_{ij}\dot{\gamma}^{(2)} + \Omega^{(3)}_{ij}\dot{\gamma}^{(3)}.
\end{aligned} \tag{3.17}$$

This implies that the crystal is completely constrained by its neighbors, as opposed to a single crystal deforming by basal glide, which would not result in rotation of the c-axis.

The change in direction with time of the normal, $\dot{\mathbf{n}}$, is then (from Eq. 3.16)

$$\frac{dn_i}{dt} = \dot{\Omega}^*_{ij}n_j = (\dot{\Omega}^b_{ij} - \dot{\Omega}^p_{ij})n_j,$$

that is

$$\frac{dn_i}{dt} = [\dot{\Omega}^*_{12}n_2 + \dot{\Omega}^*_{13}n_3, \dot{\Omega}^*_{21}n_1 + \dot{\Omega}^*_{23}n_3, \dot{\Omega}^*_{31}n_1 + \dot{\Omega}^*_{32}n_2]. \tag{3.18}$$

To calculate the rate of change of the zenith (θ) and azimuth (ϕ) angles of the normal vector, first note that $\cos\theta = n_3$, and $\tan\phi = n_2/n_1$. The time derivatives then become

$$\frac{d\theta}{dt} = \frac{\dot{n}_3}{\sqrt{1 - n_3^2}}, \tag{3.19}$$

$$\frac{d\phi}{dt} = \frac{n_1\dot{n}_2 - \dot{n}_1 n_2}{n_1^2 + n_2^2}. \tag{3.20}$$

In the absence of bulk rotation, Eqs. (3.19) and (3.20) lead to

$$\frac{d\theta}{dt} = -\frac{\dot{\gamma}_0/\tau_0^3}{12}(2\tau_{(1)}^3 - \tau_{(2)}^3 - \tau_{(3)}^3), \tag{3.21}$$

and

$$\frac{d\phi}{dt} = \frac{\dot{\gamma}_0/\tau_0^3}{4\sqrt{3}\sin\theta}(\tau_{(2)}^3 - \tau_{(3)}^3), \tag{3.22}$$

where the $\tau_{(i)}$'s are the RSS on slip systems $i = 1, 2, 3$ (see Appendix A.1.1). Equations (3.21) and (3.22) are used below to calculate the evolution of zenith and azimuth angles in uniaxial compression/extension and pure shear stress.

3.5 STRAIN RATES UNDER SPECIFIC STRESS CONDITIONS FOR GIRDLE FABRICS

Equation 3.12 is used to derive an anisotropic flow law for a girdle fabric subject to several common stress states. Figure 3.1 shows a girdle fabric, in which the zenith angle of all the c-axes is between α_0, the girdle angle, and α, the cone angle, and the azimuth angles are uniformly distributed between $0°$ and $360°$. The ODF for the girdle fabric is $F(\theta, \phi) = \sin\theta/[2\pi(\cos\alpha_0 - \cos\alpha)]$; $\alpha_0 = 0$ yields the ODF for cone fabric. For isotropic ice the ODF is $F(\theta, \phi) = \sin\theta/(2\pi)$. The strain rates depend on the anisotropy through cone angles (α) which can vary from $\alpha = 90°$ (isotropic ice) to $\alpha = 0°$ (strongly anisotropic, all crystals vertical).

It is convenient to express the strain rates normalized by the isotropic response; thus revealing the enhancement relative to isotropic ice. In the past, scalar enhancement factors have been used to describe the effects of anisotropy on the deformation rate. Care is needed when dealing with anisotropic material, since the enhancement depends on the orientation, contrary to the effect of temperature, for example, which is isotropic.
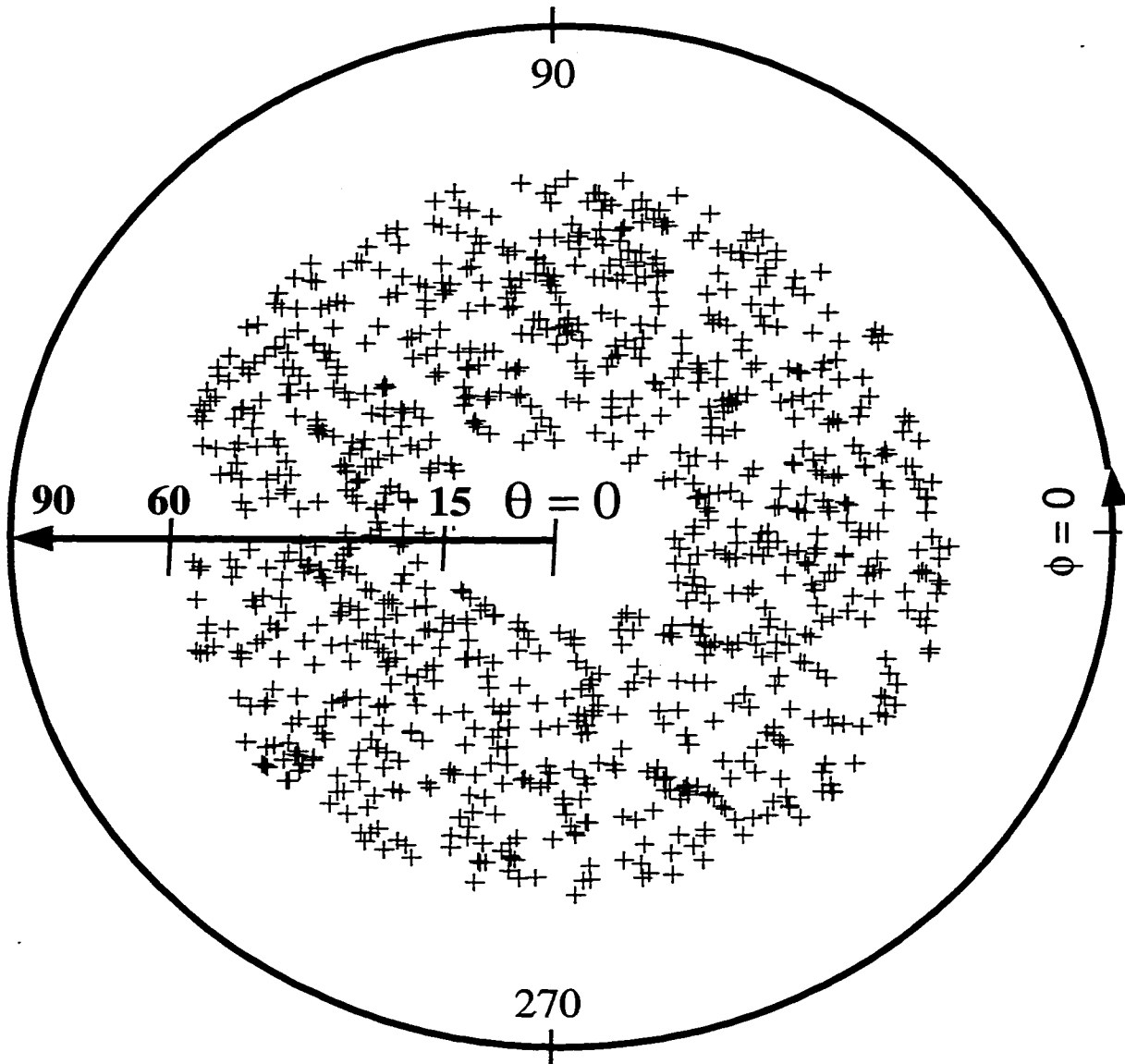
Figure 3.1: An equal area plot (Schmidt-plot) of a girdle fabric. The c-axes are distributed uniformly between $\alpha_0 = 15°$ (girdle angle) and $\alpha = 60°$ (cone angle). Also shown are the zenith angle, θ and the azimuth, ϕ.

The velocity gradient of a single crystal is used to gain insight into the deformation of crystal aggregates.

For uniaxial compression and pure shear it is possible to derive equations for the evolution of the zenith (θ) and azimuth (ϕ) angles, since there is no bulk rotation associated with the deformation; therefore no further assumptions about the fabric symmetry are needed. The homogeneous stress assumption leads to fabric evolution that is faster (as a function of strain) than is observed (*Castelnau et al.*, 1996a; *Thorsteinsson*, 2000b). The overall pattern and symmetry is though similar to other model results and observations, and the solutions here does yield useful insight into fabric development.

3.5.1 Uniaxial Compression

In vertical uniaxial compression, the only non-zero component of the Cauchy stress tensor is $\sigma_{33} = \sigma$. The maximum RSS on the basal plane is $\sigma/2$ at $\theta = 45°$ (as pointed out by *Weertman* (1963)), and it is zero at $\theta=0°$ and $90°$.

Examining the velocity gradient tensor of single crystals, $\mathbf{L}^c$, in the applied stress field is useful at this point, since the averaging method used here (*Sachs*, 1928) simply averages the deformation rates of single crystals. Figure 3.2 shows the velocity gradient of a single crystal in uniaxial compression as a function of its zenith and azimuth angles, $L_{ij}^c(\theta, \phi)$, on an equal area hemispheric plot (see Fig. 3.1). The components are in a matrix arrangement, with the L_{11}^c-component in the top left corner. When the bulk fabric has a uniform distribution of c-axes within a vertical cone or girdle, the resulting bulk response is obtained by averaging $L_{ij}^c(\theta, \phi)$ between two concentric circles. Figure 3.2 shows that although all the components are non-zero, the center-symmetric azimuth averaging will leave only the diagonal terms non-zero. We can also use Fig. 3.2 to infer the strain rates under uniaxial compression for other types of fabric (for instance tilted cone or diamond-maximum pattern); just sum the rates at all points where c-axes reside for the given pattern.

For a single crystal, the $\dot{\varepsilon}_{33}^c = L_{33}^c$ component (bottom right in Fig. 3.2; see derivation in Appendix A.1.6) is

$$\dot{\varepsilon}_{33}^c = \beta A \sigma_{33}^3 \cos^4 \theta \sin^4 \theta \frac{1}{72}. \tag{3.23}$$
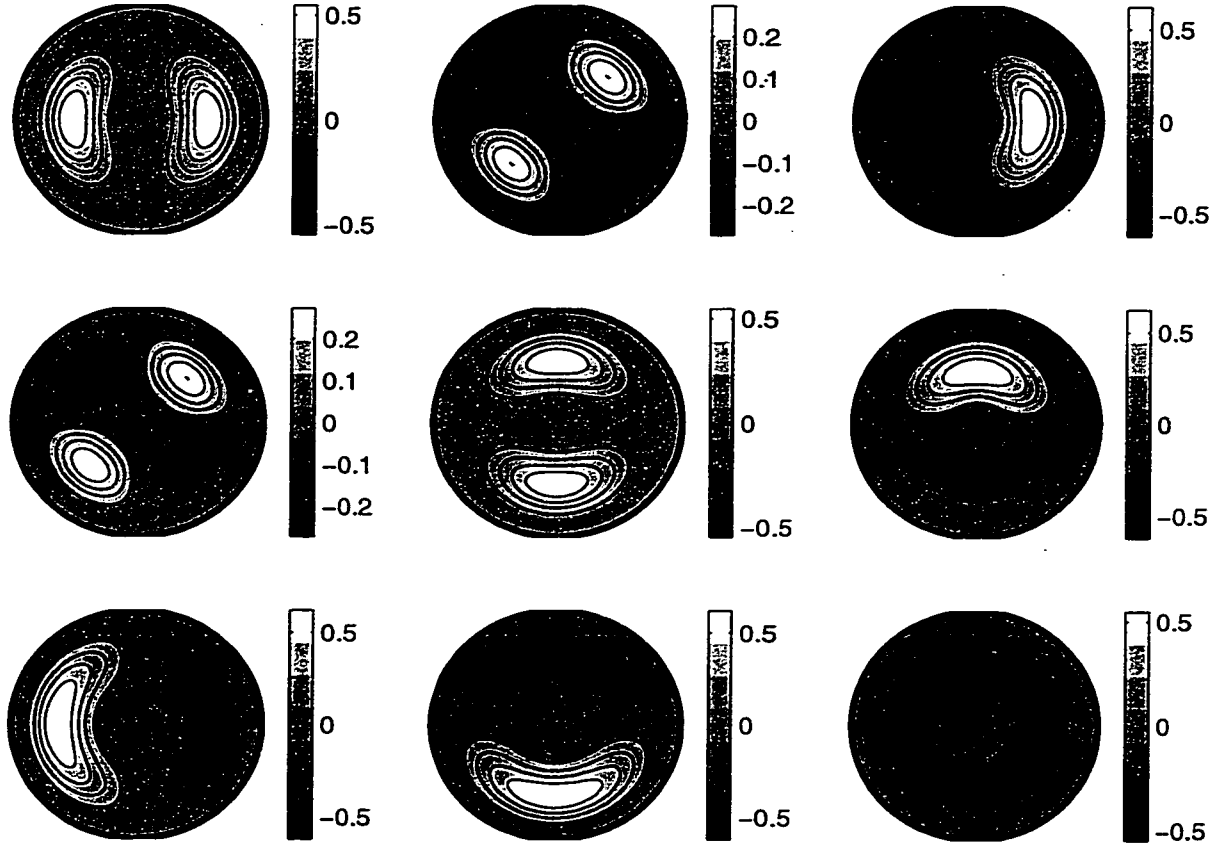
Figure 3.2: The velocity gradient tensor, $L^c_{ij}(\theta, \phi)$, of a single crystal in uniaxial compression. The crystal is deforming only by glide in the basal plane. Each plot shows a different component L^c_{ij} normalized by $(A\sigma^3)$, with the L^c_{11}-component in the top left corner and L^c_{33} in the bottom right corner. Lighter colors are positive and darker negative. See Figure 3.1 for explanation of θ and ϕ.

The bulk strain rate for isotropic ice is

$$\dot{\varepsilon}_{33} = \frac{\beta A \sigma^3}{72 \cdot 2\pi} \int_0^{2\pi} \int_0^{\pi/2} \cos^4 \theta \sin^5 \theta d\theta d\phi = \frac{\beta A \sigma^3}{9} \frac{1}{315}. \tag{3.24}$$

It is easy to show that $\dot{\varepsilon}_{11} = \dot{\varepsilon}_{22} = -\frac{1}{2}\dot{\varepsilon}_{33}$, and that all other components are zero.

For the same component, Glen's flow law (*Glen*, 1958) gives $\dot{\varepsilon}_{33} = \frac{2}{9}A\sigma^3$, so we find that β must in this case be $\beta = \frac{315 \times 9 \times 2}{9} = 630$.

The bulk strain rate $\dot{\varepsilon}_{33}$ as a function of cone angle α is

$$\dot{\varepsilon}_{33}(\alpha) = \frac{2}{9}A\sigma^3 \times \tag{3.25}$$

$$\left[\frac{\cos^5 \alpha(35\sin^4 \alpha + 20\sin^2 \alpha + 8) - 8}{8(\cos \alpha - 1)}\right].$$

For a girdle fabric,

$$\dot{\varepsilon}_{33}(\alpha, \alpha_0) = \frac{\cos \alpha - 1}{\cos \alpha - \cos \alpha_0}\left(\dot{\varepsilon}_{33}(\alpha) - \dot{\varepsilon}_{33}(\alpha_0)\right), \tag{3.26}$$

where α_0 is the girdle angle.

The maximum enhancement in uniaxial compression occurs when all the crystals form a girdle with $\theta = 45°$ (where the RSS is at maximum), then $\dot{\varepsilon}_{33}^c = \beta A \sigma^3/(16 \times 72)$, and thus the ratio

$$E_{uc}^c(max) = \frac{\dot{\varepsilon}_{33}^c(\theta = 45°)}{\dot{\varepsilon}_{33}(\alpha = 90°)} = \frac{9 \times 315}{16 \times 72} = 2.461.$$

Figure 3.3 shows the enhancement of vertical strain rate, $E = \dot{\varepsilon}_{33}(\alpha)/\dot{\varepsilon}_{33}(90°)$ for a cone angle fabric as a function of α. Ice in compression is "soft" for all cone angles down to $\alpha \simeq 36°$. For smaller cone angles the ice is "stiff". The ice becomes softer as the cone contracts from $\alpha = 90°$ since many of the "hard" horizontal crystals are removed. The ice then gets "hard" when mostly vertical crystals are left (see Fig. 3.2). The maximum strain rate for cone fabric occurs at $\alpha \simeq 57°$ (remember that the ODF for cone fabric is a sine curve) and gives enhancement of 1.678 relative to isotropic ice (Fig. 3.3).

It is commonly assumed that vertical strain rate at an ice divide remains constant from the surface down to some depth h, and then decreases to zero at the bed (*Dansgaard and Johnsen*, 1969). For isotropic ice this means that the vertical deviatoric stress is constant down to h (changes associated with temperature are neglected here since the effect is the
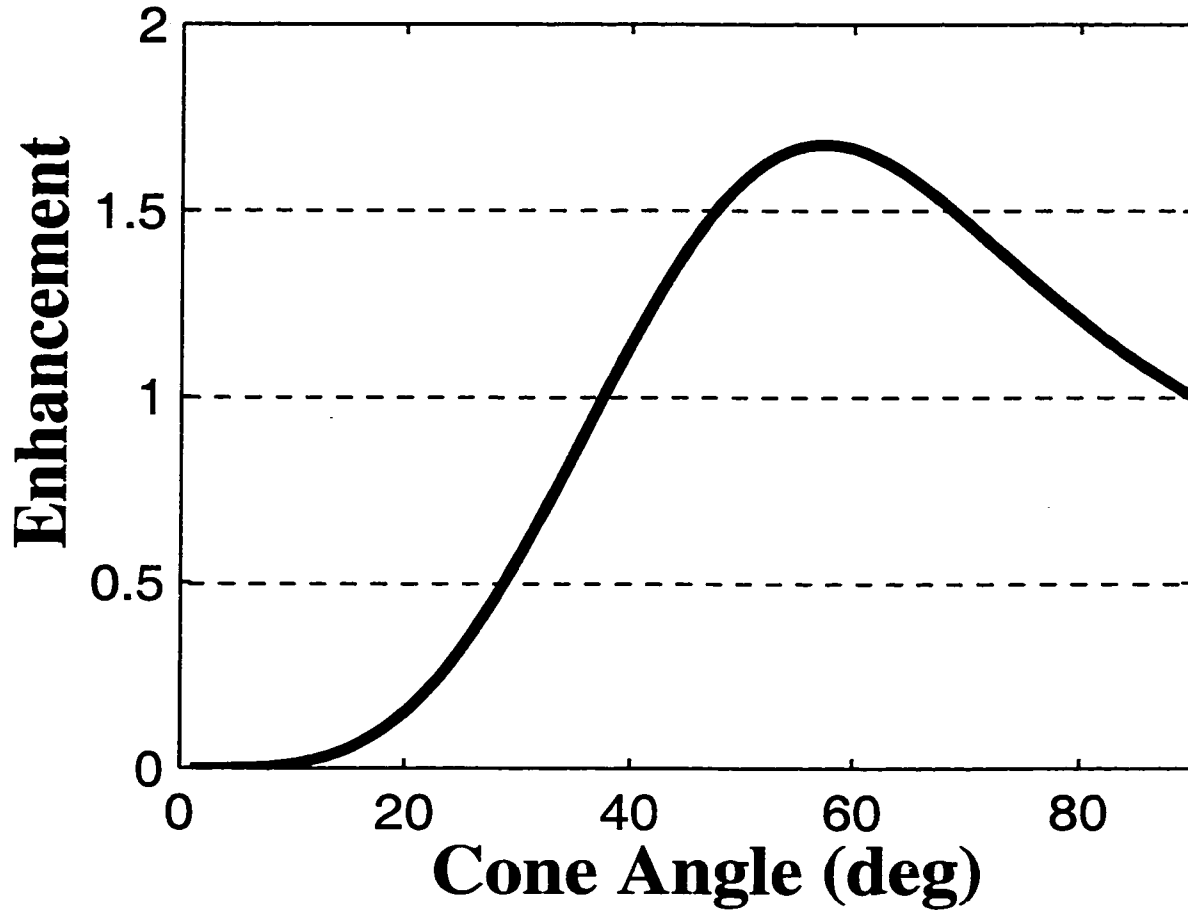
Figure 3.3: Enhancement in uniaxial compression as a function of cone angle. The enhancement is defined as $E = \dot{\varepsilon}_{33}(\alpha)/\dot{\varepsilon}_{33}(90°)$.

same for isotropic and anisotropic ice). But when anisotropy is taken into account the deviatoric stress must vary with depth since the fabric (expressed by cone angle, see Fig. 3.3) varies. If the strain rates follow the Dansgaard-Johnson pattern, and the deviatoric vertical compressive stress near the surface ($\alpha \simeq 90°$) is $\sigma = \sigma_0$, then $\sigma(\alpha = 57°) = 0.84\sigma_0$, $\sigma(\alpha = 20°) = 1.875\sigma_0$ and $\sigma(\alpha = 5°) = 11\sigma_0$. The anisotropy thus causes stress redistribution, concentrating stress on the stiff sections ($\alpha < 36°$) and reducing it on the soft sections ($\alpha > 36°$).

Fabric Development in Uniaxial Compression

Using the equations derived in Appendix A.1, we find that

$$
\begin{aligned}
dn_1/dt &= -\ \frac{\beta A(T)\sigma^3}{144}\sin^3(\theta)\cos^4(\theta)\cos(\phi), \\
dn_2/dt &= -\ \frac{\beta A(T)\sigma^3}{144}\sin^3(\theta)\cos^4(\theta)\sin(\phi), \\
dn_3/dt &= \ \frac{\beta A(T)\sigma^3}{144}\sin^4(\theta)\cos^3(\theta).
\end{aligned}
\tag{3.27}
$$

The rate equations for the azimuth and zenith angles of each crystal (Eqs. 3.19 and 3.20) then become

$$
\frac{d\phi}{dt} = 0,
\tag{3.28}
$$

$$
\frac{d\theta}{dt} = \frac{\beta A}{144}(\sigma_{33}\cos\theta\sin\theta)^3.
\tag{3.29}
$$

Figure 3.4 shows the zenith angle velocity, $d\theta/dt$, where time has been non-dimensionalized using $T = tA\sigma_{33}^3$. The azimuth angle does not change with time; if the initial fabric in vertical uniaxial compression has azimuth symmetry, it will retain that symmetry. Crystals starting at intermediate zenith angles will be rotated quickly towards vertical (towards horizontal in vertical uniaxial extension), but the slow velocity for small zenith angles (also near horizontal) means that crystals at those angles hardly rotate at all. This leads to a fabric development that is not entirely consistent with observations. This pattern results from the assumption of homogeneous stress, in which crystals near vertical and horizontal have no resolved shear stress on the basal plane. This point is examined further by *Thorsteinsson* (2000b) by introducing inter-crystalline interactions.
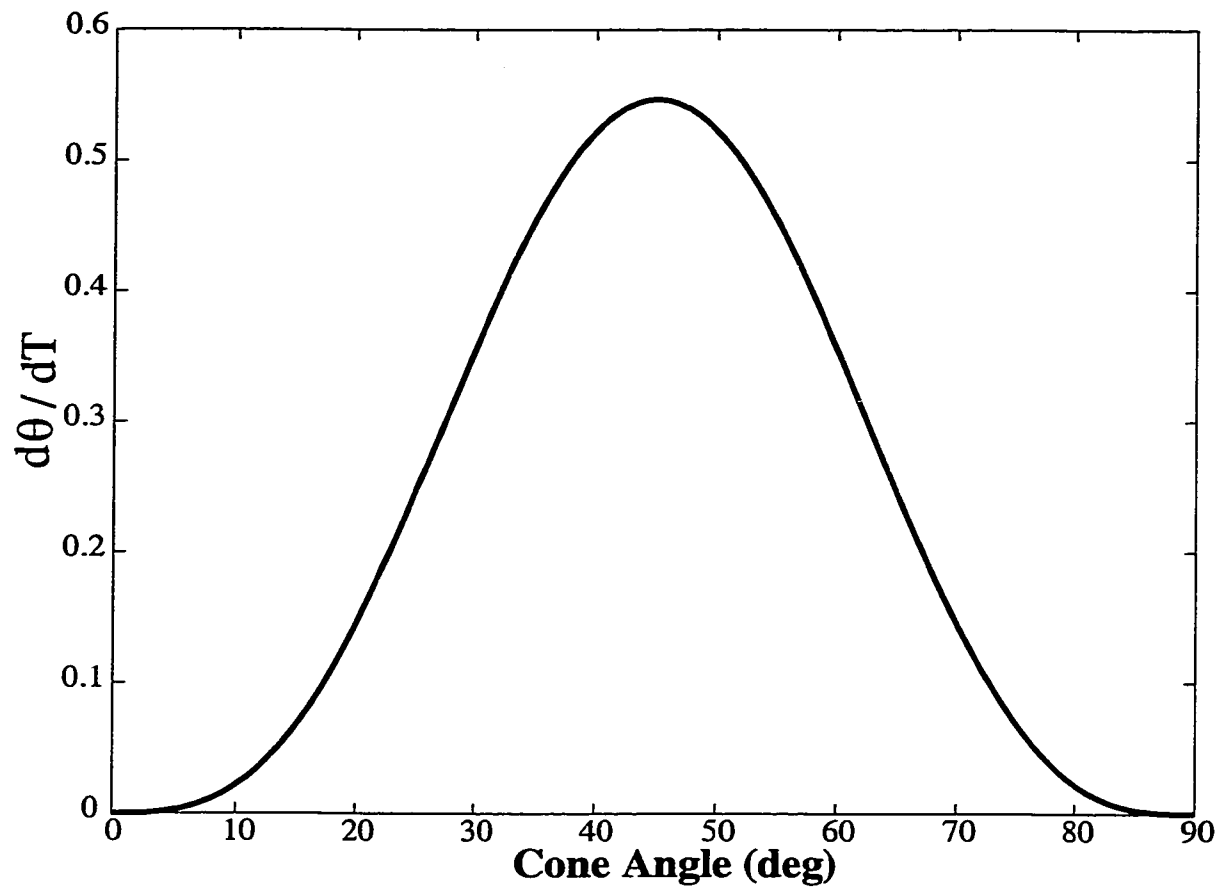
Figure 3.4: Zenith angle velocity, $d\theta/dT$, as a function of zenith angle, θ. Here $T = tA\sigma^3$.

3.5.2 Pure Shear

In pure shear the non-zero components of the stress tensor are $\sigma_{11} = \sigma$ and $\sigma_{33} = -\sigma$. Figure 3.5 shows the velocity gradient tensor of a single crystal, $\mathbf{L}^c$, in pure shear for all possible orientations (θ, ϕ). Note that the L_{22}^c component will not average to zero for all cone angles. Thus, contrary to the isotropic case, there will be an extension/compression normal to the plane of the applied stress. The same procedure to get bulk strain rates as a
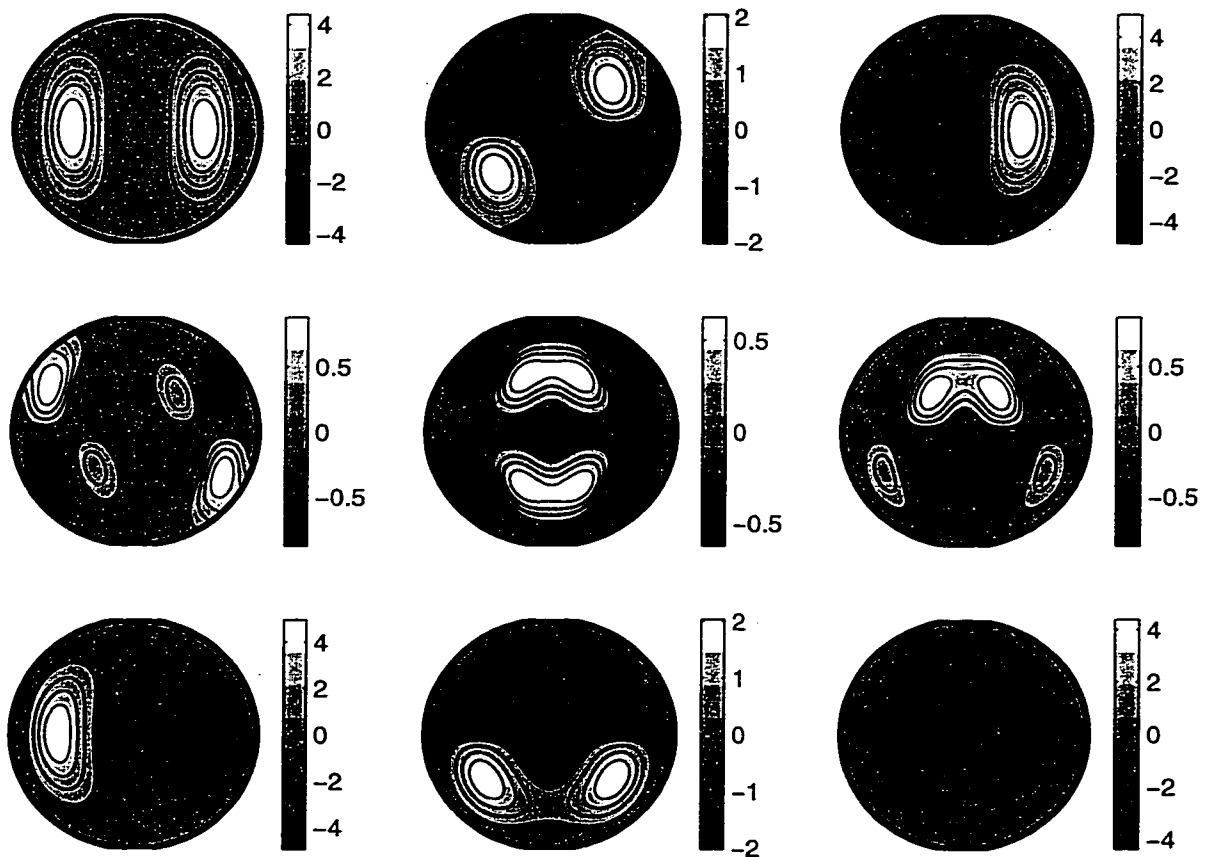
Figure 3.5: The velocity gradient tensor, $L_{ij}^c(\theta, \phi)$, of a single crystal in pure shear stress $(\sigma_{33} = -\sigma_{11})$. The crystal is deforming only by glide in the basal plane. Each plot shows a different component L_{ij}^c normalized by $A\sigma^3$, with the L_{11}^c-component in the top left corner and L_{33}^c in the bottom right corner. Lighter colors are positive and darker negative. See Figure 3.1 for explanation of θ and ϕ.

function of cone angle as for the uniaxial compression gives

$$\dot{\varepsilon}_{11}(\alpha) = A\sigma^3 \Big(384090 \cos\alpha + 49420 \cos 3\alpha$$
$$-42084 \cos 5\alpha - 2445 \cos 7\alpha + 4235 \cos 9\alpha - 393216 \Big) \tag{3.30}$$
$$/[393216(\cos\alpha - 1)],$$

$$\dot{\varepsilon}_{22}(\alpha) = \frac{35A\sigma^3}{6144(1 - \cos\alpha)} (177 \cos\alpha + 47 \cos 3\alpha) \sin^6 \alpha, \tag{3.31}$$

$$\dot{\varepsilon}_{33}(\alpha) = A\sigma^3 \Big(16384 - 15330 \cos\alpha - 3080 \cos 3\alpha$$
$$+2016 \cos 5\alpha + 255 \cos 7\alpha - 245 \cos 9\alpha \Big) \tag{3.32}$$
$$/[16384(\cos\alpha - 1)].$$

Figure 3.6 shows the non-zero components of the strain rate tensor as a function of cone angle, normalized by $A\sigma^3$ ($=\dot{\varepsilon}_{33} = -\dot{\varepsilon}_{11}$), which in this case gives the enhancement relative to isotropic ice. Note in particular that, although relatively small, the $\dot{\varepsilon}_{22}$ component is non-zero for a range of cone angles. This means that a block of ice deforming in a pure shear stress state will expand/contract in a direction perpendicular to the plane defined by the applied stress. Correspondingly, a stress σ_{22} would be required to impose plane strain rate $\dot{\varepsilon}_{11} = -\dot{\varepsilon}_{33}$, $\dot{\varepsilon}_{22} = 0$.

Fabric Development in Pure Shear

Figure 3.7 shows the path of the c-axes as the fabric develops. All the crystals are moving towards the center (compression axis, $\hat{x}_3$), but the extension along the $\hat{x}_1$-axis forces the crystals to move towards the $\hat{x}_2$-axis as they are slowly migrating towards the center. This pattern implies that the azimuth symmetry will not persist in a pure shear stress field.

3.5.3 Simple Shear

In simple shear stress state, the only non-zero components of the stress tensor are $\sigma_{31} = \sigma_{13} = \sigma$. The maximum RSS on the basal plane is σ for zenith angles of $\theta = 0°$ and $90°$, and it is zero at $45°$. Figure 3.8 shows the velocity gradient tensor for a single crystal, L^c, in simple shear stress state. The L^c_{13}-term is large for nearly vertical crystals (small zenith angle) and the L^c_{31}-term is large for nearly horizontal crystals (large zenith angle). For
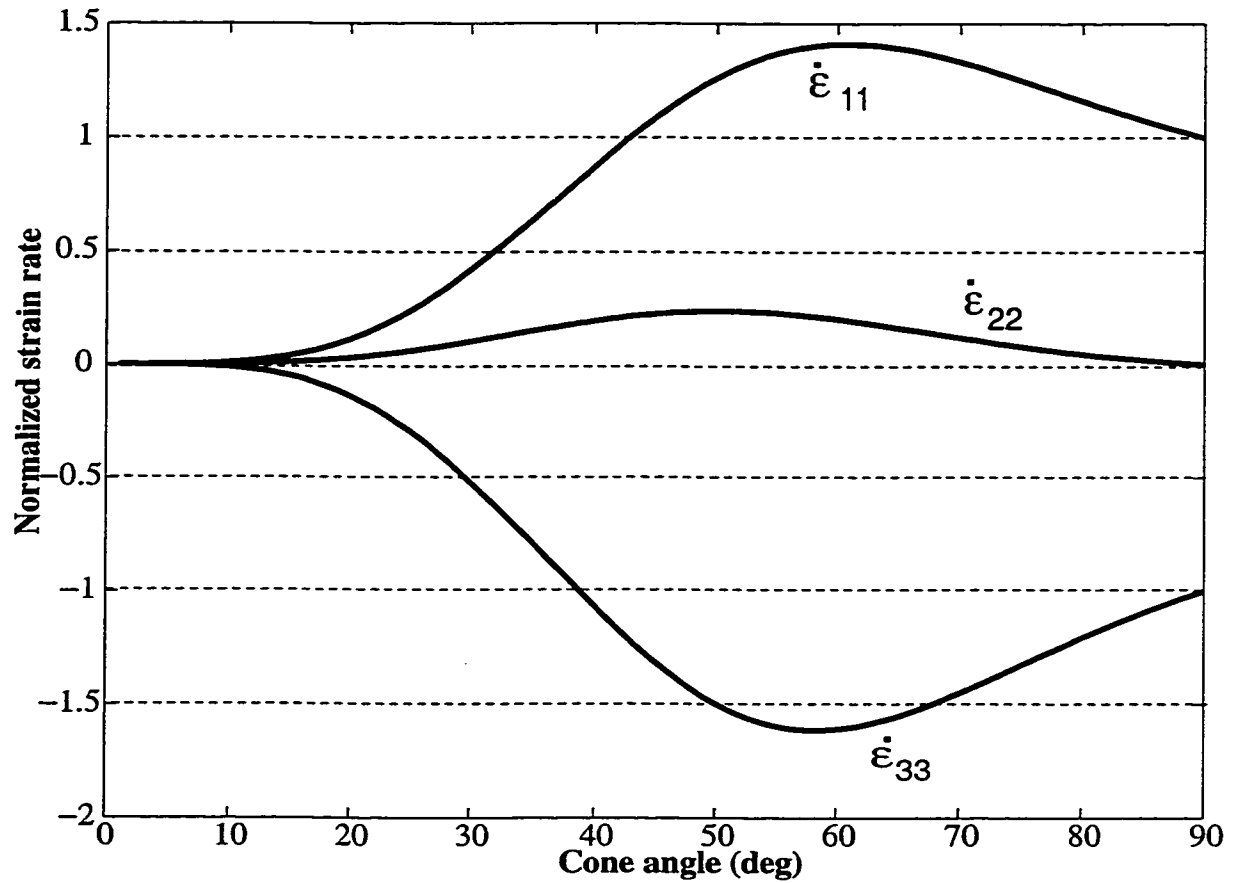
Figure 3.6: Normalized strain rate $\dot{\varepsilon}_{ij}/(A\sigma^3)$ in pure shear stress state $\sigma_{11} = -\sigma_{33}$ as a function of cone angle. Here the normalized strain rate is equal to the enhancement relative to isotropic ice. Note the non-zero strain rate $\dot{\varepsilon}_{22}$, which is transverse to the plane of applied stress.
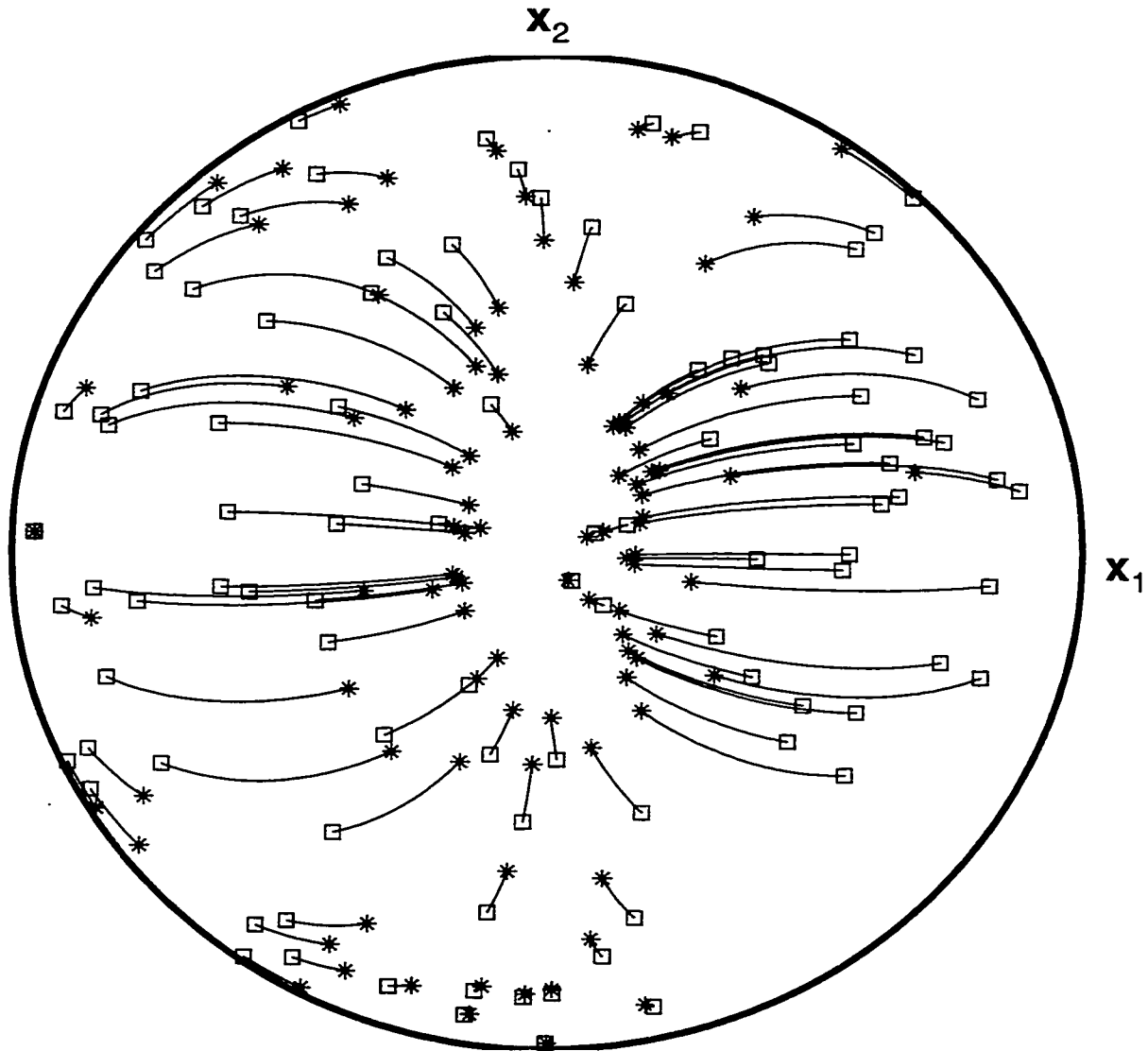
Figure 3.7: Evolution of the zenith and azimuth angles in pure shear. The boxes are the initial position ($t = 0$) and the stars are the final positions at $t = T$. Note how the axes move away from the extension axis ($\hat{x}_1$, horizontal in the plane of the page), and towards the compression axis ($\hat{x}_3$, normal to the plane of the page).

isotropic ice these two terms contribute equally to the bulk deformation and therefore there is no bulk rotation produced, which explains the need to define $\dot{\Omega}^d$ (Eq. 3.14). Also note, that although smaller, several other velocity gradient components are non-zero. They average to zero for the vertical cone distribution of c-axes used here, but for other distributions they might not.

Figure 3.8: The velocity gradient tensor, $L^c_{ij}(\theta, \phi)$, of a single crystal in simple shear stress $\sigma_{13} = \sigma_{31}$. The crystal is deforming only by glide in the basal plane. Each plot shows a different component L^c_{ij} normalized by $(A\sigma^3)$, with the L^c_{11}-component in the top left corner and L^c_{33} in the bottom right corner. Lighter colors are positive and darker negative. See Figure 3.1 for explanation of θ and ϕ.

For a single crystal, the strain rate (Eq. 3.8) is

$$
\dot{\varepsilon}_{13}^c(\theta, \phi) = \frac{\beta}{2} A \sigma_{13}^3 \frac{1}{3^4} \Big[
$$
$$
(\cos\phi(\cos^2\theta - \sin^2\theta))^4 + \frac{1}{2^4}\big[
$$
$$
(\sin^2\theta \cos\phi \cos\theta(\cos\theta\cos\phi + \sqrt{3}\sin\phi))^4
$$
$$
+ (\sin^2\theta \cos\phi - \cos\theta(\cos\theta\cos\phi - \sqrt{3}\sin\phi))^4]\Big].
$$

(3.33)

For an isotropic distribution,

$$
\dot{\varepsilon}_{13} = \frac{1}{2\pi} \int_0^{2\pi} \int_0^{\pi/2} \dot{\varepsilon}_{13}^c \sin\theta d\theta d\phi = \beta A \sigma^3 \frac{1}{630},
$$

(3.34)

Glen's flow law gives $\dot{\varepsilon}_{13} = A\sigma^3$, so as before, $\beta = 630$.

The simple shear strain rate for polycrystals with c-axes distributed uniformly within a cone with a vertical ($\hat{x}_3$-axis) symmetry axis as a function of cone angle α is

$$
\dot{\varepsilon}_{13}(\alpha) = \frac{A\sigma^3}{3072(\cos\alpha - 1)} \Big(2730\cos\alpha - 35\cos 3\alpha
$$
$$
+357\cos 5\alpha - 15\cos 7\alpha + 35\cos 9\alpha - 3072\Big).
$$

(3.35)

For a girdle fabric

$$
\dot{\varepsilon}_{13}(\alpha, \alpha_0) = \frac{\cos\alpha - 1}{\cos\alpha - \cos\alpha_0}\Big(\dot{\varepsilon}_{13}(\alpha) - \dot{\varepsilon}_{13}(\alpha_0)\Big).
$$

(3.36)

The maximum enhancement in simple shear occurs for a perfect vertical alignment of all the crystals

$$
E_{ss}(max) = \frac{\dot{\varepsilon}_{13}(\alpha = \theta = 0°)}{\dot{\varepsilon}_{13}(\alpha = 90°)} = \frac{1/144}{1/630} = \frac{35}{8} = 4.375.
$$

Figure 3.9 shows the shear strain rate, normalized to the isotropic shear strain rate, as a function of cone angle. Note that for cone angles between 60° and 90°, the deformation is actually a little slower than for isotropic ice ($E < 1$), since many of the easily deformable horizontal crystals are absent.

The typical vertical orientation of fabric implies alteration of the velocity profile in laminar flow (*Paterson*, 1994). Figure 3.10 shows velocity profiles for isotropic and anisotropic ice in laminar flow. Here the cone angle for the anisotropic ice changes linearly from 90° at the surface to 20° at the bottom, while the stress and temperature distributions are the same for both the isotropic and anisotropic ice. Due to the anisotropy, the surface
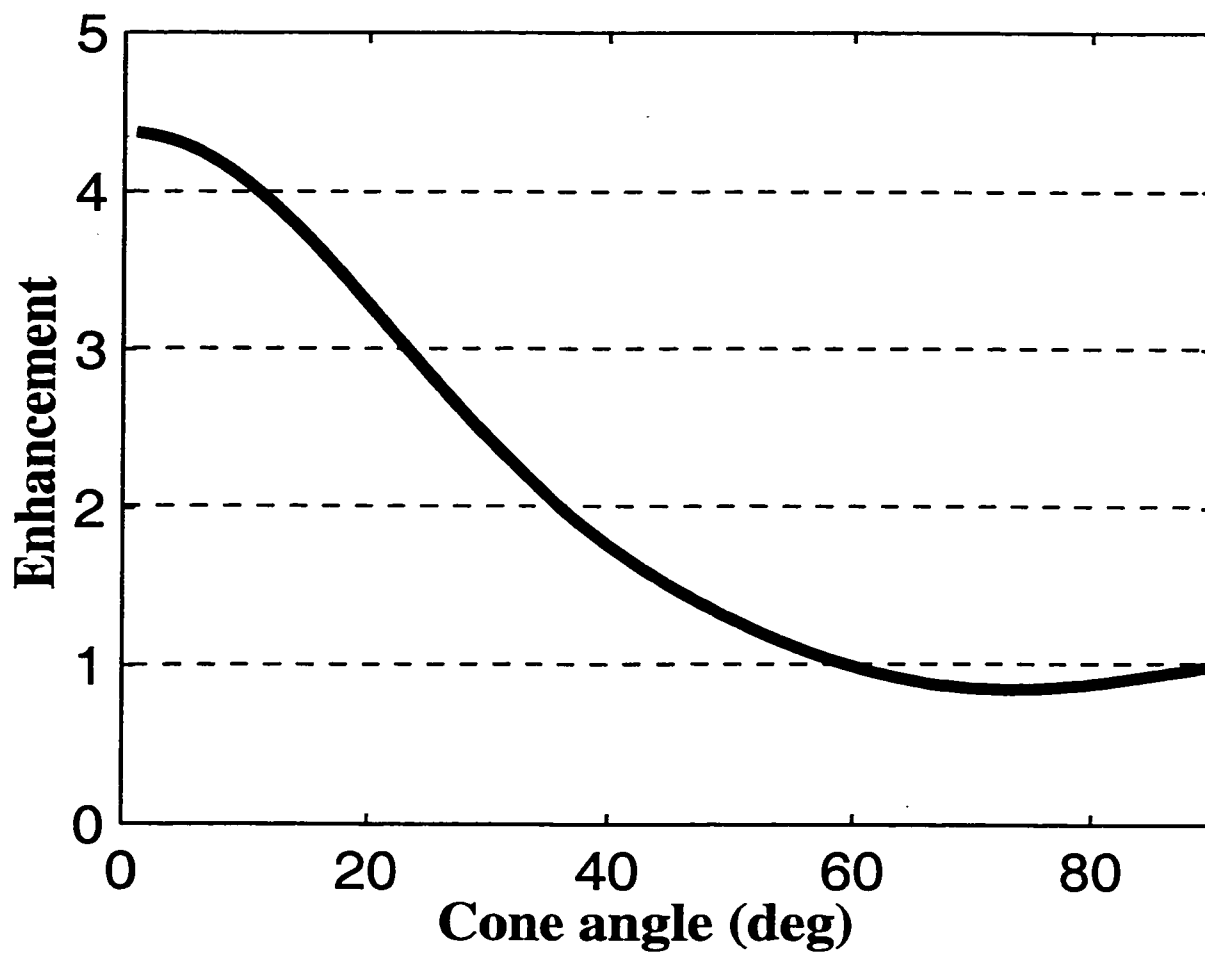
Figure 3.9: Enhancement in simple shear as a function of cone angle. Note how the enhancement is smaller than 1 for cone angles between 60° and 90°, with a minimum of $E(\alpha = 73°) = 0.857$.

velocity is 2.36 times larger than in the isotropic case, and the mean velocity is 2.5 times larger. For isotropic ice, the ratio of the mean velocity to the surface velocity $\overline{u}/u_s$ is 0.8 ($\overline{u}/u_s$=(n+1)/(n+2); n=3). This ratio ($\overline{u}/u_s$) is 0.848 in the anisotropic case examined here. It will in general be different from 0.8; by how much depends on the variation of the cone angle with depth.
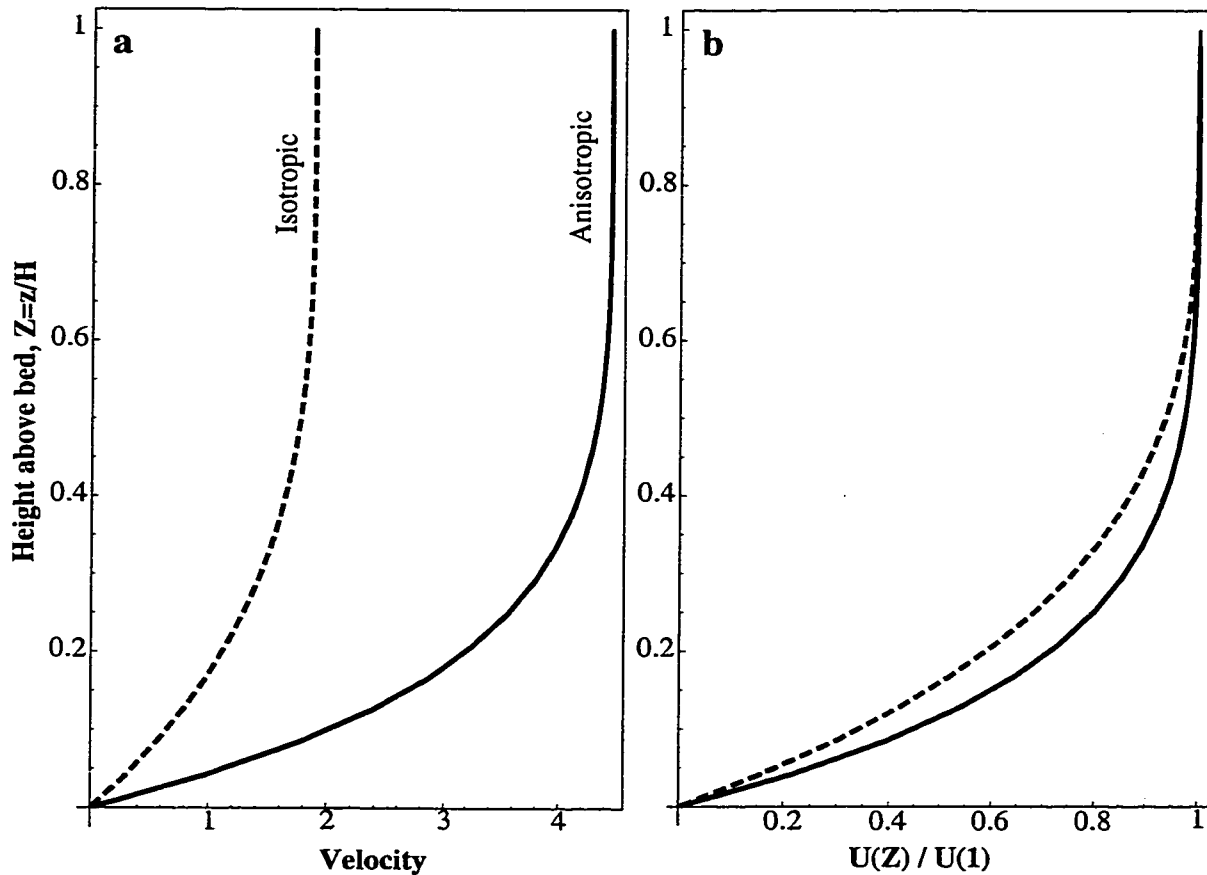
Figure 3.10: a) Horizontal velocity as a function of height above bed ($Z = z/H$, where H is the ice thickness) in laminar flow for isotropic ice ($\alpha(Z) = 90°$) and anisotropic ice ($\alpha(Z) = 20° + 70°Z$). b) The anisotropy enhances the deformation, and concentrates it closer to the bed.

3.5.4 Uniaxial compression and simple shear

Now I consider more complex stress states in which more components of the stress tensor are non-zero. As we include more terms in the equation for the resolved shear stress, τ (Eq. 3.5), the number of terms for the strain rate increases rapidly; since τ is raised to the n-th power.

The combination of uniaxial compression and simple shear stress exists in the vicinity of ice domes for example. The stress tensor in this case has the form

$$\sigma_{ij} = \begin{bmatrix} 0 & 0 & \tau \\ 0 & 0 & 0 \\ \tau & 0 & \sigma \end{bmatrix}.$$

Adding an additional mean compression does not change the deformation. Equation (3.8) shows that the stress affects the strain rate through the RSS (Eq. 3.5). The RSS on a crystal slip system is

$$\tau_{(s)} = \underbrace{(S_{13} + S_{31})\tau}_{T_{13}} + \underbrace{S_{33}\sigma}_{T_{33}},$$

which, with $n = 3$, becomes,

$$\tau_{(s)}^3 = T_{13}^3 + 3T_{13}^2 T_{33} + 3T_{13}T_{33}^2 + T_{33}^3. \tag{3.37}$$

The first and the last term are exactly the values of $\tau_{(s)}$ for simple shear and uniaxial compression acting alone. The non-zero velocity gradient components $(L_{11}, L_{22}, L_{33}, L_{13})$ as a function of stress and cone angle are given in Appendix A.1.7.

Figures 3.11 and 3.12 show the bulk vertical strain rate $(\dot{\varepsilon}_{33})$ and shear strain rate $(\dot{\varepsilon}_{13})$ as a function of vertical cone angle. For the $\dot{\varepsilon}_{33}$-component, the total strain rate is the sum of two terms (Fig. 3.11), just as for isotropic ice, but they depend on the fabric $\dot{\varepsilon}_{33}(\alpha) = (f(\alpha)\sigma^2 + g(\alpha)\tau^2)\sigma$, see Appendix A.1.7. The $\dot{\varepsilon}_{13}$-component (Fig. 3.12) has a similar form $\dot{\varepsilon}_{13}(\alpha) = (h(\alpha)\sigma^2 + j(\alpha)\tau^2)\tau$. An enhancement factor derived from the shear strain rate does thus not describe the enhancement in compression.
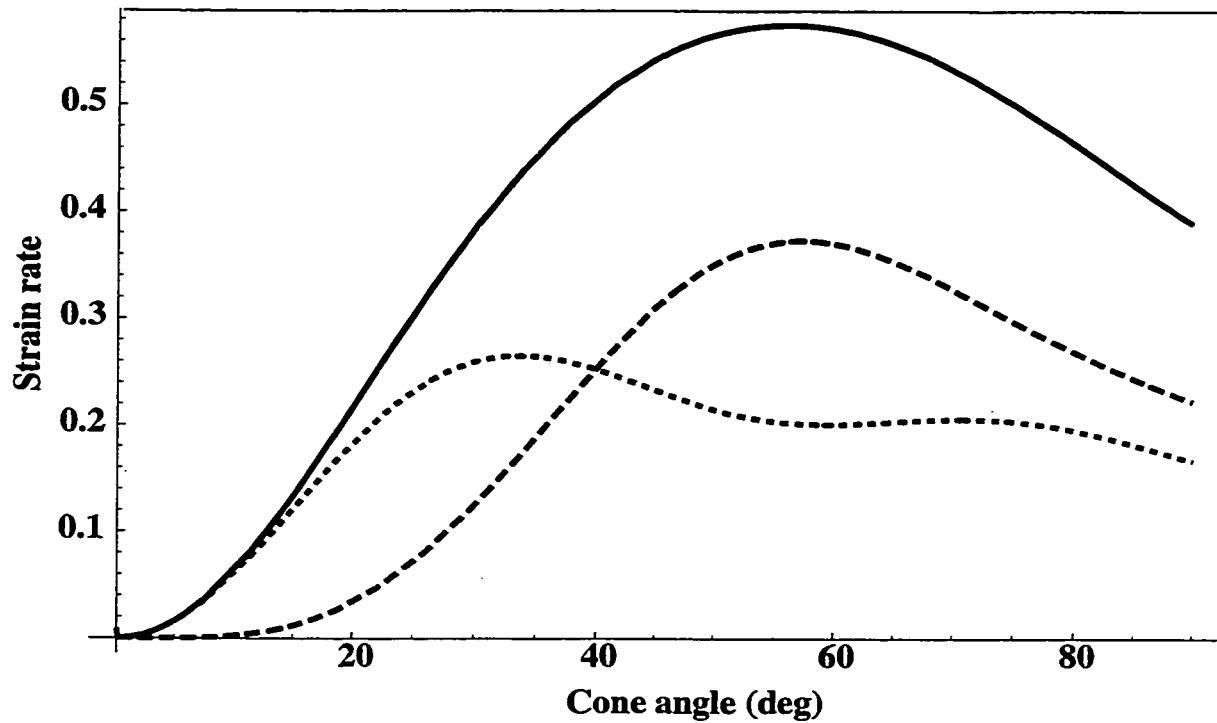
Figure 3.11: Strain rate $\dot{\varepsilon}_{33}(\alpha)$ (solid line) as a function of cone angle in combined compression and shear. The resulting strain rate is made up of two terms, one that depends on σ^3 only (dashed line), and one that depends on the shear stress and compression $\tau^2\sigma$ (dotted line). Here $\sigma = 1.0$ and $\tau = 0.5$.
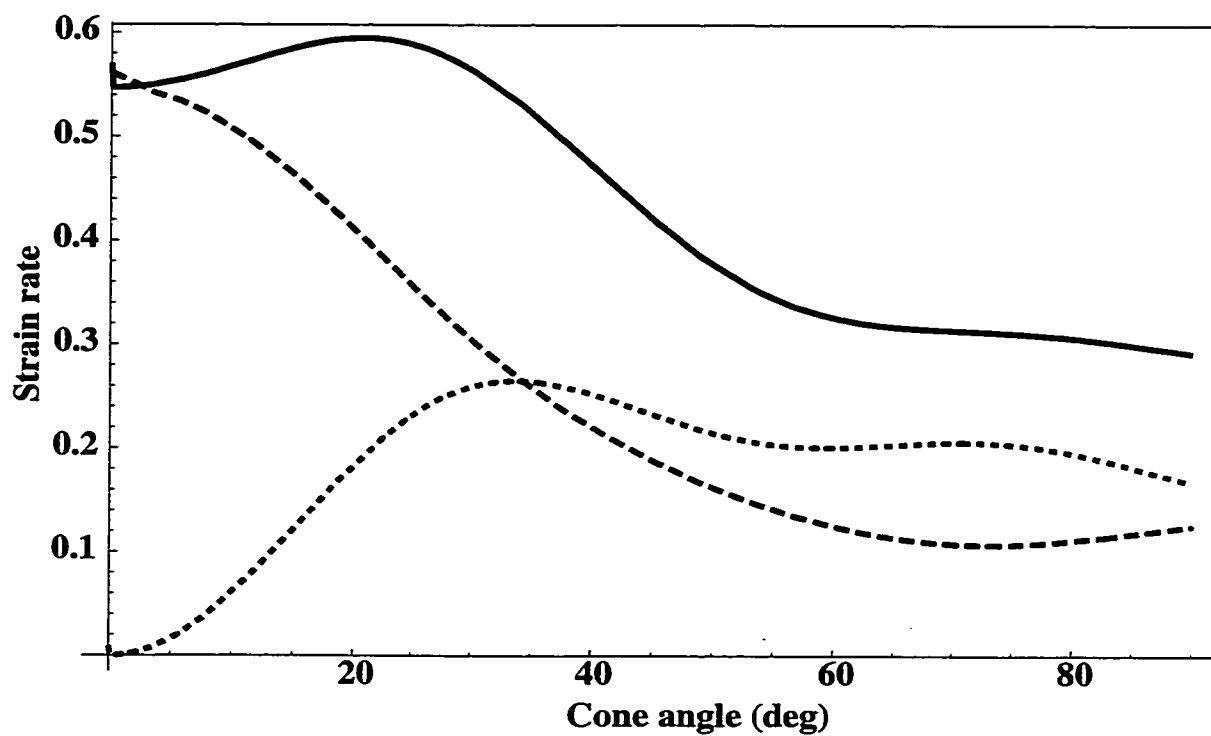
Figure 3.12: Strain rate $\dot{\varepsilon}_{13}(\alpha)$ (solid line) as a function of cone angle in combined compression and shear. The resulting strain rate is made up of two terms, one due to the shear stress τ^3 (dashed line), and one caused by the uniaxial compression stress and shear $\sigma^2\tau$ (dotted line). Here $\sigma = 1.0$ and $\tau = 0.5$.

3.5.5 Pure and simple shear stress

For this case the stress tensor has the form

$$\sigma_{ij} = \begin{bmatrix} -\sigma & 0 & \tau \\ 0 & 0 & 0 \\ \tau & 0 & \sigma \end{bmatrix},$$

and the RSS of a crystal is

$$\tau_{(s)} = (S_{13} + S_{31})\tau + S_{33}\sigma + S_{11}(-\sigma).$$

Following the same procedure as before, we find bulk $\dot{\varepsilon}_{33}$ and $\dot{\varepsilon}_{13}$ as functions of cone angle, shear (τ) and compressive (σ) stress (see Appendix A.1.8). Figure 3.13 shows the normalized bulk response $\dot{\varepsilon}_{33}(\alpha, \tau)/\dot{\varepsilon}_{33}(90°, \tau)$ as a function of cone angle and shear stress (the compressive stress is constant), and Figure 3.14 shows the $\dot{\varepsilon}_{13}(\alpha, \tau)/\dot{\varepsilon}_{13}(90°, \tau)$ component. Note how the peak enhancement in vertical strain increases with increasing shear stress, and moves from $\alpha \simeq 60°$ for $\tau/\sigma < 1$ to $\alpha \simeq 35°$ for $\tau/\sigma > 1$. Also, note the strong gradient for vertical strain rate for strongly anisotropic ice, especially with increasing shear stress. The shear strain rate has a simpler pattern, except when $\tau \sim \sigma$, where the enhancement has a fairly complex structure for strongly anisotropic ice.

The enhancement shown in Figures 3.13 and 3.14 can also be thought of as a result of tilting the cone in pure shear stress $(\tau = 0)$, since simple shear stress state can be represented as rotated pure shear stress. The tilt angle of the cone normal ξ is then given by $\xi = \arctan(\tau/\sigma)/2$. Note, in particular, that this demonstrates that even in a pure shear stress state, a tilted cone (symmetry axis not vertical) will result in a non-zero shear strain rate $(\dot{\varepsilon}_{13})$.

Now consider two bore-holes, one at a ridge, the other at a flank site. We want to measure the vertical strain rate, knowing the deviatoric compressive stress (e.g. constant stress σ_0 in the upper 2/3 of the ice thickness H, and linearly decreasing to zero in the bottom 1/3 of the ice thickness), the shear stress (zero at the ridge, linearly increasing with depth at the flank, reaching at the bed a value twice the surface compressive stress, $\tau = 2\sigma_0(1 - z/H)$) and all other parameters (temperature, dust, etc) that can affect the rheology, at both sites are the same. Now, if we assume that the fabric is the same at both sites (linear from
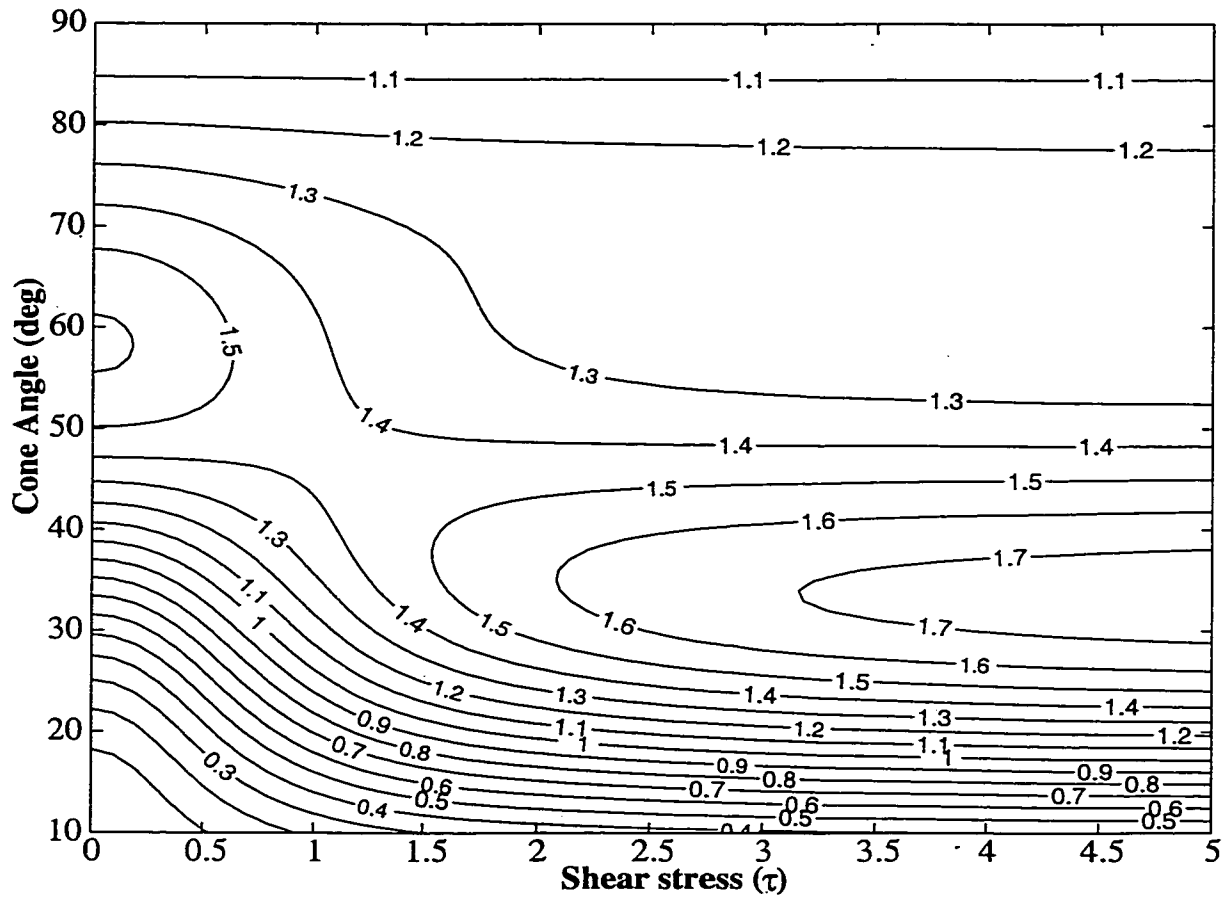
Figure 3.13: The normalized vertical strain rate, $\dot{\varepsilon}_{33}(\alpha, \sigma = -1, \tau)/\dot{\varepsilon}_{33}(\alpha = 90°, \sigma = -1, \tau)$, as a function of shear stress, τ, and cone angle, α. The pure shear stress is $\sigma_{11} = -\sigma_{33} = \sigma = -1$. Note how the compression has a maximum at around 60° when the shear stress is small and near 35° with increasing shear stress.
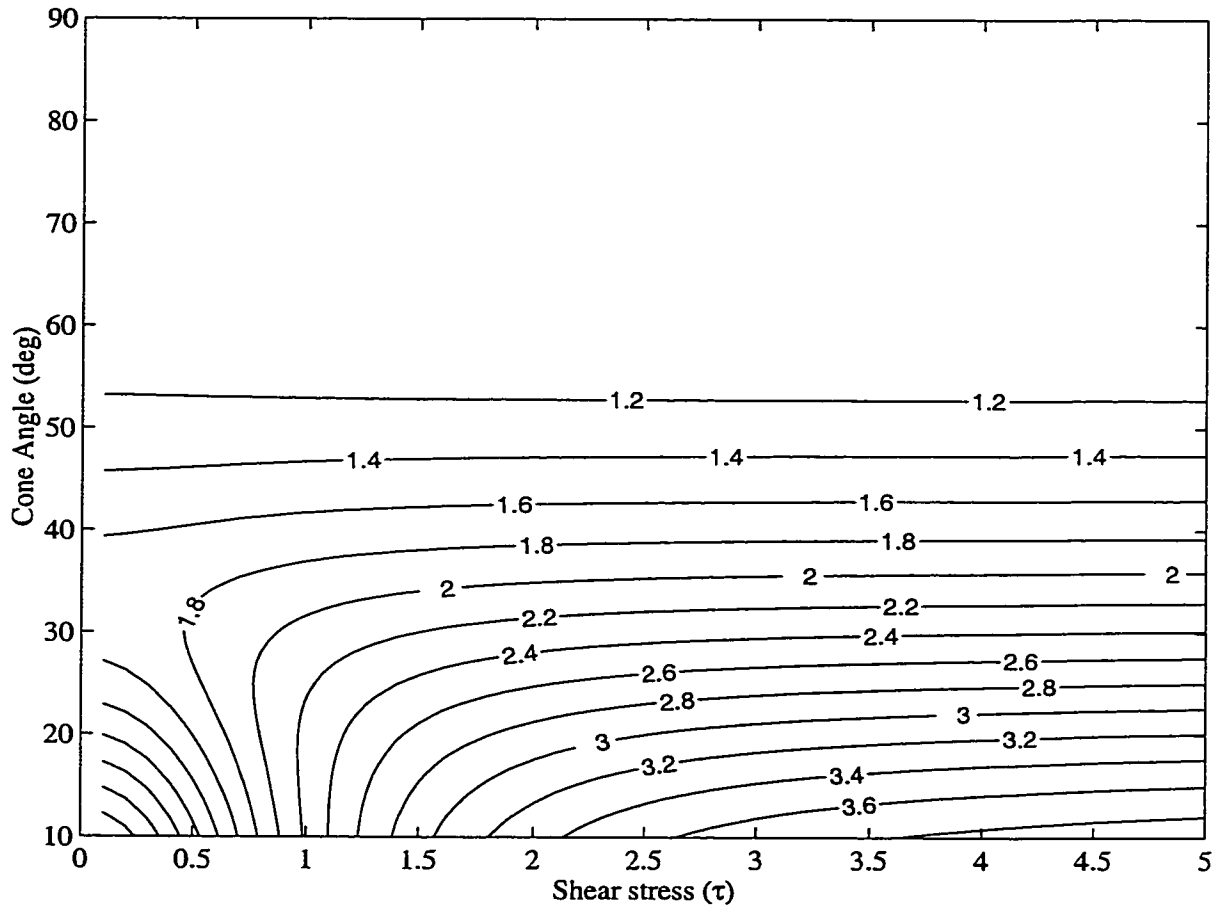
Figure 3.14: The normalized shear strain rate, $\dot{\varepsilon}_{13}(\alpha, \sigma = -1, \tau)/\dot{\varepsilon}_{13}(\alpha = 90°, \sigma = -1, \tau)$, as a function of shear stress, τ, and cone angle, α. The pure shear stress is $\sigma_{11} = -\sigma_{33} = -1$.

$\alpha = 90°$ at the surface to $\alpha = 30°$ at the bottom) does the anisotropy affect the vertical strain rate in the same manner at both sites? By comparing the enhancement at the ridge and the flank sites in Figure 3.15, we can see that the vertical strain rate pattern looks very different at these two sites. At the flank site (dashed curve), the shear stress causes the vertical compression to enhance (relative to isotropic ice) whereas at the ridge (solid curve) the ice is much stiffer. One could argue that the fabric at the flank site should evolve faster, because of higher effective stress, but even with a tighter fabric ($\alpha^* = 20° + 70°z/H$) at the flank site (dotted curve), the vertical enhancement at the divide and flank is very different. Note in particular how sensitive the vertical deformation is to small changes in the cone angle (see Fig. 3.13). In order to model the deformation accurately, the fabric must therefore be very well known.

Strain rates for any other stress combination can be calculated in an analogous manner, but adding more components to the stress tensor will quickly make the calculations cumbersome.

3.6 DISCUSSION

Several models with various levels of complexity have been used to account for the effects of anisotropy. A model described by *Johnson* (1977) uses only three parameters (λ, μ, ν) to characterize vertically symmetric transversely isotropic anisotropy. The parameters are defined as $\lambda^2 = \dot{\varepsilon}_{33}/\sigma_{33}^3$, $\mu^2 = \dot{\varepsilon}_{11}/\sigma_{11}^3$ and $\nu^2 = 2\dot{\varepsilon}_{13}/\sigma_{13}^3$. Strain rate components are obtained from

$$\dot{\varepsilon}_{11} = U\left(\mu\sigma_{11} - \tfrac{1}{2}(2\mu - \lambda)\sigma_{22} - \tfrac{1}{2}\lambda\sigma_{33}\right),$$
$$\dot{\varepsilon}_{22} = U\left(-\tfrac{1}{2}(2\mu - \lambda)\sigma_{11} + \mu\sigma_{11} - \tfrac{1}{2}\lambda\sigma_{33}\right),$$
$$\dot{\varepsilon}_{33} = U\left(-\tfrac{1}{2}\lambda(\sigma_{11} + \sigma_{22}) + \lambda\sigma_{33}\right),$$
$$\dot{\varepsilon}_{13} = \tfrac{1}{2}U\nu\sigma_{13},$$
$$\dot{\varepsilon}_{23} = \tfrac{1}{2}U\nu\sigma_{23},$$
$$\dot{\varepsilon}_{12} = \tfrac{1}{2}U(4\mu - \lambda)\sigma_{12},$$

$$(3.38)$$
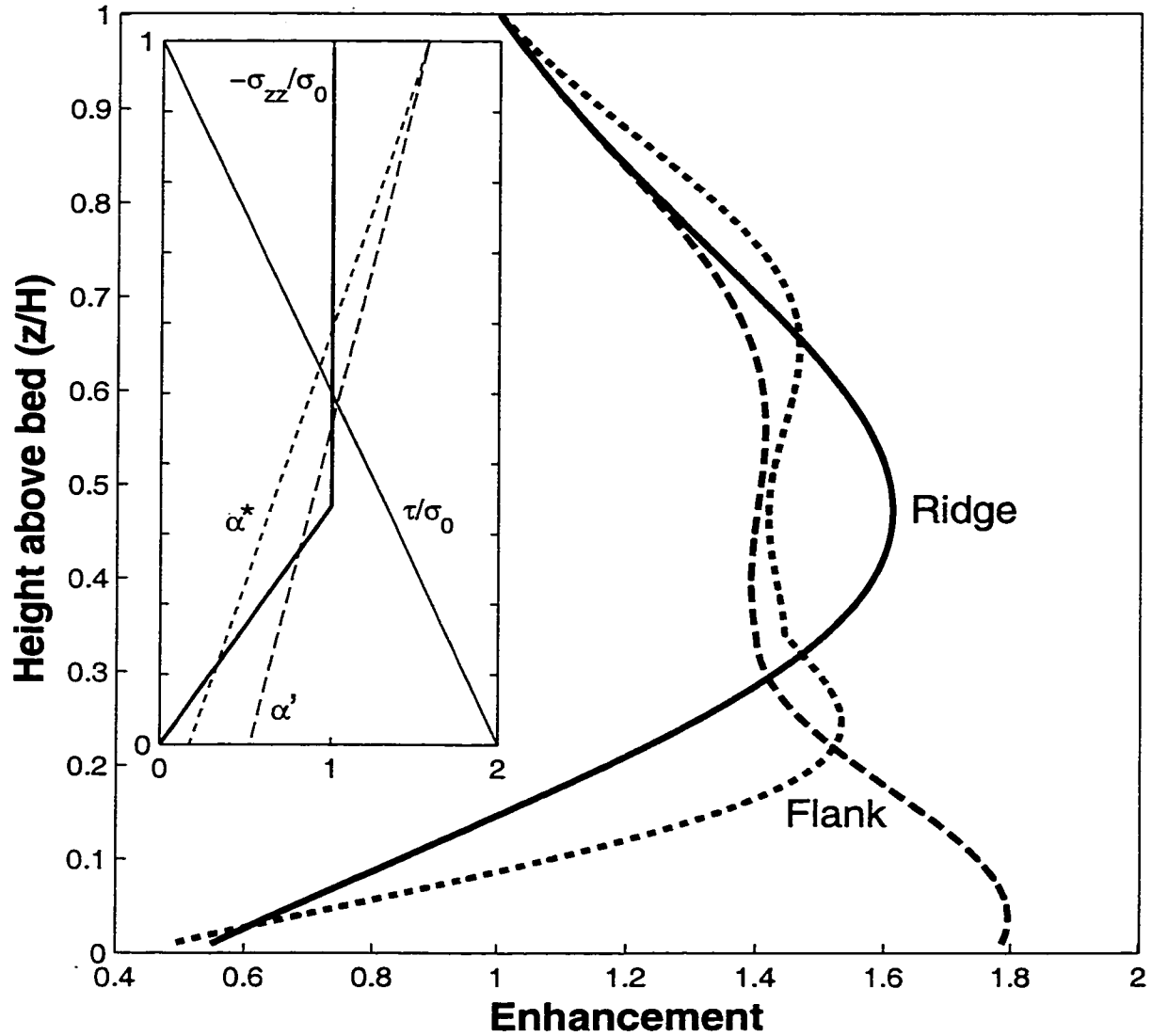
Figure 3.15: The vertical enhancement due to anisotropy at a ridge and a flank site. The normalized vertical stress (σ_{zz}/σ_0), the shear stress at the flank site (τ/σ_0) and the cone angles (in radians) are shown on the inset figure. The α' cone angles are used for the ridge and the dashed flank curve, and the α^* cone angles are used for the dotted flank curve.

where

$$
\begin{aligned}
U = {}& \tfrac{1}{2}(2\mu - \lambda)(\sigma_{11} - \sigma_{22})^2 \\
+{}& \tfrac{1}{2}\lambda\left((\sigma_{22} - \sigma_{33})^2 + (\sigma_{33} - \sigma_{11})^2\right) \\
+{}& \nu\left(\sigma_{23}^2 + \sigma_{13}^2\right) + (4\mu - \lambda)\sigma_{12}^2.
\end{aligned}
\tag{3.39}
$$

It is interesting to compare the strain rate calculated using the Johnson model to the strain rate calculated with the model developed here. Using the results from previous sections (the strain rate due to the σ_{11} stress state was not shown) we can obtain the λ, μ, ν parameters as functions of cone angle (Appendix A.1.9).

Figures 3.16 and 3.17 show a comparison of the $\dot\varepsilon_{33}$ and $\dot\varepsilon_{13}$ strain rate components calculated using the two models, respectively, in combined pure and simple shear stress. For the $\dot\varepsilon_{33}$ component the two profiles look similar for small shear stresses; the difference is due to the fact that the Johnson model uses only one stress component to define λ and μ, whereas pure shear depends on both σ_{11} and σ_{33}. As the shear stress increases the differences become more obvious. Three parameters cannot simulate the effects of anisotropy completely (5-7 are needed, as noted by *Lliboutry* (1993) and *Lliboutry and Duval* (1995)). For the $\dot\varepsilon_{13}$ component, the difference is relatively small, and similar throughout. The Johnson model captures the major effects of the anisotropy, but not all the details. As mentioned above, calculating the strain rate using Equation 3.12 becomes laborious as the number of non-zero stress components increases. The Johnson model depends only on the three parameters regardless of the stress pattern, and therefore offers a more efficient way to account for the major effects of anisotropy for highly complicated stress states.

Vertically symmetric fabric is commonly observed in both uniaxial compression and simple shear stress regimes in ice sheets (*Budd and Jacka*, 1989; *Thorsteinsson et al.*, 1997; *Gow et al.*, 1997; *Thorsteinsson et al.*, 1999). Girdle fabric describes a range of vertically symmetric fabric, from isotropic random fabric to strongly anisotropic fabric with all crystals aligned vertically, or at an angle to vertical.

The formulation presented here produces a maximum enhancement of 4.375 in simple shear. Laboratory experiments often indicate a value close to 9 (*Budd and Jacka*, 1989), although several other factors besides anisotropy may complicate the results. Some formulations of anisotropy, such as Azuma's model (*Azuma*, 1994, 1995; *Azuma and Goto-Azuma*,
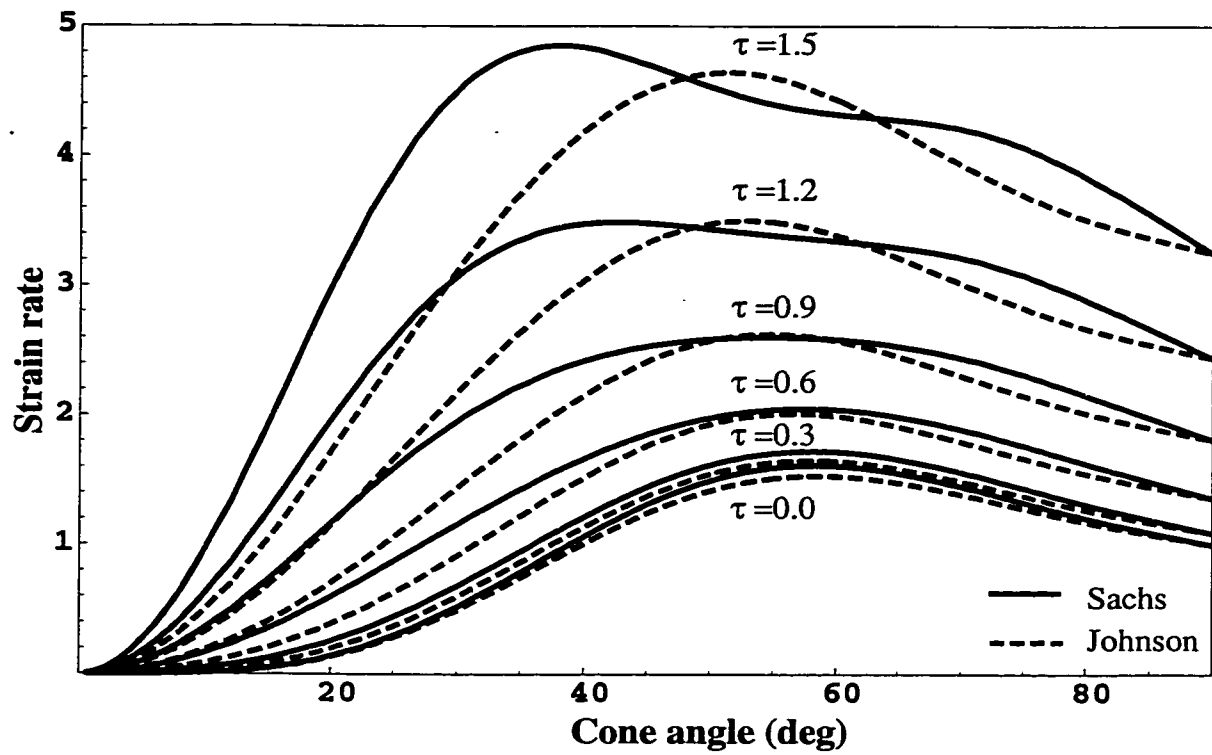
Figure 3.16: Comparing $\dot{\varepsilon}_{33}(\alpha)$ obtained using the Johnson and Sachs formulation for combined pure shear ($\sigma_{11} = -\sigma_{33} = -1$) and simple shear $\tau = \sigma_{13} = (0, 0.3, 0.6, 0.9, 1.2, 1.5)$.
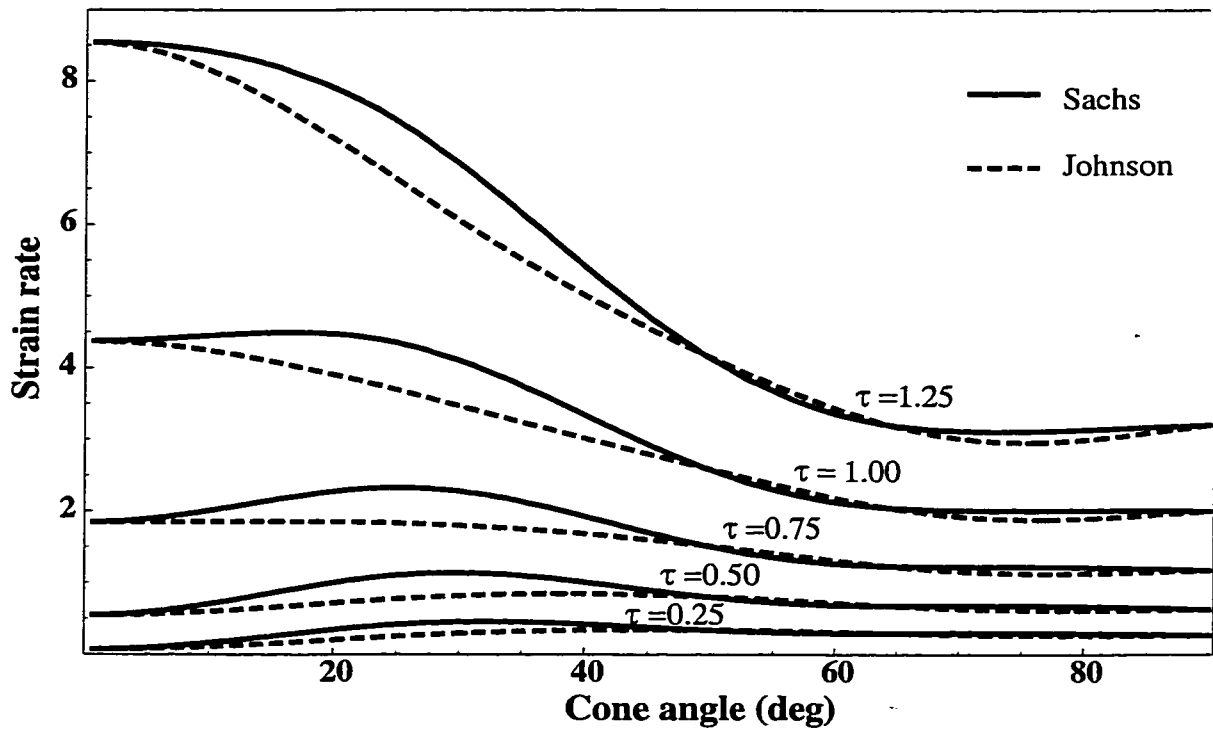
Figure 3.17: Comparing $\dot{\varepsilon}_{13}(\alpha)$ obtained using the Sachs and Johnson formulation for combined pure shear ($\sigma_{11} = -\sigma_{33} = -1$) and simple shear $\tau = \sigma_{13} = (0.25, 0.5, 0.75, 1.0, 1.25)$.

1996), the VPSC model (*Castelnau et al.*, 1996a), and the *Thorsteinsson* (2000b) model with nearest neighbor interaction, produce enhancement in simple shear that is close to 9. But, it is important to note that the style of deformation is the same in all cases. Since these models use identical crystal properties but different averaging of the crystal orientations, the ratio between the calculated strain rates for any two of these models is a well behaved scalar function of the crystal orientations. The situation is more complex for the VPSC model, since the state of stress, and not only the magnitude of stress, can vary between crystals. But those effects most likely do not significantly change the characteristics of the bulk deformation in the simple situations considered here. Different models will therefore predict qualitatively similar enhancement curves. The effects of anisotropy studied here are probably characteristic of all materials that deform by basal slip.

I model deformation of ice considering only slip in the basal plane. Other slip systems are unlikely to contribute significantly to the deformation of ice, except in very special cases. One such case is clearly demonstrated in Figure 3.3 at small cone angles ($\alpha < 10°$). Here $E \to 0$ as $\alpha \to 0$. Other slip systems, probably the pyramidal and prismatic, will determine the correct E as $\alpha \to 0$. This value is bound to be small in any case, since these other slip systems are an order of magnitude stiffer than slip systems in the basal plane.

The assumption that the stress is homogeneous ensures stress equilibrium, but not compatibility. There is almost certainly some redistribution of stress among the crystals in aggregates, but the deformation of the strongly anisotropic ice crystals is probably closer to the homogeneous stress limit than to the other well-known limit of homogeneous strain. As discussed in the introduction, experiments show that single crystal strain is not homogeneous throughout an ice aggregate (*Azuma and Higashi*, 1985); the homogeneous stress assumption explains the single crystal strain better than the homogeneous strain assumption (*Azuma*, 1995, cf. Figure 4). Although interaction with surrounding crystals modifies the stress to some extent (*Azuma*, 1995; *Sarma and Dawson*, 1996; *Castelnau et al.*, 1996a; *Thorsteinsson*, 2000b). Ice deforms almost entirely by slip on the basal plane (*Duval et al.*, 1983); which provides only two slip systems. Inhomogeneous strain, lack of slip systems all argues against the homogeneous strain assumption.

Even though I used the combination of pure and simple shear to demonstrate how the

anisotropy affects the deformation at a ridge and at a flank site, the same conclusions apply when comparing a dome (uniaxial compression) and a flank site. The solution for the dome/flank site enhancements is practically the same, for the vertically symmetric fabric used here. This is important, since the symmetry of the fabric in pure shear deformation is unlikely to maintain the azimuthal symmetry. Relating Figure 3.16 to a tilted cone, i.e. a non-vertical symmetry axis, it is clear that a small migration of the ice divide can cause significant changes in the deformation pattern (*Mangeney et al.*, 1997).

3.7 CONCLUSIONS

The effects of anisotropy studied here are characteristic of all materials deforming by basal slip. Although, I used vertically symmetric fabric to calculate the bulk deformation, the deformation rate of single crystals (Figures 3.2, 3.5 and 3.8) show the character of the deformation to be expected for non-vertical fabric.

Using girdle fabric, which is characterized by two parameters, we can explore the full range of anisotropy, for vertically symmetric orientation distributions, from isotropic fabric to strongly anisotropic fabric.

The formulation outlined here accounts for many effects of anisotropy on ice sheet flow. The strain rate enhancement in simple shear due to increasing anisotropy explains why ice gets softer at depth in ice sheets. To achieve plane strain for anisotropic ice, a stress in the third direction is necessary. In compression, ice is actually soft for cone angles larger than 57°. Using scalar enhancement factors leads to erroneous results in combined stress states. The formulation presented here represents a major improvement over the use of scalar enhancement-factors to account for anisotropic effects, while remaining relatively simple.

Chapter 4

STRAIN RATE ENHANCEMENT AT DYE 3, GREENLAND

4.1 SUMMARY

Ice at depth in ice sheets can be softer in bed-parallel shear than Glen's flow law predicts. For example, at Dye 3, Greenland, enhancement-factors of 3-4 are needed in order to explain the rate of bore-hole tilting. Previous authors have identified crystal fabric as the dominant contributor, but the role of impurities and crystal size is still incompletely resolved. Here we use two formulations of anisotropic flow laws for ice (Azuma's and Sachs' models) to account for the effects of anisotropy and show that the measured anisotropy of the ice at Dye 3, Greenland, cannot explain all the detailed variations in the measured strain rates. The jump in enhancement across the Holocene-Wisconsin boundary is larger than expected from the measured fabrics alone. Dust and soluble ion concentration divided by crystal size correlates well with the residual enhancement, indicating that most of the "excess deformation" may be due to impurities or crystal size. While the major features of the deformation at Dye 3 are explained by anisotropy and temperature, results also suggest that further research into the role of impurities and crystal size is warranted.

4.2 INTRODUCTION

The deep ice core at Dye 3, Greenland, was drilled in the summers of 1979-81, reaching near bedrock at 2037 m depth. The liquid-filled bore-hole was surveyed in 1981 after the drilling was finished and twice each year in 1983, 1985 and 1986. In addition to inclination and azimuth measurements, temperature, diameter and liquid pressure were also measured

(*Gundestrup and Hansen*, 1984; *Dahl-Jensen and Gundestrup*, 1987). The surface temperature at Dye 3 is about -20 C and the near-bedrock temperature -13 C. Hence the basal velocity is assumed to be zero. The surface velocity is determined to be 12.5 ma^{-1} by integrating the measured tilting rate in the bore hole. This agrees with independent geodetic measurements of the surface velocity (*Dahl-Jensen and Gundestrup*, 1987).

Horizontal shear strain rate can be calculated from bore-hole inclination measurements. These measurements at Dye 3 have revealed that the strain rate in the deep, Wisconsinan, ice (0-254 m above the bed) is much higher than the rate expected for pure isotropic ice. This increased deformation rate is commonly described with an enhancement factor, $E_{(ij)} = \dot{\varepsilon}_{ij}/\dot{\varepsilon}_{ij}^G$, which is the ratio of the measured strain rate over what Glen's (isotropic) flow law (*Glen*, 1958) would give. Figure 4.1, following *Dahl-Jensen and Gundestrup* (1987), shows that the enhancement factor for Dye 3 reaches in places a value approaching 4. Ice flow calculations based on Glen's flow law thus cannot reproduce the strain rates measured in the Dye 3 bore-hole. We know that crystal fabric does play a major role in the deformation of ice (*Steinemann*, 1958; *Russell-Head and Budd*, 1979; *Duval*, 1981; *Duval and LeGac*, 1982; *Budd and Jacka*, 1989; *van der Veen and Whillans*, 1990; *Alley*, 1992; *Azuma*, 1994; *Azuma and Goto-Azuma*, 1996; *Castelnau et al.*, 1996a). A strongly anisotropic aggregate of ice is much softer in simple shear applied normal to the mean c-axis direction than is isotropic ice under the same stress condition. From thin section measurements and sonic logging (*Herron et al.*, 1985; *Taylor*, 1982) at Dye 3, we know that the ice there develops an increasingly anisotropic fabric with depth.

Mechanical tests on ice extracted from the Dye 3 bore-hole should provide insight into the expected in situ mechanical behavior. Simple shear and compression tests commonly yield enhancement factors of 8 and 3 respectively for ice deforming in steady state (*Budd and Jacka*, 1989). Mechanical tests on the Dye 3 core (*Shoji and Langway*, 1985, 1988) have shown that in-situ fabrics give enhancement factors as large as 17 in uniaxial compression at near 45 degrees to vertical, clearly indicating that a strong vertical c-axis fabric contributed to the enhancement factor. However, for a given sonic velocity, i.e. constant cone angle, the enhancement factor in their experiments varied by a factor of 2-5 (*Shoji and Langway*, 1988, Fig. 6), suggesting that a factor of ~2 in enhancement may fall within the expected
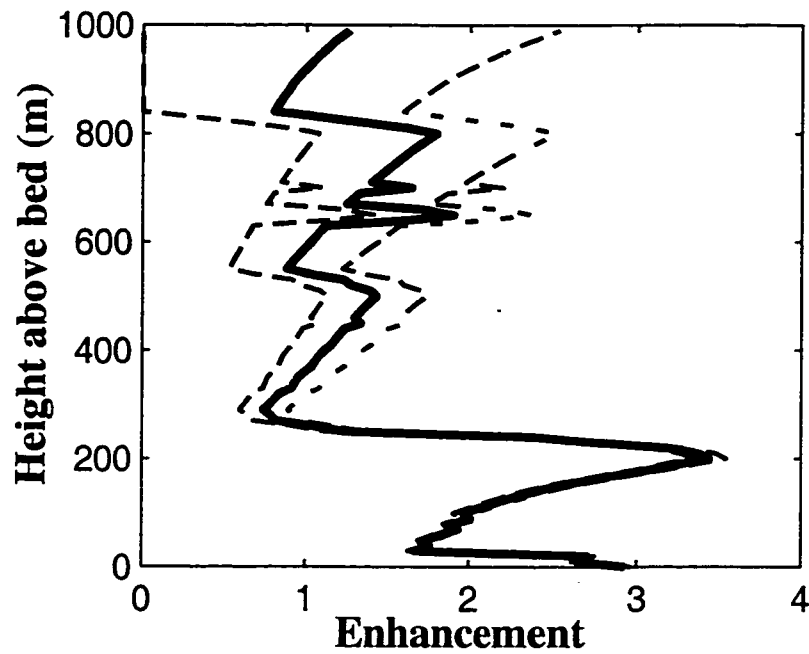
Figure 4.1: Enhancement at Dye 3, using an A_0 value that is 1.7 times the reference value from *Paterson* (1994), following *Dahl-Jensen and Gundestrup* (1987) did. The error estimates (dotted lines) are based on uncertainties reported in bore-hole tilting by *Dahl-Jensen and Gundestrup* (1987).

uncertainty limits of the experiments. Possibly damage such as micro-cracking on basal planes due to decompression could accentuate the anisotropy. Due to difficulties of testing small samples at atmospheric pressure, we need to complement these mechanical test results with models of the in situ deformation.

Pimienta et al. (1988) found no relation between impurities (soluble and insoluble), crystal size and enhancement in uniaxial and biaxial compression tests carried out on ice samples from the 2040 m Vostok ice core; they also concluded that anisotropic fabric explained all the Dye 3 deformation. However, other authors have suggested that impurities can soften ice (e.g. review by *Paterson* (1991); *Shoji and Langway* (1987); *Dahl-Jensen and Gundestrup* (1987)).

Our starting point, in examining the deformation at Dye 3, is Glen's flow law (*Glen*, 1958) which accounts for the stress and temperature dependence of ice deformation rate. First we explore the effects of fabrics on the flow properties of ice. We use a new model for anisotropic ice (*Azuma*, 1994; *Azuma and Goto-Azuma*, 1996), and also the Sachs' model (*Sachs*, 1928) to account for the anisotropy. We then explore the role of impurities on the mechanical properties of ice in order to further explain the deformation measured in the Dye 3 bore-hole.

4.3 THE CONSTITUTIVE RELATION

The two flow laws that we use both assume, in our formulation, that ice crystals deform only by slip in the basal plane and that the stress is homogeneous. The first assumption has been confirmed by experiments on ice; other slip systems are at least 60 times more difficult to activate (*Duval et al.*, 1983). The second assumption ensures stress equilibrium, but not compatibility; that is, grains can deform in such a way as to form overlaps and/or voids. This is not considered to be a serious problem because diffusional processes including grain boundary migration probably allow grains to recover without impeding the bulk deformation rate (*Means and Jessell*, 1986).

4.3.1 General Formulation of Anisotropy

When τ^s is the resolved shear stress on slip system s, then the rate of shearing, $\dot{\gamma}^s$, on that slip system is

$$\frac{\dot{\gamma}^s}{\dot{\gamma}_0} = \left(\frac{\tau^s}{\tau_0^s}\right)^n \tag{4.1}$$

where $\dot{\gamma}_0$ and τ_0^s are the reference resolved shear strain rate and shear stress respectively and n is the stress exponent. Ice has only one easy slip system, the basal plane, so we can rewrite Equation (4.1) as

$$\dot{\gamma}^s = \beta(T)\tau^{s^n} \tag{4.2}$$

where $\beta = \dot{\gamma}_0/\tau_0^n$ is a function of temperature, $\beta(T) = \beta_0 A(T)$ and β_0 will be chosen so that the strain rate for a random distribution of c-axes will match isotropic ice. The resolved shear stress τ^s is given by

$$\tau^s = S_{ij}^s \sigma_{ij} = \tilde{S}^s : \tilde{\sigma} \tag{4.3}$$

where σ_{ij} is the deviatoric Cauchy stress tensor acting on the grain and

$$S_{ij}^s = b_i^s n_j \tag{4.4}$$

is the *Schmid-tensor*, which gives the transformation from the crystal coordinate system (microscopic) to the lab coordinate system (fixed, macroscopic), $\vec{n}$ is the slip-plane normal and $\vec{b}$ is the slip direction (Burgers-vector). For ice $\vec{n}$ is the crystallographic c-axis, so we write $\vec{n} = \vec{c}$.

The strain rate is defined by $\dot{\varepsilon}_{ij} = \frac{1}{2}(L_{ij} + L_{ji})$, where $L_{ij} = \partial v_i/\partial x_j$, v_i are the velocity components and x_i the coordinates in a reference frame fixed with respect to the laboratory (*Molinary et al.*, 1987).

The strain rate in the macroscopic reference frame is related to the microscopic shear strain rates by the relation

$$\dot{\varepsilon}_{ij} = \sum_s R_{ij}^s \dot{\gamma}^s \tag{4.5}$$

where $R_{ij} = \frac{1}{2}(S_{ij} + S_{ji})$.

From Equations (4.2) and (4.5) we get (note that $R_{kl}\sigma_{kl} = S_{kl}\sigma_{kl}$ if σ_{ij} is symmetric)

$$\dot{\varepsilon}_{ij} = \beta(T) \sum_s R_{ij}^s \left(R_{kl}^s \sigma_{kl}\right)^n \tag{4.6}$$

which gives the strain rates of a single crystal in the macroscopic coordinate system.

4.3.2 Sachs' Model

In the Sachs' model (*Sachs*, 1928) the stress is assumed to be homogeneous, so that the stress acting on each grain is equal to the macroscopic stress acting on the aggregate. The stress tensor, σ_{kl}, in Equation (4.6), is thus just the stress applied to the bulk. The macroscopic strain rate of the bulk is then just the arithmetic average of the strain rates of the individual grains, given by

$$\dot{\varepsilon}_{ij}^{S} = \frac{1}{N} \sum_{g=1}^{N} \dot{\varepsilon}_{ij}^{g} \tag{4.7}$$

where $\dot{\varepsilon}^g$, the strain rate of an individual grain, is given by Equation (4.6), and N is the total number of grains.

The value of β_0, chosen to make isotropic ice behave according to Glen's flow law, is $\beta_0 = 9$.

4.3.3 Azuma's Model

For bulk deformation *Azuma* (1994) takes the mean value of the Schmid-tensor for individual grains

$$\overline{S}_{ij} = \frac{1}{N} \sum_{g=1}^{N} S_{ij}^{g} \tag{4.8}$$

where S is calculated assuming that $\vec{b} = \vec{m}$, where $\vec{m}$ is the direction of the projection of the traction, $\vec{T}$, on the basal plane. This is possible because the basal plane is nearly isotropic for $2 < n < 4$ (*Kamb*, 1961). The traction is given by

$$T_i = \sigma_{ij} c_j \tag{4.9}$$

and its direction, $\vec{m}$, by

$$\vec{m} = \frac{\vec{c} \times (\vec{T} \times \vec{c})}{|\vec{c} \times (\vec{T} \times \vec{c})|} \tag{4.10}$$

Consequently for ice we can write the Schmid-tensor as $S_{ij} = m_i c_j$.

The macroscopic strain rate is then given by

$$\dot{\varepsilon}_{ij}^{A} = \beta(T)\overline{R}_{ij}(\overline{R}_{kl}\sigma_{kl})^n \tag{4.11}$$

This model effectively replaces each crystal with a crystal having the mean orientation, given by the average value of S.

The value of β is chosen to make the Azuma model reproduce Glen's flow law in the case of isotropic ice, i.e. random c-axis fabric. This value is $\beta_0 = 18$, which is twice the value found for Sachs' model.

4.3.4   Comparison of the two Models

The degree of anisotropy is described as a cone angle, which is the apex angle of a cone within which all the c-axes are uniformly distributed. Isotropic ice has a cone angle of 90 degrees; anisotropic ice has smaller cone angles. The cone can be parallel or oblique to the direction of gravity. For Dye 3, the vertical symmetry of thin section fabrics and orthogonal components of the sonic velocities on the ice core (*Herron et al.*, 1985), strongly suggest that the cone axis is vertical at Dye 3. The same assumptions apply to the interpretation of the bore-hole sonic velocities (*Taylor*, 1982).

In simple shear, strongly anisotropic ice can deform as much as 9 times faster than isotropic ice, according to Azuma's model, and 4.5 times faster according to Sachs' model (Fig. 4.2). In uniaxial compression along the cone axis of progressively more anisotropic samples, the ice gets softer by as much as a factor of 3 between cone angles of 90 and 60 degrees, because these fabrics contain progressively fewer hard grains oriented near 90 deg. Samples with cone angles smaller than 60 degrees get progressively stiffer with decreasing cone angle (Fig. 4.2), because there is less resolved shear stress on the basal planes. Note that Sachs' model and Azuma's are identical in the case of a single crystal; it is only through the choice of β_0 for isotropic ice that we get the different strain rates for cone angle of 0 degrees, i.e. single crystal.

4.4   DATA SOURCES

We use Dye 3 bore hole tilt measurements for strain rates (*Dahl-Jensen and Gundestrup*, 1987, Fig. 2). The measurements were made every 2.5 - 5 m from near the bedrock up to 330 m. From there to the surface they were made at 25 m intervals. In measurements
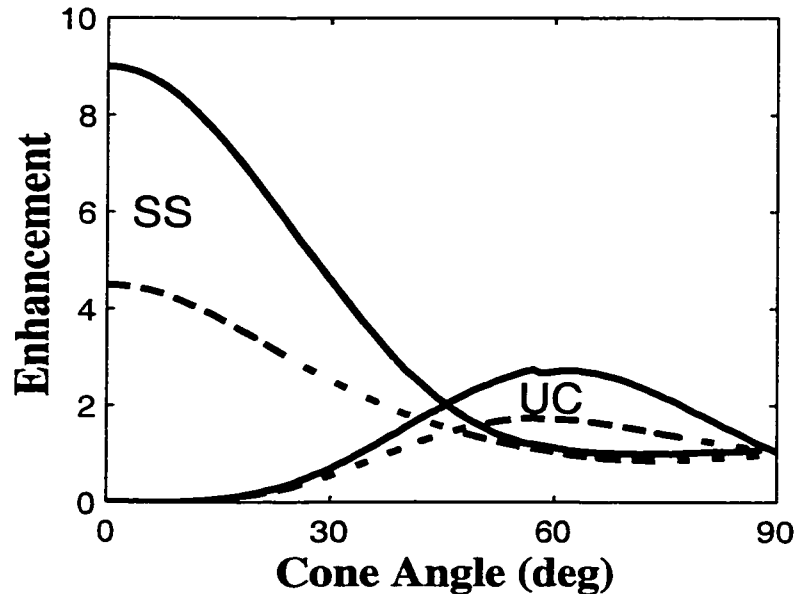
Figure 4.2: Enhancement in simple shear (SS) and uniaxial compression (UC) calculated from Sachs' (dashed lines) and Azuma's (full lines) models.

above 1200 m the standard deviations on $\partial u/\partial z$ are of the same order of magnitude as the parameters themselves (*Dahl-Jensen and Gundestrup*, 1987). Almost all the deformation takes place in the lower-most 1000 m; therefore all our calculations are done there.

We use the stress state values given by *Dahl-Jensen* (1985), who calculated the stresses and made corrections due to the local topography.

The temperature profile (*Gundestrup and Hansen*, 1984) shows that most of the change in temperature happens in the lower-most 400 m. This results in an enhancement (through the temperature dependence of the flow laws) of a factor of 2 between 400 m and bed. The data that we use for strain rate, stress and temperature are shown in Figure 4.3.

Fabric data were obtained in two ways. *Herron et al.* (1985) measured fabrics in thin sections (Fig. 4.4). The thin section measurements are based on observations of $N \approx$ several hundred crystal axes at selected depths. The fabric is expressed by *Herron et al.* (1985) in several ways, including (1) the apex angle of a cone containing 90% of the crystal c-axes, and (2) the normalized length R/N of the resultant vector $\vec{R}$ obtained by summing all N c-axis vectors. Thin section measurements of fabric were made on the core at 50-100 m
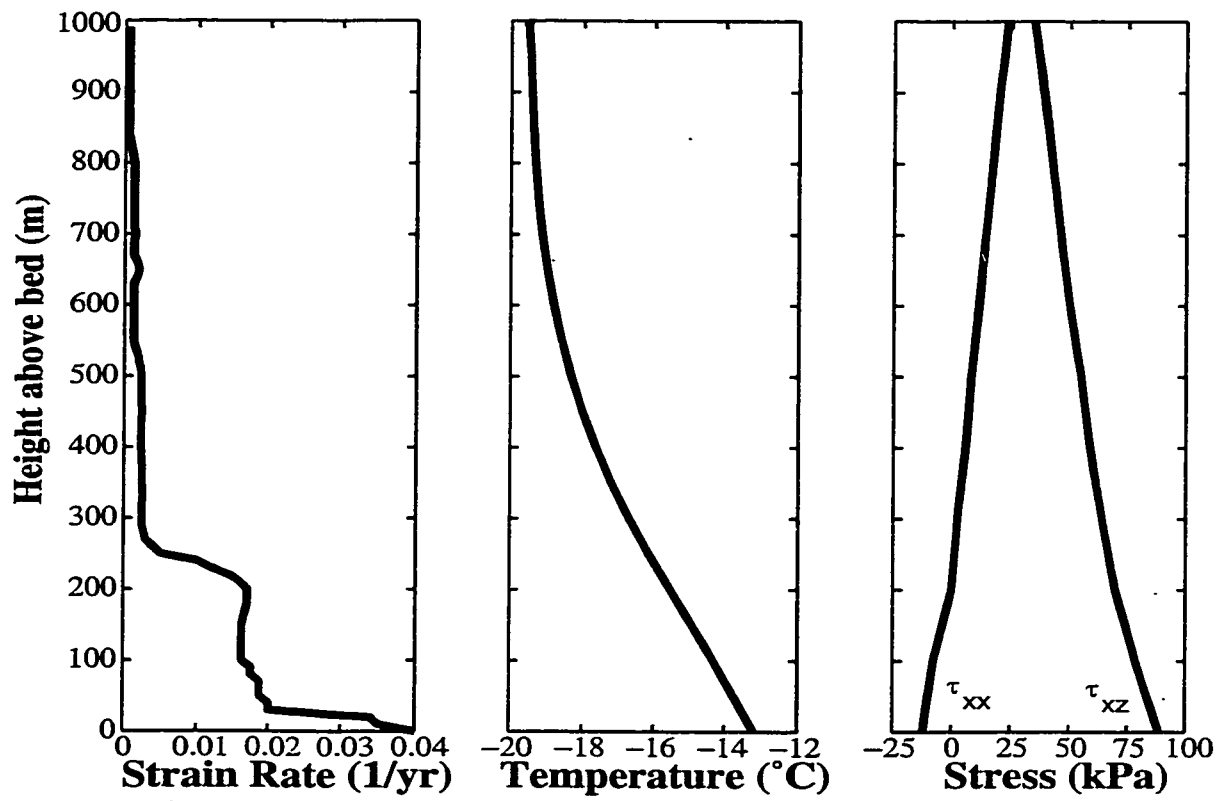
Figure 4.3: Measured horizontal strain rates and temperature, and the calculated stress at Dye 3.

intervals.
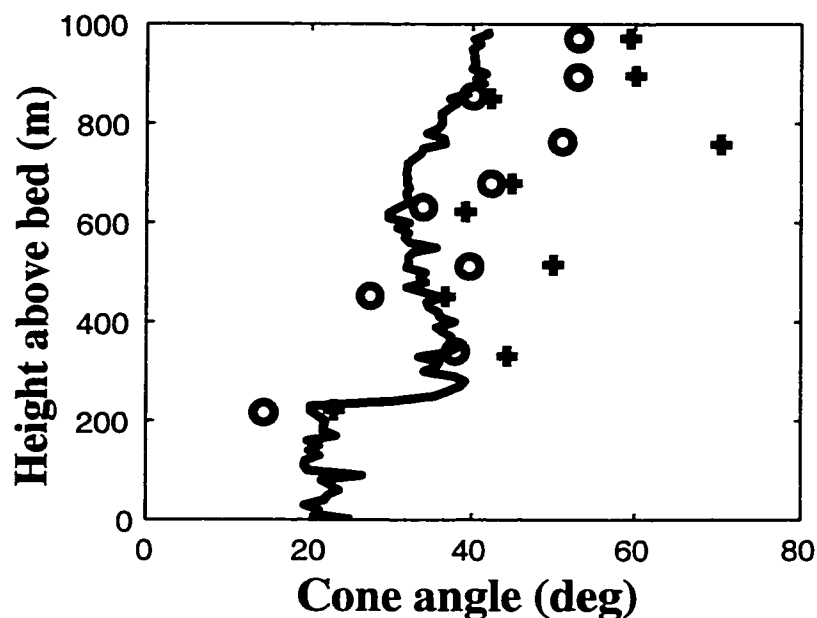
Figure 4.4: Measured cone angles. The solid line is cone angle calculated from compressional wave velocity measurements (*Taylor*, 1982), the crosses are cone angles enclosing 90% of the c-axes from the thin section data, and the o are cone angles with uniformly distributed c-axes giving the same R/N statistics as the measured thin sections (*Herron et al.*, 1985).

Fabric data were also obtained from bore hole sonic logging measurements *Taylor* (1982) using vertically traveling compressional waves. The velocity measurements were made through 7 m of ice, which is the spacing between the source and receiver. Velocities were calculated at 3.33 m intervals. Inclination data for the bore hole were used to correct for variations in propagation angle. Wave velocities can be used to interpret fabric in terms of the cone (apex) angle because ice is elastically anisotropic, and the elastic anisotropy has the same symmetry as the plastic anisotropy. *Bennett* (1968) derived the relationship between ice fabrics and wave velocities that was used to calculate the cone angle from the compressional wave velocity. We use the same model of uniformly distributed crystal axis within a cone when interpreting the compression wave velocities and calculating the mechanical properties of the ice.

The difference between the inferred cone angles from the sonic log and the 90% cones

from thin sections (Fig. 4.4) is mainly due to the non-uniform distributions of c-axes within the 90% cones from the thin sections, as was pointed out by *Herron et al.* (1985); the 90% cone angle is a relatively poor statistic for representing the average orientation of crystals in a thin section. For example, if 80% of the c-axes cluster tightly near the vertical, while the others have high inclinations, then the 90% cone angle must be large enough to enclose half of the outliers. Yet, the deformation rate of this sample could be very different from the deformation rate of a sample with uniformly distributed c-axes spanning the 90% cone, and the tight central cluster alone might better characterize the deformation rate of the sample. R/N is a better statistic than the 90% contour cone angle for expressing the fabric distribution, because every c-axis in a thin section, rather than only those near the 90% contour line, contributes to R/N. In order to compare the sonic velocity cone angles and the thin section data, we use the cone angles for uniformly distributed c-axes that would have the same R/N statistic as each measured thin section. These equivalent cone angles, shown by open circles in Figure 4.4, are clearly a better match to the sonic log cone angles. It is also important to remember the very different scales that these two methods measure. The sonic log gives an average cone angle through 7 m of ice, while the thin sections are only about 0.5 mm thick. This may account for the higher variability of the cone angles from the thin sections. There are also a number of complexities that arise in thin section measurements. Coarse grains can bias the measurements by passing through the plane of the thin section in many places. Polygonization can give the sense of small crystal size, but the c-axes, due to the subdivision process are very similar for the new grains (*Alley et al.*, 1995b). Hence, groupings and other features of the c-axes are likely (*Herron et al.*, 1985; *Alley et al.*, 1997) that reveal a huge amount about active processes but may not average over a large enough volume to capture the fabric controlling the deformation. We note that the thin sections are very important as a tool to infer the symmetry and distribution of c-axis, and also of course if one is modeling ice on cm scales.

4.5 CALCULATIONS

We perform two sets of calculations. First we calculate the strain rate, using information on stress, temperature and fabric. Second we calculate the fabric using the information on stress, temperature and measured strain rates.

We use $\sim$1000 c-axes for each point of calculation, which are at 10m intervals from the bed to 1000 m height (recall that *Dahl-Jensen and Gundestrup* (1987) found virtually no deformation above 1000 m).

For the calculations we used n = 3 (*Budd and Jacka*, 1989) and the Arrhenius relation $A(T) = A_0 \exp\left(-\frac{Q}{RT}\right)$ for the temperature dependence, where $Q = 60 kJ mol^{-1}$ (*Paterson*, 1994, p. 96), and $R = 8.314 J mol^{-1} K^{-1}$. Using $A(-20C) = 1.7 \cdot 10^{-16} (kPa)^{-3} s^{-1}$ (*Paterson*, 1994) as a reference value we find $A_0 = 4.15 \cdot 10^{-4} (kPa)^{-3} s^{-1}$, using the values for Q and R defined above.

We view the value of A_0 as an adjustable parameter; values reported vary by factors of $\sim$2 (*Paterson*, 1994, Table 5.1). In our calculations we therefore use $\mathcal{A}_0 = f_C^X A_0$, where f is a factor chosen using two different criteria (C) for given flow law X (X = S, A or G refers to Sachs' model, Azuma's model or isotropic (Glen's) flow law). First we choose f such that the strain rates that we calculate in the Holocene ice match the measured strain rates as closely as possible with each flow law; we call these scalars f_H^X. For our second approach, we ensure that the strain rate in the Wisconsin ice is never over-predicted after we account for the anisotropy. This is equivalent to saying that the impurities can only have a softening effect on the ice; we call these scalars f_W^X.

To characterize the effects, in addition to fabric, that might be necessary to explain the measured bore-hole tilting, we define k through

$$\dot{\varepsilon}^m = \dot{\varepsilon}^X (1 + k) \tag{4.12}$$

where m refers to measured values and X refers to the flow law description used. k is thus a measure of how much excess deformation remains at each depth after we have accounted for the anisotropy. k should thus be 0 if the flow law "X" could explain all the strain rate measured.

Table 4.1: The value of f_C^X for the different criteria and flow laws used:

	Sachs	Azuma	Isotropic
Holocene	$f_H^S = 0.91$	$f_H^A = 0.54$	$f_H^G = 2.06$
Wisconsin	$f_W^S = 0.81$	$f_W^A = 0.41$	$f_W^G = 2.84$

4.6 RESULTS

Figures 4.5 and 4.6 show the calculated strain rates and excess deformation, k, using the two criteria f_H^X and f_W^X respectively. The values of f_C^X's are found in Table 1. We note that both anisotropic models capture some of the major features of the measured profile. However, neither of them can explain all the variations.

In particular, note the large strain rate just below the Holocene-Wisconsin boundary, located 254 m above the bottom of the bore hole. Deformation rate increases by a factor of 4 over a short depth interval. However, temperature and stress vary smoothly across the boundary, and the fabric, while it changes at the boundary, still cannot account for the factor of 4 with either of the anisotropic flow models that we use. Perhaps other anisotropic flow models might be able to account for this factor of 4, although we are not aware of any that do. Another possibility is that the stiff (more strongly anisotropic) Wisconsin ice acts as a stress guide, therefore raising the longitudinal stress σ'_{xx}. A simple calculation shows that in order to have the same strain rate $\dot{\epsilon}_{xx}$ for a layer with 20 deg cone as for a layer with a 40 deg cone, one needs to increase σ'_{xx} by a factor of 2. Increasing σ'_{xx} by a factor of 2 at Dye 3, has a very small effect on $\dot{\epsilon}_{xz}$. Even in the extreme case where the longitudinal stress was zero before, and is now one-half of the shear stress the increase in shear strain rate for cone angle of 20 deg is only about 10%. So large errors in the longitudinal stress, as long as they are smaller than about half the shear stress will not change the shear strain rate by much.

We note further that between 100 and 200 m the measured strain rates are constant or even slightly *decreasing* with increasing depth, while stress and temperature, i.e. factors that should *increase* deformation rate in *any* flow model, *increase* with increasing depth.
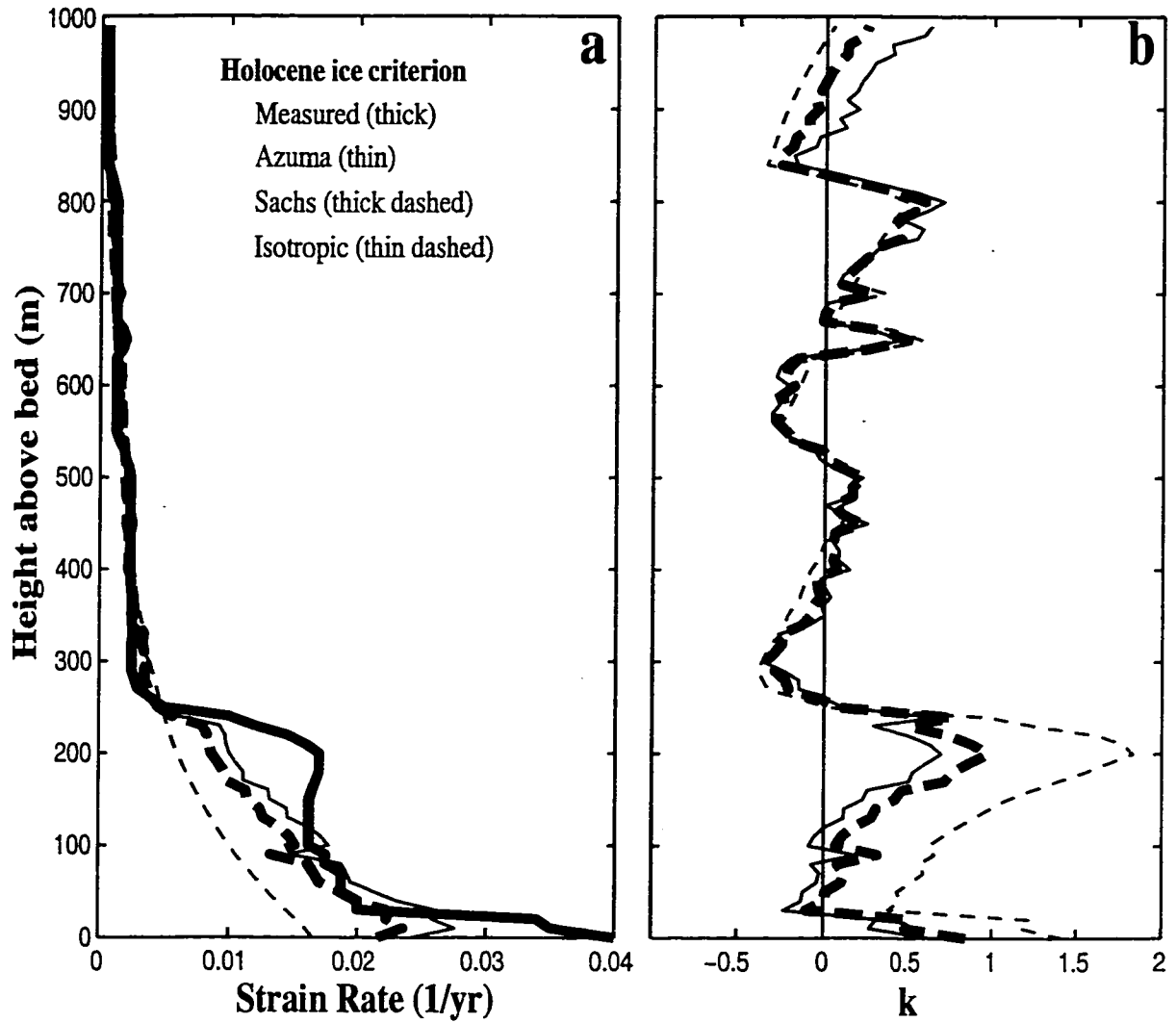
Figure 4.5: (a) Measured (solid line) and calculated horizontal strain rates, using the Holocene-ice criterion. (b) The corresponding k values for Azuma (thin solid line), Sachs (thick dashed line) and isotropic (thin dashed line) ice.
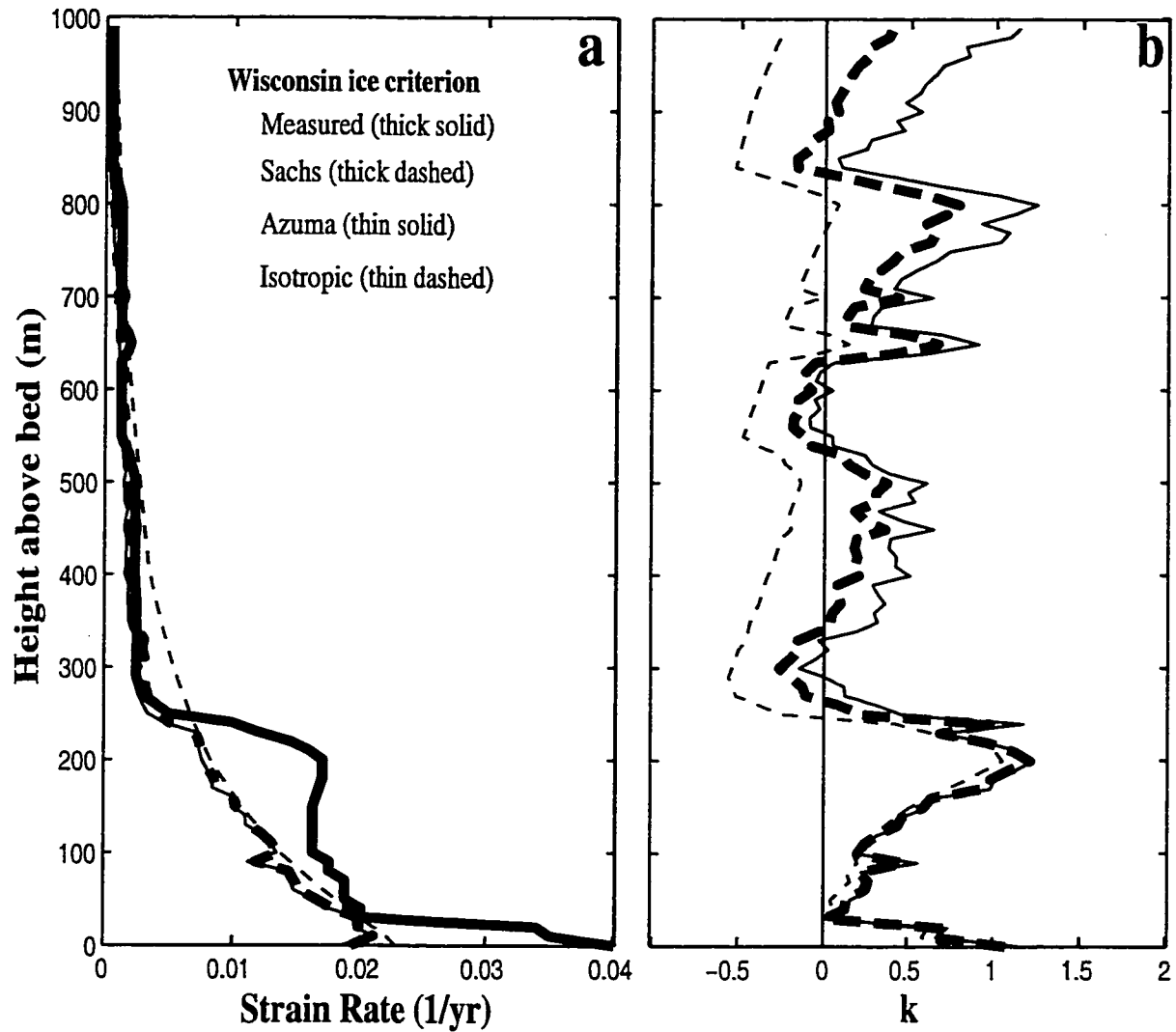
Figure 4.6: a) Measured (solid line) and calculated horizontal strain rates, using the Wisconsin ice criterion. b) The corresponding k-values for Azuma (thin solid line), Sachs (thick dashed line) and isotropic (thin dashed line) ice.

The degree of anisotropy is constant, or even slightly increasing over the same depth interval, and thus should either not affect or else should also increase the deformation rate. From this observation, we must conclude that some factor in addition to fabric anisotropy is required to explain the observed deformation rate, regardless of how the response to fabric is modelled.

The mechanical tests of *Shoji and Langway* (1985, 1988) further strengthen this conclusion, for they show a monotonic relation between enhancement and sonic velocities.

Figure 4.7 shows the cone angles, calculated using Azuma's and Sachs' models, required to explain all the measured strain rates solely with fabric variations, using the f_H^X's that we obtained for the Holocene ice. Common to both profiles is the fact that in order to explain the jump in strain rate below the Holocene-Wisconsin boundary, very strong anisotropy is necessary in the Wisconsin ice. In fact a single crystal fabric would not be enough, but we terminated our calculations at 2 degree cone angles. The cone angle profile that we derive using the Wisconsin ice criterion has essentially the same features as seen in Figure 4.7 and leads to the same conclusions. The sonic velocity data do not support such strong anisotropy in this region.

4.7 INCLUDING IMPURITIES

So far we have "accounted" for the effects of stress, temperature and fabric. But excess deformation, k, remains unexplained. Now we examine the role of other possible factors, individually or combined, we will call them "Y", that may influence the rheology of ice. We consider impurities, dust and dissolved ion concentrations, and crystal size. We rewrite Equation (4.12) as

$$\dot{\varepsilon}^m = \dot{\varepsilon}^X (1 + k_Y + k^*) \qquad (4.13)$$

where k_Y is the deformation correlated with the dust or ion concentration, crystal size, or some combination of these. k^* will be (we hope) a random residual. In other words, we have assumed that the excess deformation is due to some "Y" plus an error term, $k = k_Y + k^*$.

We assume that $k_Y = (Y/a)^p$, where Y can be concentration, crystal size, or some combination of those, and a and p are constants to be determined by the data. We then
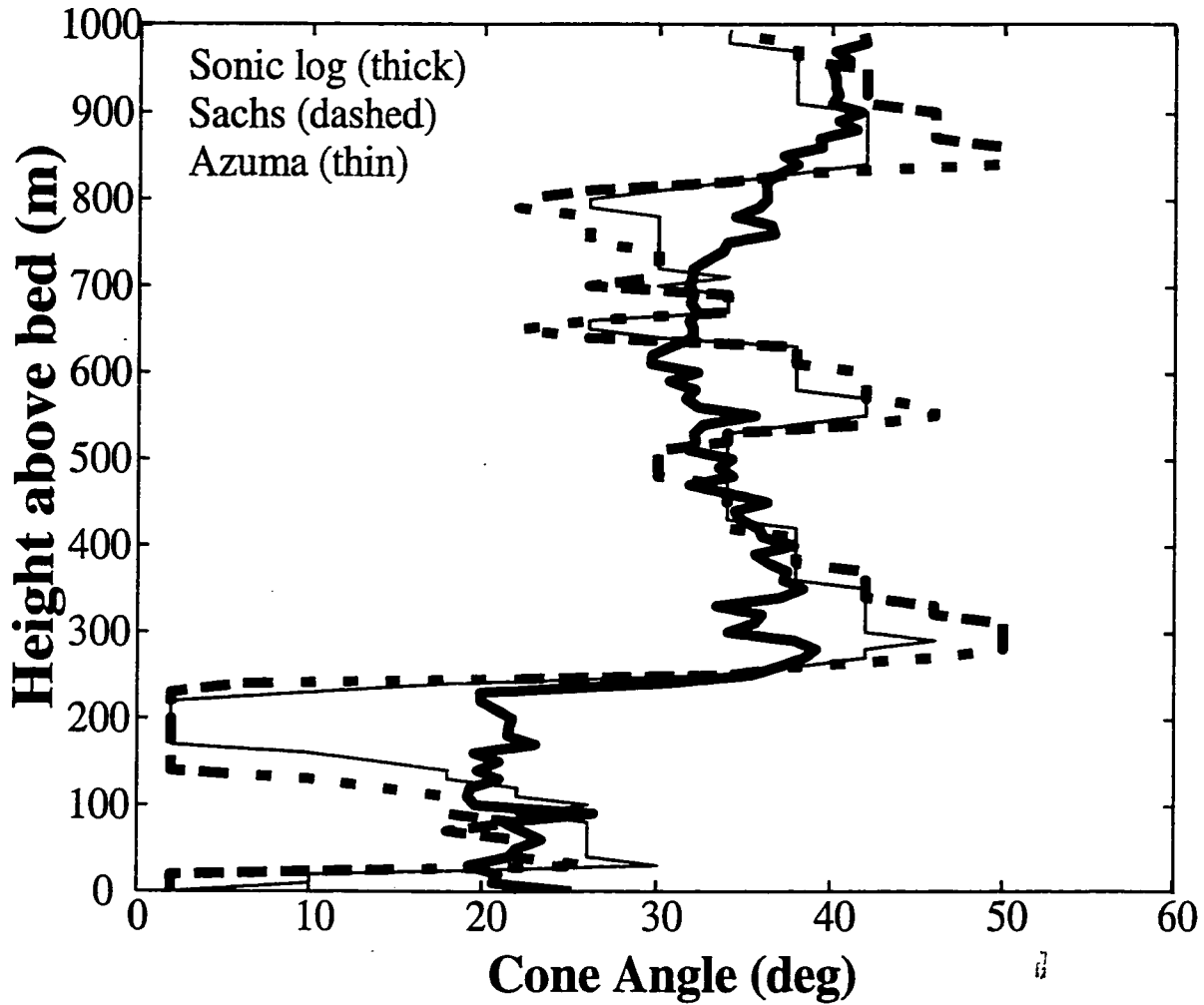
Figure 4.7: Bold line shows cone angles obtained from the compressional wave velocity measurements (sonic log). Other two curves show cone angles required by the two anisotropic models (Sachs and Azuma), to produce the best match to the measured strain rates for the given temperature and stress. Here we use the f_H^X value determined from the Holocene ice criterion.

find a and p that minimize $N\bar{\sigma}^2 = \sum_{j=1}^{N}(k^j - k_Y^j)^2$, where N is the number of data points. The correlation between k and k_Y is then given as $\rho = cov(k, k_Y)/(\sigma_k \sigma_{k_Y})$ (*Barlow*, 1989, p. 16). The best correlation, and smallest $\bar{\sigma}$ were found for dust and for ion concentration divided by crystal size.

The dust concentration at Dye 3 (*Hammer et al.*, 1985), correlates well with the dissolved ions ($\rho = 0.829$) and the inverse crystal size. We get the smallest $\bar{\sigma}^2$ when comparing k and the dust concentration, by using a linear relationship $k_d = a \cdot C(z)$, where C is the concentration in mg/kg averaged over $\sim$5 m depth to replicate the smoothness of the sonic log by the 7 m tool. The calculations are done between 30 m and 250 m above the bed, and therefore avoid the silty ice layer in the lowermost 23 m. Figure 4.8 shows that the dust concentration is highly correlated to the excess deformation, k. The value of a ranges between 0.35 and 0.77 for the two flow law formulations and $\mathcal{A}_0$ selection criteria we used. The correlation coefficient ρ_d for Azuma's model is 0.83 and for Sachs' 0.88.

We do the same calculations for soluble ions divided by crystal size, as suggested by *Cuffey et al.* (1996), using the sum of Cl^-, SO_4^{2-} and NO_3^- concentrations (*Dahl-Jensen and Gundestrup*, 1987). For the relation $k_{i/c} = [C_i/(aD)]^p$, where C_i is the concentration [mg/kg] and D the crystal size [mm], we find $p = 1$ or 2, and a $= 286$ to 404. The values of p and a for each case are shown in Figure 4.8, which also shows that the correlation is good with k. The correlation coefficients are 0.84 (HI) and 0.86 (WI) for Azuma's model and 0.86 for Sachs' model.

The values of $\bar{\sigma}^2$ and ρ for both the criteria (Holocene, HI, and Wisconsin, WI), the two flow models used and both k_Y's are summarized in Table 2.

A correlation between residual enhancement and dust does not necessarily mean that dust softens the ice. As noted above, dust also correlates strongly with the dissolved ions and the inverse crystal size, and since these are all so closely correlated it is difficult to say which one is responsible for the deformation. Ice containing small crystals often has strong anisotropy (*Paterson*, 1991); our direct use of the measured anisotropy already incorporates this effect. We cannot distinguish whether the insoluble dust or the dissolved ions make the ice softer, since they correlate so well; we argue that dissolved ions are more likely, although some of the arguments apply to dust as well.
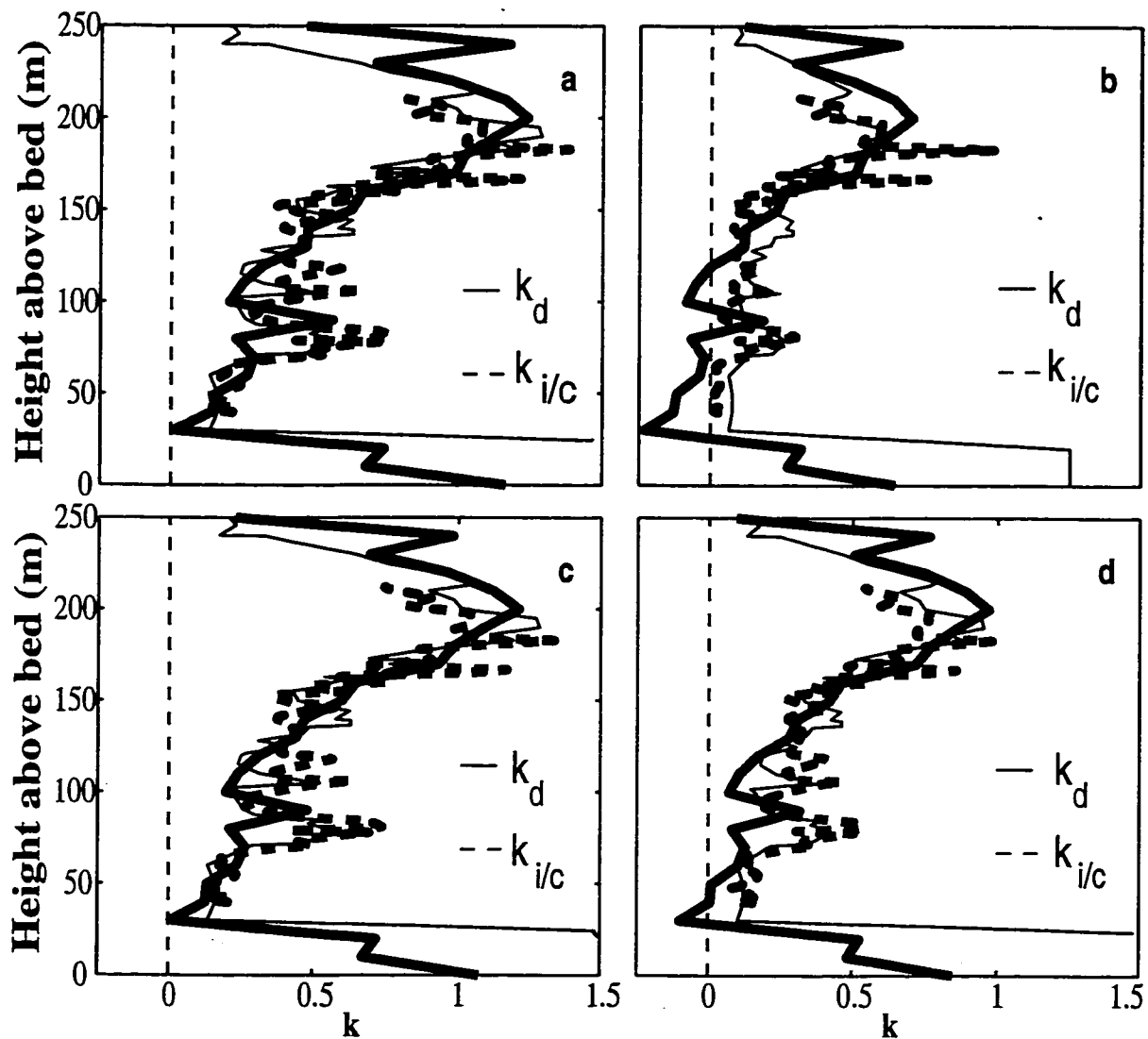
Figure 4.8: Relating the dust concentration (C_d), using a linear function $k_d = C_d/a$ (thin line), and the ion concentration (C_i) divided by crystal size (D), using a function $k_{i/c} = [C_i/(aD)]^p$ (thick dashed line), to the excess enhancement $k = k_Y + k^*$ (thick line) calculated with the two flow laws and criteria described in text. The values of a and p are given in Table 2. (a) Azuma's model using the Wisconsin ice (WI) criterion, (b) Azuma using the Holocene ice (HI) criterion, (c) Sachs' model using WI and (d) Sachs' using HI.

Table 4.2: The parameters a and p, and the statistics for the correlation of the excess enhancement, k, with dust, $k_d = (C_d/a)^p$, and ion concentration divided by crystal size, $k_{i/c} = [C_i/(aD)]^p$:

	k_d				$k_{i/c}$			
	a	p	ρ	$10^{-2}\bar{\sigma}^2$	a	p	ρ	$10^{-2}\bar{\sigma}^2$
Sachs, HI	1.75	1	0.88	1.34	404	1	0.86	2.99
Sachs, WI	1.30	1	0.88	1.44	296	1	0.86	3.25
Azuma, HI	2.86	1	0.83	1.89	400	2	0.84	2.29
Azuma, WI	1.30	1	0.83	1.56	286	1	0.86	3.40

At concentrations observed in the Dye 3 core and most other ice-sheet ice, laboratory experiments and simple theory generally lead one to expect that increased impurity concentration will increase deformation rates (see review in *Paterson* (1994), p. 88-89). Solid impurities (e.g. silt, volcanic ash) at high concentrations in cold ice may decrease strain rates in laboratory experiments (e.g. *Hooke et al.* (1972)), but have little effect at low concentrations characteristic of non-basal ice-sheet ice. Some field data seem to indicate a softening effect of solid impurities (*Swinzow*, 1962), especially at high temperature (*Echelmeyer and Zhongxiang*, 1987), although determining mechanisms is always difficult in such field settings. *Budd and Jacka* (1989) concluded from a review of the field that solid impurities have little effect on creep deformation at ice-sheet concentrations and sub-freezing temperatures.

Experiments with soluble impurities (*Jones and Glen*, 1980; *Nakamura and Jones*, 1970, 1973; *Paterson*, 1991) indicate that their presence typically increases deformation of ice, although effects may be sensitive to the temperature, concentration, and nature of the impurity. As one example, in constant strain-rate tests in tension on single crystals of ice, introduction of 1.3 ppm HCl reduced the peak stress by about a factor of 2 (*Nakamura and Jones*, 1973).

Several mechanisms may be active (e.g. *Nakamura and Jones* (1973); *Weertman* (1973); *Perez et al.* (1980); *Paterson* (1994)). Motion of dislocations through the ice lattice may create mismatches at bonds (Bjerrum defects) that must be removed by diffusional processes

to allow continued motion. Soluble impurities that substitute in the ice lattice create defects that speed this diffusional relaxation. Impurities also may create liquid zones or thicker disordered zones along dislocation cores and at grain boundaries that speed diffusional processes and cause or allow faster deformation.

Impurity concentrations can affect grain sizes (e.g., *Alley and Woods* (1996)), and at least some models allow a grain-size effect on ice deformation rates. However, as reviewed by *Budd and Jacka* (1989) (cf. *Duval and LeGac* (1980)), grain size does not seem to affect deformation rates significantly within the range of ice-sheet conditions, and often is more of a response to deformation than a control on deformation.

Thus, a likely explanation is that soluble impurities speed diffusional processes and thus increase ice-deformation rates by introducing point defects, and perhaps also by increasing the volume of disordered or liquid material through which diffusion is enhanced. The smaller crystal size at high soluble impurity levels would greatly facilitate this process. Whatever the mechanism, the literature suggests that the impurity loading in the Wisconsin ice at Dye 3 is likely to cause some softening, as deduced previously by *Paterson* (1991).

4.8 DISCUSSION

By using anisotropic flow models, we can explain a large fraction of the total deformation. While we agree with Azuma and Goto-Azuma (1996) that the anisotropy explains most of the strain rate, there are still some important differences, especially in the Wisconsin ice. In general we cannot tell from this study whether Azuma's flow law or Sachs model is better for predicting the behavior of this ice.

Our approach in Equations (4.12) and (4.13) is to incorporate additional physical processes into the deformation model until the "unexplained deformation rate" k approaches zero. If stress, temperature and anisotropy were to explain all the measured deformation, then k in Equation (4.12) would be zero. Our Wisconsin ice criterion for selecting A_0 assumes that addition of impurities can only soften the ice, at least for the concentrations observed at Dye 3. This leads to values of k in the Wisconsin ice that are mostly less than 1. The Holocene ice criterion does result in a few negative values of k in the Wisconsin ice,

i.e. the ice should be stiffer than the model predicts (lower $\mathcal{A}_0$ value) rather than softer, but those negative k values are very small, and the absolute value of k is always less than 1. Most of the variation in k seen in the Holocene ice in both cases can be attributed to uncertainties in the measured strain rates.

Measurements on the ice core show that the impurity content changes rapidly right at the Holocene-Wisconsin boundary. Within the Wisconsin ice there are large variations in impurity concentration which are correlated with the k-value, the excess enhancement after accounting for fabric.

Sonic logging is a very important method to get information about the fabric in bore-holes. Sonic logs that average over distances a bit shorter than 7 m would be helpful, particularly in regions of rapid changes such as the Holocene-Wisconsin boundary and close to the bed. Thin section measurements are very time-consuming, but necessary to draw conclusions about the c-axis distribution; are the c-axes within a cone, is the cone vertical and are the c-axis uniformly distributed within it, or does the ice have a multiple maximum fabric ? Finally we point out that if we know that the c-axes distribution can be characterized by some distribution other than a uniform vertical cone (tilted cone, girdle, etc.), the sonic velocities for that distribution can be calculated and used to infer parameters of that distribution in the ice sheet.

4.9 CONCLUSIONS

The enhancement at Dye 3 (Fig. 4.1) has previously been attributed to various combinations of properties including fabric anisotropy, impurities and crystal size. By accounting for anisotropy, we can explain $\sim$75% of the peak enhancement at Dye 3. The strong correlation between the excess deformation and dust concentration or ion concentration divided by crystal size suggests that most of the excess deformation after accounting for fabric anisotropy can be attributed to the impurities.

We can thus write a flow law for the instantaneous deformation rate as

$$\dot{\varepsilon}_{ij} = \beta_0 A(T)[1 + f(C,T)]R_{ij}\tau^n \tag{4.14}$$

where β_0 is a constant, $A(T) = A_0 \exp\left(-\frac{Q}{RT}\right)$, $f(C,T)$ is a function of crystal size and/or

impurity concentration whose importance may vary with temperature, R_{ij} is the symmetric part of the Schmid-tensor (Equation 4.4) and τ is the resolved shear stress (Equation 4.3). More work is needed to clarify the form of $f(C, T)$. Our simple linear temperature-independent form $f(C, T) = C(z)/a$ worked well for the dust concentration and the limited range of temperatures at Dye 3; however, it does not adequately reproduce the deformation of the silty bottom 23 meters, nor does it have a strong theoretical basis. For the ion concentration divided by crystal size a similar relation also worked well. We feel duly cautioned by the subtitle to *Paterson* (1991), "Impurities - like patriotism - are sometimes the last refuge of scoundrels (*Bohren*, 1983)". However, now that the effects of both temperature and fabric anisotropy can be incorporated in ice flow models, we conclude that impurities clearly emerge as the largest remaining factor influencing ice deformation at Dye 3. This conclusion may also apply elsewhere.

Chapter 5

FABRIC DEVELOPMENT WITH NEAREST NEIGHBOR INTERACTION AND DYNAMIC RECRYSTALLIZATION

This chapter is based on a paper with the same title submitted to Journal of Geophysical Research. Paul Duval, E. D. Waddington and C. F. Raymond provided helpful review comments.

5.1 SUMMARY

The fabric development of strongly anisotropic crystal aggregates is modeled by taking into account the 3-D arrangement of crystals. The nearest neighbor interaction (NNI) with the crystals arranged in a cubic array redistributes the stresses between the crystals and leads to a more homogeneous strain of crystals with increasing interaction. Without NNI the model is equivalent to the homogeneous stress (lower bound) assumption. The NNI slows down the rate of fabric development. The maximum strain rate relative to isotropic increases as the NNI increases. Recrystallization is modeled from energy balance considerations, and polygonization is formulated in terms of stress differences. Results from modeling the fabric development in ice show that including NNI leads to a more realistic fabric evolution than the homogeneous stress model.

5.2 INTRODUCTION

Fabric development has very important effects on the physical properties of crystal aggregates of many common earth minerals. An initially isotropic polycrystal undergoing ductile deformation will develop lattice-preferred orientation (anisotropy) as a result of intra-crystalline slip. The preferred orientation of mantle minerals, mainly olivine crystals, is known to cause seismic shear-wave splitting in the crust and the upper mantle (*Savage*, 1999). In ice-sheets the fabric evolution has been well documented, from extensive thin section measurements on ice-cores (*Alley et al.*, 1995b; *Gow et al.*, 1997; *Thorsteinsson et al.*,

1997) and sonic logging in bore-holes and on the ice-cores themselves (*Kohnen and Gow*, 1979; *Taylor*, 1982; *Anandakrishnan et al.*, 1994; *Thorsteinsson et al.*, 1999).

Several hypotheses have been used to model fabric development; best known are the Taylor-Bishop-Hill (TBH), Visco-Plastic Self Consistent (VPSC) and Sachs hypotheses. In the TBH-hypothesis the key assumption made is that all the crystals in the aggregate experience the same amount of strain, which guarantees compatibility (no voids or overlaps form), but not stress equilibrium (*Bishop and Hill*, 1951). To achieve arbitrary deformation for every crystal, a minimum of 4-5 independent slip systems is required (*Wenk and Christie*, 1991). Models based on the TBH-hypothesis have mainly been used for crystals where the plastic anisotropy is not very strong, and many easy slip systems are available, such as calcite (*Wenk and Christie*, 1991). The VPSC-method compromises between compatibility and stress equilibrium. VPSC models commonly assume that the neighborhood of each crystal is replaced with a Homogeneous Equivalent Medium (HEM), which has the average properties of the aggregate. The HEM can have an anisotropic rheology (*Lebensohn and Tome*, 1993, 1994; *Molinary et al.*, 1987), and the HEM can be defined to encompass any given volume around a given crystal (*Molinary et al.*, 1987; *Wenk et al.*, 1991). The VPSC scheme is an iterative scheme, and as such it is sometimes difficult to visualize the redistribution of stress and strain between crystals at each step. The VPSC method has been used to model peridotite, olivine, quartz and ice, to name only a few (*Wenk et al.*, 1991; *Castelnau et al.*, 1996c). Finally there are models based on *Sachs* (1928) hypothesis, more precisely the homogeneous stress assumption, where the stress on each crystal is assumed to be the same. It guarantees full stress equilibrium, but not compatibility. *Thorsteinsson et al.* (1999) used this model to examine the effect of anisotropy on the deformation of the bore-hole in the ice sheet at Dye 3, Greenland.

According to the TBH-hypothesis the crystals are fully constrained by their neighbors, in VPSC they are partially constrained through the HEM and in Sachs-hypothesis they are completely unconstrained, since the crystal deformation depends only on the applied stress. For the fabric development, on the other hand, the rotations are completely constrained in the Sachs model (*Castelnau et al.*, 1996c).

During fabric development, the nearest neighboring crystals adjacent to the crystal being

considered in the aggregate are expected to have important effects on the deformation of the crystal. *Azuma* (1995) found, by means of in situ observation of plane strain deformation of polycrystalline ice, that the deformation of single crystals depended very strongly on the interaction with its neighbors. Azuma formulated a fabric evolution model, that is partly based on these findings (*Azuma*, 1994, 1995; *Azuma and Goto-Azuma*, 1996). *Sarma and Dawson* (1996) found, using a finite element modeling study of polycrystals, that neighbor interactions were the main factor in determining the variation of the single crystal strain at a given bulk equivalent strain.

Recrystallization is an important mechanism in fabric development. For temperatures (T) close to the melting point ($T > -12°C$ for ice) migration recrystallization is active. The high temperature allows the nucleation of new, strain-free grains and the rapid migration of grain boundaries (*Duval and Castelnau*, 1995). In studies of high temperature (-5°C to 0°C) creep of ice *Kamb* (1972) found that after only about 0.04 shear strain there was already strong evidence of recrystallization. Another recrystallization process is polygonization, in which grains are effectively divided due to rearrangement of dislocations into sub-boundaries (dislocation walls). The effect on the fabric development from this process is less significant since the orientation of the new crystal usually deviates by less than 5° from the parent crystal.

The purpose of this paper is to present a new model for the fabric development. The model modifies the homogeneous stress assumption by redistributing the stress through explicit nearest neighbor interaction (NNI). If there is no NNI, the model reduces to a homogeneous stress model. The effects of nearest neighbor interaction on the behavior of crystal aggregates are examined. Recrystallization, both migration recrystallization and polygonization, is considered. Migration recrystallization depends on the dislocation density and crystal size, both of which have to be taken into account.

In order to model the fabric development for a given material, one has to know the initial orientation distribution of the slip system (s) normals (and Burgers vectors) and their respective "viscosities", $\eta^s = \dot{\gamma}_0^s / \tau_0^{s\,n}$, where $\dot{\gamma}_0^s$ and τ_0^s are reference shear strain rate and shear stress respectively and n is the stress exponent (inverse of strain rate sensitivity; cf. Eq. 5.3).

Ice (I_h, hexagonal) is used as the model material, since it has only one easy slip system, the basal plane (0001) < $11\bar{2}0$ > (*Ashby and Duval*, 1985), and good information about fabric and texture exists from recent ice-core studies (*Thorsteinsson et al.*, 1997; *Gow et al.*, 1997). Resistance to shear τ_0 on other slip systems (prism ($10\bar{1}0$) < $11\bar{2}0$ > and pyramidal ($11\bar{2}2$) < $\bar{1}\bar{1}23$ >) is 20 times or higher than on the basal plane slip system (*Castelnau et al.*, 1997). The fabric development is qualitatively known from thin-section and sonic-logging measurements. The c-axes rotates towards the compression axis (*van der Veen and Whillans*, 1994; *Morland and Staroszczyk*, 1998; *Gödert and Hutter*, 1998; *Thorsteinsson*, 2000a).

In this paper I will use fabric to refer to the orientation distribution of symmetry axes, and texture to refer to the size and shape of crystals.

5.3 THE MODEL

In the model the crystals are arranged on a 3-dimensional cubic grid. Each crystal then has 6 nearest neighbors, as illustrated in Figure 5.1. The cubic arrangement is used to find nearest neighbors at all stages of the deformation. In this section I begin by writing the constitutive equation for a single crystal, and explaining how the nearest neighbor interaction (NNI) is taken into account. The bulk deformation and crystal rotations are then derived. Finally, I describe how recrystallization (normal grain growth, polygonization and migration recrystallization) is included in the model. Since the recrystallization depends on the dislocation density, an evolution equation for the dislocation density is also a part of the model.

5.3.1 Constitutive Relations

The resolved shear stress (RSS) of each slip system s is

$$\tau^s = S_{kl}^s \Sigma_{kl}^c, \tag{5.1}$$

where Σ_{kl}^c is the state of stress in the crystal, and S_{kl}^s is the Schmid-tensor for the slip system. The Schmid-tensor gives the transformation from the crystal coordinate system
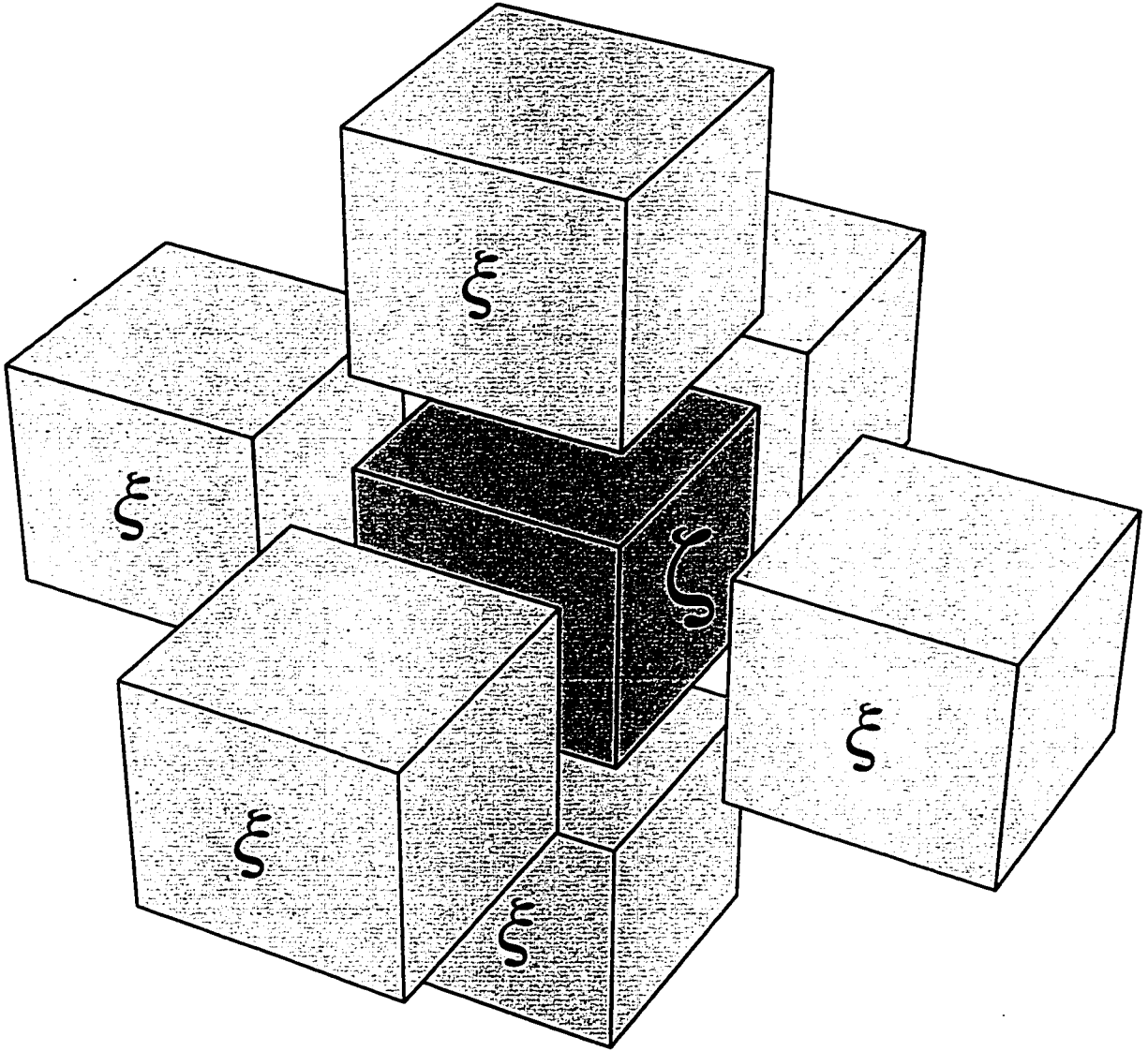
Figure 5.1: Illustration of the crystal arrangement used in the calculations. The center crystal is called ζ, and. its six nearest neighbors are called ξ.

(microscopic) to the lab coordinate system (fixed, macroscopic)

$$S_{ij} = b_i n_j, \qquad (5.2)$$

where $\vec{n}$ is the slip plane normal and $\vec{b}$ is the slip direction (Burgers-vector).

The rate of shearing $\dot{\gamma}^s$, on slip system s, is

$$\frac{\dot{\gamma}^s}{\dot{\gamma}_0^s} = \left|\frac{\tau^s}{\tau_0^s}\right|^{n-1} \frac{\tau^s}{\tau_0^s}, \qquad (5.3)$$

where $\dot{\gamma}_0^s$ and τ_0^s are the reference resolved shear strain rate and shear stress respectively and n is the stress exponent.

The nearest neighbor interaction (NNI) is modeled by defining a local softness parameter, $\mathcal{E}$, for each crystal. The stress acting on the center crystal (Σ_{ij}^c) is modified by $\mathcal{E}^c$ according to

$$\Sigma_{ij}^c = \mathcal{E}^c \sigma_{ij}, \qquad (5.4)$$

where σ_{ij} is the Cauchy stress tensor acting on the crystal aggregate. The softness $\mathcal{E}$ depends on the assigned strength of interaction, defined by the contribution of the center crystal (ζ) and the neighbors (ξ) to $\mathcal{E}$, and on the magnitudes of the RSS of the neighbors compared to the center crystal. The contributions (ζ, ξ) thus determine the strength of interaction, and the magnitudes of the RSS of the neighbors determine the softness. The local softness parameter of each crystal $\mathcal{E}^c$ is calculated from the ratio of the magnitude of the resolved shear stress (RSS) $\mathcal{T}^c$ of the crystal, relative to the RSS's $\mathcal{T}_i^\xi$ of its neighboring crystals, and the relative contribution assigned to the neighbor crystals

$$\mathcal{E}^c = \frac{1}{\zeta + 6\xi} \left(\zeta + \xi \sum_{i_\xi=1}^{6} \frac{\mathcal{T}_i^\xi}{\mathcal{T}^c} \right), \qquad (5.5)$$

where ζ is the contribution of the center crystal and ξ the contribution of each neighbor, and

$$\mathcal{T} = \left| \sum_s \tau^s \hat{b}^s \right| = \left| \sum_s S_{kl}^s \sigma_{kl} \hat{b}^s \right|, \qquad (5.6)$$

where $\hat{b}^s$ is a unit vector in the direction of the Burgers vector. Since the RSS can be zero, there is a specified roof for the maximum value of $\mathcal{E}$.

Setting $\zeta = 1$ and $\xi = 0$ in Eq. (5.5) gives $\mathcal{E} = 1$, and we get the homogeneous stress model, where there is no neighbor interaction. Setting $\zeta = 6$ and $\xi = 1$ the center crystal contributes as much as all the neighbors together, and for $\zeta = 1$ and $\xi = 1$ the center crystal contributes as much as each of the neighbors. The effects of varying ζ and ξ are explored below.

The strain rate is defined by $\dot{\varepsilon}_{ij} = \frac{1}{2}(L_{ij} + L_{ji})$, where $L_{ij} = \partial v_i / \partial x_j$ is the velocity gradient, the v_i's are the velocity components and x_i the coordinates in a stationary macroscopic reference frame (Molinary et al., 1987). The velocity gradient in the macroscopic reference frame is related to the microscopic shear strain rates by

$$L_{ij}^c = \sum_s S_{ij}^s \dot{\gamma}^s. \tag{5.7}$$

The strain rate in the macroscopic reference frame is then given by

$$\dot{\varepsilon}_{ij}^c = \sum_s R_{ij}^s \dot{\gamma}^s, \tag{5.8}$$

where $R_{ij} = \frac{1}{2}(S_{ij} + S_{ji})$.

Equations (5.3) and (5.7) show that the velocity gradient of a single crystal in the macroscopic coordinate system is

$$L_{ij}^c = \sum_s \dot{\gamma}_0^s S_{ij}^s \left| \mathcal{E}^c S_{kl}^s \frac{\sigma_{kl}}{\tau_0^s} \right|^{n-1} \mathcal{E}^c S_{kl}^s \frac{\sigma_{kl}}{\tau_0^s}, \tag{5.9}$$

where S_{ij} is the Schmid tensor. The modeled velocity gradient of the bulk is

$$L_{ij}^m = \frac{1}{N} \sum_{c=1}^N L_{ij}^c. \tag{5.10}$$

5.3.2 Rotation of Single Crystals

To calculate the fabric development, we need to formulate how the crystals rotate with respect to the external reference frame and with respect to each other. The rotation rate of the crystal lattice is given by

$$\dot{\Omega}^* = \dot{\Omega}^b - \dot{\Omega}^p, \tag{5.11}$$

where $\dot{\Omega}^b$ is the bulk rotation rate, and $\dot{\Omega}^p$ is the plastic rotation rate of a single crystal. The plastic rotation rate of single crystals is

$$\dot{\Omega}_{ij}^p = \frac{1}{2} \left(L_{ij}^c - L_{ji}^c \right). \tag{5.12}$$

We impose the boundary condition of a bulk rotation rate; therefore we need to add a rotation rate $\dot{\Omega}^d$ to the bulk velocity gradient L_{ij}^m calculated from the model. This arises since the applied stress tensor is a symmetric second order tensor, and for isotropic material the deformation gradient will have the same symmetry as the stress, i.e. $L_{13} = L_{31}$. The bulk rotation rate can be used, for instance, to describe a simple shear experiment. The bulk velocity gradient is thus $L_{ij} = L_{ij}^m + \dot{\Omega}_{ij}^d$ (*Castelnau and Duval*, 1994), where $\dot{\Omega}_{ij}^d$ is found from

$$\dot{\Omega}_{ij}^d = \dot{\Omega}_{ij}^b - \dot{\Omega}_{ij}^m, \tag{5.13}$$

and

$$\dot{\Omega}_{ij}^m = \frac{1}{2}\left(L_{ij}^m - L_{ji}^m\right). \tag{5.14}$$

For irrotational deformation (uniaxial compression/tension, pure shear)

$$\dot{\Omega}^d = -\dot{\Omega}^m.$$

For simple shear (σ_{13} only non-zero stress component) of an isotropic material, $L_{13}^m = L_{31}^m$ are the only non-zero components of the velocity gradient, and

$$\dot{\Omega}_{13}^d = \dot{\varepsilon}_{13} - \dot{\Omega}_{13}^m, \quad \dot{\Omega}_{31}^d = -\dot{\varepsilon}_{13} - \dot{\Omega}_{31}^m,$$

where $\dot{\varepsilon}_{13} = (L_{13}^m + L_{31}^m)/2$. $\dot{\Omega}_{13}^m = \dot{\Omega}_{31}^m = 0$, and therefore $L_{13} = 2L_{13}^m$ and $L_{31} = 0$, which is precisely the condition for simple shear.

The change in orientation for $\vec{n}$ is then (Eq. 5.11)

$$\dot{n}_i = \dot{\Omega}_{ij}^* n_j. \tag{5.15}$$

In the following I consider deformation by dislocation glide on the basal plane slip system, using ice as the model material. *Kamb* (1961) showed that for the observed range of the stress exponent, $2 < n < 4$, the expected response to simultaneous glide along the a-axes differs so slightly from the hitherto-postulated a-axis-independent, non-crystallographic glide as to be practically undetectable experimentally. The resistance to slip on the basal plane is the same for the three a-axes, and we only consider the basal slip system for ice; therefore we can write

$$\frac{\dot{\gamma}_0^s}{\tau_0^{sn}} = \beta A(T), \tag{5.16}$$

where β is a constant, and $A(T) = A_0 \exp\left(-\frac{Q}{RT}\right)$, A_0 is a constant, Q is the thermal activation energy, R is the gas constant, and T the temperature. β is chosen such that an isotropic distribution yields the same strain rates as Glen's flow law (*Glen*, 1958), or some reliable measurements.

In the model calculations below, the change in the zenith and azimuth angle of the normal ($\vec{n}$) is calculated for each crystal. This also allows us to update the orientation of the three Burgers-vectors in the basal plane (*Thorsteinsson*, 2000a).

5.3.3 Recrystallization

For most polycrystalline materials, there are at least three recrystallization regimes: normal grain growth, polygonization and migration recrystallization. The fabric (crystal orientations) is not affected by normal grain growth, where grain size increases according to a parabolic growth law (*Gow*, 1971; *Alley et al.*, 1986). As the crystals strain, sub-boundaries (dislocation walls) may form due to heterogeneous deformation within grains that relieves stress concentrations. The formation of sub-boundaries can lead to the division of the parent crystal into two new crystals, as the misorientation of sub-boundaries increases. This is called polygonization, and it leads to the formation of two crystals with a small misorientation angle ($\sim 5°$).

The formation of sub-boundaries, by dislocations forming dislocation walls, can create small (fraction of parent crystal size) crystals that are in a strain shadow. Being strain energy-free, these small crystals can act as seeds for migration recrystallization. The idea adopted in this model is that within the crystal aggregate there are many such seeds. They are not accounted for in the model, since they are too small to contribute significantly to the deformation. When the temperature gets high enough for grain boundary migration to be very efficient, these seeds can quickly consume highly strained crystals, thus reducing the free energy of the system. These small crystals in the aggregate are also envisioned to allow for grain growth; where crystals grow by consuming them.

The number of crystals is kept constant in the calculations, so the volume (mass) can change discontinuously during recrystallization when new crystals replace old ones of differ-

ent size. Only one of the two crystals resulting from polygonization is kept in the calculation; the choice is random. Since the orientations of the two parts are similar, this assumption does not significantly affect the NNI or the fabric. The discontinuity in volume would have to be accounted for if the crystal size were to be modeled accurately. During migration recrystallization the new crystal is smaller (possibly equal in size) than the parent crystal, and the "missing mass" becomes "seeds".

Polycrystalline ice is used as the model material, since good information about the transition between these recrystallization regimes exists from ice core studies.

Grain growth

During normal grain growth the crystal diameter increases with time (*Gow*, 1971; *Alley et al.*, 1986), according to

$$D^2 - D_0^2 = K \cdot t, \tag{5.17}$$

where t is time, and D_0 is the crystal diameter at $t = 0$. The grain growth factor

$$K = K_0 \exp(-\frac{Q}{RT}), \tag{5.18}$$

where T is the temperature, Q is activation energy and K_0 is a constant that depends on impurity concentration. In the calculations below, $K_0 = 8.2 \cdot 10^{-9}$ m^2 s^{-1} and $Q = 40$ kJ mol^{-1} represent ice (*Alley et al.*, 1986).

I have also used the difference in stored energy due to dislocations E_{disl} (see Eq. (5.21) below) to calculate the changes in crystal size (*Wenk et al.*, 1997). The growth factor is then

$$\tilde{K} = (E_{disl}^{av} - E_{disl}^{i})K', \tag{5.19}$$

where E_{disl}^{i} is the stored energy of the crystal, E_{disl}^{av} is the average stored energy for the whole sample and K' is a constant that depends on temperature and impurities. This allows some crystals to grow (if $E_{disl}^{av} > E_{disl}^{i}$), and others to contract ($E_{disl}^{av} < E_{disl}^{i}$).

Polygonization

In the GRIP ice-core from the Greenland ice-sheet, polygonization (rotation recrystallization) is active below 650 m depth where the vertical strain is about 0.25 (*Thorsteinsson*

et al., 1997). *De La Chapelle et al.* (1998) found a lower bound for the dislocation density associated with the formation of a grain boundary by considering the energy associated with a dislocation density ρ and the energy corresponding to the formation of a grain boundary. They estimated that the dislocation density has to be greater than $\rho_{poly} \sim 5.4 \cdot 10^{10} \text{m}^{-2}$, which is the minimum dislocation density needed to form a wall. Here polygonization is modeled by considering a proxy for bending moments. Crystals that have low RSS are likely to experience heterogeneous stress from their neighboring crystals, which are deforming. These stresses apply bending moments, which are relieved when the dislocations organize themselves into walls (sub-boundaries), effectively dividing the crystal (*Duval and Castelnau*, 1995). To account for polygonization in the model, the magnitude of the RSS of the crystal is compared to the magnitude of the applied stress. If that ratio is smaller than a given value, δ, and the dislocation density $\rho > \rho_{poly}$, then the crystal will polygonize. The orientation is changed by $\Delta\theta$, the crystal size is halved and the dislocation density ρ is reduced by ρ_{poly}.

Typical values used to model ice are $\delta = 0.065$ and $\Delta\theta = 5°$.

Migration recrystallization

Migration recrystallization is generally active when the temperature is close to the melting point. In ice it is active when the temperature exceeds $\sim -12°C$, but for colder temperatures it is generally not observed (*Duval and Castelnau*, 1995). To model migration recrystallization, the energy associated with grain boundaries, and stored energy must be considered. The energy associated with grain boundaries is

$$E_{gb} = \frac{3\gamma_{gb}}{D}, \tag{5.20}$$

where $\gamma_{gb} = 0.065 \text{ J m}^{-2}$ (for high angle boundaries), and D the crystal diameter. The stored energy due to a dislocation denisty ρ is difficult to estimate, but can be expressed as

$$E_{disl} \simeq \kappa\rho Gb^2 \ln\frac{R_e}{b}, \tag{5.21}$$

where G is the shear modulus, b is the length of the Burgers-vector, κ is $(4\pi)^{-1}$ for screw and $[4\pi(1-\nu)]^{-1}$ for edge dislocations, where $\nu \simeq 0.3$ is the Poisson's ratio, and R_e is the

mean average of the dislocation strain field range (*Mohamed and Bacroix*, 2000; *Kuhlmann-Wilsdorf*, 1998, 1999). R_e is commonly approximated by $1/\sqrt{\rho}$, but *Mohamed and Bacroix* (2000) found that this lead to an underestimate of E_{disl}. I therefore treat κ as an adjustable parameter, but leave $R_e = 1/\sqrt{\rho}$. For ice, $G \simeq 3.4 \cdot 10^9$ Pa and $b = 4.5 \cdot 10^{-10}$ m.

Migration recrystallization is included by considering the balance between the stored energy E_{disl} associated with the dislocation density and the grain boundary energy E_{gb}. As the crystals strain, the dislocation density increases, and it becomes energetically favorable to recrystallize if the energy due to the dislocation density (E_{disl}) exceeds the grain boundary energy E_{gb} that is created by the recrystallization. Therefore we need to track the crystal size and dislocation density. The dislocation density ρ increases with time (*De La Chapelle et al.*, 1998) as

$$\frac{\partial \rho}{\partial t} = \frac{\dot{\varepsilon}}{bD} - \alpha \rho \frac{K}{D^2}, \tag{5.22}$$

where α is a constant slightly greater than 1, K is the grain growth factor and D the crystal diameter. The first term on the right hand side represents the production of dislocations necessary to maintain the strain rate, and the second term represents the absorption of dislocations at grain boundaries. In the model, the crystal size D and dislocation density ρ are calculated at each step. When $E_{disl} > E_{gb}$, the crystal recrystallizes. The crystal is then replaced with a new strain-free crystal, with dislocation density ρ_0. The size of the new crystal scales with the effective stress $\sigma_e^2 = \sigma_{kl}\sigma_{kl}/2$ as $D_0 \sim \sigma_e^{-1.33}$ (*Guillope and Poirier*, 1979; *Ross et al.*, 1980; *Shimizu*, 1998, 1999). A totally random orientation for the new grain is not to be expected; some subset of possible zenith angles seems most likely. In uniaxial compression of ice, for instance, a small girdle fabric forms (*Budd and Jacka*, 1989). This indicates that new crystals that form in orientations with high RSS are favored to grow. The orientation of the new crystal is chosen, at random, from a specified range of possible angles in the model. In uniaxial compression, for example, new crystals can form between 35° and 55°, with a higher probability for the larger angles.

5.4 MODEL RESULTS

Here the effects of nearest neighbor interaction (NNI) on the fabric development and bulk behavior is explored, and the recrystallization assumptions examined. The results are then compared with data from the GRIP ice-core.

5.4.1 Nearest Neighbor Interaction

First we examine the effects of the NNI on the fabric development. The fabric development is calculated without any recrystallization. Three types of NNI are used, $(\zeta, \xi) = (1,0)$, $(6,1)$ and $(1,1)$, which will be called no-NNI, mild-NNI and full-NNI respectively.

Figure 5.2 shows model results for ice deformed under uniaxial compression stress and Figure 5.3 shows the results for ice deformed in pure shear stress. Each row shows the results for different NNI. The first plot in each row shows the strain rate, $\dot{\varepsilon}_{33}$, normalized by the initial isotropic strain rate, as a function of axial strain

$$\varepsilon_{33} = \sum_{i=1}^{N} \dot{\varepsilon}_{33}^{i} \Delta t_{i},$$

where Δt_i is the time it takes to complete the strain step i, and N is the number of steps. The second plot in each row shows the strain of single crystals as a function of the bulk equivalent strain, $\varepsilon_{eq} = \sum_{i=1}^{N} \dot{\varepsilon}_{eq}^{i} \Delta t_{i}$, where

$$\dot{\varepsilon}_{eq} = \sqrt{\frac{2}{3} \dot{\varepsilon}_{kl} \dot{\varepsilon}_{kl}}.$$

The results are displayed as a density plot, where the percentage of crystals within a given strain (range) at a given bulk strain (range) are shown. The final plot in each row is the resulting fabric at the end of the model run.

In the uniaxial compression model run, the maximum strain rate generally increases with increasing NNI. In pure shear, that effect is very small, since the fabric evolution is less favorable for the deformation; the fabric locks up. The strain of individual crystals with no-NNI in uniaxial compression follows two primary branches, zero-strain or rapid-strain. Many of the crystals are simply not deforming. With increasing NNI, the spread diminishes and for full-NNI all the crystals deform to some extent. Similar observations apply to the

pure shear deformation. The NNI tends to make all the crystals deform to the same extent. For the final fabric, increasing the NNI tends to slow down the overall concentration of crystals. There is also a distinct change in character of the final fabric; compare the top and bottom row of Figs. 5.2 and 5.3.
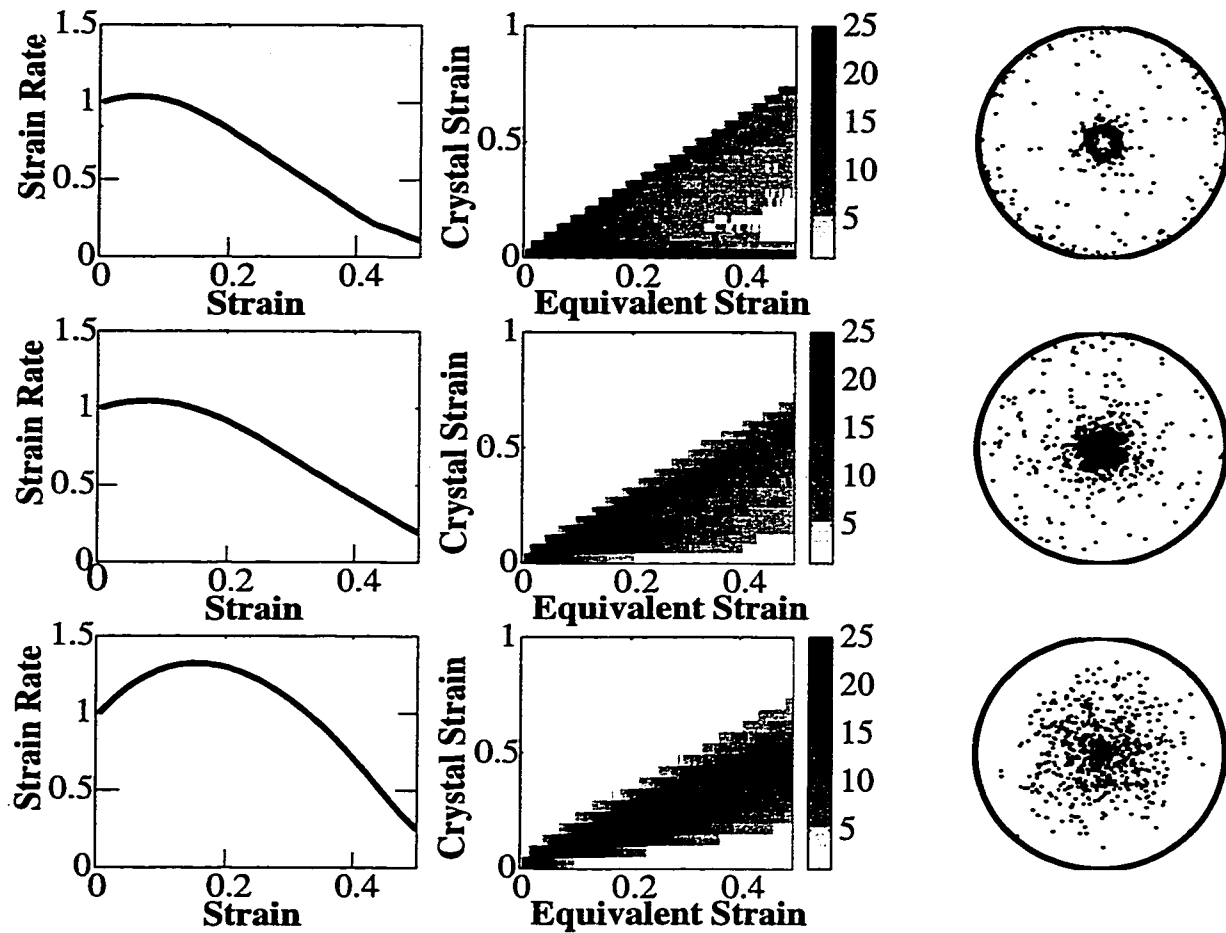
Figure 5.2: Model results for uniaxial compression deformation for varying NNI (TOP: no-NNI (1,0), CENTER: mild-NNI (6,1), BOTTOM: full-NNI (1,1)). The left column shows the normalized vertical strain rate versus the vertical strain. The center column shows the distribution of single crystal strain as a function of bulk equivalent strain, where the color bar shows the percentage of crystals with a given strain. The right column shows the final fabric achieved in each case.

It is clear from the final fabric in Fig. 5.2 that the rate of change of the zenith angle θ (zenith angle velocity $d\theta/dt$), changes as the NNI changes. Figure 5.4 shows the zenith
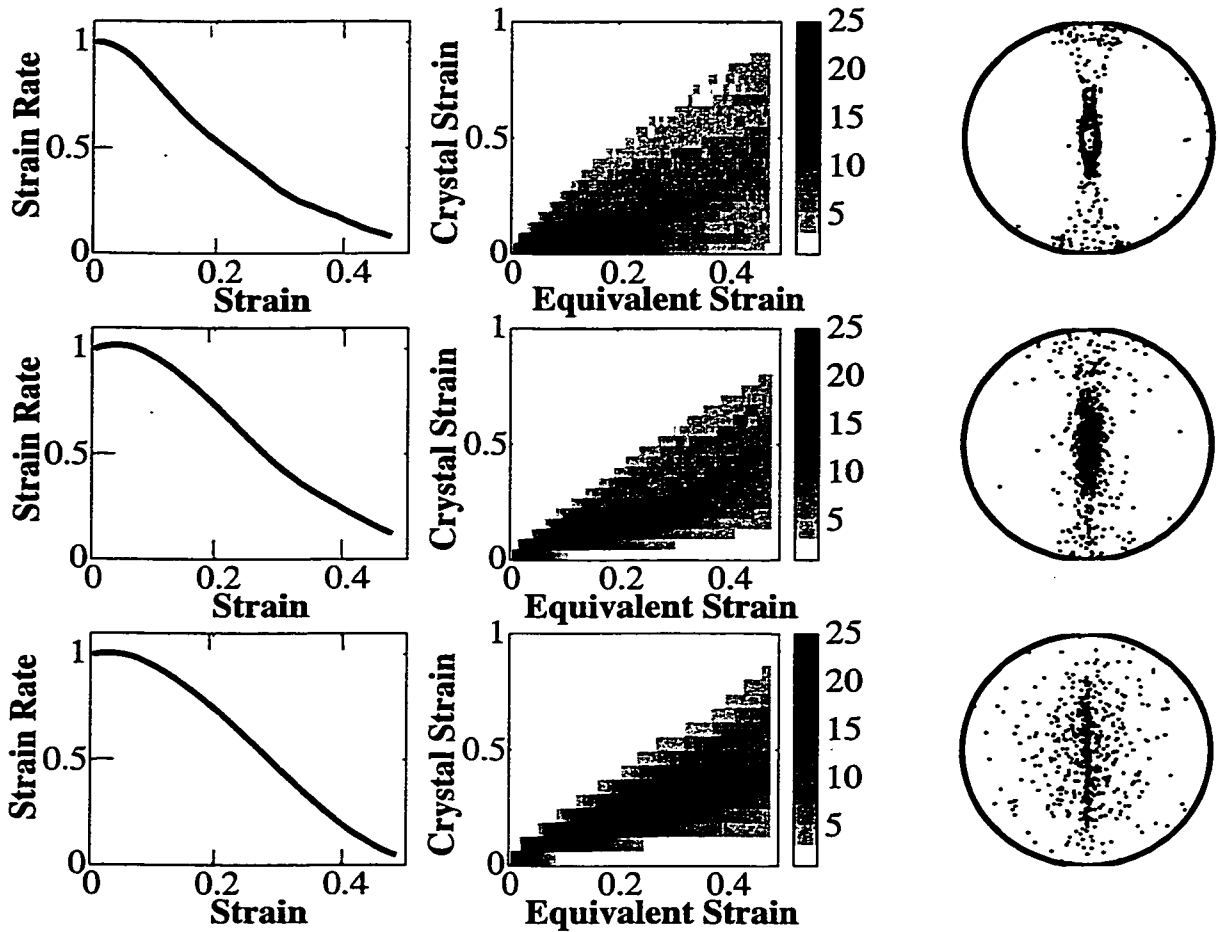
Figure 5.3: Model results for pure shear stress state deformation for varying NNI (TOP: no-NNI (1,0), CENTER: mild-NNI (6,1), BOTTOM: full-NNI (1,1)). The left column shows the normalized vertical strain rate versus the vertical strain. The center column shows the distribution of single crystal strain as a function of bulk equivalent strain, where the color bar shows the percentage of crystals with a given strain. The right column shows the final fabric achieved in each case.

angle velocity for the no-NNI, mild-NNI and full-NNI. When there is no-NNI the zenith angle velocity of each crystal as a function of zenith angle is a constant. When there is NNI, the zenith angle velocity at a given zenith angle depends on the nearest neighbors. The mean velocity at a given zenith angle is thus different from the no-NNI case. From Fig. 5.2 we see that the maximum zenith angle velocity, of the bulk average, decreases as the interaction increases, but the velocity is more uniform over a range of zenith angles.
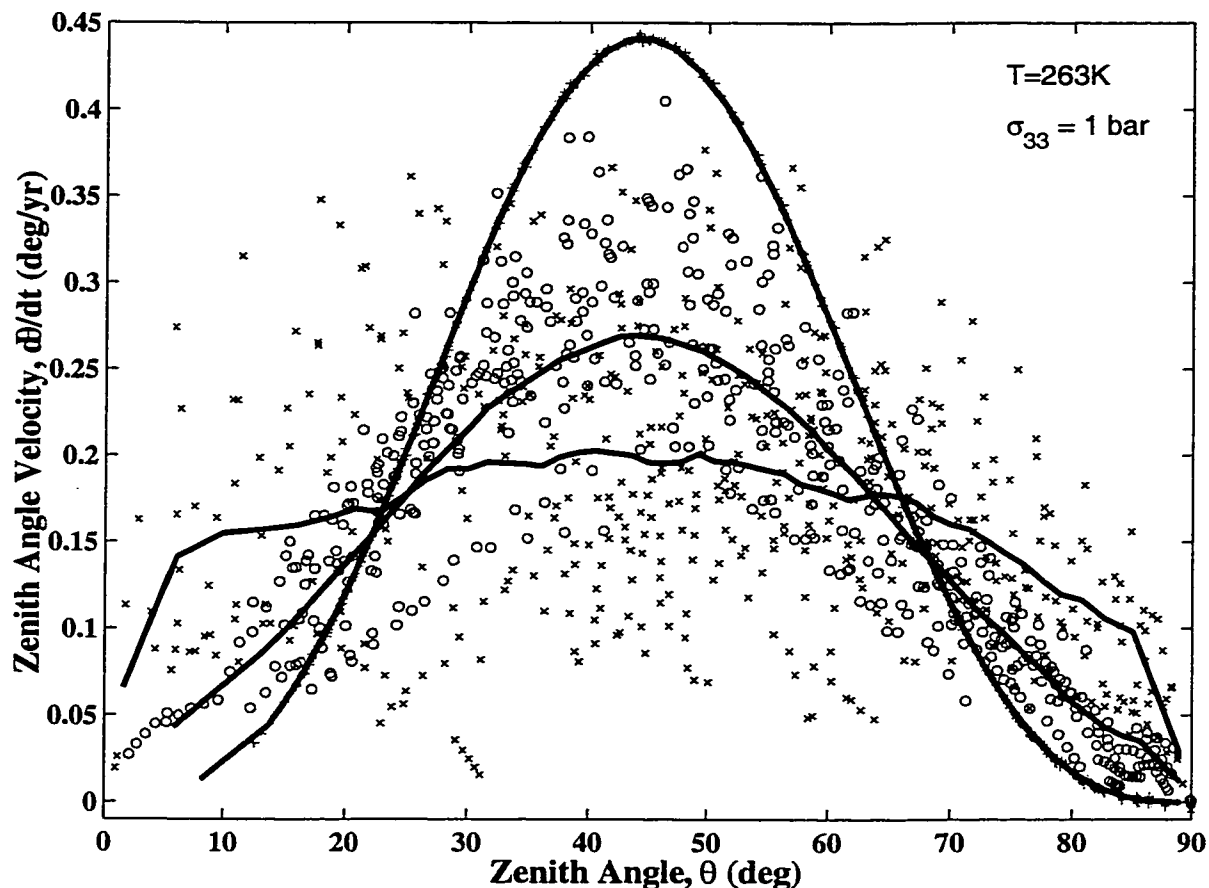
Figure 5.4: Zenith angle velocity, $d\theta/dt$, in uniaxial compression as a function of zenith angle, θ, for different levels of NNI. The +'s result from no-NNI (1,0), o's from mild-NNI (6,1) and x's from full-NNI (1,1). In each case a mean velocity curve is plotted, which uses the average over $\sim 5°$ steps. Note that the +'s are almost completely hidden behind the curve for the no-NNI case. Only a few of the 50×10^3 data points for each level of NNI are shown here.

5.4.2 Checking Recrystallization Assumptions

In the following, the model is initialized by assigning an initial fabric which has a random distribution of c-axes (isotropic ice) as before, randomly assigned crystal size of 3 mm to 5 mm diameter with a mean of 4 mm, and a constant dislocation density of $\rho_0 = 5 \cdot 10^9$ m^{-2} for the crystals. The stress level is approximately 0.1 bar, and in the examples below the crystal size remained essentially constant (short time required to achieve the strain).

The results of uniaxial compression with mild-NNI and polygonization are shown in Figure 5.5. The strain rate versus strain, single crystal strain density and the final fabric are shown in the top row, and the polygonization events are shown below. Here the temperature is too low for migration recrystallization to be active. Polygonization starts at a vertical strain of about 0.03. The initial dislocation density in this run was $\rho_0 = 5 \cdot 10^9$ m^{-2}, the minimum dislocation density to form sub-boundaries is $\rho_{poly} = 5.4 \cdot 10^{10}$ m^{-2} and $\delta = 0.065$. This means that if the magnitude of the RSS for a crystal is less than 6.5% of the applied stress magnitude, then the crystal can polygonize if the dislocation density is high enough. Each time a crystal polygonizes, the dislocation density is reduced by ρ_{poly}. The zenith angle changes by $\pm 5°$, if the crystal is within 30° of vertical the sign is positive (crystal moves away from vertical), otherwise the sign is chosen at random. The strain rate is higher than in the case without polygonization, since crystals in "hard" orientations are preferentially removed by the polygonization criteria. The single crystal strain distribution is more homogeneous at a given bulk equivalent strain, and the final fabric is not as strong (compare with the center row of Fig. 5.2).

Figure 5.6 shows the results when migration recrystallization is active. The strain rate versus strain, single crystal strain density and final fabric are shown in the top row, and the recrystallization events below. Initially all the crystals have the same dislocation density ($\rho_0 = 5 \cdot 10^9$ m^{-2}), so the E_{disl} is very small relative to the grain boundary energy. But, as the crystals strain at different rates, the stored energy (E_{disl}) increases and in some crystals eventually reaches E_{gb}; the vertical stress is 0.1 bar so crystal growth/contraction is negligible during the time it takes to deform the sample. I used $\kappa = 0.2$; smaller values did not result in strong girdle fabrics. Larger values of κ is would initiate migration recrys-

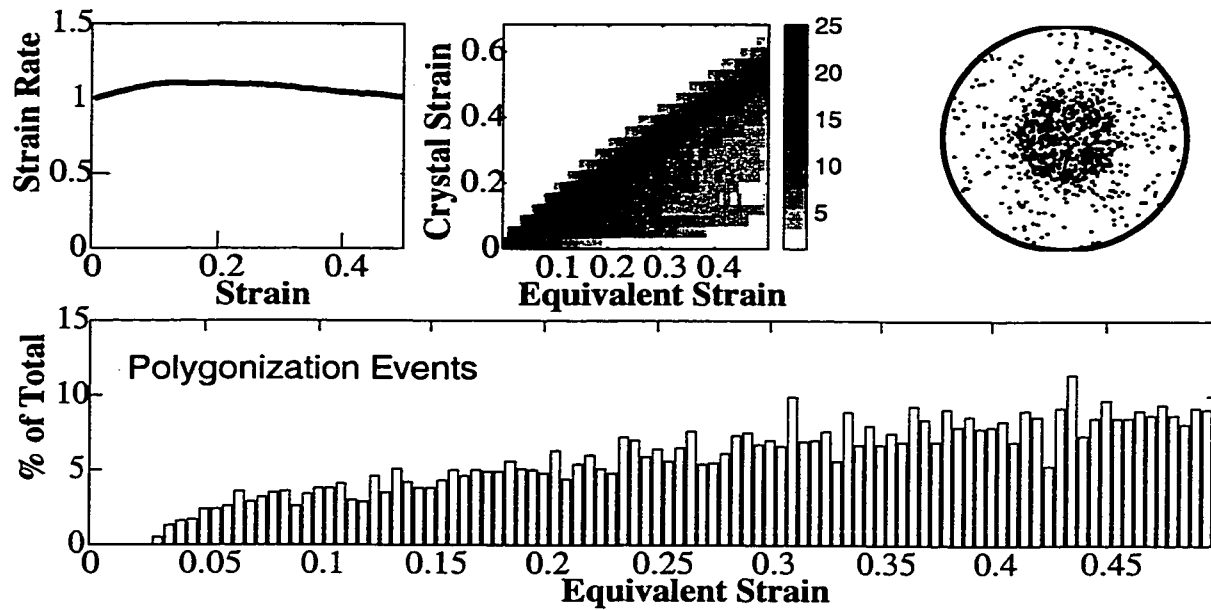Figure 5.5: Results from uniaxial compression with mild-NNI, $(\zeta, \xi) = (6, 1)$ and polygonization ($\delta = 0.065$). The top row shows the normalized strain rate versus axial strain, strain density of single crystals and the final fabric. The bottom row shows the polygonization events after each strain step as a percentage of the total number of crystals. Each step is equal to an equivalent strain of 0.005.
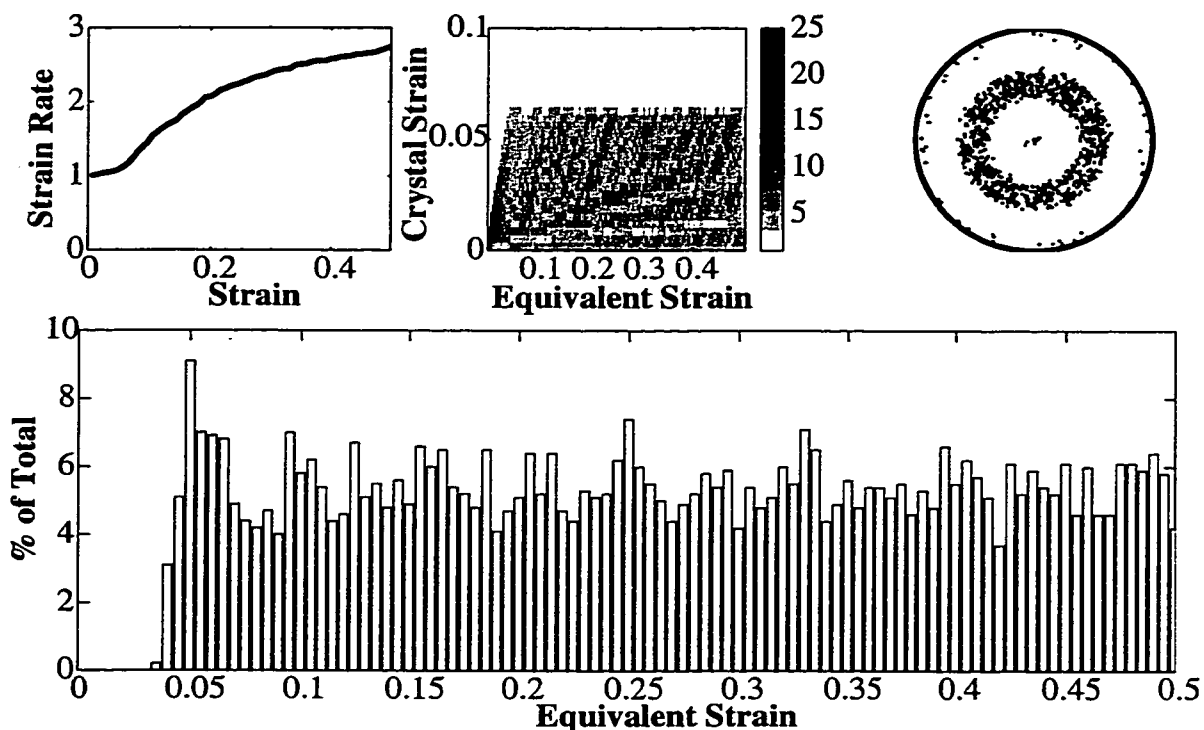
Figure 5.6: The normalized strain rate versus axial strain, single crystal strain density and final fabric for mild-NNI in uniaxial compression with migration recrystallization. The bottom row shows the recrystallization events after each strain step as a percentage of the total number of crystals. Each step is equal to a equivalent strain of 0.005.

tallization for lower dislocation density, i.e. at lower strains. When the stored energy of a crystal exceeds E_{gb}, that crystal will recrystallize. The first recrystallization event occurs after 0.03 equivalent strain, and about 5% of the crystals recrystallize at each step (0.005 equivalent strain) after that. The strain rate increases rapidly at first, but after about 0.2 strain it levels off, approaching normalized strain (enhancement, $E = \dot{\varepsilon}/\dot{\varepsilon}_{isotropic}$) of about 3. A similar pattern is observed in laboratory experiments (Budd and Jacka, 1989). Single crystals acquire only about 0.06 strain before their E_{disl} exceeds the E_{gb}; the crystal size is about 4.2 mm throughout.

Comparison of model results with measured fabric is complicated, especially since the initial fabric is often not truly random. At GRIP, Greenland, the fabric close to the surface does not have an isotropic orientation distribution. This is clearly demonstrated in Figure

5.7, showing the c-axis orientations of the ice at 139 m depth. The strain (< 0.1) that the ice has experienced is insufficient to reorient the crystals significantly, yet the fabric is far from the isotropic sin-curve distribution characteristic of isotropic ice.

Keeping in mind the complications mentioned above, Figure 5.8 shows a comparison of the model results, using mild-NNI with polygonization, with fabric data from the GRIP bore-hole, Greenland (*Thorsteinsson et al.*, 1997). The vertical strain is about 0.25 at 650 m depth and about 0.5 at 1293 m depth. The initial fabric in the model was isotropic and the criterion for polygonization are the same as above. The temperature is below $-12°C$ so there is no migration recrystallization. The zenith angle averaging includes all the 1000 crystals used in the model run. The results are in broad agreement with the measured fabric. Model runs with no interaction (no-NNI) lead to a much stronger fabric and can be ruled out, but full-NNI cannot be ruled out.

5.4.3 Sensitivity to the Number of Crystals Used

This model can be used to calculate the instantaneous deformation for a pre-described fabric. The question is then, how many crystals are needed to calculate the strain rate. I now examine how many crystals are needed to give an accurate description of isotropic ice. In the model the crystal orientations are chosen at random; an infinite number of crystals is needed to exactly satisfy isotropy. Since a finite number of crystals is used, the calculations of strain rate must depend to some extent on the number of crystals used; obviously 100 crystals chosen at random cannot uniquely cover the lower hemisphere. I choose to model isotropic ice, since that gives the largest area that must be covered with crystals. For any given number of crystals the strain rate is calculated 100 times, for a new random fabric each time. I then calculate the mean and standard deviation (STD) of the strain rates for the 100 numerical experiments. Since the correct strain rate for infinite number of crystals is known analytically (*Thorsteinsson*, 2000a), it can be used to normalize the resulting strain rates. Figure 5.9 shows how the number of crystals used in a calculation effects the accuracy. Note that the STD reduces greatly as the number of crystals increases from 100 to about 5000. The improvement between 5000 and 10000 crystals is minimal. I conclude
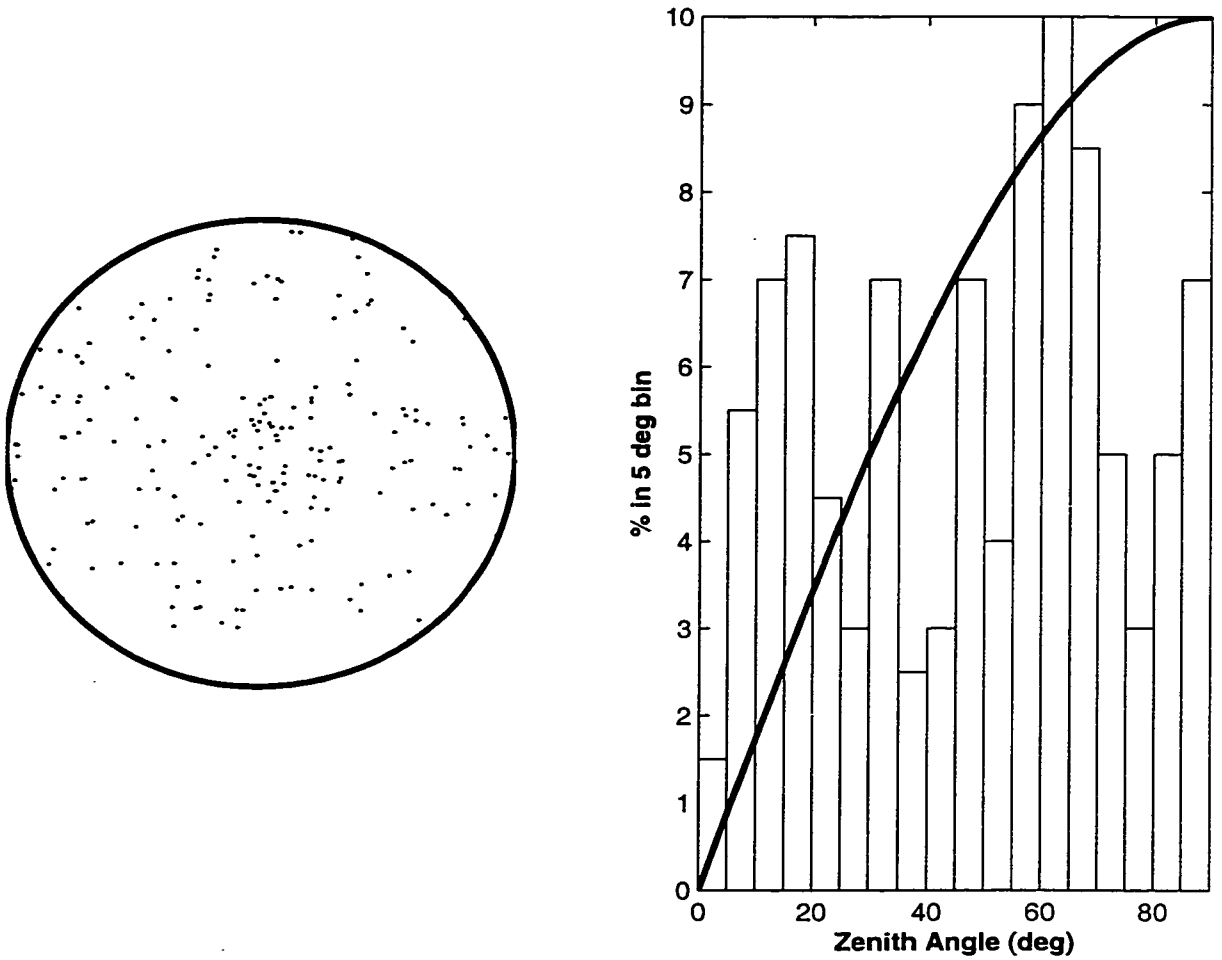
Figure 5.7: Fabric at 139 m depth in the GRIP bore-hole, Greenland (*Thorsteinsson et al.*, 1997). The Schmidt-plot shows the distribution of all the 200 crystal c-axes, and the bar plot shows the number of crystals in 5° zenith angle bins. The distribution is far from the isotropic distribution shown by the solid line.
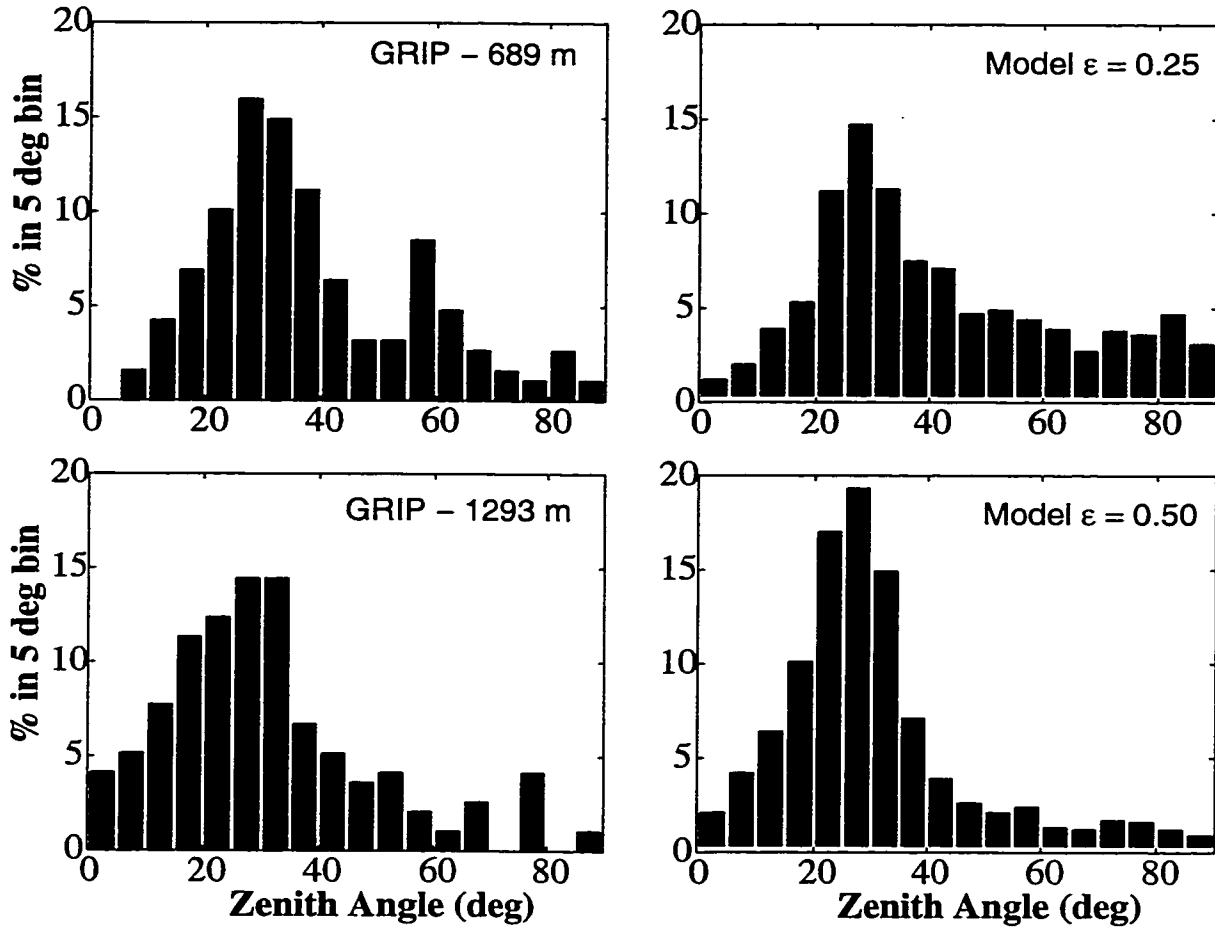
Figure 5.8: Comparison of the measured and calculated zenith angle distributions at two depths in the GRIP core. The measured fabric (left column) is obtained from thin sections done on the GRIP ice-core (*Thorsteinsson et al.*, 1997). The zenith angles are binned in 5° bins (188 crystals at 689 m and 194 at 1293 m), and the same applies to the 1000 crystals from the model. The model calculations (right column) were done with mild-NNI and $\delta = 0.065$.

that accurate results are achieved using a 20×20×20 arrangement of crystals.

Note also that the ratio of crystals at the surface of the cubic arrangement to the total number of crystals, $R_d = S/V = 4d^2/d^3 = 4/d$ goes from 40% for 10^3 crystals, to 20% for 20^3 crystals. This is important since we use a periodic arrangement of crystal boxes for the NNI (that is, the arrangement shown in Fig. 5.1 is repeated for 20^3 crystals in each box).
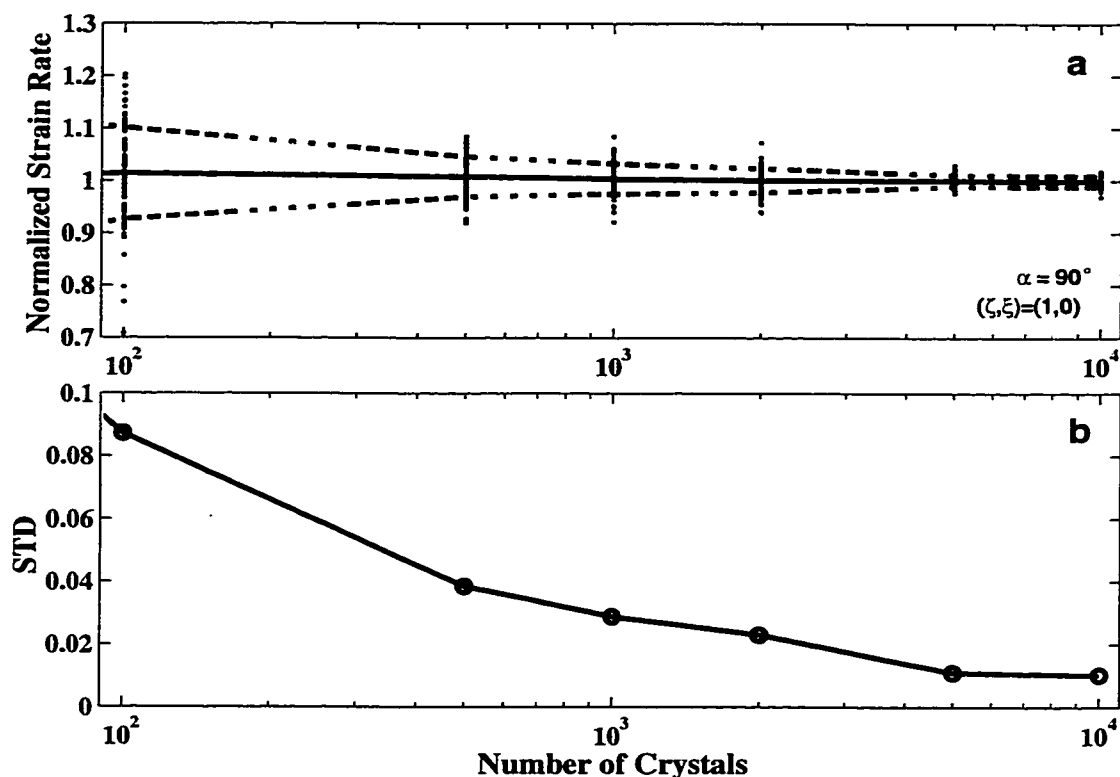
Figure 5.9: Examining the effect of the number of crystals used in the calculations. (a) Normalized strain rate (calculated divided by theoretical) of an isotropic ice with no-NNI as a function of the number of crystals used in the simulation. (b) The standard deviation of the normalized strain rates as a function of the number of crystals used.

Having established that ~ 8000 crystals can be used to adequately represent the strain rate, the strain rate as a function of cone angle (α) can now be modeled. The cone angle α is half the apex angle of a vertical cone, within which the crystals are evenly distributed. Figure 5.10 shows the normalized strain rate, $\dot{\varepsilon}_{33}(\alpha)/\dot{\varepsilon}_{33}(90°)$, in uniaxial compression as a function of cone angle. With increasing interaction the maximum strain rate increases.

Figure 5.11 shows how increasing NNI increases the maximum enhancement in a simple shear stress state.
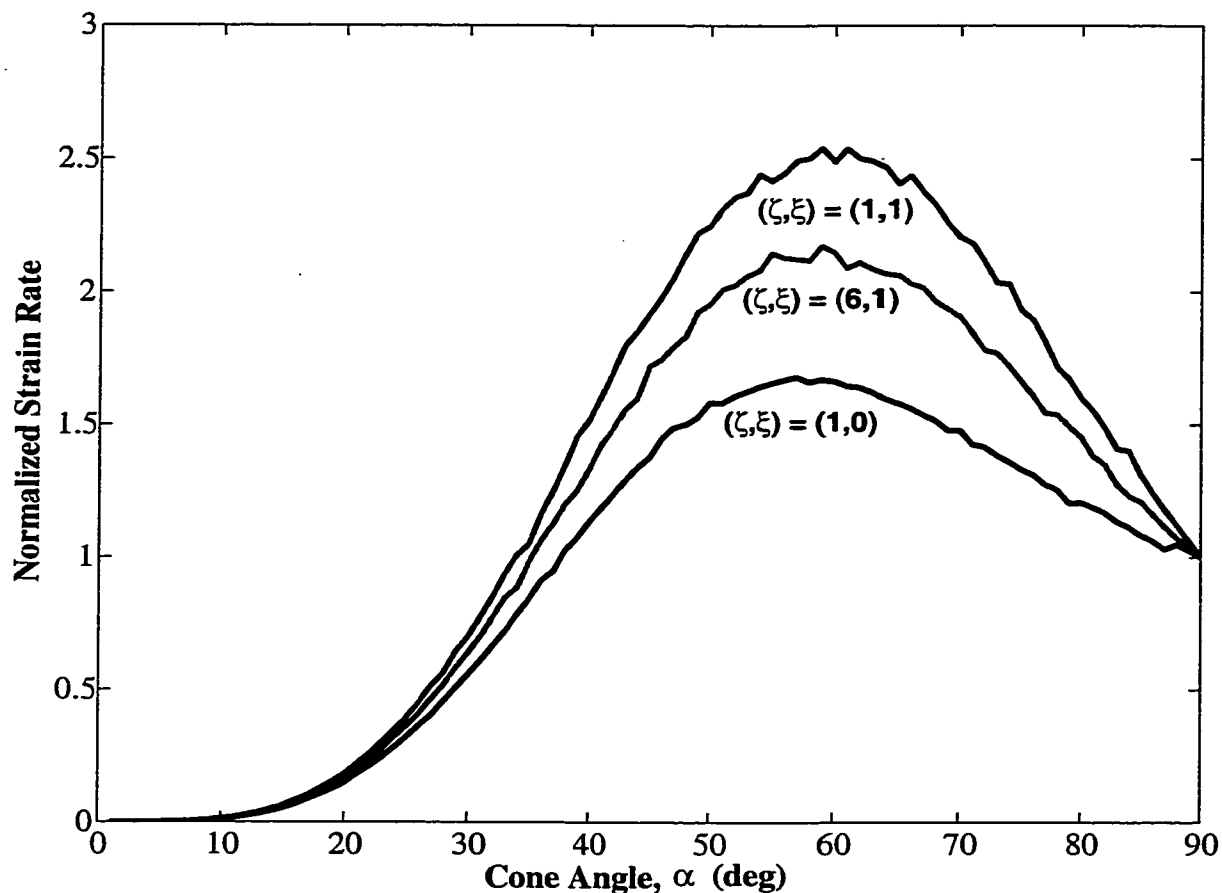
Figure 5.10: Normalized strain rates in uniaxial compression as a function of cone angle for no (1,0), mild (6,1) and full (1,1) nearest neighbor interaction.

5.5 DISCUSSION

In the model the level of stress for each crystal is dependent on the orientation of the crystal and, except for no-NNI, the orientation of the nearest neighbors. The crystals are arranged on a cubic grid, but the formulation applies equally well to other crystal arrangements. The model can easily be extended to include next-to-nearest neighbor interaction, which would presumably make a smaller contribution to the local softness. The nearest neighbor

Figure 5.11: Normalized strain rates in simple shear stress as a function of cone angle for no (1,0), mild (6,1) and full (1,1) nearest neighbor interaction.

interaction leads to more enhanced deformation rates for cone angles between 40° and 90° in uniaxial compression along the direction of the cone (Fig. 5.2). The same is not true in pure shear (Fig. 5.3), because the deformation quickly moves the crystals into unfavorable orientations, where the RSS is smaller.
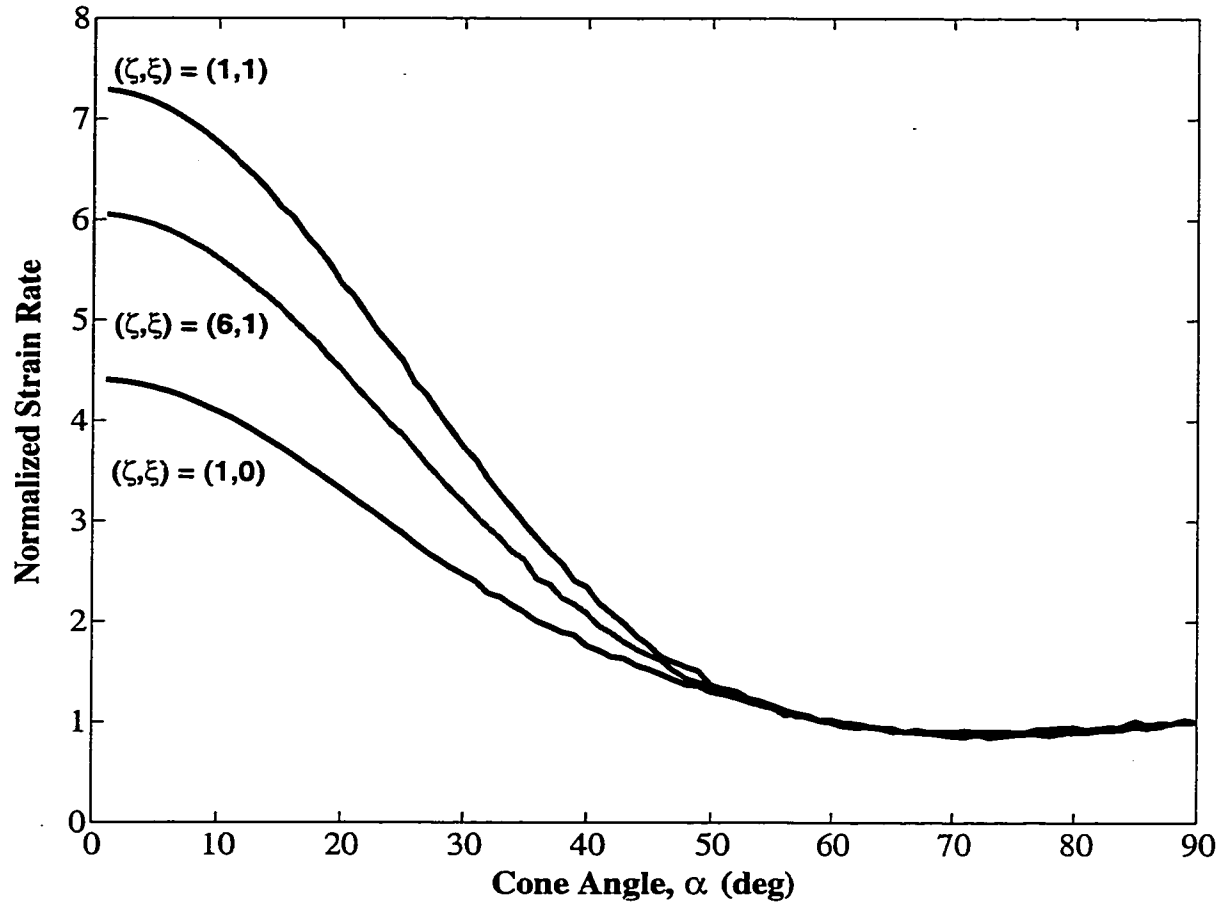
Fabric plots from various ice cores show that the crystals in uniaxial compression do move toward and reach vertical, and few are left near horizontal. This indicates that some NNI is needed, since the zenith angle velocities for no-NNI (Fig. 5.4) go quickly to zero near horizontal and vertical, and therefore the crystal c-axes in compression (Fig. 5.2) do not reach vertical, nor do they move out of horizontal starting positions. The strength of NNI is difficult to constrain from available thin section data, since the fabric plots have a large scatter.

Since I keep track of crystal size in the model, it would be possible to assign weight according to crystal size. I did not do that here since the crystal size used was fairly uniform and deformation of ice under the conditions modeled does not show a strong dependence on crystal size (*Duval and LeGac*, 1980), although in some cases size may be important when mechanisms other than intra-crystalline slip contribute to the deformation (*Goldsby and Kohlstedt*, 1996). During grain growth, crystals smaller than some critical size are being consumed. These crystals also act as seeds for recrystallization and can be pictured as tiny strain-free sub-crystals that do not contribute to the deformation, but can quickly consume highly strained crystals. To model the grain size evolution accurately, a better model of the grain size statistics is needed; especially since the total number of crystals is held constant in the model.

Whether the simple relation for grain growth (Eq. 5.17), or the one dependent on the stored energy (Eq. 5.19) is used does not change the results of the fabric evolution or strain history. When the stored energy E_{disl} (Eq. 5.21) is used to calculate grain boundary migration rates (*Wenk et al.*, 1997), some grains grow and others can contract. But to model crystal size evolution realistically, consideration of differences in the stored energy between neighboring crystals would be necessary to allow for inhomogeneous crystal growth. Ice, for instance, often shows interlocking crystal texture (*Duval and Castelnau*, 1995); a simple expansion or contraction of each crystal would not explain those observations.

The polygonization takes place in the model when the crystals are most likely to be effected by the inhomogeneity of the stress state at the single crystal level. This is achieved by comparing the magnitude of the RSS on the basal plane of the crystal to the magnitude of the applied stress. If that ratio is low, it is likely that the crystal experiences forces from deforming neighbors. Crystals with higher RSS and high dislocation density can also form sub-boundaries (P. Duval, pers. communication). That is partly accounted for by the fact that as the crystals strain, they eventually rotate into orientations with low RSS, and therefore can polygonize.

Migration recrystallization is difficult to model. Very complex models of dislocation interactions and grain boundary migration are needed to incorporate the fundamental physics. The approach taken here is to parameterize this process, by considering the energies involved. But even the energy associated with a dislocation density ρ is difficult to estimate (*Mohamed and Bacroix*, 2000; *Kuhlmann-Wilsdorf*, 1998). The resulting fabric, using Eq. (5.21) with $\kappa = 0.2$ gives reasonable results. $\kappa = 0.2$ is similar to suggested values for a mix of screw and edge dislocations, $\kappa = 0.1$ (*Mohamed and Bacroix*, 2000), is very reasonable. There is also considerable uncertainty about the orientation of newly recrystallized grains. For ice the girdle pattern obtained in Figure 5.6 is commonly observed (*Budd and Jacka*, 1989). That clearly indicates that there is a preferred orientation for the newly formed grains, but whether it is due to oriented nucleation or oriented growth is uncertain (*Branger et al.*, 2000; *Rajmohan and Szpunar*, 2000).

Figure 5.12 shows a comparison of the fabric modeled in uniaxial compression, after an axial strain of 0.5, using Azuma's model (*Azuma*, 1994), and the model described here with no-NNI (homogeneous stress; Sachs model), mild-NNI and full-NNI. Also shown, for comparison, is the fabric at 1293 m depth in the GRIP bore-hole (*Thorsteinsson et al.*, 1997), where the strain is ~ 0.5 (*Castelnau et al.*, 1996c). There is active polygonization at this depth in the GRIP core, but as we have seen, this does not change the fabric significantly. The fabrics predicted by the Azuma and Sachs model evolve too quickly. In ice sheets the fabric is much closer to the mild- and full-NNI cases; compare those to the GRIP fabric at 1293 m depth. The VPSC model yields fabrics that are very similar to the mild-NNI (VPSC spherical) and full-NNI (VPSC ellipsoidal) cases (*Castelnau et al.*, 1996a,

Azuma   **no-NNI**   **GRIP - 1293 m**

mild-NNI   **full-NNI**
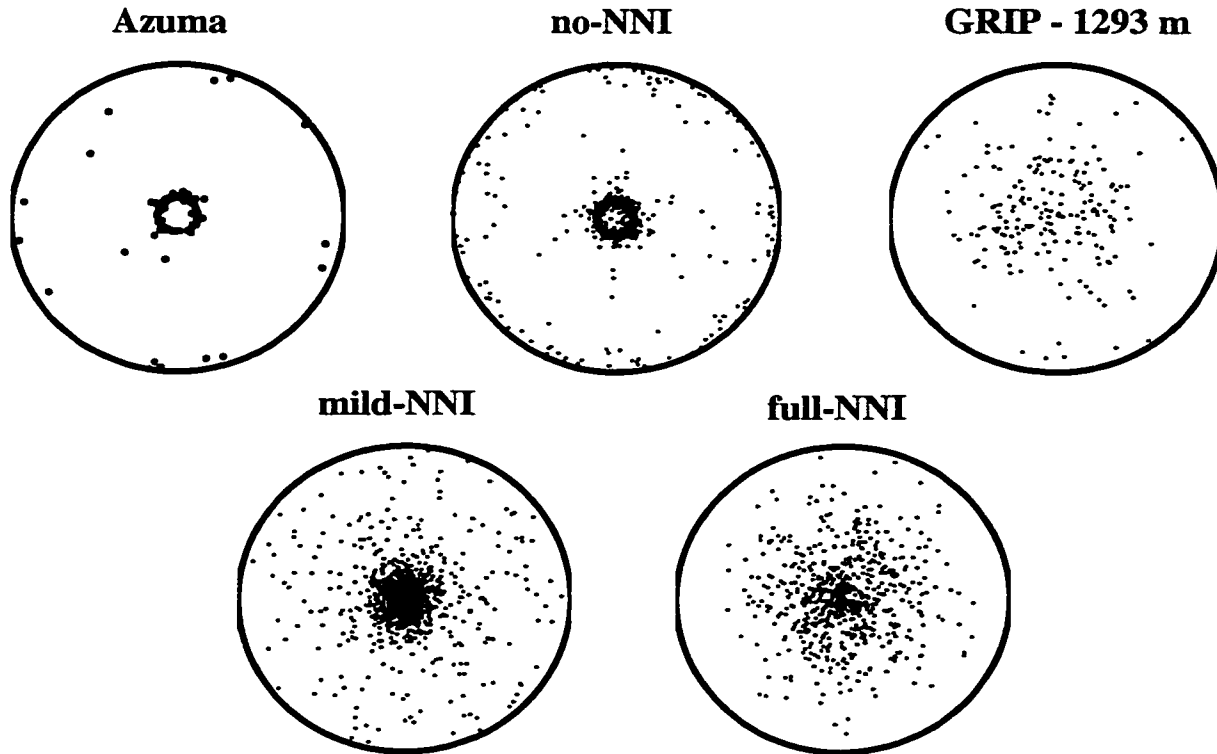
Figure 5.12: Comparison of modeled fabric in uniaxial compression, after 0.5 strain. Azuma's model (*Azuma*, 1994) and the no-NNI version of the model described here predict fabric that evolves too quickly, compared to the GRIP fabric. The mild-NNI and full-NNI are in much closer agreement. Note that the fabric plot for Azuma's model has 100 crystals, GRIP fabric has 194, and other plots have 1000 crystals.

Fig. 8, for strain of 0.4). VPSC spherical refers to model runs where the crystals remain spherical throughout, and VPSC ellipsoidal to model runs where the shape is represented by an evolving ellipsoid (*Molinary et al.*, 1987).

5.6   CONCLUSIONS

The nearest neighbor interaction (NNI) changes the overall pattern of fabric development. With increasing interaction the strain of single crystals gets more evenly distributed; this changes the rate of fabric development. From comparison with measured fabric, I conclude that some NNI is necessary, but the strength is difficult to assess. The recrystallization

part of the model yields realistic results, but more data are needed to constrain the free parameters.

Chapter 6

MEASURING ANISOTROPY

6.1 SUMMARY

We characterize fabric in terms of cone angles using three different standard methods, i.e. (1) measured V_P (V_{SH} and V_{SV}) sonic velocities, (2) R/N statistics and (3) cone angle fits to the actual crystal orientation distributions. The cone angles inferred using these three methods are often very different. Calculated strain rates, using the cone angles obtained by these three methods, are then compared to the strain rate calculated for the real fabric. Overall the deformation rates calculated with the cone angles inferred from sonic velocity measurements give the most realistic deformation rates. A reliable method of characterizing the anisotropy is essential to verify results from fabric evolution models, both at small and large scales.

6.2 INTRODUCTION

To model bore hole deformation, and ice sheet flow in general, we must know the rheological parameters that affect ice deformation. Although our knowledge of the constitutive equation for ice is far from perfect, several important improvements have been made in recent years. One of these is the inclusion of anisotropy in the constitutive equation (*van der Veen and Whillans*, 1990; *Alley*, 1992; *Lliboutry*, 1993; *Anandakrishnan et al.*, 1994; *Azuma*, 1994; *Azuma and Goto-Azuma*, 1996; *Castelnau et al.*, 1996a; *Lliboutry and Duval*, 1995; *Gödert and Hutter*, 1998; *Morland and Staroszczyk*, 1998; *Staroszczyk and Gagliardini*, 1999; *Thorsteinsson*, 2000a). The anisotropic rheology of polycrystalline ice results from the alignment (non-random orientation) of single anisotropic ice crystals due to intracrys-

talline slip. The orientation distribution of the crystals is called the fabric, and texture refers to the size and shape of crystals.

From sonic velocity and thin section studies on ice-cores in Greenland (Dye 3 (*Taylor*, 1982; *Herron et al.*, 1985; *Thorsteinsson et al.*, 1999), GRIP (*Thorsteinsson et al.*, 1997), GISP2 (*Gow et al.*, 1997)), and Antarctica (Vostok [ref], Byrd (*Bennett*, 1972; *Bentley*, 1972; *Kohnen and Gow*, 1979)) a coherent picture of the fabric evolution emerges. At these sites, the stress state is dominantly vertical compression near the surface and compression and/or simple shear at greater depths these stress patterns produce a vertically symmetric, transversely isotropic, vertical cone distribution of c-axes. The orientation generally strengthens with depth, and the ice becomes more anisotropic. When the temperature rises above $-12°C$, migration recrystallization becomes active, which generally randomizes the fabric.

To model the deformation of anisotropic ice, we can use information about zenith and azimuth angles of the c axes of individual ice crystals. This works well when examining the deformation of a few thousand crystals. But, to model deformation on a larger scale, the number of crystals to track quickly increases beyond practical limits. An alternative is to use an orientation distribution function (ODF) to characterize the fabric. Then the fabric can be parameterized using only a few variables. A vertically symmetric cone angle fabric is commonly observed in ice sheets, and it can be parameterized by a single variable, the cone angle α.

Figure 6.1 shows the three types of fabric that we will use in our analysis: cone, girdle and flat fabric. The cone angle distribution is an equal area distribution within a cone with a half apex angle α (the cone angle). A girdle fabric is defined by an inner, α_0, and an outer, α, angle. Inner angle of zero gives a cone fabric. The zenith angle distribution for girdle and cone fabric is a sine curve; which gives an equal number of crystals per unit surface area on an unit sphere. Flat fabric is defined by a maximum zenith angle, and the number of crystals in any x° zenith angle bin is the same. The flat fabric therefore has a higher concentration towards the center since there are as many crystals between 0° and 20° as there are between 20° and 40°, even though the surface area on the unit sphere is smaller.

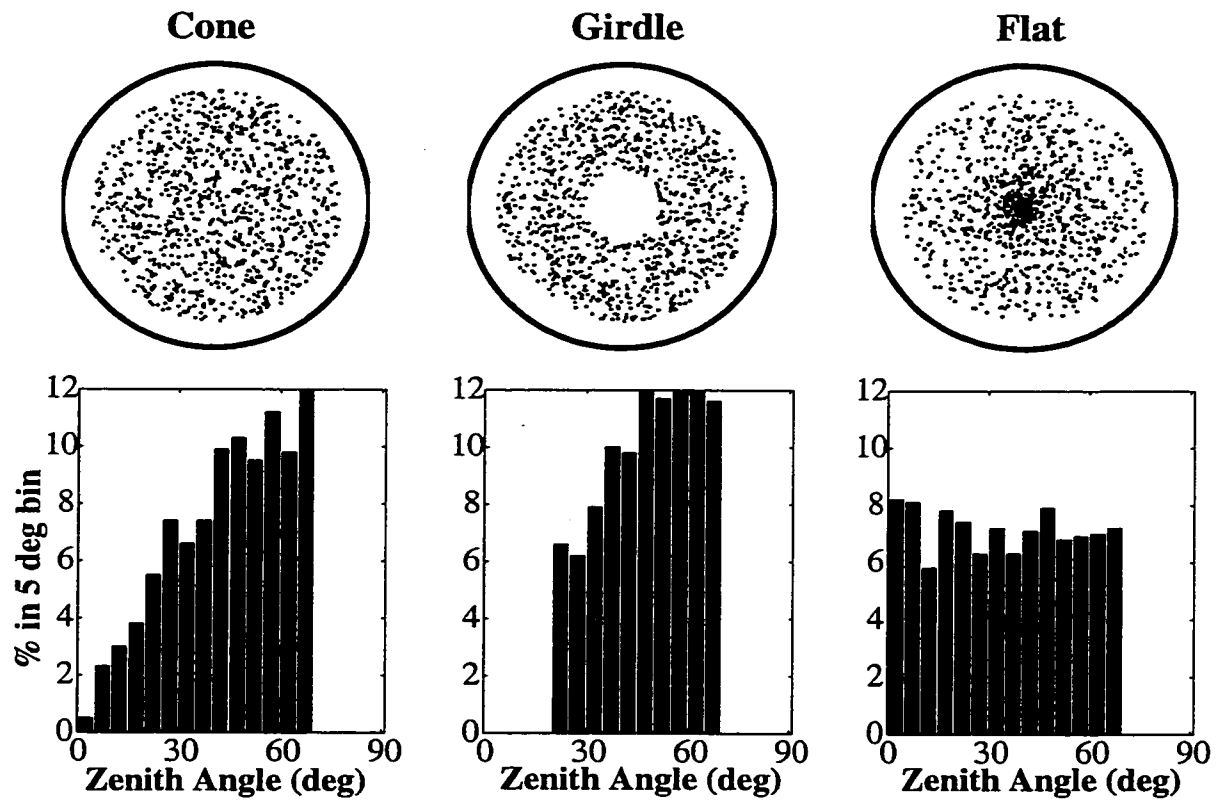In this paper we examine two methods of measuring fabric, thin sections and sonic

Figure 6.1: Equal area plots (upper row) and zenith angle distributions (lower row) for the three types of fabric used. The cone angle and the maximum zenith angle for the flat distribution is 70°, and the girdle angle is 20°.

velocity. From the velocity or the thin section measurements we want to find a method to characterize the fabric (Figure 6.2). Here we characterize the fabric using a cone angle, since, most fabric data indicate that a vertically symmetric fabric is very common. There are many ways to assign cone angles to a given ice sample. We describe and compare three commonly used methods; cone angle fit (CAF) and R/N statistics which are based on thin section data, and a relation of sonic velocity to a given fabric. These three methods yield different estimates of cone angles for the same actual fabric. To estimate which method is the most appropriate for predicting deformation, we compare the strain rates in uniaxial compression and simple shear, calculated with the interpreted cone angles, to the strain rate calculated using actual fabric. We use the analytical formulation described in *Thorsteinsson* (2000a), and the *Thorsteinsson* (2000b) numerical model, to calculate the strain rates resulting from the inferred cone angles and from the actual fabric. It is important to remember that there are other orientation distributions that could just as well be modeled.

Bennett (1968) derived relationships between ice crystal fabrics and sonic velocities. Those relations are reviewed, and formulated for cone and girdle fabric. Although our analytical formulation uses both cone and girdle angle, we will for simplicity talk about girdle fabric when it applies to both cone and girdle fabric.

We use the summation convention for repeated indices, and write partial derivatives as $\partial_i = \partial/\partial x_i$. Tensors are written with upper case letters C or in component form, C_{ijkl}, vectors are boldface k, or k_i, and unit directional vectors are specified by $\hat{k} = (l, m, n)$, where l, m, n are the direction cosines in the x, y, and z-direction respectively.

6.3 WAVE VELOCITIES IN ICE

In this section we derive relationships for the wave velocities, which depend only on the propagation angle in single ice crystals. For crystal aggregates, the bulk velocity, is a function of fabric (cone angle) and the propagation angle.
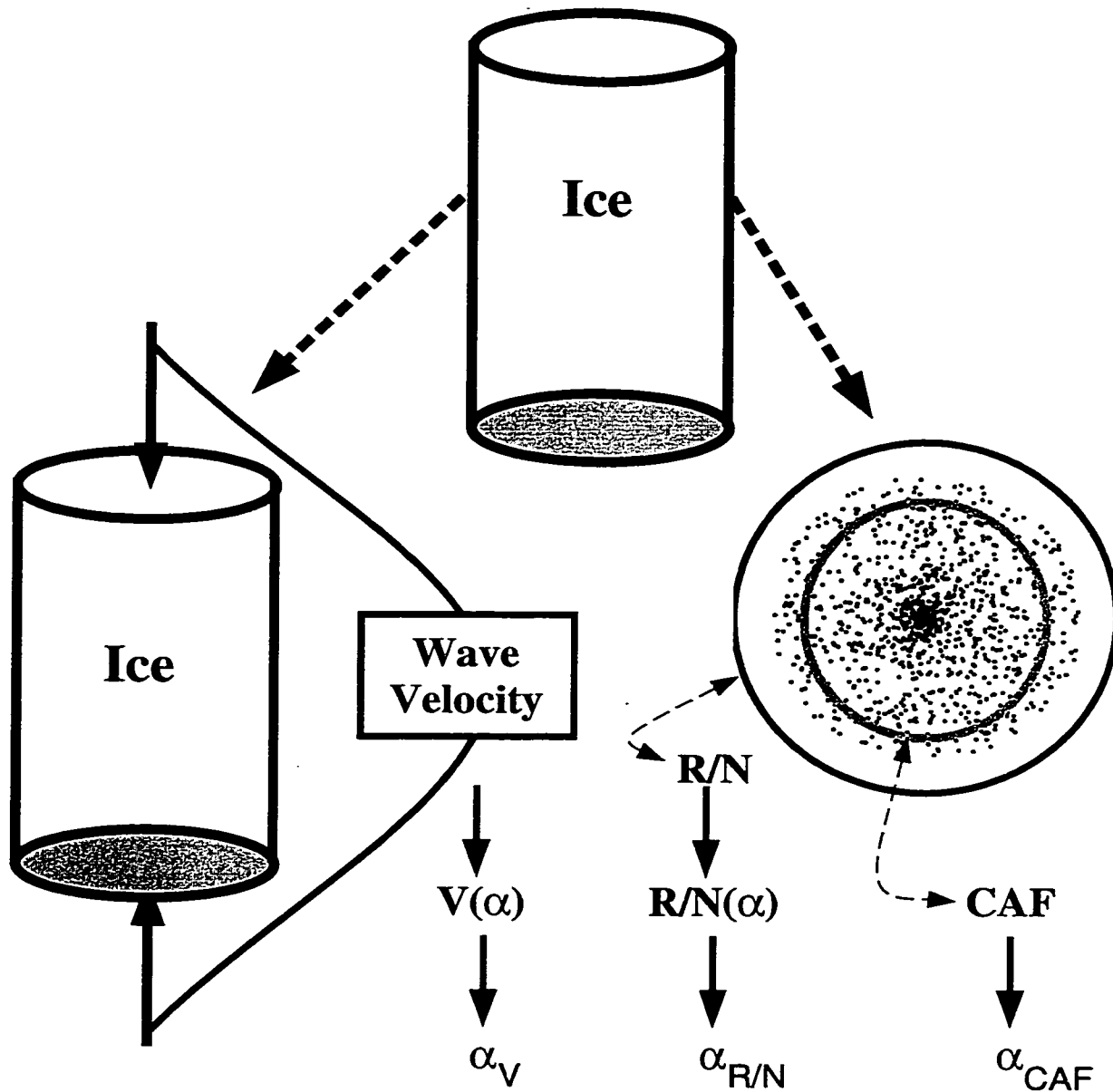
Figure 6.2: Two methods of measuring and three ways to characterize fabric. One measurement method is the directional sonic velocity through the ice, and the other is to make a thin section. We then get a velocity, R/N statistics value and a cone angle from the cone angle fit (CAF). To interpret the velocity and R/N values we need a relation between cone angles and velocity and R/N values. We therefore have three estimates of the cone angle for this piece of ice.

6.3.1 Single Ice Crystals

The generalized three-dimensional form of Hooke's law is

$$\sigma_{ij} = C_{ijkl}\partial_l u_k, \tag{6.1}$$

where u_k is displacement, σ_{ij} is the stress tensor, and C_{ijkl} is the stiffness (elastic moduli) tensor.

The equation of motion for waves propagating with infinitesimal displacements is described by the dynamic equilibrium equation

$$\rho\partial_t^2 u_i = \partial_j \sigma_{ij} = C_{ijkl}\partial_j\partial_l u_k, \tag{6.2}$$

where ρ is the density of the medium.

For a plane wave propagating in direction $\hat{\mathbf{k}}$, with $\mathbf{k}$ as the wavenumber vector, with size $k = |\mathbf{k}|$, the displacement vector is given by

$$u_i(\mathbf{x}) = u_i^0 \exp[i(\mathbf{k}\cdot\mathbf{x} - \omega t)], \tag{6.3}$$

where ω is the frequency and u_i^0 is the wave amplitude.

Substituting Eq. (6.3) into Eq. (6.2) leads to three homogeneous equations for the displacement components u_i^0

$$(C_{ijlm}k_l k_j - \rho\omega^2\delta_{im})u_i^0 = 0. \tag{6.4}$$

Non-trivial solutions exist if the determinant of the coefficients is zero, $|C_{ijlm}k_l k_j - \rho\omega^2\delta_{im}| = 0$. The eigenvalues $\lambda = \rho\omega^2$ of this equation define three frequencies $\omega = \sqrt{\lambda/\rho}$ associated with a given wave vector $\mathbf{k}$. Solving Eq. (6.4) gives three orthogonal eigenvectors $\mathbf{u}^0$, describing the direction of the displacement associated with each frequency. For anisotropic media the direction of propagation does not coincide, in general, with the wave vector (*Tomé*, 1998).

The phase velocities are then calculated from

$$V = \frac{\omega}{k} = \sqrt{\frac{\lambda}{\rho}\frac{1}{k}}. \tag{6.5}$$

120

Each phase velocity corresponds to one of three wave types. The largest eigenvalue is associated with the displacement u^0 that is closest in direction to k this is called the quasi-longitudinal wave, and the other two are the quasi-shear waves.

Single ice I_h crystals have hexagonal symmetry, and the velocity in a crystal can be calculated by considering the propagation of plane waves in a transversely isotropic medium. For transversely isotropic material, only 5 of the 81 terms in C_{ijkl} are non-zero, as can be shown from symmetry considerations (*Crampin*, 1984).

The phase velocities in transversely isotropic media (*Vernik and Nur*, 1992) are

$$V_{1,2}^2 = l^2\frac{C_{11}+C_{44}}{2\rho} + n^2\frac{C_{33}+C_{44}}{2\rho}$$
$$\pm\sqrt{(l^2\frac{C_{11}-C_{44}}{2\rho} - n^2\frac{C_{33}-C_{44}}{2\rho})^2 + l^2n^2(\frac{C_{13}+C_{44}}{\rho})^2}, \tag{6.6}$$

and

$$V_3^2 = l^2\frac{C_{66}}{\rho} + n^2\frac{C_{44}}{\rho}, \tag{6.7}$$

where $l = \sin\xi$, $n = \cos\xi$ and ξ is the angle between the c-axis and the propagation direction $\hat{k}$. V_1 is associated with the quasi-longitudinal wave, V_2 is associated with the quasi-shear wave whose direction of particle motion is nearly perpendicular to the propagation direction and V_3 is associated with the true shear wave, whose direction of particle motion is perpendicular to the propagation direction.

TABLE 1. The elastic constants [GPa] (*Hobbs*, 1974), where T is temperature in $°C$.

$C_{11} = 12.904\,(1 - 1.489\cdot10^{-3}T - 1.85\cdot10^{-6}T^2)$
$C_{12} = 6.487\,(1 - 2.072\cdot10^{-3}T - 3.62\cdot10^{-6}T^2)$
$C_{13} = 5.622\,(1 - 1.874\cdot10^{-3}T)$
$C_{33} = 14.075\,(1 - 1.629\cdot10^{-3}T - 2.93\cdot10^{-6}T^2)$
$C_{44} = 2.819\,(1 - 1.601\cdot10^{-3}T - 3.62\cdot10^{-6}T^2)$
$C_{66} = (C_{11} - C_{12})/2$

Figure 6.3 shows the three phase velocities V_1, V_2 and V_3 for a single crystal as a function of the angle ξ between the direction of propagation and the symmetry axis (c-axis), using the C_{ij}'s given in Table 1 and $\rho_0 = 917$ kg m^{-3}.
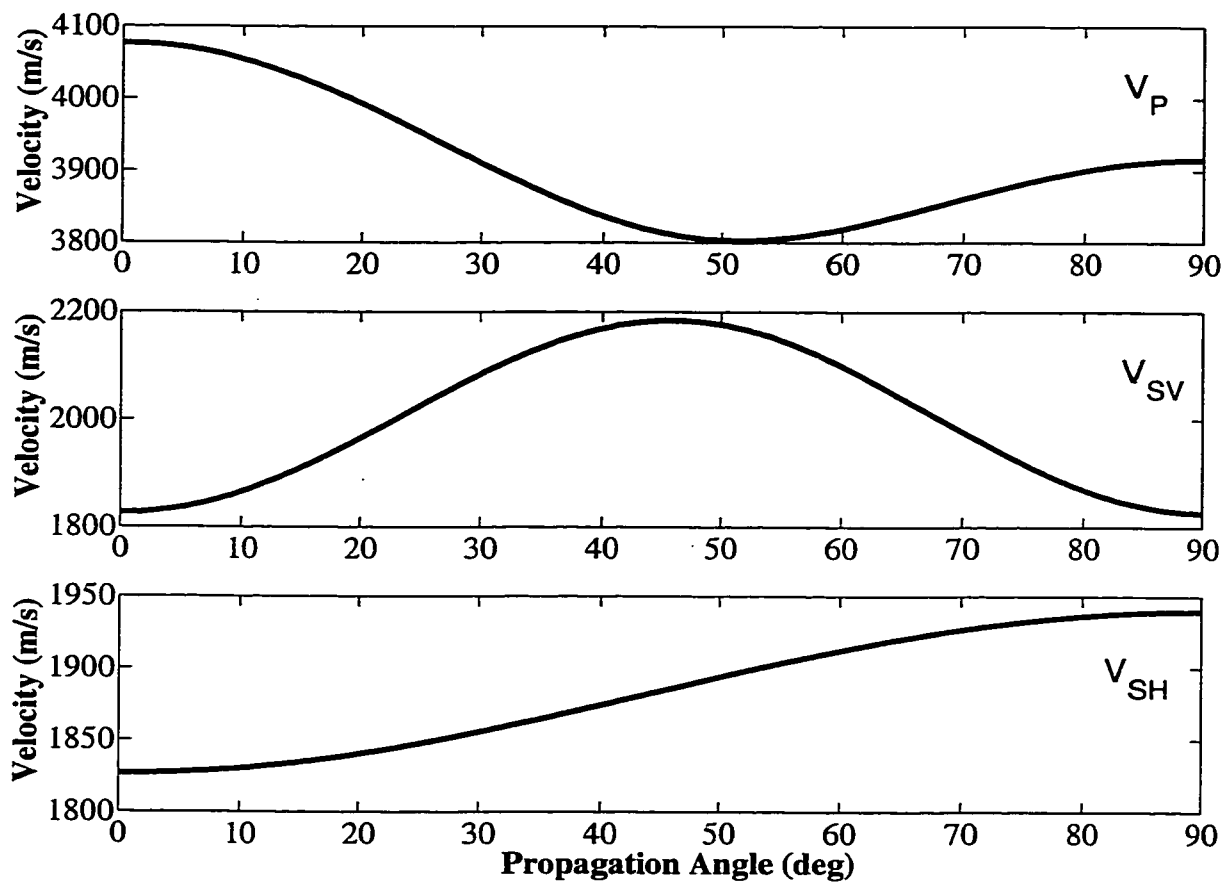
Figure 6.3: The $V_1(V_P)$, $V_2(V_{SV})$ and $V_3(V_{SH})$ phase velocities for a single crystal of ice. A propagation angle of zero is parallel to the c-axis, and a propagation angle of 90° is in the basal plane.

6.3.2 Velocities for Crystal Aggregates

There are several methods of relating the single crystal properties to the properties of an aggregate; homogeneous strain, homogeneous stress, or somewhere between.

The approach adopted here (*Bennett*, 1968) is to assume that the square of the slowness S, where $S = V^{-1}$, is proportional to the crystal compliance $\mathcal{S}$, where $\mathcal{S}_{ijkl}C_{klmn} = \delta_{im}\delta_{jn}$ (*Nye*, 1985), in the direction of wave propagation ($\hat{\mathbf{k}}$). A condition of constant stress at the wave front is assumed.

According to *Bennett* (1972) the stiffness constant C in the direction of propagation is ρV^2, and the compliance is

$$\mathcal{S} = 1/(\rho V^2) = S^2/\rho. \tag{6.8}$$

The space averaging of S^2/ρ with respect to a chosen direction of propagation $\hat{\mathbf{k}}$, yields the mean compliance in the $\hat{\mathbf{k}}$ direction (*Bennett*, 1972). With this assumption, we can relate the single crystal properties to the properties of the crystal aggregate, as long as the same types of stress and strain are experienced by the individual crystals upon the passage of a plane wave through the crystal aggregate. These conditions are only approximated in the actual case, since each crystal is finite in size and the boundary conditions at the crystal interfaces are not evaluated (*Bennett*, 1968).

The exact slowness surfaces of single crystals are found by taking the inverse of Eqs. (6.6) and (6.7). For a given density and temperature, those can be approximated by

$$S_1 = a_1 - b_1 \cos 4\xi - c_1 \cos 2\xi, \tag{6.9}$$

$$S_2 = a_2 + b_2 \cos 4\xi, \tag{6.10}$$

$$S_3 = a_3 + b_3 \cos 2\xi, \tag{6.11}$$

where ξ is the angle between the c-axis and the propagation direction $\hat{\mathbf{k}}$. The difference between the above equations for the slowness and the exact inverse using Eqs. (6.6) and (6.7) is less than 1%.

TABLE 2. The a, b and c constants for $\rho = 917$ kg m^{-3} in μs m^{-1} (*Bennett*, 1968).

$$a_1 = 256.28 \quad a_2 = 501.97 \quad a_3 = 531.40$$
$$b_1 = 5.92 \quad b_2 = 45.37 \quad b_3 = 15.94$$
$$c_1 = 5.08$$

Now we formulate the equations for the slownesses in terms orientation distributions symmetric about and propagation angles relative to vertical $\hat{z}$. Figure 6.4 shows the coordinates used in the calculations. The $y = 0$ plane is the symmetry plane, so the propagation direction $\hat{k}$ will always be in the x,z plane and we only need to know the angle between the propagation direction $\hat{k}$, and vertical ($\hat{z}$), which we shall call φ. The propagation direction is then

$$\hat{k} = (\sin\varphi, 0, \cos\varphi),$$

and the c-axis orientation

$$c = (\cos\phi\sin\theta, \sin\phi\sin\theta, \cos\theta).$$

The compliance due to pure compressive stress is $\rho S_P = S_1^2$. For shear, whose couple is perpendicular to $\hat{k}$, but whose couple plane includes $\hat{k}$, the compliance may be approximated by $\rho S_S = S_2^2 \cos^2\tau + S_3^2 \sin^2\tau$. The slowness for compressional waves is $S_P = S_1$ and for the two shear velocities (approximately, *Bennett* (1968)) $S_{SV} = S_2\cos^2\tau + S_3\sin^2\tau$ and $S_{SH} = S_2\sin^2\tau + S_3\cos^2\tau$, where τ is the angle between the $\hat{x}, \hat{z}$ plane and the $\hat{k}, c$ plane,

$$\sin^2\tau = \frac{\sin^2\phi\sin^2\theta}{\sin^2\xi}, \tag{6.12}$$

$$\cos^2\tau = \frac{\cos\varphi\cos\phi\sin\theta - \sin\varphi\cos\theta}{\sin^2\xi}. \tag{6.13}$$

We want to calculate $S = S(\varphi, \phi, \theta)$, so we need to derive equations for ξ also. We have that

$$\hat{k}\cdot c = \cos\xi = \sin\varphi\cos\phi\sin\theta + \cos\varphi\cos\theta. \tag{6.14}$$

Whether we choose to approximate the slowness surface, or use the inverse of Eq. (6.6) and (6.7), we can now write the phase velocities/slownesses as a function of propagation direction φ, and single crystal orientation ϕ and θ relative to $\hat{z}$.
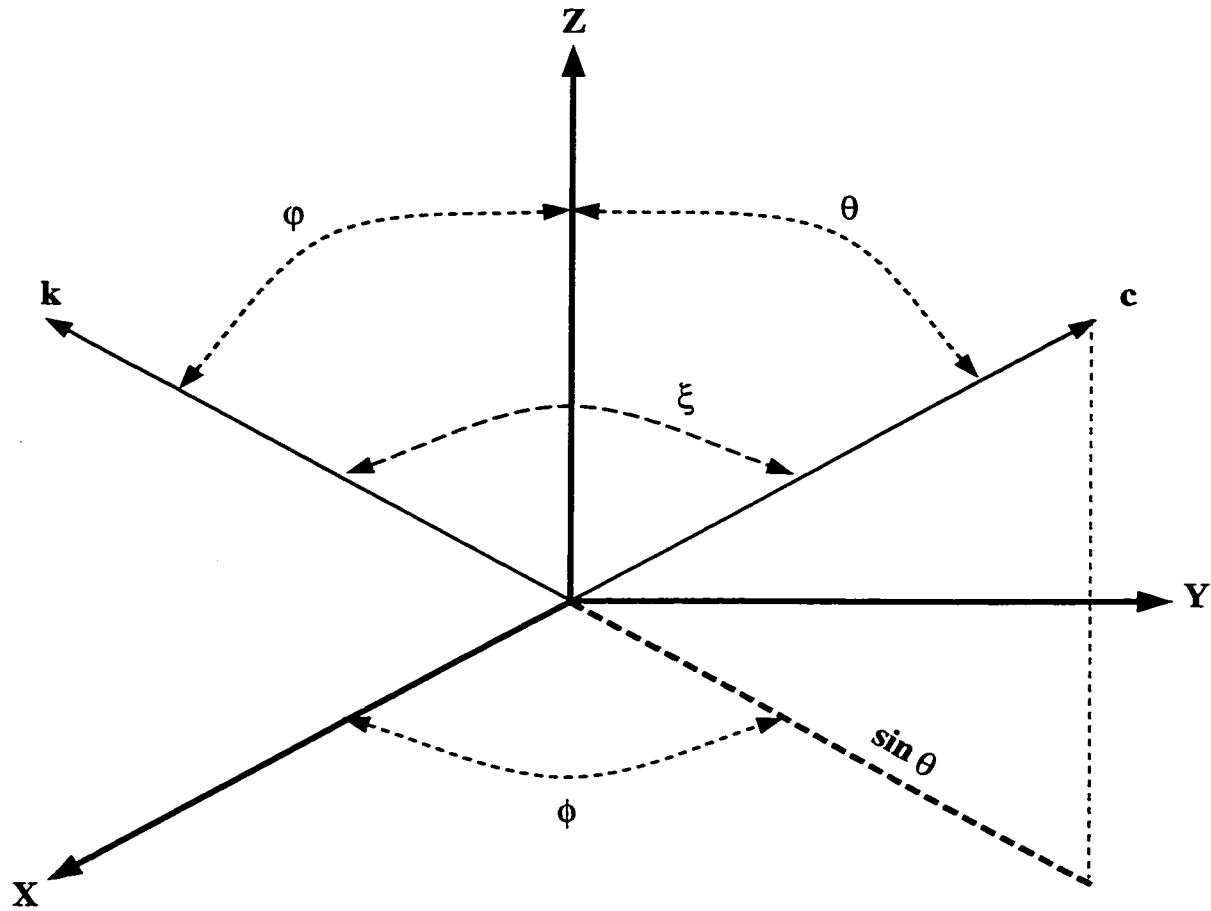
Figure 6.4: The coordinate system and angles used in the calculations. The propagation direction of the plane wave is **k**, the crystal symmetry axis **c** and vertical is $\hat{z}$.

The three slownesses are now given by

$$S_P(\phi, \theta, \varphi) = (a_1 - b_1 + c_1) + (8b_1 - 2c_1)$$
$$(\sin \varphi \sin \theta \cos \phi + \cos \varphi \cos \theta)^2 \qquad (6.15)$$
$$-8b_1(\sin \varphi \sin \theta \cos \phi + \cos \varphi \cos \theta)^4,$$

$$S_{SV}(\phi, \theta, \varphi) = (a_2 + b_2) - 2b_2 \sin^2 \phi \sin^2 \theta$$
$$-8b_2(\cos \varphi \cos \phi \sin \theta - \sin \varphi \cos \theta)^2 \qquad (6.16)$$
$$(\sin \varphi \cos \phi \sin \theta + \cos \varphi \cos \theta)^2,$$

$$S_{SH}(\phi, \theta, \varphi) = (a_2 + b_2) - 2b_3$$
$$(\cos \varphi \cos \phi \sin \theta - \sin \varphi \cos \theta)^2$$
$$-8b_2 \sin^2 \phi \sin^2 \theta \qquad (6.17)$$
$$(\sin \varphi \cos \phi \sin \theta + \cos \varphi \cos \theta)^2.$$

Equations (6.15), (6.16) and (6.17) allow us to calculate the velocity for any given distribution of c-axes. Below we calculate the velocities for a cone fabric.

Velocities for Cone Fabric

The mean slowness surface for a cone or girdle fabric is

$$S_{mean} = \frac{\int_0^{2\pi} \int_{\alpha_0}^{\alpha} S(\phi, \theta, \varphi) \sin \theta d\theta d\phi}{\int_0^{2\pi} \int_{\alpha_0}^{\alpha} \sin \theta d\theta d\phi}, \qquad (6.18)$$

where α is the cone angle and α_0 the girdle angle. For a cone fabric $(\alpha_0 = 0)$ we get

$$S_P(\alpha, \varphi) = (a_1 + \tfrac{b_1}{15} + \tfrac{c_1}{3})$$
$$+\tfrac{1}{15}(16b_1 - 10c_1)(\cos \alpha + \cos^2 \alpha)$$
$$-\tfrac{8}{5}b_1(\cos^3 \alpha + \cos^4 \alpha)$$
$$-\sin^2 \varphi((4b_1 - c_1)(\cos \alpha + \cos^2 \alpha) \qquad (6.19)$$
$$-8b_1(\cos^3 \alpha + \cos^4 \alpha))$$
$$+b_1 \sin^4 \varphi(3(\cos \alpha + \cos^2 \alpha) - 7(\cos^3 \alpha + \cos^4 \alpha)),$$

$$S_{SV}(\alpha, \varphi) = a_3 - \tfrac{1}{15}(8b_2 - 5b_3)(1 + \cos \alpha + \cos^2 \alpha)$$
$$+\tfrac{4}{5}b_2(\cos^3 \alpha + \cos^4 \alpha)$$
$$+b_2 \sin^2 \varphi \cos^2 \varphi(3(\cos \alpha + \cos^2 \alpha) \qquad (6.20)$$
$$-7(\cos^3 \alpha + \cos^4 \alpha)),$$

$$S_{SH} \quad (\alpha, \varphi) = a_3 - \tfrac{1}{15}(8b_2 - 5b_3)(1 + \cos\alpha + \cos^2\alpha)$$

$$+ \tfrac{4}{5}b_2(\cos^3\alpha + \cos^4\alpha)$$

$$+ \sin^2\varphi((b_2 - b_3)(\cos\alpha + \cos^2\alpha) \tag{6.21}$$

$$- b_2(\cos^3\alpha + \cos^4\alpha)).$$

The corresponding velocities in m s^{-1} are then $V_P = 10^6/S_P$, $V_{SV} = 10^6/S_{SV}$ and $V_{SH} = 10^6/S_{SH}$, using the values of the a, b, c's in Table 2.

To correct for variations in density, we multiply the slowness by $\sqrt{\rho/\rho_0}$. Thus $S(\alpha, \varphi, \rho) = \sqrt{\rho/\rho_0}S(\alpha, \varphi)$, where $\rho_0 = 917$ kg m^{-3}, or for the velocity

$$V(\rho) = \sqrt{\frac{\rho_0}{\rho}}V(\rho_0). \tag{6.22}$$

This can be seen by factoring out ρ in Eqs. (6.6) and (6.7).

Figure 6.5 shows the V_P wave-velocity as a function of the propagation (φ) and cone (α) angles. Isotropic ice has a cone angle α of 90°, and a single crystal has $\alpha = 0°$. A propagation angle of $\varphi = 0°$ is along vertical (the symmetry axis), and $\varphi = 90°$ is horizontal. The fastest velocity, $V_P = 4077$ m s^{-1} is obtained for an effectively single crystal oriented vertically (all the crystals perfectly aligned), for vertically traveling waves.

Figures 6.6 and 6.7 show the V_{SV} and V_{SH} velocities as function of cone and propagation angles.

We can compare this method of averaging (and approximations) to the Voigt (continuous strain) and Reuss (continuous stress) bounds. The wave velocities for isotropic material can be written as (Segel, 1987)

$$V_P^2 = \frac{E(1 - \nu)}{\rho(1 + \nu)(1 - 2\nu)}, \tag{6.23}$$

and

$$V_S^2 = \frac{E}{2\rho(1 + \nu)}, \tag{6.24}$$

where E is the Young's modulus and ν is Possion's ratio. The Voigt average gives

$$E_V = \frac{(A - B + 3C)(A + 2B)}{2A + 3B + C}, \quad \nu_V = \frac{A + 4B - 2C}{4A + 6B + 2C}, \tag{6.25}$$

and the Reuss average

$$E_R = \frac{5}{3A + 2B + C}, \quad \nu_R = -\frac{2A + 8B - C}{6A + 4B + 2C}, \tag{6.26}$$

Figure 6.5: P-wave velocities as a function of cone and propagation (φ) angle. Isotropic ice has a cone angle of 90°, and vertical (down core) is $\varphi = 0°$.

Figure 6.6: S_{SV}-wave velocities as a function of cone and propagation (φ) angle. Isotropic ice has a cone angle of 90°, and vertical (down core) is $\varphi = 0°$.

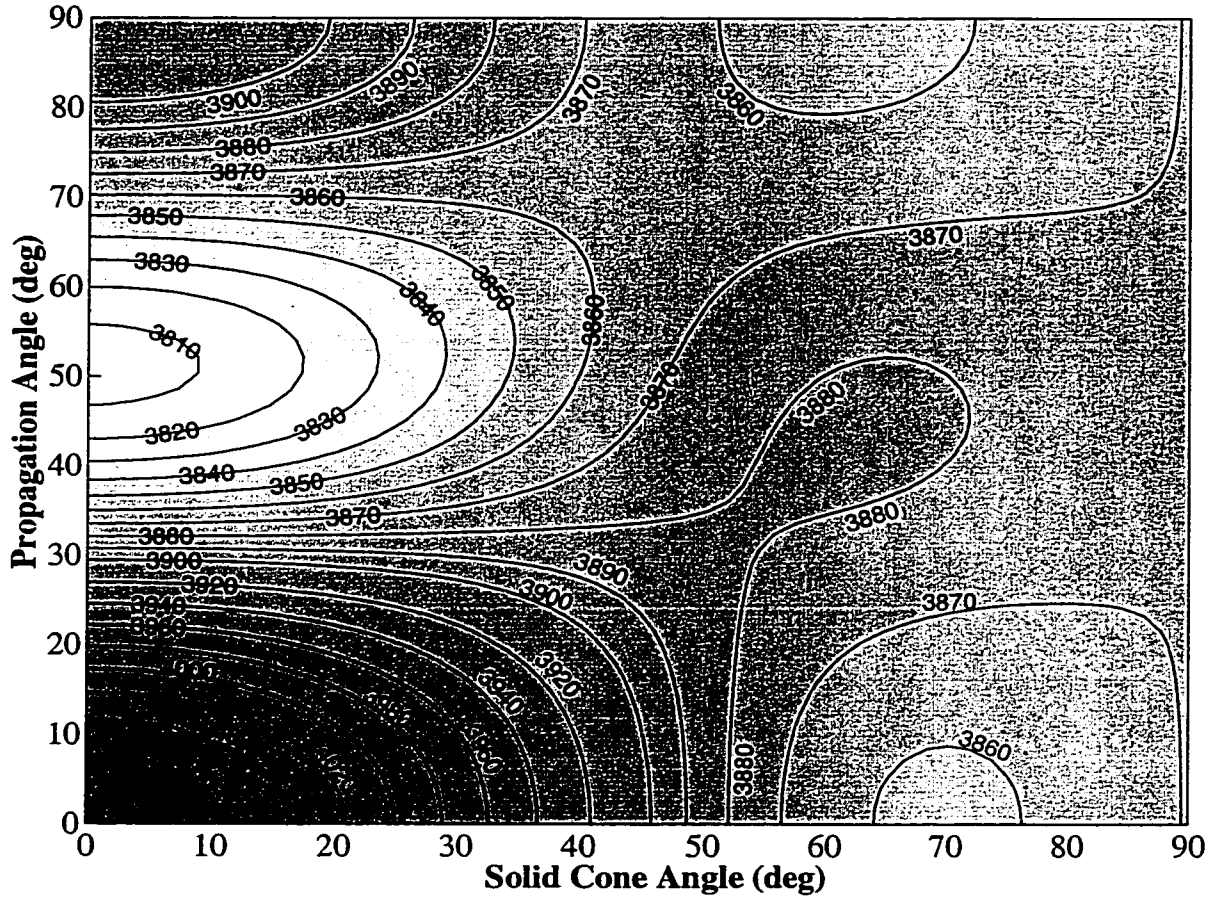Figure 6.7: S_{SH}-wave velocities as a function of cone and propagation (φ) angle. Isotropic ice has a cone angle of 90°, and vertical (down core) is $\varphi = 0°$.
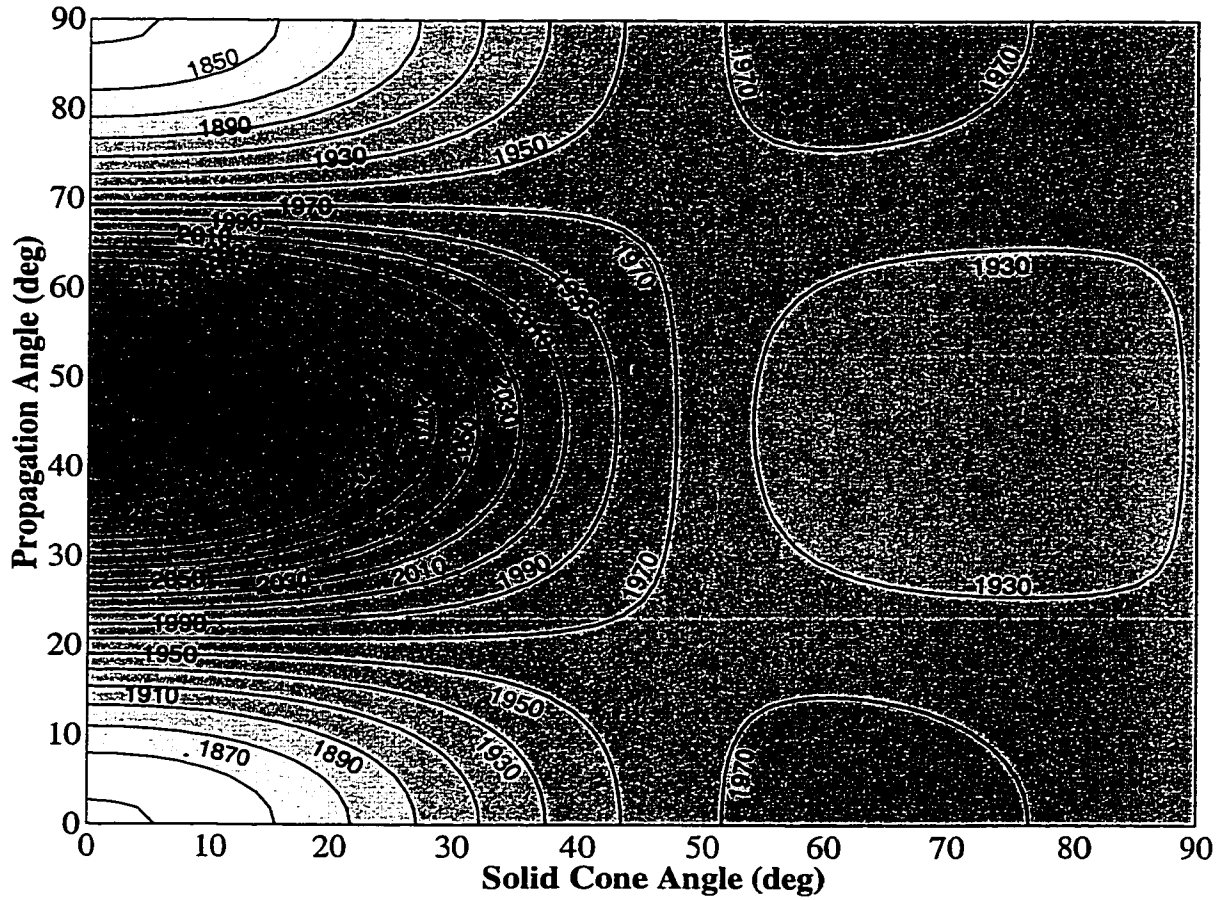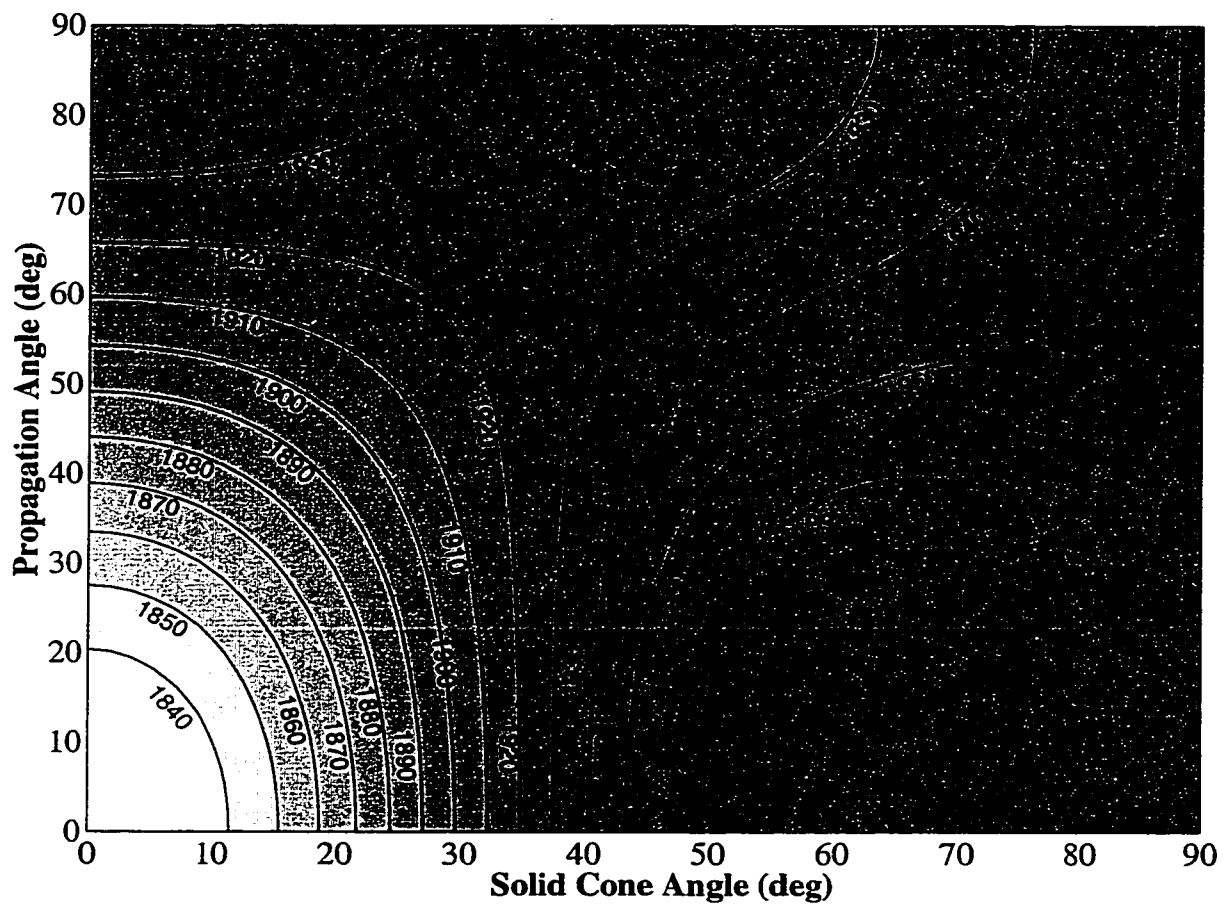
with

$$A = (X_{11} + X_{22} + X_{33})/3, \quad B = (X_{23} + X_{13} + X_{12})/3, \quad C = (X_{44} + X_{55} + X_{66})/3, \quad (6.27)$$

where X_{ij} are the components of the elastic moduli C in the Voigt average and the components of the compliance S for the Reuss average (*den Toonder et al.*, 1999). Using values of C and S listed in *Nanthikesan and Sunder* (1994) for ice at -16°C we calculate the upper and lower bounds of E and ν, and the values according to Bennett's method. We find that the Young's modulus calculated by Bennett's method ($E_{Bennett} = 9.18$ GPa) is between the Voigt and Reuss bounds ($E_{Voigt} = 9.30$ GPa, $E_{Reuss} = 9.09$ GPa). The Poisson's ratio is closer to the Reuss bound ($\nu_{Bennett} = 0.330$, $\nu_{Reuss} = 0.330$, $\nu_{Voigt} = 0.326$). Using these values the P-wave velocity according to Bennett's method ($V_P = 3849$ m s^{-1})is slightly larger then what the Voigt bound gives ($V_P = 3847$ m s^{-1}), which is slightly larger than the Reuss bound ($V_P = 3831$ m s^{-1}).

6.4 THIN SECTIONS

In thin section analysis, the orientation, zenith and azimuth angle of each c-axis is measured on a Rigsby stage (*Paterson*, 1994). Thin sections typically contain a few hundred crystals; this makes it difficult to estimate how representative the thin section maybe of the average fabric. To infer a cone angle from a thin section two methods are most commonly used. One, CAF, is to find a cone that contains 90% of the c-axes of the real fabric. The other, R/N, is a statistical test which is seldom reported in terms of cone angles. Below we describe these two methods.

6.4.1 Fabric Statistics, R/N

In this method, each c-axis is represented by a unit vector. The orientation strength is then obtained by taking the vector sum of all the N c-axes which gives both the length R and direction. If they are all perfectly aligned, the length of the resulting vector is $R = N$.

To relate R/N to cone angles, we assume a vertically symmetric fabric. Therefore we sum only over the vertical component of each c-axis; we are interested only in the orientation

strength along the vertical (symmetry) axis. The ice crystals are assumed to be uniformly distributed within a cone, with an cone angle α. The area of the cone, equivalent to the number of crystals for a continuous distribution, is

$$N = A = \int_0^{2\pi} \int_0^\alpha \sin\theta d\theta d\phi = 2\pi(1 - \cos\alpha), \tag{6.28}$$

and the sum of all vertical components is

$$R = \int_0^{2\pi} \int_0^\alpha \cos\theta \sin\theta d\theta d\phi = \frac{\pi}{2}(1 - \cos 2\alpha). \tag{6.29}$$

Then the strength of orientation, R/N, as a function of cone angle, is

$$\frac{R}{N} = \frac{1}{4}\left[\frac{1 - \cos 2\alpha}{1 - \cos\alpha}\right]. \tag{6.30}$$

When all the crystals are vertical, $R/N = 1$, and when the orientation is completely random $R/N = 1/2$.

6.4.2   Cone Angle Fit

Once the orientations of many c-axes have been measured and mapped onto an equal area plot, we can assign a cone angle to the fabric. A common practice is to fit a cone to the fabric such that 80-90% of all the c-axes are contained within it. We call this method cone angle fit (CAF). A serious difficulty with this method is that a few crystals outside a main concentration can stretch the cone far out. With thin sections there is also the general problem of obtaining statistically significant samples (*Thorsteinsson*, 2000b), since the number of measured c-axes is usually small (few hundred crystals). *Anandakrishnan et al.* (1994) found that the cone angles inferred from V_P velocity measurements on 110 mm samples from the GISP2 ice core were very similar to cone angles determined by the 80% criterion. There were about 8 CAF data points in the depth range of 800 m to 1700 m.

6.5   COMPARISON OF FABRIC ESTIMATIONS

Now that we have introduced three different methods to describe fabric in terms of cone angles, we can examine how different they are for a real fabric. To do that we generate

a sample of 200 crystals, which we call the "real" fabric. We calculate the inferred cone angles using the three methods described above. Then the strain rates in simple shear and uniaxial compression are calculated using the inferred cone angles and the flow law formulated for a cone angle fabric (*Thorsteinsson*, 2000a). We compare the strain rates calculated from the inferred cone angles to the "correct" strain rates, which are calculated from the analytical solution for the cone and flat fabric distributions used. Figure 6.8 shows the variation of shear strain and vertical strain rate (*Thorsteinsson*, 2000a), V_P velocities and R/N statistics as a function of cone angle. The variation in shear strain rate, as a function of cone angle, is very similar to the variation of V_P velocities. Neither the V_P velocity curve or the R/N curve have similar variation, as a function of cone angle, as the strain rate in uniaxial compression. We might therefore expect that using V_P velocities to predict strain rate in simple shear is most likely to give correct predictions of strain rate.

How well each cone angle matches the correct strain rate is measured by the performance, which is calculated as

$$E = (\dot{\varepsilon}^{cone}/\dot{\varepsilon}^{correct} - 1) \times 100,$$

where $\dot{\varepsilon}$ is the strain rate. Figure 6.9 shows the performance (E) for the three different methods when estimating simple shear strain rates, with a flat real fabric. We see that for large cone angles, the CAF and R/N methods do not come close to predicting applicable cone angles. When predicting strain rates in simple shear for a cone real fabric (results not shown), both the R/N and V_P methods work very well (<2% error over all cone angles). The cone angle fit method has higher errors (up to ~9%) for cone angles between 15° and 80°, which is partly due to the definition used, 90% of all c-axes within the cone, but this method is also much more sensitive to irregularities in the distribution.

Figure 6.10 shows a similar comparison for uniaxial compression strain rates. For a cone angle distribution, both R/N and V_P methods have less than 5% error, but the cone angle fit method has larger errors (~15%, again forced by the definition since the real fabric is a cone). For a flat fabric none of the methods works really well.

At Dye 3, Greenland, the sonic velocity has been measured using a 7 m averaging length. In Figure 6.11 we compare the cone angles inferred from the sonic log to R/N and CAF
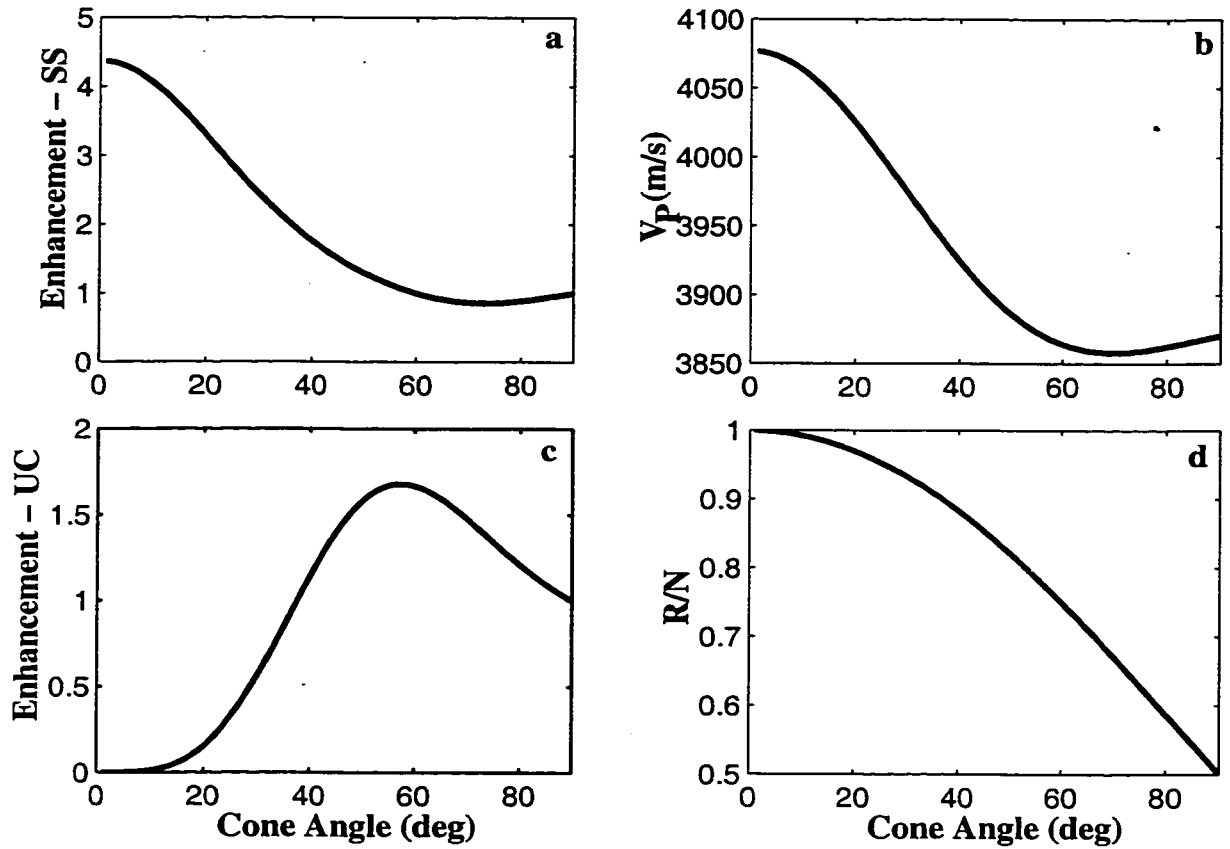
Figure 6.8: Theoretical curves for: (a) Normalized shear strain rate in simple shear (SS), (b) V_P velocity, (c) Normalized vertical strain rate in uniaxial compression (UC) and (d) R/N statistics as a function of cone angle.
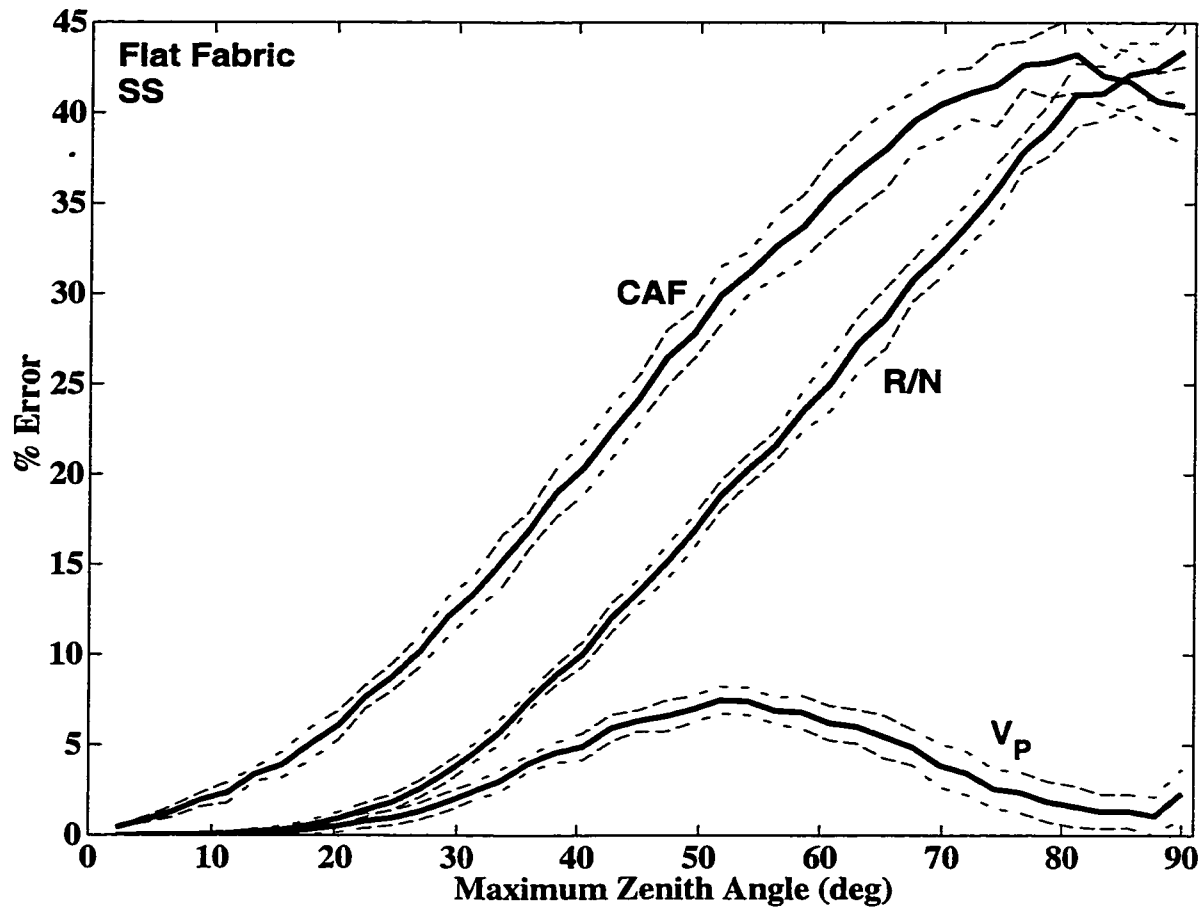
Figure 6.9: Performance (see text) of the V_P, R/N and CAF fabric estimation methods for a flat distribution of c-axes in simple shear. The solid lines are the averages of 20 runs with 200 crystals, and the dotted lines show one standard deviation (STD).
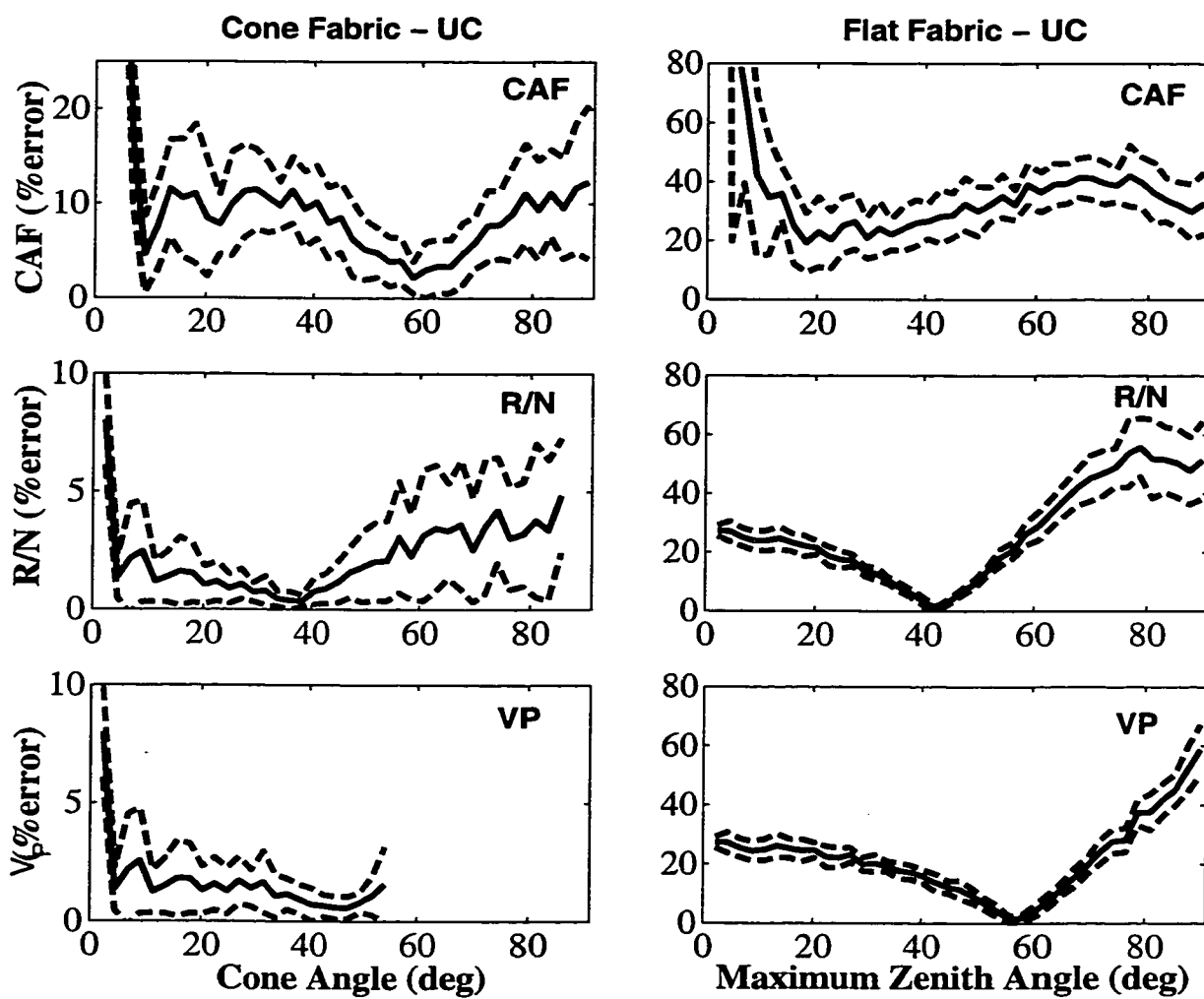
Figure 6.10: Performance of fabric estimation methods for uniaxial compression. Here the cone angle are obtained using the CAF methods, R/N statistics and V_P velocities. The solid lines are the averages of 20 runs with 200 crystals, and the dotted lines show the STD.

data.
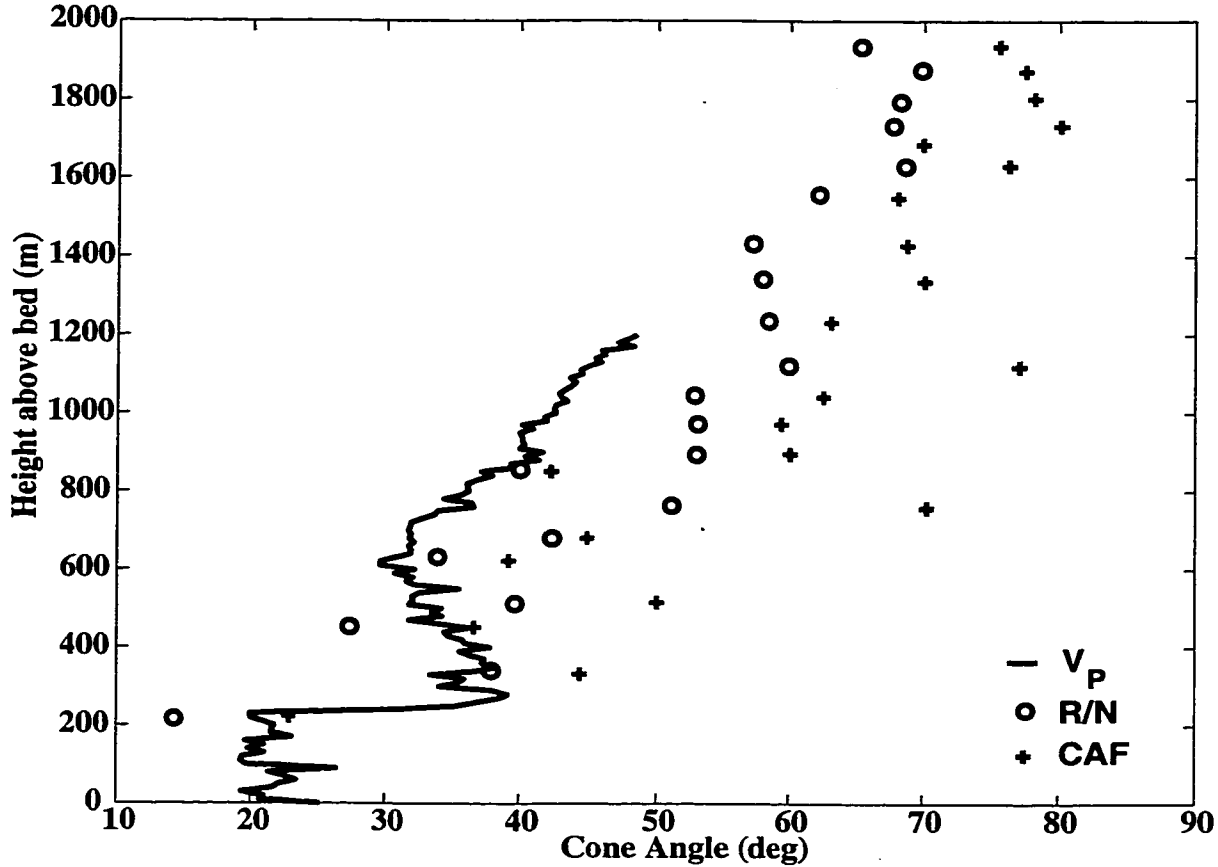
Figure 6.11: The inferred cone angles at Dye 3, Greenland, as a function of height above bed. The V_P measurements are continuous (solid line), measuring the velocity through 7 m of ice vertically (*Taylor*, 1982) The R/N data (open circles) were converted into cone angles using Eq. (6.30) and the cone angle fit (pluses) is from *Herron et al.* (1985). Note the large variations between individual thin sections.

We use thin section data (*Thorsteinsson et al.*, 1997) to calculate the cone angles at GRIP, Greenland, according to V_P, R/N and CAF methods. To calculate cone angles from the V_P-velocity method from the thin sections, we first calculated the velocity on a single crystal basis, using the orientation of single crystals. The mean velocity was then used to find the cone angle corresponding to the mean velocity. The results in Figure 6.12 are similar to the data at Dye 3 (Fig. 6.11).
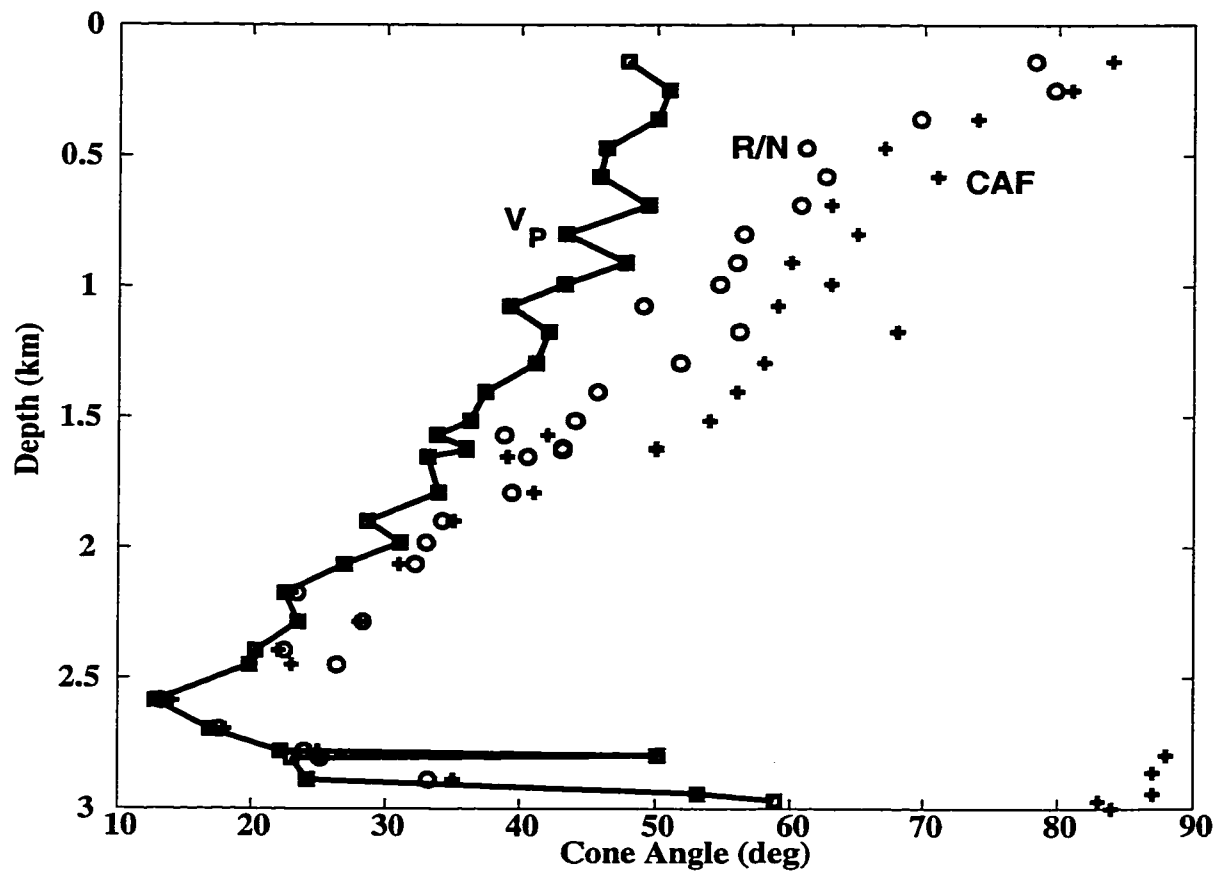
Figure 6.12: The inferred cone angles at depth in the GRIP bore-hole, Greenland, obtained using the cone angle fit (pluses), R/N (open circles) and sonic velocity (V_P, solid line) methods.

Figure 6.13 shows the sensitivity of the inferred cone angle to errors in the R/N and V_P measurements. For the sonic velocity measurements we assign 0.25% error, corresponding roughly to 10 m s^{-1} (*Taylor*, 1982). Since we typically have only about 200 crystals, we assign an error of 6% to the R/N measurements. This error was determined by examination of the sensitivity of the strain rate, calculated on a single crystal basis to the number of crystals used (*Thorsteinsson*, 2000b). The cone angles inferred from the V_P velocity are at
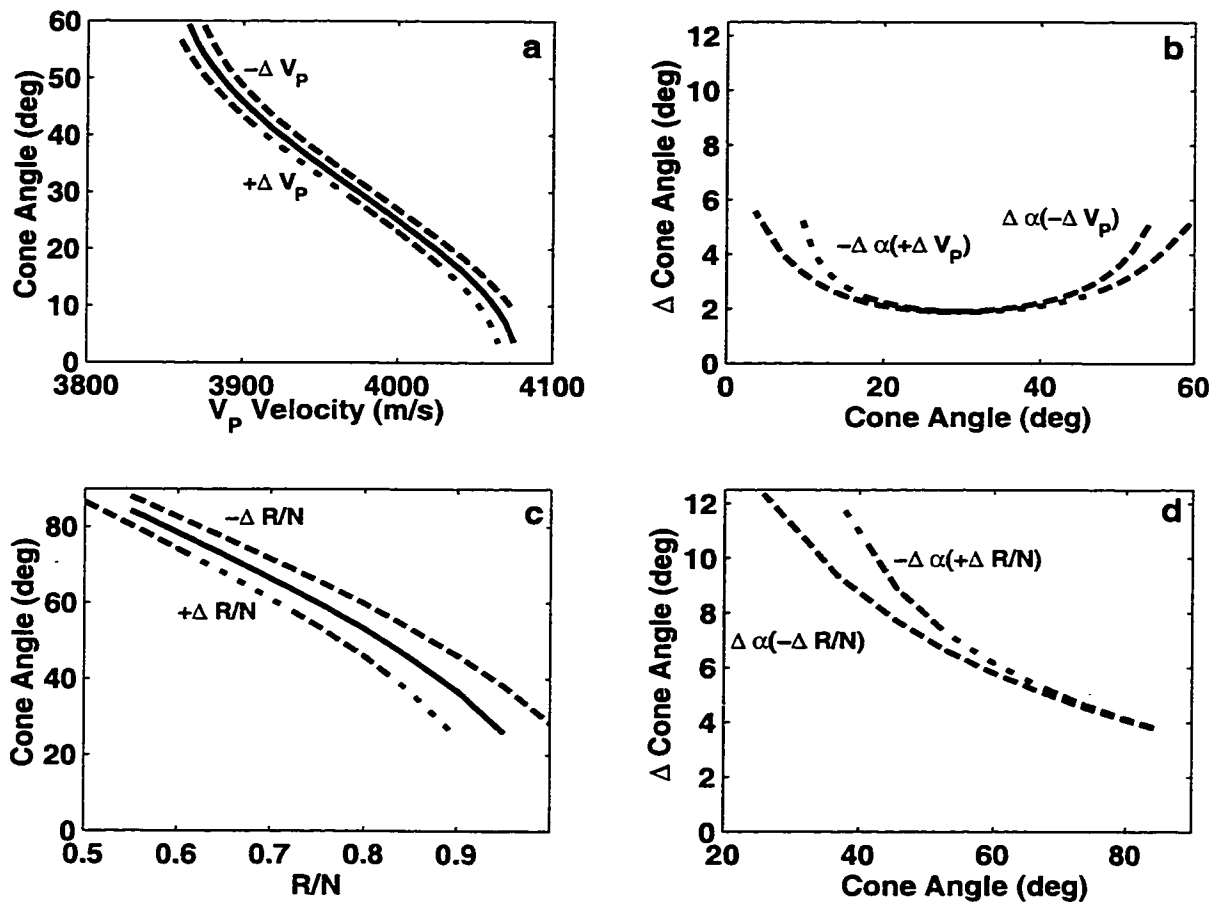
Figure 6.13: The sensitivity of the cone angle inversion to errors in the V_P and R/N measurements. (a) The V_P velocity (solid curve), and $V_P \pm \Delta V_P$ (dashed and dotted curves respectively), where $\Delta V_P = 0.0025 V_P$. (b) The change in inferred cone angle from the correct value ($\alpha(V_P)$) for too high $\alpha(V_P + \Delta V_P)$, or too low velocity estimates $\alpha(V_P - \Delta V_P)$. (c) The R/N (solid curve), and $R/N \pm 0.06 R/N$. (d) The change in cone angle due to 6% errors in R/N.

most $\sim \pm 5°$ from the correct value, while the cone angles inferred from the R/N statistics can be in error by as much as $\pm 12°$.

6.5.1 Cone or Girdle ?

Figure 6.14 shows the V_P velocity, and enhancement in uniaxial compression, pure shear and simple shear, as a function of cone and girdle angle. If we now pick a velocity or enhancement
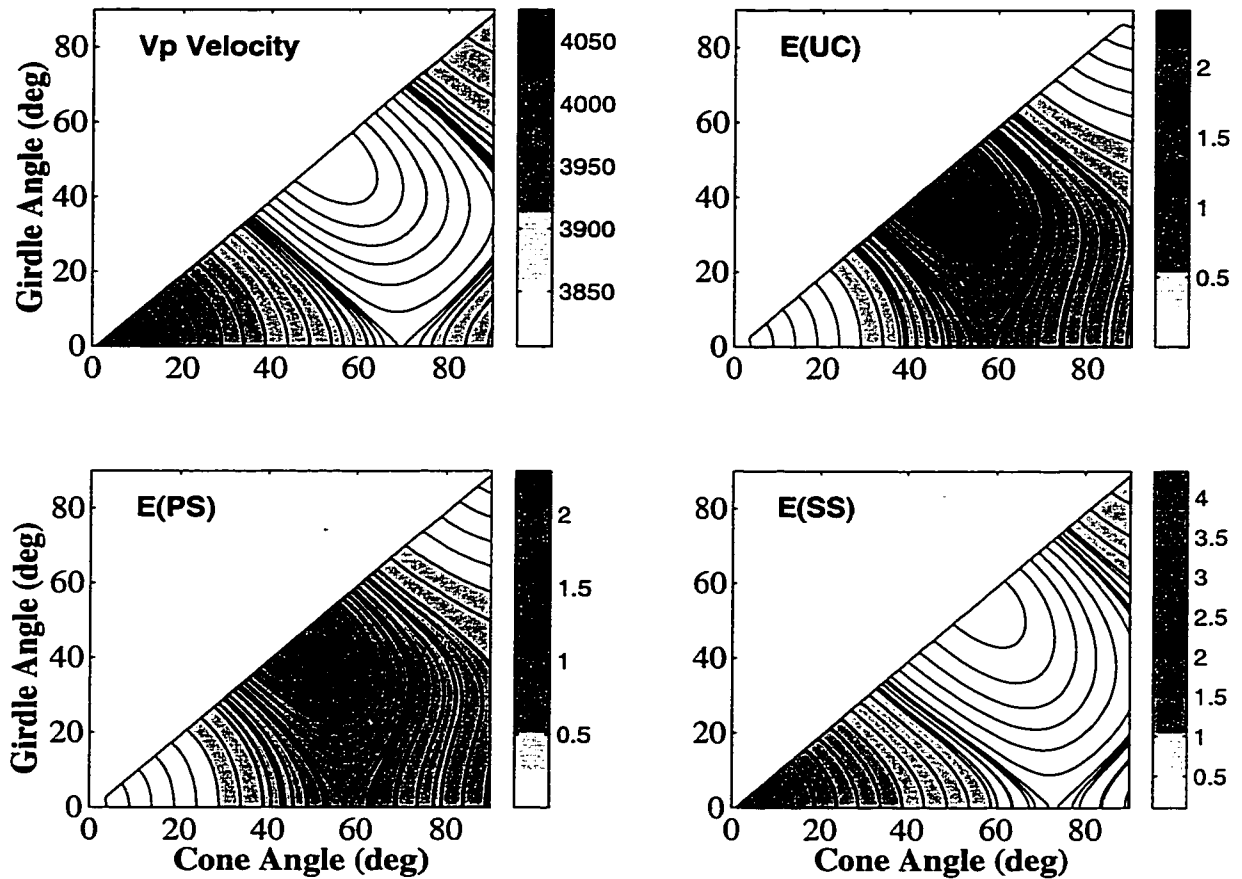
Figure 6.14: Contour plots of V_P velocity and enhancement (relative to isotropic ice), E, in uniaxial compression (UC), pure (PS) and simple shear (SS), as a function of cone (α) and girdle (α_0) angles.

value for a given cone angle (α; $\alpha_0 = 0$) there are infinite number of combinations of (α, α_0) pairs that yield the same value. Moreover, the path of the contour lines $E(\alpha, \alpha_0) = const.$ is fairly similar in all cases. This implies that if we interpret V_P velocities as a cone, even

though the actual fabric is a girdle, we will in most cases calculate the correct deformation rate.

6.6 DISCUSSION

The two methods to measure fabric, thin sections and sonic velocity, give information on very different scales. The thin sections measure several hundred crystals in an 1 mm thick thin section, while the sonic logging tool used in the Dye 3 bore hole measured average speed over 7 m.

We use 200 crystals for the comparison of the different fabric estimation methods. Sonic velocities will typically average over $\sim 10^6$ (?) crystals, so the error bars associated with the performance plots, which are based on 200 crystals for the V_P method should be taken as extreme.

The propagation angle for the sonic velocities is equivalent to the tilt of the symmetry axis. The propagation angle makes it easy to correct for bore-hole tilt, if the inclination is known.

It is very important to have thin section data along with the sonic velocities, since the fabric symmetry and type can be characterized only from thin sections.

6.7 CONCLUSIONS

We have shown that measuring sonic (V_P) velocities provides the "best" estimate of the cone angle for use in anisotropic constitutive equations where the fabric is expected to be vertically symmetric. The dependence of V_P velocity on cone angles (anisotropy) is very similar to the simple shear deformation rate. It is, however, necessary to have thin section data to determine the type of fabric.

Chapter 7

FOLDING IN STRONGLY ANISOTROPIC MEDIA

This chapter is based on a manuscript that awaits further input from possible co-authors. Presently E. D. Waddington is a co-author.

7.1 SUMMARY

Conditions for passive folding in a viscous medium are derived for combination of uniaxial compression or pure shear with simple shear deformation. For folding to be possible in a steady state flow field $R > \mathcal{H}$, where $\mathcal{H}$ is the ratio of compressive/extensive deformation to shear deformation, and R is the roughness (inverse slope) of a line element. Analytical equations for particle tracks in steady state allow us to model the evolution of layers. The effects of anisotropy are explored using an analytical solution for strain rate as a function of a vertically symmetric c-axis orientation distribution called a cone fabric (*Thorsteinsson*, 2000a). Strong anisotropy (small cone angle, strong clustering of crystals), which makes the material softer in horizontal shear, facilitates folding, i.e. smaller roughness elements can fold. The relation is complicated by the fact that for a range of cone angles the material is also softer in compression/extension. Simulating a layer with varying tilt of the cone symmetry axis demonstrates that asymmetry in the fabric is a potential source of layer perturbations.

7.2 INTRODUCTION

Our knowledge of past climate conditions comes largely from ice-core and other sedimentary records. Interpretation of these records relies on the assumption that the stratigraphic layering is intact. For marine and lacustrine sedimentary cores, bioturbation and tectonic displacements are a major concern. For the ice-core records, layer stratigraphy is usually assumed to have remained intact except very close to the bed. But the loss of correlation

of $\delta^{18}O$ (*Alley et al.*, 1995a) and other climatic indicators below 2750 m depth (some 270 m above the bed) in the ice-core records from GRIP and GISP2, Greenland, has pointed to the possibility of layer disturbance at considerable heights above the bed.

Layer perturbations such as wiggles (undulating annual layers) and folding have the potential of severely complicating the chronological interpretation of ice-cores, and in general any stratigraphic sequences. In an ice sheet that has a Z-fold an ice-core could conceivably go through the same layer three times.

The origin of layer perturbations has been an elusive problem. Of the various potential sources (sastrugi, accumulation variations), almost all except anisotropy are unlikely (*Waddington et al.*, 2000). Several authors have pointed out that asymmetry of the fabric might lead to layer perturbations (*Azuma and Goto-Azuma*, 1996; *Castelnau et al.*, 1998).

Here we derive criteria for the folding of layer disturbances in a steady state flow field in uniaxial compression or pure shear stress combined with a simple shear stress state. Equations for particle tracks allow us to model the evolution of layers. The effects of anisotropy on the folding criteria and the implications for ice core site selection are explored using the anisotropic flow law formulated by *Thorsteinsson* (2000a).

Finally, we consider the origin of disturbances to the layering. For fabric symmetries that are not compatible with the stress state, the deformation of anisotropic material is very different from isotropic. Fast changes in stress state, such as flow over bumps, divide migration, and variations in accumulation, can cause the fabric to be incompatible with the current stress state. We examine the effects of incompatible stress and fabric, both as an evolutionary problem, using the model of *Thorsteinsson* (2000b), and as an instantaneous response using an analytical formulation (*Thorsteinsson*, 2000a).

7.3 FOLDING OF LAYER DISTURBANCES IN STEADY STATE DEFORMATION FIELD

For a homogeneous three dimensional deformation field in uniaxial compression or pure shear combined with simple shear we can solve for the position of a particle at any given

time by solving the coupled first order differential equations (*Ramberg*, 1975)

$$
\begin{bmatrix} \dot{x}_1 \\ \dot{x}_2 \\ \dot{x}_3 \end{bmatrix} = \begin{bmatrix} L_{11} & 0 & L_{13} \\ 0 & L_{22} & 0 \\ 0 & 0 & L_{33} \end{bmatrix} \begin{bmatrix} x_1 \\ x_2 \\ x_3 \end{bmatrix},
\tag{7.1}
$$

where $\dot{x}_i = dx_i/dt$ and $L_{ij} = \partial u_i/\partial x_j$ is the velocity gradient, and u_i is the velocity component in direction x_i ($x_1 = x, x_2 = y, x_3 = z$).

The particle position, in steady state, is then given by the solution to Eq. (7.1)

$$
x(t; x_0, z_0) = e^{L_{11}t}x_0 + \frac{L_{13}}{L_{11} - L_{33}}(e^{L_{11}t} - e^{L_{33}t})z_0,
\tag{7.2}
$$

$$
y(t; y_0) = e^{L_{22}t}y_0,
\tag{7.3}
$$

$$
z(t; z_0) = e^{L_{33}t}z_0,
\tag{7.4}
$$

where $x_0 = x(t = 0)$ and $z_0 = z(t = 0)$. This solution assumes that the L_{ij}'s are constants in time and space and the displacement at the origin $x_i = 0$ is zero. We use Equations (7.2) and (7.4) to derive a criterion for folding below. By defining the $<x, z>$ plane as the shear plane, we can formulate our equations in two-dimensions; noting that variations in the y-direction are allowed.

7.3.1 Non-dimensional Numbers

It is convenient to define several non-dimensional numbers at this point, in order to simplify the equations. First we define R as the roughness, and m as the smoothness

$$
R = \frac{1}{m} = -\frac{z_A(t) - z_B(t)}{x_A(t) - x_B(t)},
\tag{7.5}
$$

where A and B are two points on a layer, connected by a straight line (see Figure 7.1).

We define a shear number, $\mathcal{H}$, as

$$
\mathcal{H} = (L_{11} - L_{33})/L_{13}.
\tag{7.6}
$$

The shear number is a measure of how hard it is to shear the material, relative to compressing/extending it. When $\mathcal{H}$ is large, compression/extension dominates over the shear and folding is unlikely; it is hard to generate folds.

We also non-dimensionalize time as

$$T = \frac{1}{2}(L_{11} - L_{33})t, \tag{7.7}$$

and the spatial variables $X = x/L$ and $Z = z/L$, where L is a characteristic length scale.

7.3.2 Passive Folding

To derive criterion for folding we consider two particles, A and B, as shown in Figure 7.1. Particle A at time $t = 0$ is at $x = 0, z = A$, or in our notation $x_A(0; 0, A)$, and particle B is at $x_B(0; \mathcal{L}, 0)$. For folding to occur, particle A must reach an x-position greater than that of particle B at some later time, $x_A(t; 0, A) > x_B(t; \mathcal{L}, 0)$ (*Waddington et al.*, 2000). An equivalent approach is to consider when a line with slope $R_0 = 1/m_0 = A/\mathcal{L}$ reaches
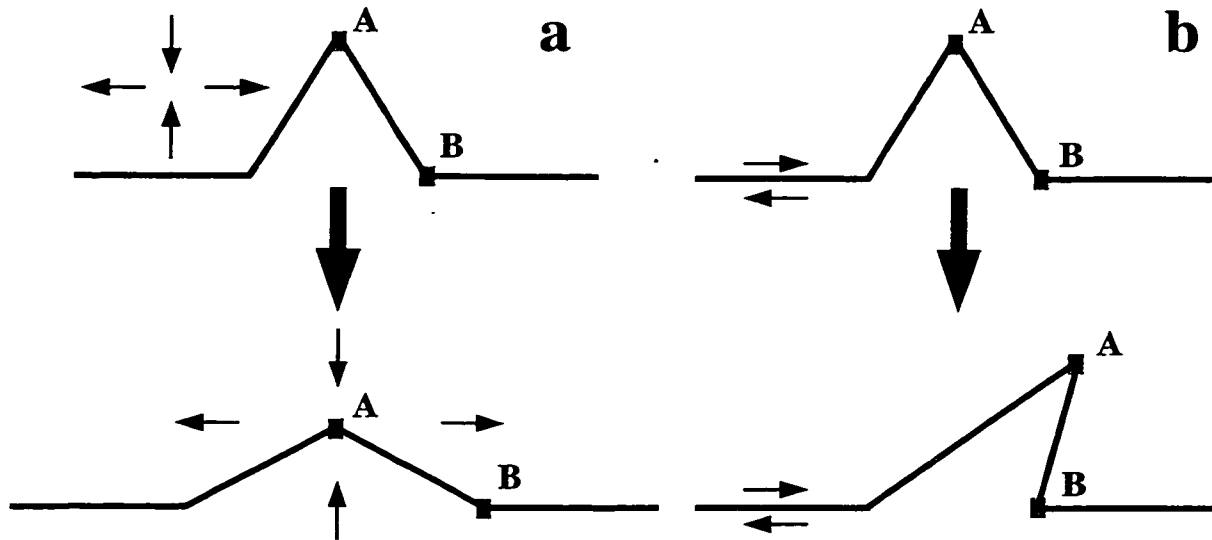

Figure 7.1: Evolution of layer disturbances in steady state flow fields. (a) pure shear deformation tends to flatten disturbances, while (b) simple shear can overturn the perturbation and cause folding.

vertical, and consequently overturns. Using Eq. (7.2) to solve for $x_A(t; 0, A) - x_B(t; \mathcal{L}, 0) > 0$ we get

$$\frac{A}{\mathcal{L}} > \frac{L_{11} - L_{33}}{L_{13}},$$

or using the non-dimensional notation

$$R_0 > \mathcal{H}, \quad \text{or} \quad m_0 \mathcal{H} < 1. \tag{7.8}$$

The time it takes particle A to reach particle B in the horizontal position, $x_A(t; 0, \mathcal{A}) - x_B(t; \mathcal{L}, 0) = 0$, is

$$t_f = -\frac{1}{L_{11} - L_{33}} \ln\left(1 - \frac{L_{11} - L_{33}}{L_{13}}\frac{\mathcal{L}}{\mathcal{A}}\right),$$

or using the non-dimensional variables

$$T_f = -\ln\sqrt{1 - \mathcal{H}m_0}. \tag{7.9}$$

7.3.3 Anisotropic Strain Rates

We use the homogeneous stress assumption (*Sachs*, 1928) to formulate an anisotropic flow law. The derivation of the velocity gradient, L_{ij}, as a function of cone angle can be found in *Thorsteinsson* (2000a). We use ice I_h as the deforming material. Ice obeys a power law with a stress exponent $n = 3$; most minerals of geophysical interest have $n > 1$. Appendix A.1 gives the equations for the non-zero components of the velocity gradient, L_{11}, L_{22}, L_{33} and L_{13}, in uniaxial compression combined with simple shear (UC&SS) stress state as a function of cone angle, as are the non-zero components in combined pure and simple shear (PS&SS) stress state.

The anisotropy breaks the one-to-one correspondence between stress and strain rate components that exists for isotropic materials. We can examine how the anisotropy changes the strain rate, relative to the isotropic response, by plotting the ratio of anisotropic strain rate to the isotropic strain rate. Figure 7.2 shows the normalized vertical strain rate, $L_{33}(\alpha, \tau)/L_{33}(90°, \tau)$, as a function of cone angle α and shear stress τ in combined uniaxial compression and simple shear stress state (the compressive stress is constant). The peak enhancement in vertical strain increases with increasing shear stress, and the maximum (for a given value of τ) moves from $\alpha \simeq 60°$ for $\tau/\sigma < 1$ to $\alpha \simeq 35°$ for $\tau/\sigma > 1$. The vertical strain rate varies greatly, as a function of cone angle, for strongly anisotropic ice (see Figure 7.2). Figure 7.3 shows the normalized shear strain rate, the $L_{13}(\alpha, \tau)/L_{13}(90°, \tau)$
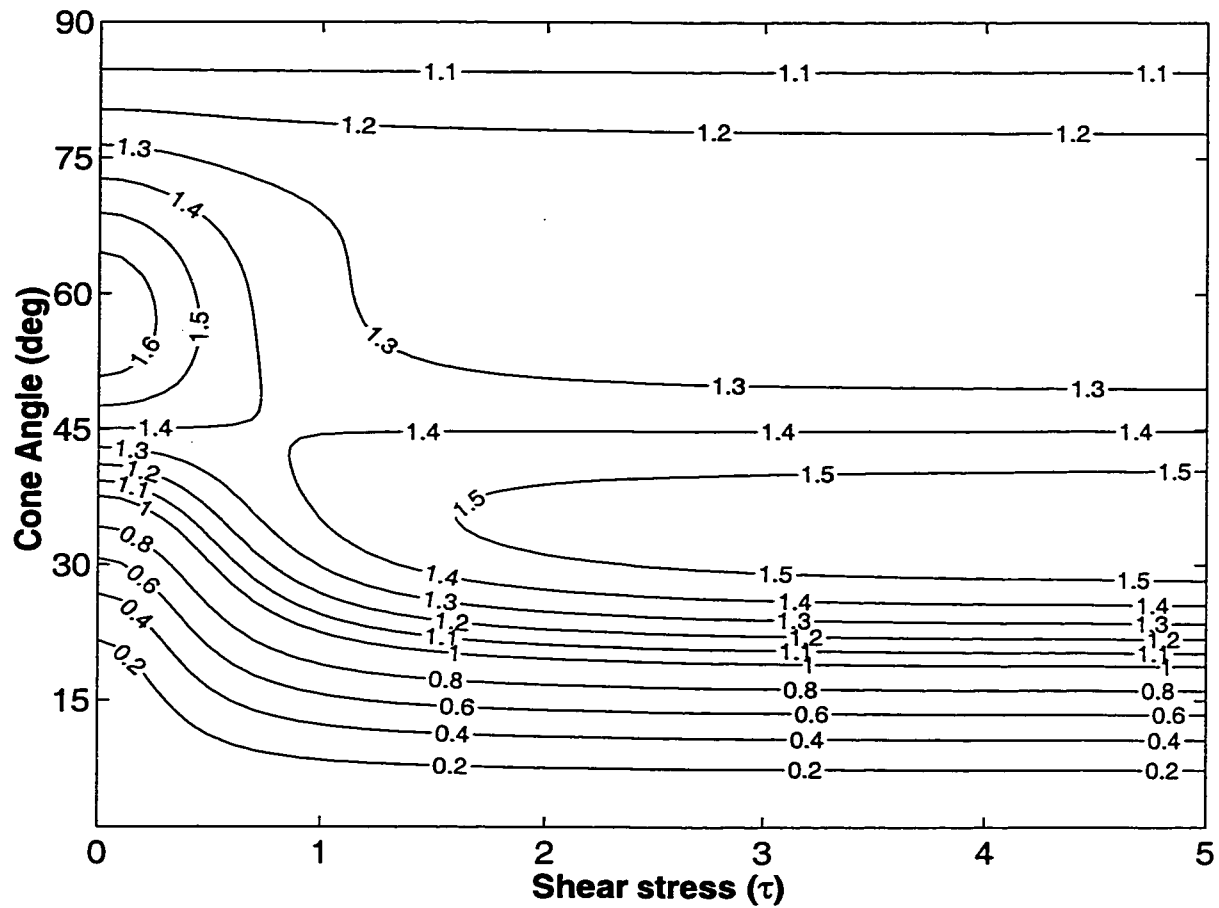
Figure 7.2: The normalized vertical strain rate, $L_{33}(\alpha, \sigma, \tau)/L_{33}(90°, \sigma, \tau)$, as a function of shear stress, τ, and cone angle, α. The compressive stress is $\sigma = 1$. Note how the compression has a maximum at around 60° when small shear stress and near 35° with increasing shear stress.
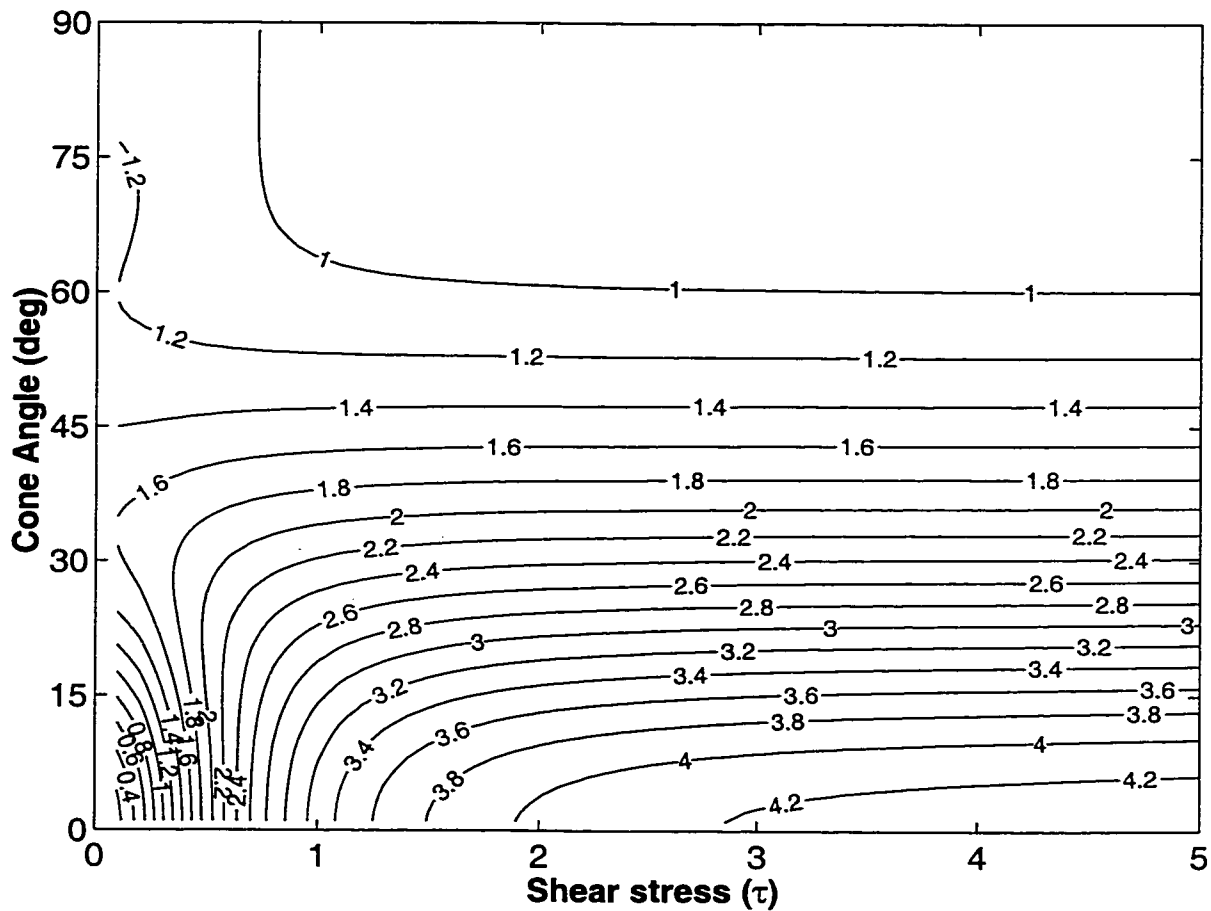
Figure 7.3: The normalized shear velocity gradient, $L_{13}(\alpha, \sigma, \tau)/L_{13}(90°, \sigma, \tau)$, as a function of shear stress, τ, and cone angle, α. The compressive stress is $\sigma = 1$.

component. The shear strain rate has a simpler pattern, except when $\tau < \sigma$, where the enhancement is a strong function of τ, for strongly anisotropic ice.

We now examine the dependence of the shear number $\mathcal{H}$ on the anisotropy and stress. Figure 7.4 shows the shear number $\mathcal{H}$ as a function of cone angle and shear stress in combined uniaxial compression and simple shear stress state. The folding criterion (Eq. 7.8) shows that the roughness, R, has to be larger than $\mathcal{H}$ for folding to be possible. Figure 7.5 shows
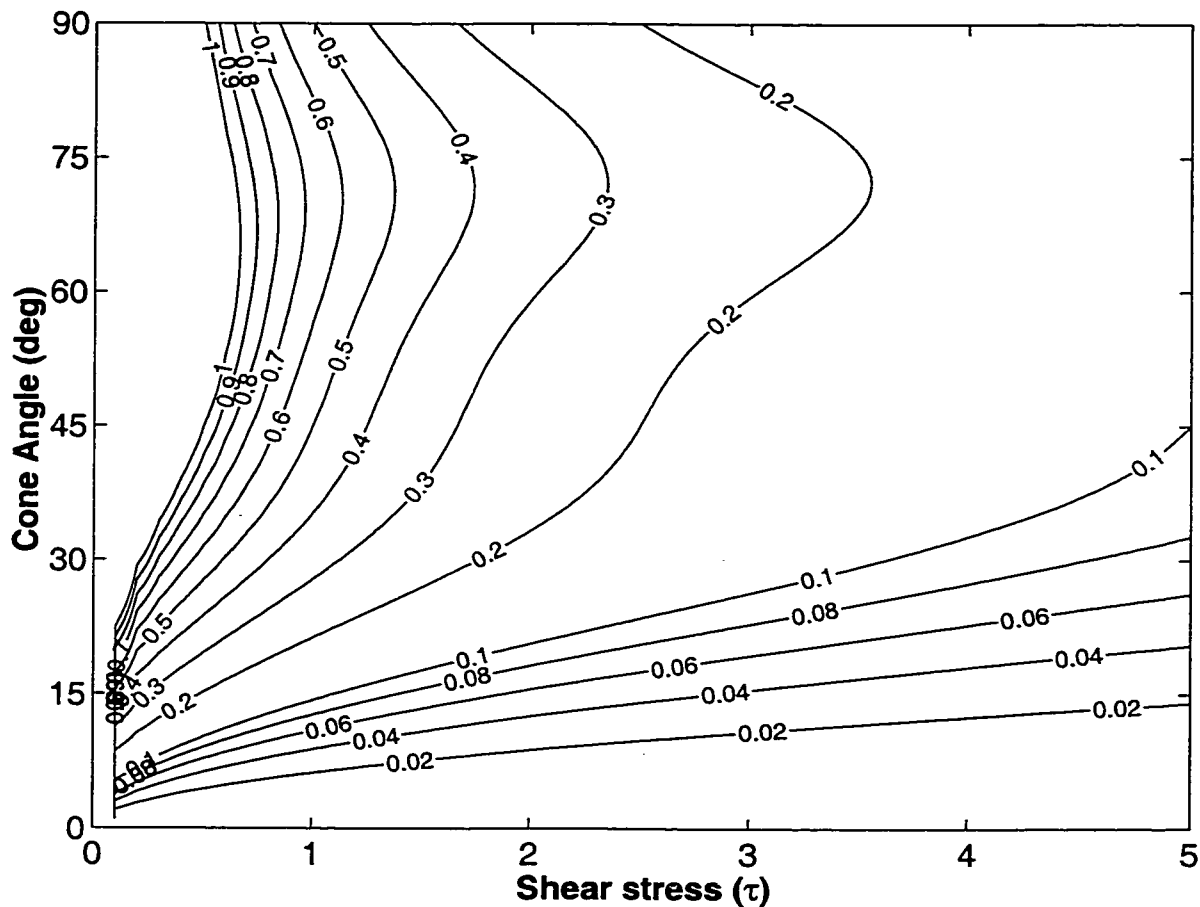
Figure 7.4: Shear Number $\mathcal{H}$ as a function of cone angle and simple shear stress in combined uniaxial compression $\sigma = 1$ and simple shear stress state. The roughness R must be greater than $\mathcal{H}$ for folding to be possible.

the shear number $\mathcal{H}$ as a function of cone angle and shear stress in combined pure and simple shear (PS&SS) stress state. Folding is more difficult in PS&SS than UC&SS since

the layer flattening, extension in the x-direction, is stronger. This is illustrated in Figure
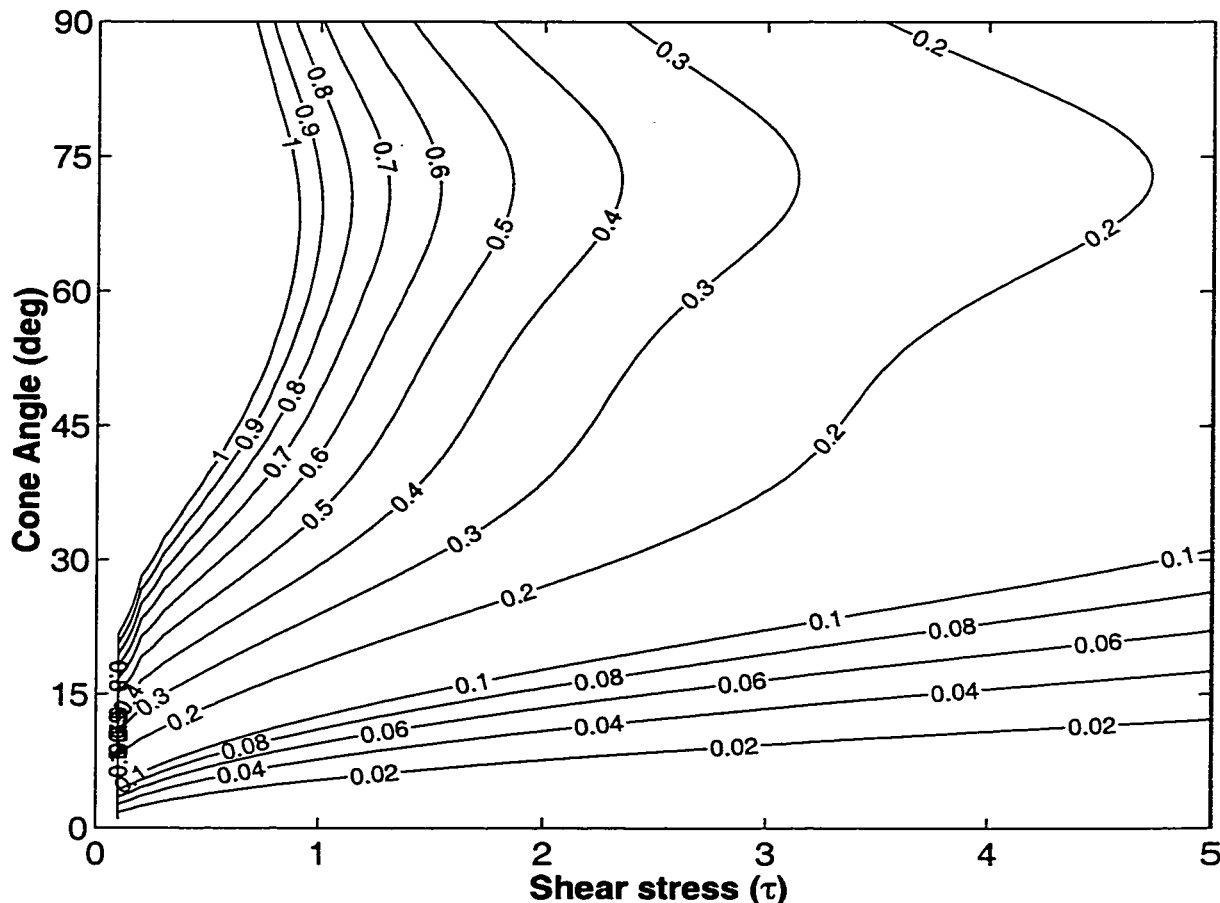
Figure 7.5: Shear Number $\mathcal{H}$ as a function of cone angle and simple shear stress in combined pure shear $\sigma = 1/\sqrt{2}$ and simple shear stress state.

7.6, which shows profiles (profiles of Fig. 7.4 and 7.5) of the shear number for different levels of shear stress, as a function of cone angle. For isotropic material, obeying a constitutive equation of the form $\dot{\varepsilon}_{ij} = A(T)\sigma_e^{n-1}\sigma_{ij}$ (Glen's flow law (*Glen*, 1958)), where σ_e is the effective stress, it can be shown that $\mathcal{H} = \sigma/(2\tau)$, which is indeed observed for $\alpha = 90°$.

The evolution of layers is calculated using Eqs. (7.2) and (7.4). Figures 7.7 and 7.8 show the evolution of a wiggle in isotropic and anisotropic media, respectively. The amplitude is $\mathcal{A} = 1$, the base length is $\mathcal{L} = 10$, and where the roughness is approximated by a straight-
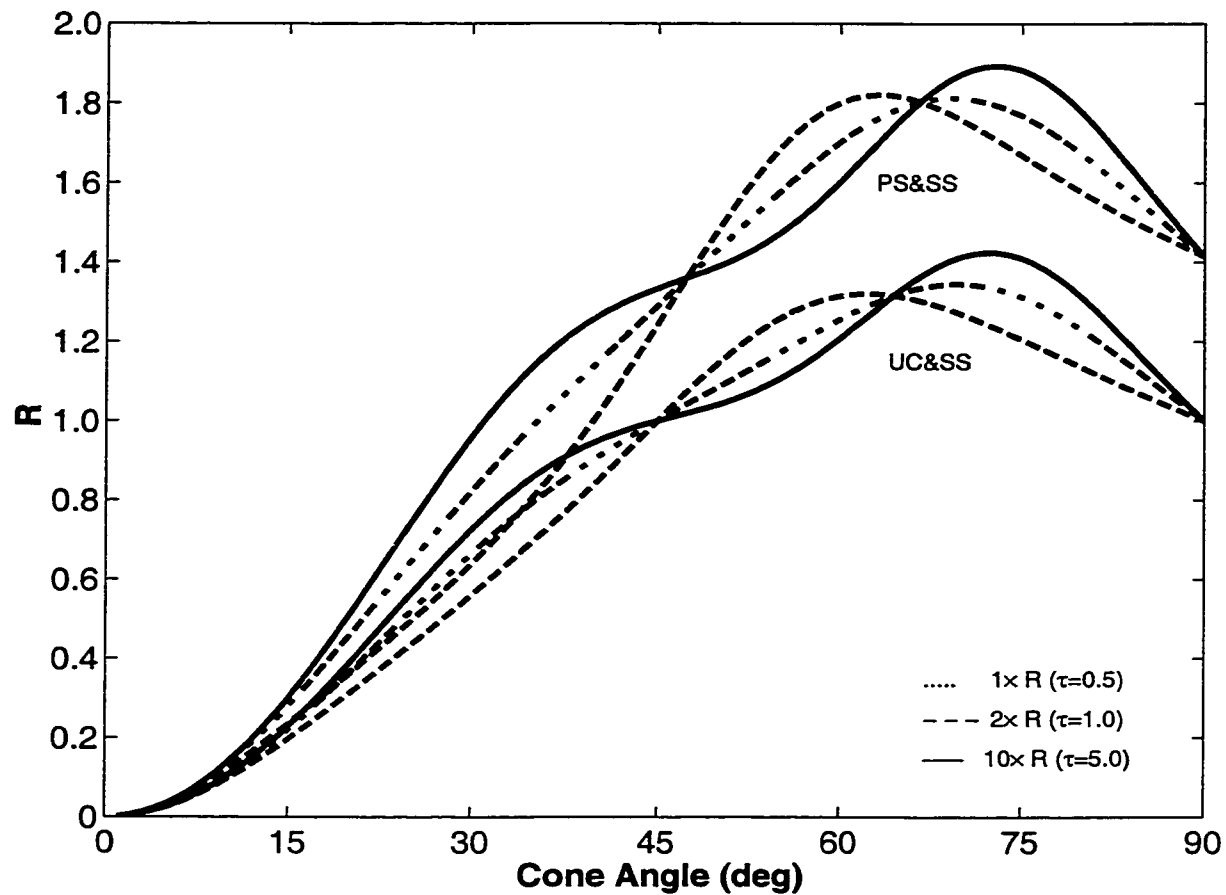
Figure 7.6: The minimum roughness, $R = A/\mathcal{L} = 1/m$, needed for folding as a function of cone angle α for different levels of shear stress. The two sets of lines represent the uniaxial compression $(\sigma = 1)$ and simple shear, and pure $(\sigma = 1/\sqrt{2})$ and simple shear stress combinations. The solid lines are $10 \times R$ with $\tau = 5.0$, the dashed lines are $2 \times R$ with $\tau = 1.0$ and the dotted lines give R with $\tau = 0.5$. Note the change in shape as the shear stress changes.

line element between points A and B, which has a roughness $R = 0.1$. The stress state is PS&SS, with $\sigma = 1$ and $\tau = 4$. Under these conditions folding will never occur in the isotropic medium (Fig. 7.7). In the anisotropic medium on the other hand, folding occurs
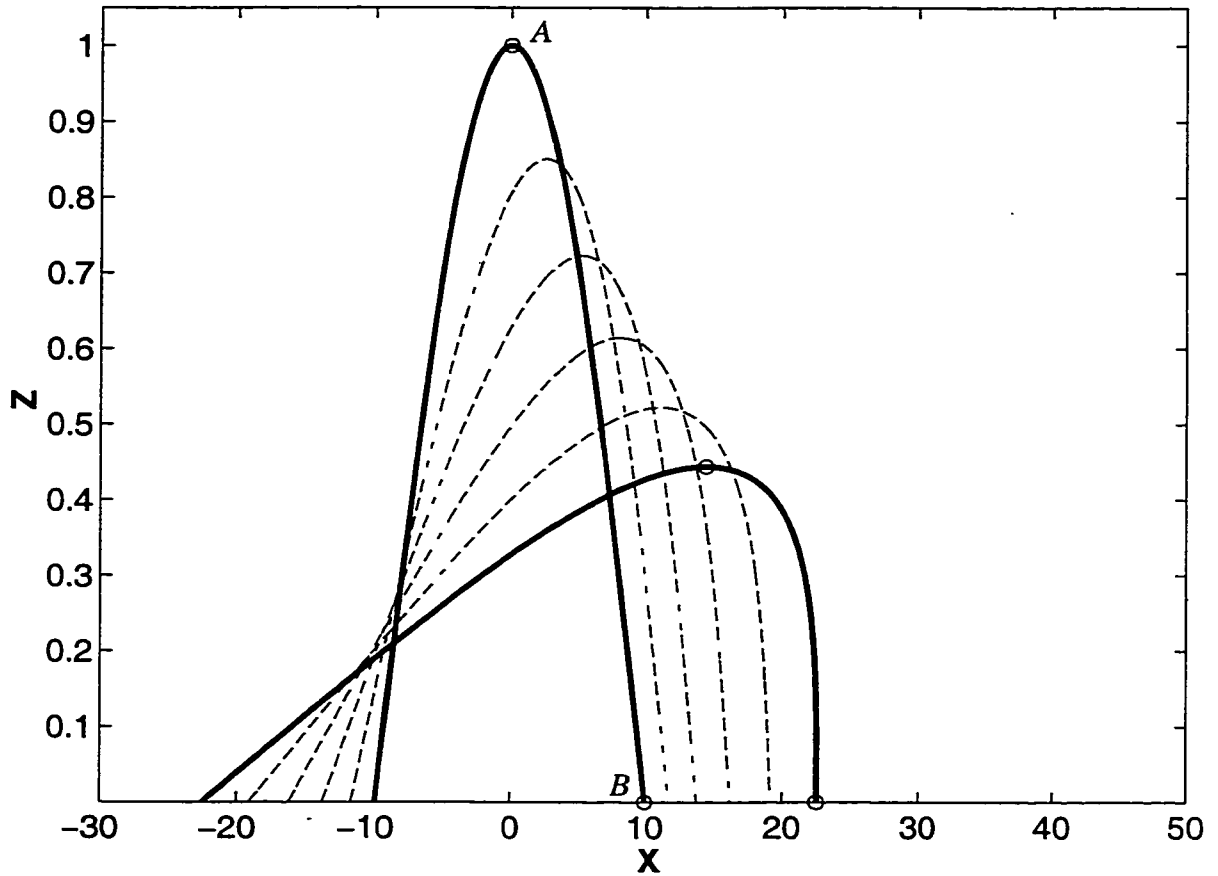
Figure 7.7: Evolution of a wiggle in combined pure and simple shear stress state. The material is isotropic $\alpha = 90°$, the shear stress is $\tau = 4$ and the compressive stress is $\sigma = 1.0$. Approximating the slope of this sinusoidal curve as $1/10$, the top point A will never overtake the bottom point B, see Fig. 7.1.

rapidly under the same conditions (Fig. 7.8). The profiles are taken at equal time intervals, and at the same time in both figures.
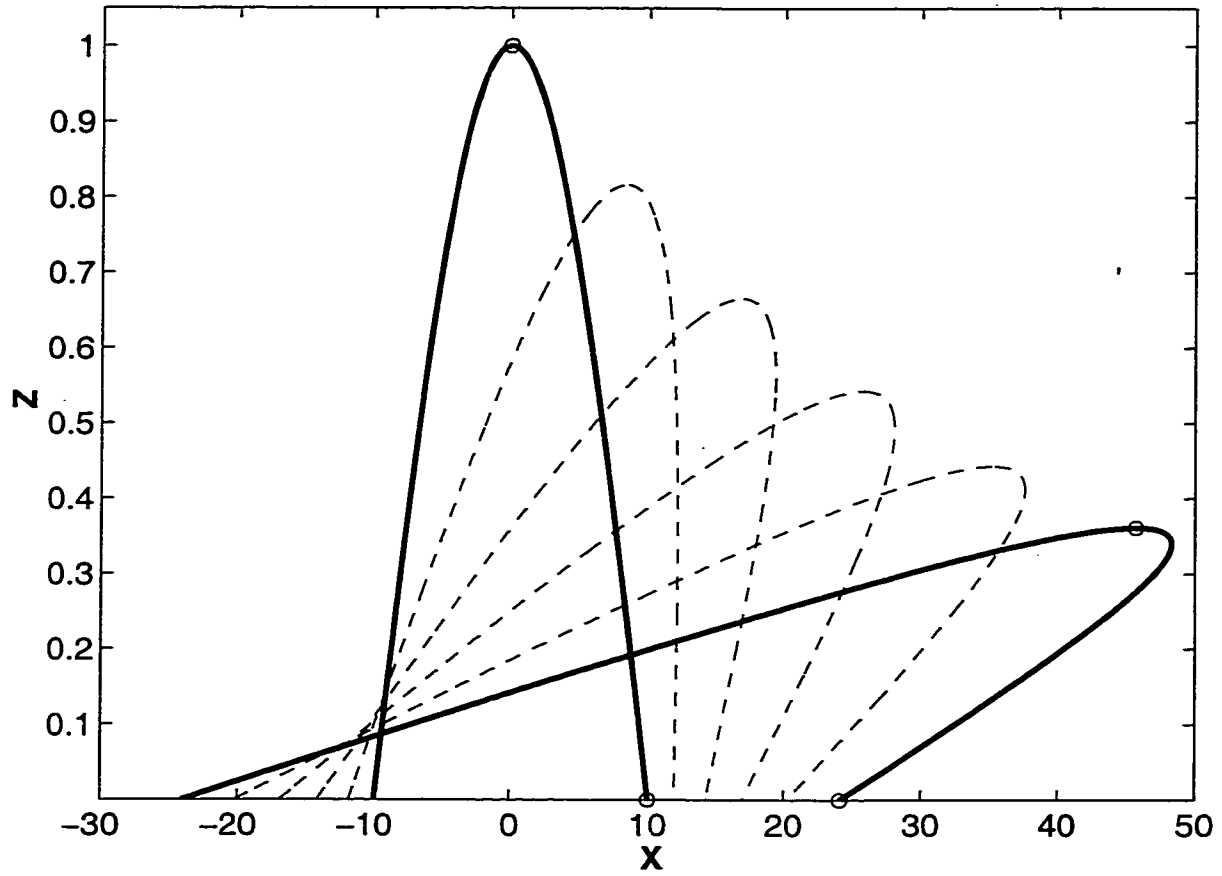
Figure 7.8: Evolution of a bump under the same conditions as in Fig. 7.7, except that the material is now strongly anisotropic, with a cone angle $\alpha = 20°$. In this case the wiggle overturns easily.

7.4 ORIGIN OF LAYER DISTURBANCES

There are several possible sources for layer disturbances, including sastrugi, boudins, accumulation variations, anisotropy. Of these, all but anisotropy seem an unlikely source for the disruption of stratigraphy observed at GRIP and GISP2 (*Waddington et al.*, 2000). Anisotropy may lead to layer disruption in several ways which are examined below.

7.4.1 Tilted Cones

If the symmetry axis of the cone is non-vertical (see Figure 7.9) the deformation will be a combination of pure and simple shear, even if the imposed stress state is only pure shear stress (*Azuma and Goto-Azuma*, 1996; *Thorsteinsson*, 2000a). To simulate a layer with
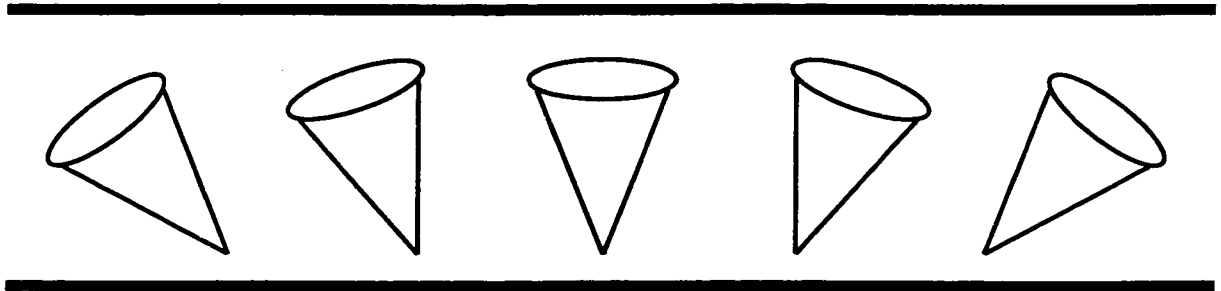
Figure 7.9: A layer with 20° cones that have a sinusoidal variation of the tilt angle, with a maximum tilt of ±40°.

a sinusoidal variation of the tilt of the cone symmetry axis we can rotate the pure shear stress tensor, since the fabric has a fixed vertical symmetry. Figure 7.10 shows the shear and compressive stressess that arise when we rotate the stress field to a maximum angle of 40°. The shear stress τ varies between ±3, while the compressive stress σ varies between -5 and -4. The evolution of an initially flat layer with a 20° cone who's symmetry axis is titled sinusoidally is shown in Figure 7.11. The sense of shear is in the direction of the tilt of the cone, creating the asymmetry; compare the layer around $X = 0$ and $X = 20$.
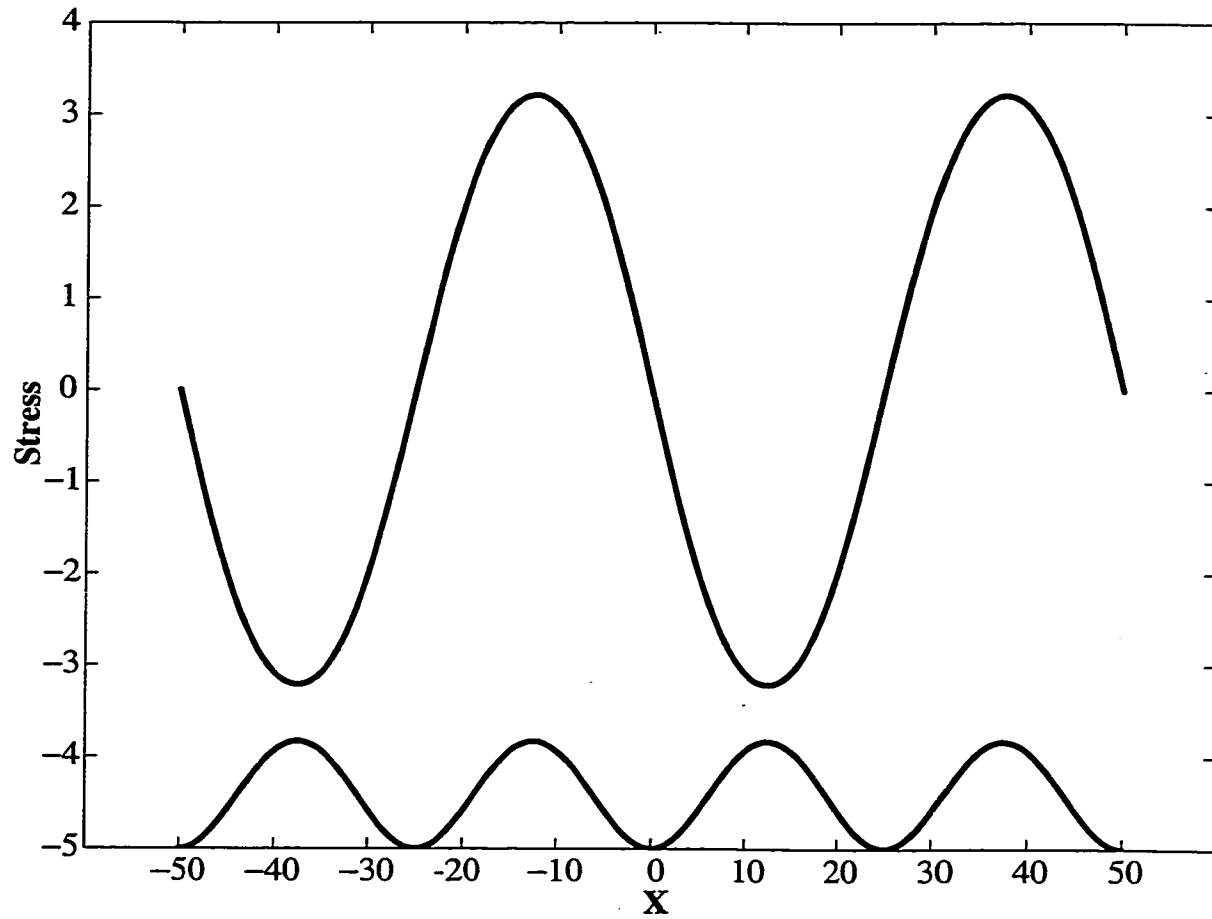
Figure 7.10: Variations in the pure σ and simple shear τ stresses as a function of horizontal position. These variations correspond to a sinusoidal rotation of a pure shear stress tensor by a maximum angle of $\pm 40°$.
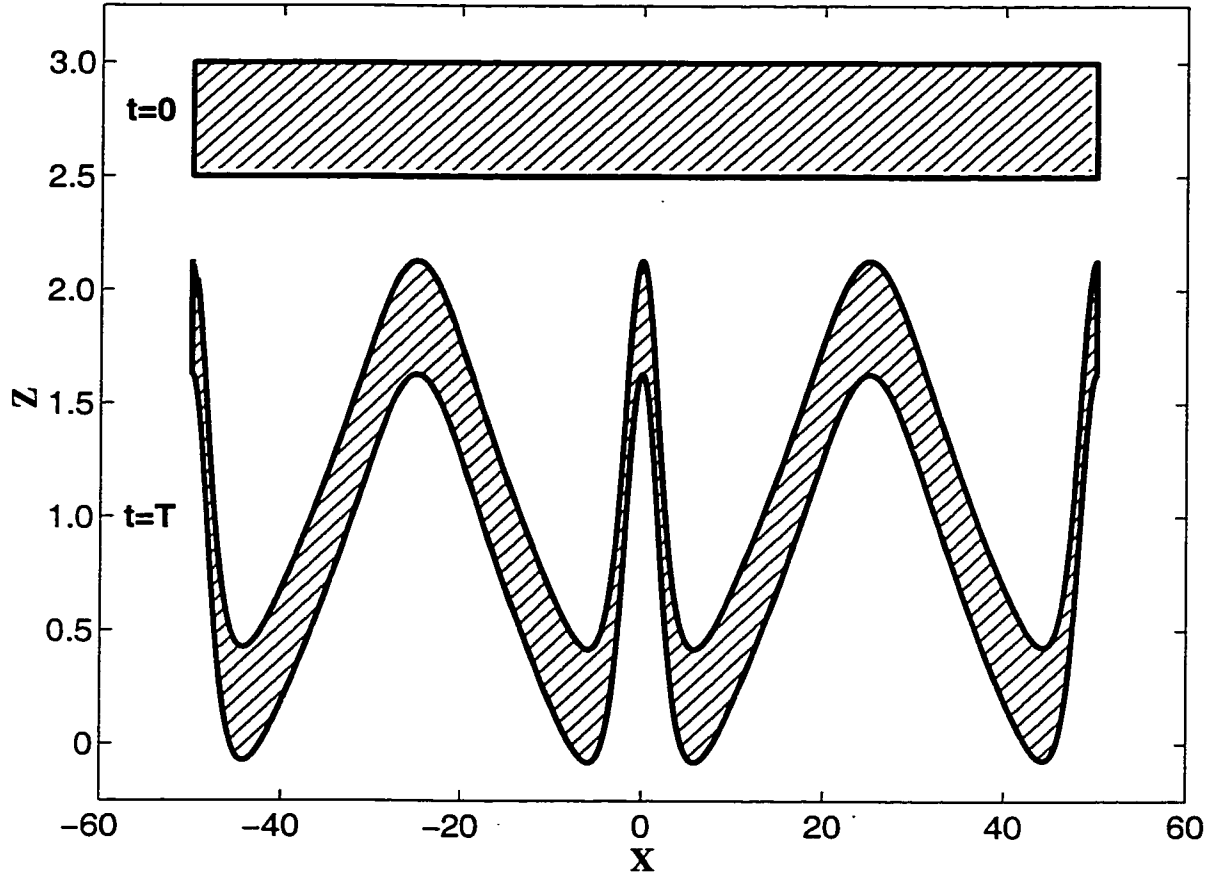
Figure 7.11: The geometry of an initially flat layer ($t = 0$) after deformation in a "quasi"-pure shear stress field ($t = T$), using the stress in Fig. 7.10 to simulate a spatially variable tilt of a 20° cone.

7.4.2 Evolution of Tilted Fabric

If the symmetry axis of the cone is tilted away from vertical in uniaxial compression, the strain rates will be very different from those arising from the deformation of a vertically symmetric fabric. Figure 7.12 shows layer thickness as a function of time for layers with a cone tilted by 0°, by 20° and by 40°. The vertical strain rate $\dot{\epsilon}_{zz}$ and c-axes rotation are calculated using the fabric evolution model described in *Thorsteinsson* (2000b). The c-axes rotate toward vertical, but do not preserve the cone fabric. The layer thickness h as a function of time is

$$\frac{h}{H} = \exp\left(\sum_i \dot{\epsilon}^i_{zz} \Delta t_i\right),\qquad(7.10)$$

where H is the initial thickness of the layer, and Δt_i is the time step. Since it is easiest to compress crystals orientated close to 45°, the tilted 40° cones have higher vertical strain rates initially.

7.4.3 Stripes

In a study of vertical thin sections from the GISP2 ice core *Alley et al.* (1997) found that the expected vertical c-axis fabric was interrupted by planes of grains, with the c-axes oriented approximately in the dip direction of the planes. These features were called stripes because of their appearance when intersected by vertical thin sections. The stripes are typically one to very few grains in thickness. If they are orientated close to vertical their length is a few grains, but if they are orientated further away from vertical, they tend to be longer. *Alley et al.* (1997) hypothesized that stripes form through organized polygonization, such that after polygonization of the center grain, the stress on neighbor grains will tend to rotate them so that they will be parallel to the polygonized grain. The stripe would then grow through internal spinning of grains at the end of a stripe, i.e. shear on the stripes plane would force the grain at the end into the same orientation.

We have seen above that non-vertical alignment of crystals will complicate the deformation, and potentially give rise to layer disturbances. Stripes are therefore a potential source of small-scale folding.
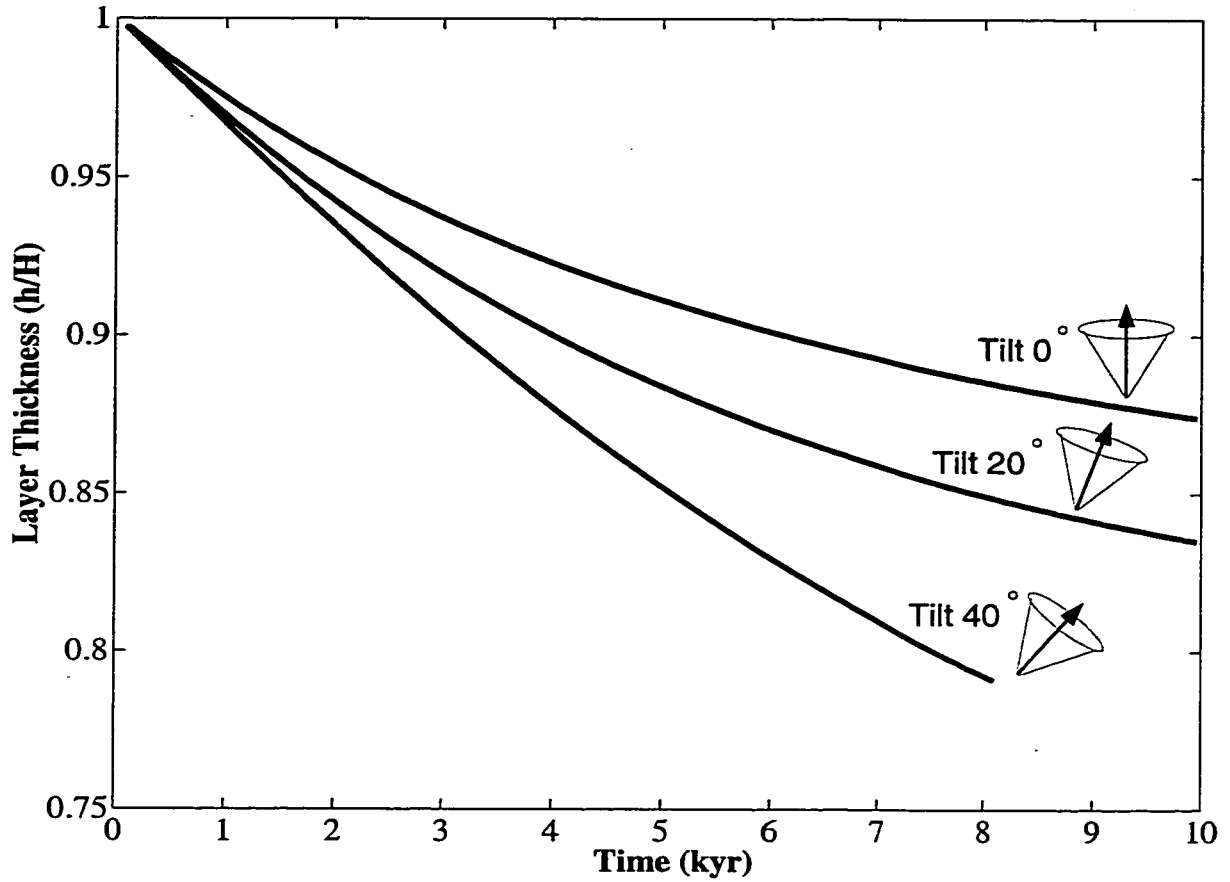
Figure 7.12: Evolution of layer thickness, in uniaxial compression, as a function of time for different tilts of the original cone fabric. The three lines show the layer thickness for the initial condition of a vertically symmetric 40° cone tilted by: 0° (top), 20° (middle) and 40° (bottom). The fabric then evolves freely in uniaxial compression stress (mild-NNI, $\sigma = -0.2$ bar (*Thorsteinsson*, 2000b)).

7.5 DISCUSSION

The origin of layer disturbances in ice sheets is an elusive problem. Several authors have suggested that anisotropy may play a significant role in that process (*Azuma and Goto-Azuma*, 1996; *Castelnau et al.*, 1998). We simulated the effects of tilted cones on the shape of a horizontal layer and found that tilted cones can indeed produce severely distorted layers.

Finding the state of stress in a layer with a different rheology to the adjacent layers can be a difficult problem. Two extreme cases are to assume that a) the stress is continuous across the interface, or b) that the velocity gradient is continuous. The true state is likely some compromise between these extremes. In our calculations we have assumed that the stress state is known, therefore our results probably show the maximum effect of anisotropy.

7.6 CONCLUSIONS

Under steady state stress conditions anisotropy does strongly influence the roughness needed to generate folds. Flow instabilities associated with an asymmetric fabric could be a source of layer disturbances. Under an ice divide, in a plain strain regime, asymmetric fabric can lead to distortion of horizontal layers.

Chapter 8

EPILOGUE

Accounting for anisotropy in the deformation of ice represents an important step toward a more complete physically based flow law for glaciers and ice sheets. Other deformation mechanisms in addition to dislocation glide (Chapter 2) may contribute to the deformation, especially at low stress and small crystal size.

The anisotropy of ice markedly changes its deformation response to stress, often in a non-intuitive way. The vertically symmetric fabric I used for most applications (Chapter 3, 6, and 7) is relatively common. Even though this fabric is relatively simple its effects on deformation yields some surprises. For instance the enhancement in uniaxial compression, and small de-enhancement in simple shear over a range of cone angles (Chapter 3) can result in complicated vertical strain rates or stresses (Chapter 7).

The analysis of the Dye 3 data (Chapter 4) clearly demonstrated that even though we can now explain 75% of the deformation when fabric-induced anisotropy is taken into account, there is still a significant uncertainty in the flow law for ice. More specifically, the effects of crystal size and/or impurities also need to be included. Recently, D. M. Cole (*Cole and Gould*, 1990; *Cole*, 1995) has developed a model that relates the dislocation density to the strain history of ice, and is working on the effects of impurities on the dislocation density [Cole, pers. comm.]. I hope to collaborate with Dr. Cole in the future to apply similar theoretical approaches to the GISP2 borehole as I did with the Dye 3 borehole, taking the extra step of using dislocation density instead of ad hoc correlations to impurities and crystal size. There is certainly a possibility that crystal size will still have to be included, but then probably due to some grain boundary effects, such as grain boundary sliding or migration.

The model for fabric evolution developed in Chapter 5 accounts for the physical arrangement of crystals. It is computationally fast; typical runs with 100 strain steps and 1000

crystals take less than 30 seconds on a Pentium 75 MHz PC computer. There is therefore the potential of including the model in finite element simulations, where 1000 crystals or so could represent each region of ice, and the evolution of fabric could be traced through the flow field.

To verify any such models of fabric evolution we need a reliable method of measuring fabric. In Chapter 6, three different ways to estimate fabric were compared. I compare strain rate calculated using an inferred cone angle with the strain rate calculated using the actual fabric. Sonic velocities gave the best estimates of cone angles for the different types of fabric studied. Thin section data give precise information about the crystal orientations, but at a very localized scale.

In Chapter 7, the analytical constitutive equations derived in Chapter 3 were used to examine how anisotropy affects the folding criteria. Anisotropy enhances the possibility of folding, especially when shear stresses exceed normal stresses.

Accounting for anisotropy represents an important step toward a physically based flow law. Writing the flow law in terms of dislocation density and velocity of dislocations represents the next major step. Other processes such as grain boundary migration, sliding, and diffusion are still largely unresolved. A flow law for ice could be written as

$$\dot{\varepsilon} = \dot{\varepsilon}_{disl} + \dot{\varepsilon}_{diff} + \dot{\varepsilon}_{gb} + \dot{\varepsilon}_{other},\qquad(8.1)$$

where $\dot{\varepsilon}_{disl}$ is the strain rate due to dislocation glide, $\dot{\varepsilon}_{diff}$ strain rate due to diffusion processes, $\dot{\varepsilon}_{gb}$ strain rate due to grain boundary processes, and $\dot{\varepsilon}_{other}$ other processes contributing to the strain rate.

Including anisotropy into large scale models (finite element) is an important next step. To take the evolution of fabric into account, one could either couple two models, one of the flow field and the other a sub-mesh for the fabric evolution, or simplify the fabric evolution. The evolution of the fabric is particularly important, since the locations of ice divides are known to change (*Marshall and Cuffey*, 2000). This changes the spatial distribution of stress, and can result in non-symmetric fabric patterns, which can serve as nuclei for folding. Accounting for anisotropy will lead to better estimates of time scales for potential ice cores and better location criteria for future ice cores.

BIBLIOGRAPHY

Alley, R. B., Flow-law hypotheses for ice-sheet modeling, *Journal of Glaciology*, *38*(129), 245–256, 1992.

Alley, R. B., and G. W. Woods, Impurity influence on normal grain growth in the GISP2 ice core, *Journal of Glaciology*, *42*(141), 255–260, 1996.

Alley, R. B., J. H. Perepezko, and C. R. Bentley, Grain growth in polar ice: I. Theory, *Journal of Glaciology*, *32*(112), 413–424, 1986.

Alley, R. B., A. Gow, S. J. Johnsen, J. Kipfstuhl, D. Meese, and T. Thorsteinsson, Comparison of deep ice cores, *Nature*, *373*(6513), 393–394, 1995a.

Alley, R. B., A. Gow, and D. Meese, Mapping c-axis fabrics to study physical processes in ice, *Journal of Glaciology*, *41*(137), 197–203, 1995b.

Alley, R. B., A. J. Gow, D. A. Meese, J. J. Fitzpatrick, E. D. Waddington, and J. F. Bolzan, Grain-scale processes, folding, and stratigraphic disturbance in the GISP2 ice core, *Journal of Geophysical Research*, *102*(C12), 26819–26830, 1997.

Anandakrishnan, S., J. Fitzpatrick, R. B. Alley, A. Gow, and D. Meese, Shear-wave detection of asymmetric c-axis fabrics in the GISP2 ice core, Greenland, *Journal of Glaciology*, *40*(136), 491–496, 1994.

Ashby, M. F., and P. Duval, The creep of polycrystalline ice, *Cold Regions Science and Technology*, *11*(3), 285–300, 1985.

Azuma, N., A flow law for anisotropic ice and its application to ice sheets, *Earth and Planetary Science Letters*, *128*(3-4), 601–614, 1994.

Azuma, N., A flow law for anisotropic ice under uniaxial compressive deformation, *Cold Regions Science and Technology*, *23*(2), 137–147, 1995.

162

Azuma, N., and K. Goto-Azuma, An anisotropic flow law for ice-sheet ice and its implications, *Annals of Glaciology*, *23*, 202–208, 1996.

Azuma, N., and A. Higashi, Formation processes of ice fabric pattern in ice sheets, *Annals of Glaciology*, *6*, 130–134, 1985.

Bai, Q., S. Mackwell, and D. Kohlstedt, High-temperature creep of olivine single crystals. 1. Mechanical results for buffered samples, *Journal of Geophysical Research*, *96*(B2), 2441–2463, 1991.

Baker, I., Observation of dislocations in ice, *J. Phys. Chem. B*, *101*(32), 6158–6162, 1997.

Ball, P., *Life's Matrix: A biography of water*, Farrar, Strauss and Giroux, New York, 1st edn., 2000.

Barber, D. J., Dislocations and microstructures, in *Preferred Orientations in deformed Metals and Rocks: An Introduction to Modern Texture Analysis*, edited by H.-R. Wenk, pp. 149–182, Academic Press, 1985.

Barlow, R. J., *Statistics. A guide to the use of statistical methods in the physical sciences*, John Wiley and Sons, New York, 1st edn., 1989.

Bennett, H. F., An investigation into velocity anisotropy through measurements of ultrasonic wave velocities in snow and ice cores from Greenland and Antarctica, *Ph. D. Thesis, University of Wisconsin (Unpublished)*, p. 110, 1968.

Bennett, H. F., Measurements of ultrasonic wave velocities in ice cores from Greenland and Antarctica, *CRREL Research Report 237*, pp. 1–61, 1972.

Bentley, C. R., Seismic-wave velocities in anisotropic ice: A comparison of measured and calculated values in and around the deep drill hole at Byrd Station, Antarctica, *Journal of Geophysical Research*, *77*(23), 4406–4420, 1972.

Bishop, J. F. W., and R. Hill, A theory of the plastic distortion of a polycrystalline aggregate under combined stresses, *Phil. Mag. (7th Ser.)*, *42*, 414–427, 1951.

Blacic, J. D., Effect of water on the experimental deformation of olivine, in *Flow and fracture of rocks*, edited by H. C. Heard, I. Y. Borg, N. L. Carter, and C. B. Raileigh, Geophysical Monograph 16, pp. 109–115, Washington D. C., American Geophysical Union, AGU, 1972.

Bohren, C. F., Colours of snow, frozen waterfalls, and icebergs, *J. Optical Society of America*, *73*(12), 1646–1652, 1983.

Branger, V., M. H. Mathon, T. Baudin, and R. Penelle, "In-situ" neutron diffraction study of the cube crystallographic texture development in Fe53%-Ni alloy during recrystallization, *Scripta Materialia*, *43*(4), 325–330, 2000.

Budd, W., and T. Jacka, A review of ice rheology for ice sheet modelling, *Cold Regions Science and Technology*, *16*(2), 107–144, 1989.

Castelnau, O., and P. Duval, Simulations of anisotropy and fabric development in polar ices, *Annals of Glaciology*, *20*, 277–282, 1994.

Castelnau, O., P. Duval, R. Lebensohn, and G. R. Canova, Viscoplastic modeling of texture development in polycrystalline ice with self-consistent approach: Comparison with bound estimates, *Journal of Geophysical Research*, *101*(B6), 13851–13868, 1996a.

Castelnau, O., P. Duval, R. Lebensohn, and G. R. Canova, Viscoplastic modeling of texture development in polycrystalline ice with self-consistent approach: Comparison with bound estimates, *Journal of Geophysical Research*, *101*(B6), 13851–13868, 1996b.

Castelnau, O., T. Thorsteinsson, J. Kipfstuhl, P. Duval, and G. R. Canova, Modelling fabric development along the GRIP ice core, central Greenland, *Annals of Glaciology*, *23*, 194–201, 1996c.

Castelnau, O., G. Canova, , R. Lebensohn, and P. Duval, Modelling viscoplasctic behavior of anisotropic polycrystalline ice with a self-consistent approach, *Acta Materialia*, *45*(11), 4823–4834, 1997.

Castelnau, O., H. Shoji, A. Mangeney, H. Milsch, P. Duval, A. Miyamoto, K. Kawada, and O. Watanabe, Anisotropic behavior of GRIP ices and flow in Central Greenland, *Earth and Planetary Science Letters*, *154* (1-4), 307–322, 1998.

Chastel, Y. B., P. R. Dawson, H.-R. Wenk, and K. Bennett, Anisotropic convection with implications for the upper mantle, *Journal of Geophysical Research*, *98* (B10), 17757–17771, 1993.

Cole, D. M., A model for the anelastic straining of saline ice subjected to cyclic loading, *Philosophical Magazine A*, *72* (1), 231–248, 1995.

Cole, D. M., and L. D. Gould, Reversed direct-stress testing of ice: Equipment and example results, *Cold Regions Science and Technology*, *18* (3), 295–302, 1990.

Crampin, S., An introduction to wave propagation in anisotropic media, *Geophys. J. R. astr. Soc.*, *76*, 17–28, 1984.

Cuffey, K. M., H. Conway, A. Gades, B. Hallet, R. Sletten, and C. F. Raymond, Tunneling in the name of Science: Meserve Glacier revisited, *Supplement to EOS, Transactions, AGU*, *77* (46), 57, 1996.

Dahl-Jensen, D., Determination of the flow properties at Dye 3, South Greenland, by borehole-tilting measurements and perturbation modelling, *Journal of Glaciology*, *31* (108), 92–98, 1985.

Dahl-Jensen, D., and N. Gundestrup, Constitutive properties of ice at Dye 3, Greenland, in *The Physical Basis of Ice Sheet Modelling (Symposium at Vancouver 1987)*, pp. 31–43, International Association of Hydrological Sciences Publication 170, 1987.

Dansgaard, W., and S. J. Johnsen, A flow model and a time scale for the ice core from Camp Century, Greenland, *Journal of Glaciology*, *8* (53), 215–223, 1969.

Dawson, P. R., and H.-R. Wenk, Texturing of the upper mantle during convection, *Philosophical Magazine A*, *80* (3), 573–598, 2000.

De La Chapelle, S., O. Castelnau, V. Lipenkov, and P. Duval, Dynamic recrystallization and texture development in ice as revealed by the study of deep ice cores in Antarctica and Greenland, *Journal of Geophysical Research*, *103*(B3), 5091–5105, 1998.

den Toonder, J. M. J., J. A. W. van Dommelen, and F. P. T. Baaijens, The relation between single crystal elasticity and the effective elastic behaviour of polycrystalline materials: theory, measurements and computation, *Modelling Simul. Mater. Sci. Eng.*, *7*, 909–928, 1999.

Durham, W. B., S. H. Kirby, and L. A. Stern, Creep of water ices at planetary conditions: A compilation, *Journal of Geophysical Research*, *102*(E7), 16293–16302, 1997.

Duval, P., Creep and fabrics of polycrystalline ice under shear and compression, *Journal of Glaciology*, *27*(95), 129–140, 1981.

Duval, P., and O. Castelnau, Dynamic recrystallization of ice in polar ice sheets, *Journal de Physique IV*, *5*(C3), 197–205, 1995.

Duval, P., and H. LeGac, Does the permanent creep-rate of polycrystalline ice increase with crystal size?, *Journal of Glaciology*, *25*(91), 151–157, 1980.

Duval, P., and H. LeGac, Mechanical behavior of Antarctic ice, *Annals of Glaciology*, *3*, 92–96, 1982.

Duval, P., M. F. Ashby, and I. Anderman, Rate-controlling processes in the creep of polycrystalline ice, *Journal of Physical Chemistry*, *87*(21), 4066–4074, 1983.

Echelmeyer, K., and W. Zhongxiang, Direct observation of basal sliding and deformation of basal drift at sub-freezing temperatures, *Journal of Glaciology*, *33*(113), 83–98, 1987.

Fukuda, A., T. Hondoh, and A. Higashi, Dislocation mechanisms of plastic deformation of ice, *Journal de Physique*, *48*(C1), 163–173, 1987.

Glen, J. W., The flow law of ice, in *Physics of the movement of the ice*, pp. 171–183, International Association of Hydrological Sciences Publication 47, 1958.

Glen, J. W., The rheology of ice, in *Ice and Snow (Properties, processes, and applications)*, edited by W. D. Kingery, pp. 3–7, The M.I.T. Press, 1963.

Gödert, G., and K. Hutter, Induced anisotropy in large ice shields: theory and its homogenization, *Continuum Mech. Thermodyn.*, *10*(5), 293–318, 1998.

Goldsby, D., and D. Kohlstedt, Creep of fine-grained ice I, in *International Symposium on the Physics and Chemistry of Ice*, pp. 75–76, 1996.

Goldsby, D. L., and D. L. Kohlstedt, Grain boundary sliding in fine-grained ice I, *Scripta Materialia*, *37*(9), 1399–1406, 1997.

Gow, A. J., Depth-time-temperature relationships of ice crystal growth in polar glaciers, *CRREL Research Report 300*, pp. 1–19, 1971.

Gow, A. J., D. A. Meese, R. B. Alley, J. J. Fitzpatrick, S. Anandakrishnan, G. A. Woods, and B. C. Elder, Physical and structural properties of the Greenland Ice Sheet Project 2 ice core: A review, *Journal of Geophysical Research*, *102*(C12), 26559–26575, 1997.

Green, H. W., and S. N. Radcliffe, Deformation processes in the upper mantle, in *Flow and fracture of rocks*, edited by H. Heard, I. Y. Borg, N. L. Carter, and C. B. Raileigh, Geophysical Monograph 16, pp. 139–157, American Geophysical Union, Washington D.C., 1972.

Guillope, M., and J. P. Poirier, Dynamic recrystallization during creep of single-crystalline Halite: An experimental study, *Journal of Geophysical Research*, *84*(B10), 5557–5567, 1979.

Gundestrup, N. S., and B. L. Hansen, Bore-hole survey at Dye 3, South Greenland, *Journal of Glaciology*, *30*(106), 282–288, 1984.

Hammer, C. U., H. B. Clausen, W. Dansgaard, A. Neftel, P. Kristinsdottir, and E. Johnson, Continuous impurity analysis along the Dye 3 deep core, in *Greenland Ice Core: Geophysics, Geochemistry and the Environment*, Geophysical Monograph 33, pp. 90–94, American Geophysical Union, 1985.

Herron, S. L., C. C. Langway, and K. A. Brugger, Ultrasonic velocities and crystalline anisotropy in the ice core from Dye 3, Greenland, in *Greenland Ice Core: Geophysics, Geochemistry and the Environment*, Geophysical Monograph 33, pp. 23–31, American Geophysical Union, 1985.

Hobbs, P. V., *Ice Physics*, Claredon Press, Oxford, 1974.

Hook, J. R., and H. E. Hall, *Solid State Physics*, John Wiley and Sons, Chichester, 2nd edn., 1991.

Hooke, R. L., et al., Mechanical properties of polycrystalline ice: An assessment of current knowledge and priorities for research, *Cold Regions Science and Technology*, *3*, 263–275, 1980.

Hooke, R. L., B. H. Dahlin, and M. T. Kauper, Creep of ice containing dispersed fine sand, *Journal of Glaciology*, *11*(63), 327–336, 1972.

Ignat, M., and H. J. Frost, Grain boundary sliding in ice, *Journal de Physique*, *48*(C1), 189–195, 1987.

Jacka, T. H., Laboratory studies on relationships between ice crystal size and flow rate, *Cold Regions Science and Technology*, *8*, 31–42, 1984.

Johnson, A. F., Creep characterization of transversely isotropic metallic materials, *J. Mech. Phys. Solids*, *25*, 117–126, 1977.

Jones, S. J., and J. W. Glen, The effect of dissolved impurities on the mechanical properties of ice crystals, *Philosophical Magazine*, *8*(19), 13–24, 1980.

Kamb, W. B., The glide direction in ice, *Journal of Glaciology*, *3*, 1097–1106, 1961.

Kamb, W. B., Experimental recrystallization of ice under stress, in *Flow and Fracture of Rocks*, edited by H. Heard, I. Y. Borg, N. L. Carter, and C. B. Raileigh, no. 16 in Geophysical Monograph Series, pp. 211–241, Washington, D.C., American Geophysical Union, AGU, 1972.

Karato, S., Inner core anisotropy due to the magnetic field-induced preferred orientation of iron, *Science*, *262*(5140), 1708–1711, 1993.

Kohnen, H., and A. J. Gow, Ultrasonic velocity investigations of crystal anisotropy in deep ice cores from Antarctica, *CRREL Research Report 79-10*, pp. 1–18, 1979.

Kuhlmann-Wilsdorf, D., Questions you always wanted (or should have wanted) to ask about workhardening, *Mater. Res. Innovat*, *1*(4), 265–297, 1998.

Kuhlmann-Wilsdorf, D., The theory of dislocation-based crystal plasticity, *Philosophical Magazine A*, *79*(4), 955–1008, 1999.

Lebensohn, R., and C. Tome, A self consistent anisotropic approach for the simulation of plastic deformation and texture development of polycrystals: Application to zirconium alloys, *Acta Metall. Mater*, *41*(9), 2611–2624, 1993.

Lebensohn, R., and C. Tome, A self-consistent viscoplastic model: prediction of rolling textures of anisotropic polycrystals, *Material Science and Engineering A*, *175*(1-2), 71–82, 1994.

Liu, F., I. Baker, and M. Dudley, Dislocation-grain boundary interactions in ice crystals, *Philosophical Magazine A*, *71*(1), 15–42, 1995.

Liu, F., I. Baker, and M. Dudley, Dynamic observations of dislocation generation at grain boundaries in ice, *Unpublished*, 2000.

Lliboutry, L. A., *Very Slow Flows of Solids (Basics of Modeling in Geodynamics and Glaciology)*, Martinus Nijhoff Publishers, Dordrecht, 1987.

Lliboutry, L. A., Anisotropic, transversely isotropic nonlinear viscosity of rock ice and rheological parameters inferred from homogenization, *International Journal of Plasticity*, *9*(5), 619–632, 1993.

Lliboutry, L. A., and P. Duval, Various isotropic and anisotropic ices found in glaciers and polar ice caps and their corresponding rheologies, *Annales Geophysicae*, *3*(2), 207–224, 1995.

Mangeney, A., F. Califano, and K. Hutter, A numerical study of anisotropic, low-Reynolds numbers, free surface flows for ice sheet modelling, *Journal of Geophysical Research*, *102*(B10), 22749–22764, 1997.

Marshall, S. J., and K. M. Cuffey, Peregrinations of the Greenland Ice Sheet divide in the last glacial cycle: implications for central Greenland ice cores, *EPSL*, *179*(1), 73–90, 2000.

Means, W. D., and M. W. Jessell, Accommodation migration of grain boundaries, *Tectonophysics*, *127*(1-2), 67–86, 1986.

Mohamed, G., and B. Bacroix, Role of stored energy in static recrystallization of cold rolled copper single and multicrystals, *Acta Materialia*, *48*(13), 3295–3302, 2000.

Molinary, A., G. Canova, and S. Ahzi, A self consistent approach of the large deformation polycrystal viscoplasticity, *Acta Metall.*, *35*(12), 2983–2994, 1987.

Morland, L. W., and R. Staroszczyk, Viscous response of polar ice with evolving fabric, *Continuum Mech. Thermodyn.*, *10*(3), 135–152, 1998.

Nakamura, T., and S. J. Jones, Softening effect of dissolved hydrogen chloride in ice crystals, *Scripta Metallurgica*, *4*, 123–126, 1970.

Nakamura, T., and S. J. Jones, Mechanical properties of impure ice crystals, in *Physics and Chemistry of Ice*, edited by E. Whalley, S. J. Jones, and L. W. Gold, pp. 365–369, Royal Society of Canada, Ottawa, 1973.

Nanthikesan, S., and S. S. Sunder, Anisotropic elasticity of polycrystalline ice I_h, *Cold Regions Science and Technology*, *22*(2), 149–169, 1994.

Nicolas, A., and N. I. Christensen, Formation of anisotropy in upper mantle peridotites - a review, in *Composition, Structure and Dynamics of the Lithosphere-Asthenosphere System*, edited by K. Fuchs, and C. Froidevaux, Geodynamics Series 16, pp. 111–123, American Geophysical Union, 1987.

Nye, J. F., The distribution of stress and velocity in glaciers and ice sheets, *Proceedings of the Royal Society of London, Ser A*, *219*(1139), 477–489, 1957.

Nye, J. F., *Physical properties of crystals*, Oxford, 1st edn., 1985.

Paterson, W. S. B., Why ice-age ice is sometimes "soft", *Cold Regions Science and Technology*, *20*(1), 75–98, 1991.

Paterson, W. S. B., *The Physics of Glaciers*, Pergamon, 3rd edn., 1994.

Perez, J., C. Mai, J. Tatibouet, and R. Vassoille, Dynamic behaviour of dislocations in HF-doped ice Ih, *Journal of Glaciology*, *25*(91), 133–149, 1980.

Petrenko, V. F., and R. W. Whitworth, Structure of ordinary ice I_h. Part II: Defects in ice. Volume 2: Dislocations and Plane Defects, *CRREL Special Report 94-12*, p. 24, 1994a.

Petrenko, V. F., and R. W. Whitworth, Structure of ordinary ice I_h. Part II: Defects in ice. Volume 1: Point Defects, *CRREL Special Report 94-4*, p. 36, 1994b.

Pimienta, P., P. Duval, and V. Y. Lipenkov, Flow behavior of ice along the 2040m Vostok core, Antarctica, *Annals of Glaciology*, *10*, 137–140, 1988.

Poirier, J.-P., Introduction to the physics of the earth's interior, in *Cambridge topics in Mineral Physics and Chemistry (3)*, edited by A. Putnis, and R. C. Lieberman, p. 264, Cambridge University Press, Cambridge, 1991.

Pshenichnyuk, A. I., V. V. Astanin, and O. A. Kaibyshev, The model of grain-boundary sliding stimulated by intragranular slip, *Philosophical Magazine A*, *77*(4), 1093–1106, 1998.

Rajmohan, N., and J. A. Szpunar, A new model for recrystallization of heavily cold-rolled aluminum using orientation-dependent stored energy, *Acta Materialia*, *48*(13), 3327–3340, 2000.

Ramberg, H., Particle paths, displacement and progressive strain applicable to rocks, *Tectonophysics*, *28*(1-2), 1–37, 1975.

Ribe, N., and Y. Yu, A theory for plastic deformation and textural evolution of olivine polycrystals, *Journal of Geophysical Research*, *96*(B5), 8325–8335, 1991.

Ringwood, A. E., *Origin of the Earth and Moon*, Springer-Verlag, 1st edn., 1979.

Ross, J., H. Lallemant, and N. Carter, Stress dependence of recrystallized-grain and subgrain size in olivine, *Tectonophysics*, *70*(1-2), 39–61, 1980.

Russell-Head, D., and W. Budd, Ice-sheet flow properties derived from bore-hole shear measurements combined with ice-core studies, *Journal of Glaciology*, *24*(90), 117–130, 1979.

Sachs, G., Zur Ableitung einer Fließbedingung, *Zeitschrift des Vereines Deutscher Ingenieure*, *72*(22), 734–736, 1928.

Sarma, G. B., and P. R. Dawson, Texture predictions using a polycrystal plasticity model incorporating neighbor interactions, *International Journal of Plasticity*, *12*(8), 1023–1054, 1996.

Savage, M. K., Seismic anisotropy and mantle deformation, *Reviews of Geophysics*, *37*(1), 65–106, 1999.

Segel, L. A., *Mathematics applied to continuum mechanics*, Dover, New York, 1st edn., 1987.

Shimizu, I., Stress and temperature dependence of recrystallized grain size: A subgrain misorientation model, *Geophysical Research Letters*, *25*(22), 4237–4240, 1998.

Shimizu, I., A stochastic model of grain size distribution during dynamic recrystallization, *Philosophical Magazine A*, *79*(5), 1217–1231, 1999.

Shoji, H., and C. C. Langway, Mechanical properties of fresh ice core from Dye 3, Greenland, in *Greenland Ice Core: Geophysics, Geochemistry and the Environment*, Geophysical Monograph 33, pp. 39–48, American Geophysical Union, 1985.

Shoji, H., and C. C. Langway, Flow velocity profiles and accumulation rates from mechanical tests on ice core samples, in *The Physical Basis of Ice Sheet Modelling. (Symposium at Vancouver 1987)*, pp. 67–77, International Association of Hydrological Sciences Publication 170, 1987.

Shoji, H., and C. C. Langway, Flow-law parameters of the Dye 3, Greenland, deep ice core, *Annals of Glaciology*, *10*, 146–150, 1988.

Staroszczyk, R., and O. Gagliardini, Two orthotropic models for strain-induced anisotropy of polar ice, *Journal of Glaciology*, *45*(151), 485–494, 1999.

Steinemann, S., Resultats experimentaux sur la dynamique de la glace et leurs correlations avec le mouvement et la petrographie des glaciers, in *Physics of the movement of the ice*, pp. 184–198, International Association of Hydrological Sciences Publication 47, 1958.

Swinzow, G. K., Investigation of shear zones in the ice sheet margin, Thule area, Greenland, *Journal of Glaciology*, *4*(32), 215–229, 1962.

Taylor, K. C., Sonic logging at Dye 3, Greenland, *MS Thesis, University of Wisconsin (Unpublished)*, pp. 1–64, 1982.

Thorsteinsson, T., Deformation of strongly anisotropic materials, *Journal of Glaciology (submitted)*, 2000a.

Thorsteinsson, T., Fabric development with nearest neighbor interaction and dynamic recrystallization, *Journal of Geophysical Research (submitted)*, 2000b.

Thorsteinsson, T., J. Kipfstuhl, and H. Miller, Textures and fabrics in the GRIP ice core, *Journal of Geophysical Research*, *102*(C12), 26583–26599, 1997.

Thorsteinsson, T., E. D. Waddington, K. C. Taylor, R. B. Alley, and D. D. Blankenship, Strain-rate enhancement at Dye 3, Greenland, *Journal of Glaciology*, *45*(150), 338–345, 1999.

Tomé, C., Properties of textured polycrystals, in *Texture and Anisotropy*, pp. 283–325, Cambridge University Press, 1998.

Tsenn, M., and N. Carter, Upper limits of power law creep of rocks, *Tectonophysics*, *136*(1-2), 1–26, 1987.

van der Veen, C., and I. Whillans, Flow laws for glacier ice: Comparison of numerical predictions and field measurements, *Journal of Glaciology*, *36*(124), 324–339, 1990.

van der Veen, C., and I. Whillans, Development of fabric in ice, *Cold Regions Science and Technology*, *22*(2), 171–195, 1994.

van der Veen, C. J., State of balance of the cryosphere, *Reviews of Geophysics*, *29*(3), 433–455, 1991.

Vernik, L., and A. Nur, Ultrasonic velocity and anisotropy of hydrocarbon source rocks, *Geophysics*, *57*(5), 727–735, 1992.

Waddington, E. D., J. F. Bolzan, and R. B. Alley, Potential for stratigraphic folding near ice sheet centers, *Journal of Glaciology (submitted)*, 2000.

Wallace, J. M., and P. V. Hobbs, *Atmospheric Science (An introductory survey)*, Academic Press, San Diego, 1st edn., 1977.

Weertman, J., The Eshelby-Schoeck viscous dislocation damping mechanism applied to the steady-state creep of ice, in *Ice and Snow (Properties, processes, and applications)*, edited by W. D. Kingery, pp. 28–33, The M.I.T. Press, Cambridge, Massachusetts, 1963.

Weertman, J., Creep of ice, in *Physics and Chemistry of Ice*, edited by E. Whalley, S. J. Jones, and L. W. Gold, pp. 320–337, Royal Society of Canada, Ottawa, 1973.

Weiss, J., and E. M. Schulson, Grain-boundary sliding and crack nucleation in ice, *Philosophical Magazine A*, *80*(2), 279–300, 2000.

Wenk, H.-R., and J. M. Christie, Comments on the interpretation of deformation textures in rocks, *Journal of Structural Geology*, *13*(10), 1091–1110, 1991.

Wenk, H.-R., K. Bennett, G. Canova, and A. Molinari, Modelling plastic deformation of peridotite with the self-consistent theory, *Journal of Geophysical Research*, *96*(B5), 8337–8349, 1991.

Wenk, H.-R., G. Canova, Y. Brechet, and L. Flandin, A deformation-based model for recrystallization of anisotropic materials, *Acta Materialia*, *45*(8), 3283–3296, 1997.

Whitworth, R. W., Velocity of dislocations in ice on (0001) and ($10\bar{1}0$) planes, *Journal of Physical Chemistry*, *87*, 4074–4078, 1983.

Appendix A

DEFORMATION OF STRONGLY ANISOTROPIC MATERIALS

A.1 Expressions for Components

A.1.1 The Resolved Shear Stress (RSS)

The RSS (Eq. 3.5) is in general given by

$$
\begin{aligned}
\tau_{(s)} = {}& n_1 b_1^{(s)} \sigma_{11} + n_2 b_2^{(s)} \sigma_{22} + n_3 b_3^{(s)} \sigma_{33} \\
&+ (n_1 b_2^{(s)} + n_2 b_1^{(s)}) \sigma_{12} + (n_1 b_3^{(s)} \\
&+ n_3 b_1^{(s)}) \sigma_{13} + (n_2 b_3^{(s)} + n_3 b_2^{(s)}) \sigma_{23},
\end{aligned}
\tag{A.1}
$$

which leads to

$$
\begin{aligned}
\tau_{(1)} = \frac{1}{12} \Big[& 4\cos(2\theta)[\sigma_{13}\cos\phi + \sigma_{23}\sin\phi] \\
&+ [\sigma_{11} + \sigma_{22} - 2\sigma_{33} + (\sigma_{11} - \sigma_{22})\cos(2\phi) \\
&+ 2\sigma_{12}\sin(2\phi)]\sin(2\theta) \Big],
\end{aligned}
\tag{A.2}
$$

$$
\begin{aligned}
\tau_{(2)} = \frac{1}{12} \Big[& -2[\sigma_{13}\cos\phi\cos(2\theta) + \sigma_{23}\cos^2\theta\sin\phi] \\
&+ 2\cos\theta\sin\theta[\sigma_{33} - \sigma_{11}\cos^2\phi - \sigma_{22}\sin^2\phi - \sigma_{12}\sin(2\theta)] \\
&+ 2\sigma_{23}\sin\phi\sin^2\theta + \sqrt{3}[2\sigma_{23}\cos\phi\cos\theta - 2\sigma_{13}\cos\theta\sin\phi \\
&+ [2\sigma_{12}\cos(2\phi) + (\sigma_{22} - \sigma_{11})\sin(2\phi)]\sin\theta] \Big],
\end{aligned}
\tag{A.3}
$$

and

$$
\begin{aligned}
\tau_{(3)} = \frac{1}{6} \Big[& -\sigma_{23}\cos^2\theta\sin\phi - \sigma_{11}\cos^2\phi\cos\theta\sin\theta \\
&+ \sin\theta[-\sqrt{3}\sigma_{12}\cos(2\phi) + \sigma_{23}\sin\phi\sin\theta] \\
&+ \cos\theta[\sqrt{3}\sigma_{13}\sin\phi + (\sigma_{33} - \sigma_{22}\sin^2\phi)\sin\theta] \\
&\cos\phi[\sigma_{13}\cos(2\theta) + \sqrt{3}[\sigma_{23}\cos\theta \\
&+ (\sigma_{22} - \sigma_{11})\sin\phi\sin\theta] + \sigma_{12}\sin\phi\sin(2\theta)] \Big].
\end{aligned}
\tag{A.4}
$$

A.1.2 Strain Rate Tensors for Single Crystal Slip Systems

The strain rate for each slip system, which are used in Equation (3.8) are given below. I use $s\theta = \sin\theta$ and $c\theta = \cos\theta$,

$$\frac{\dot{\varepsilon}_{ij}^{(1)}}{\beta A(T)\tau_{(1)}^n} = \frac{1}{6}\begin{bmatrix} c^2\phi s(2\theta) & 2c\phi c\theta s\phi s\theta & c\phi c(2\theta) \\ & s^2\phi s(2\theta) & c(2\theta)s\phi \\ symm & & -s(2\theta) \end{bmatrix}, \tag{A.5}$$

$$\frac{\dot{\varepsilon}_{ij}^{(2)}}{\beta A(T)\tau_{(2)}^n} = \tfrac{1}{12}\Big[\{-2c\phi s\theta(c\phi c\theta + \sqrt{3}s\phi),$$
$$s\theta(\sqrt{3}c(2\phi) - c\theta s(2\phi)), -c\phi c(2\theta) - \sqrt{3}c\theta s\phi\},$$
$$\{\dot{\varepsilon}_{12}, 2s\phi s\theta(\sqrt{3}c\phi - c\theta s\phi), \sqrt{3}c\phi c\theta - c(2\theta)s\phi\},$$
$$\{\dot{\varepsilon}_{13}, \dot{\varepsilon}_{23}, 2c\theta s\theta\}\Big], \tag{A.6}$$

and

$$\frac{\dot{\varepsilon}_{ij}^{(3)}}{\beta A(T)\tau_{(3)}^n} = \tfrac{1}{12}\Big[\{2c\phi s\theta(\sqrt{3}s\phi - c\phi c\theta),$$
$$-s\theta(\sqrt{3}c(2\phi) + c\theta s(2\phi)), \sqrt{3}c\theta s\phi - c\phi c(2\theta)\},$$
$$\{\dot{\varepsilon}_{12}, -2s\phi s\theta(\sqrt{3}c\phi + c\theta s\phi),$$
$$-\sqrt{3}c\phi c\theta - c(2\theta)s\phi\}, \{\dot{\varepsilon}_{13}, \dot{\varepsilon}_{23}, 2c\theta s\theta\}\Big]. \tag{A.7}$$

A.1.3 The Rotation Tensors of each Slip System

The rotation tensors, $\Omega^{(s)}$ in Eq. (3.17), are

$$\Omega_{ij}^{(1)} = \frac{1}{6}\begin{bmatrix} 0 & 0 & \cos\phi \\ 0 & 0 & \sin\phi \\ -\cos\phi & -\sin\phi & 0 \end{bmatrix}, \tag{A.8}$$

$$\Omega_{ij}^{(2)} = \tfrac{1}{12}$$
$$\begin{bmatrix} 0 & -\sqrt{3}s\theta & -c\phi - \sqrt{3}c\theta s\phi) \\ \sqrt{3}s\theta & 0 & -s\phi + \sqrt{3}c\theta c\phi \\ c\phi + \sqrt{3}c\theta s\phi & s\phi - \sqrt{3}c\theta c\phi & 0 \end{bmatrix}, \tag{A.9}$$

and

$$\Omega_{ij}^{(3)} = \tfrac{1}{12}$$
$$\begin{bmatrix} (0 & \sqrt{3}s\theta & -c\phi + \sqrt{3}c\theta s\phi \\ -\sqrt{3}s\theta & 0 & -s\phi - \sqrt{3}c\theta c\phi \\ c\phi - \sqrt{3}c\theta s\phi & s\phi + \sqrt{3}c\theta c\phi & 0 \end{bmatrix}. \tag{A.10}$$

A.1.4 Plastic Rotation Rate of the Normal

Calculating the components (Eq. 3.18)

$$\frac{dn_1^p}{dt} = -\frac{\beta A(T)}{12}$$
$$\left[(2\tau_{(1)}^3 - \tau_{(2)}^3 - \tau_{(3)}^3)\cos\theta\cos\phi - \sqrt{3}(\tau_{(2)}^3 - \tau_{(3)}^3)\sin\phi\right],$$

(A.11)

$$\frac{dn_2^p}{dt} = -\frac{\beta A(T)}{12}$$
$$\left[(2\tau_{(1)}^3 - \tau_{(2)}^3 - \tau_{(3)}^3)\cos\theta\sin\phi + \sqrt{3}(\tau_{(2)}^3 - \tau_{(3)}^3)\cos\phi\right],$$

(A.12)

and

$$\frac{dn_3^p}{dt} = \frac{\beta A(T)}{12}(2\tau_{(1)}^3 - \tau_{(2)}^3 - \tau_{(3)}^3)\sin\theta.$$

(A.13)

A.1.5 Rate of Change of the Zenith and Azimuth Angles

The rate of change of the zenith angle (Eq. 3.19) is

$$\frac{\partial\theta}{\partial t} = -\frac{\beta A(T)}{12}(2\tau_{(1)}^3 - \tau_{(2)}^3 - \tau_{(3)}^3)$$
$$\pm(\dot{\Omega}_{31}^b\cos\phi + \dot{\Omega}_{32}^b\sin\phi),$$

(A.14)

and the rate of change for the azimuth (Eq. 3.20) is

$$\frac{\partial\phi}{\partial t} = \frac{\beta A(T)}{4\sqrt{3}\sin\theta}(\tau_{(2)}^3 - \tau_{(3)}^3)$$
$$\pm(\dot{\Omega}_{21}^b\cos^2\phi - \dot{\Omega}_{12}^b\sin^2\phi + (\dot{\Omega}_{23}^b - \dot{\Omega}_{13}^b)\tan^{-1}\theta).$$

(A.15)

A.1.6 Single Crystal Strain Rate Components

For a single crystal in uniaxial compression (Eq. 3.23)

$$\dot{\varepsilon}_{33} = \frac{1}{2}\sum_s 2\beta A(c_3 b_3^{(s)})[c_3 b_3^{(s)}\sigma_{33}]^n$$
$$= \beta A\sigma_{33}^3 c_3^4(b_3^{(1)3} + b_3^{(2)3} + b_3^{(3)3}).$$

(A.16)

In simple shear we get for a single crystal (Eq. 3.33)

$$\dot{\varepsilon}_{13} = \frac{1}{2}\beta A\sum_s(c_1 b_3^{(s)} + c_3 b_1^{(s)})[(c_1 b_3^{(s)} + c_3 b_1^{(s)})\sigma_{13}]^n$$
$$= \frac{\beta}{2}A\sigma_{13}^3\sum_s(c_1 b_3^{(s)} + c_3 b_1^{(s)})^4.$$

(A.17)

A.1.7 The Velocity Gradient in Uniaxial Compression and Simple Shear

The non-zero velocity gradient components, as a function of stress and cone angle, in combined uniaxial compression and simple shear stress are (with $A(T) = 1$)

$$
\begin{aligned}
L_{11} = \; & (\sigma^3(-64 + \cos^5(\alpha)(249 - 220\cos(2\alpha) \\
& +35\cos(4\alpha))))/(576(\cos(\alpha) - 1)) \\
& +(\tau^2\sigma(-2048 + 1785\cos(\alpha) + 245\cos(3\alpha) \\
& +63\cos(5\alpha) + 60\cos(7\alpha) - 105\cos(9\alpha))) \\
& /(6144(\cos(\alpha) - 1)),
\end{aligned}
\tag{A.18}
$$

$$
L_{22} = L_{11},
\tag{A.19}
$$

$$
\begin{aligned}
L_{33} = \; & (6\sigma\tau^2(1024 - 945\cos(\alpha) - 105\cos(3\alpha) \\
& +21\cos(5\alpha) - 30\cos(7\alpha) + 35\cos(9\alpha)) \\
& +\sigma^3(2048 - 1890\cos(\alpha) - 420\cos(3\alpha) + 252\cos(5\alpha) \\
& +45\cos(7\alpha) - 35\cos(9\alpha)))/(9216(\cos(\alpha) - 1)),
\end{aligned}
\tag{A.20}
$$

$$
\begin{aligned}
L_{13} = \; & (\sigma^2\tau(-1024 + 945\cos(\alpha) + 105\cos(3\alpha) \\
& -21\cos(5\alpha) + 30\cos(7\alpha) - 35\cos(9\alpha)) \\
& +\tau^3(-3072 + 2730\cos(\alpha) - 35\cos(3\alpha) + 357\cos(5\alpha) \\
& -15\cos(7\alpha) + 35\cos(9\alpha)))/(1536(\cos(\alpha) - 1)).
\end{aligned}
\tag{A.21}
$$

A.1.8 The Velocity Gradient in Pure and Simple Shear

The non-zero velocity gradient components in combined pure and simple shear stress state, as a function of stress and cone angle are (with $A(T) = 1$)

$$
\begin{aligned}
L_{11} = \; & -[32\sigma\tau^2(-12288 + 11655\cos(\alpha) \\
& +595\cos(3\alpha) + 273\cos(5\alpha) + 150\cos(7\alpha) \\
& -385\cos(9\alpha)) + \sigma^3(-393216 + 384090\cos(\alpha) \\
& +49420\cos(3\alpha) - 42084\cos(5\alpha) - 2445\cos(7\alpha) \\
& +4235\cos(9\alpha))]/(393216(\cos(\alpha) - 1)),
\end{aligned}
\tag{A.22}
$$

$$L_{22} = -35\sigma\cos(\alpha)\sin(\alpha)^4(-83\sigma^2 - 192\tau^2$$

$$+12(3\sigma^2 - 8\tau^2)\cos(2\alpha)$$ (A.23)

$$+(47\sigma^2 - 96\tau^2)\cos(4\alpha))/(12288(\cos(\alpha) - 1)),$$

$$L_{33} = [8\sigma\tau^2(-6144 + 5565\cos(\alpha) + 665\cos(3\alpha)$$

$$-21\cos(5\alpha) + 180\cos(7\alpha) - 245\cos(9\alpha))$$

$$+3\sigma^3(-16384 + 15330\cos(\alpha) + 3080\cos(3\alpha)$$ (A.24)

$$-2016\cos(5\alpha) - 255\cos(7\alpha) + 245\cos(9\alpha))]$$

$$/(49152(\cos(\alpha) - 1)),$$

$$L_{13} = \tau[-24576(\sigma^2 + \tau^2) + 105(217\sigma^2 + 208\tau^2)\cos(\alpha)$$

$$+35(55\sigma^2 - 8\tau^2)\cos(3\alpha) + 21(11\sigma^2 + 136\tau^2)\cos(5\alpha)$$

$$+30(17\sigma^2 - 4\tau^2)\cos(7\alpha) + 35(-25\sigma^2 + 8\tau^2)\cos(9\alpha)]$$ (A.25)

$$/(12288(\cos(\alpha) - 1)).$$

A.1.9 The Johnson Parameters

Here we derive the parameters λ, μ, ν (Eq. 3.38) as a function of cone angle (normalized with $A(T)$)

$$\lambda^2 = \Big(-2048 + 1890\cos(\alpha) + 420\cos(3\alpha) - 252\cos(5\alpha),$$

$$-45\cos(7\alpha) + 35\cos(9\alpha)\Big)/[9216(\cos(\alpha) - 1)]]$$

$$\mu^2 = \Big(262144 - 280350\cos(\alpha) + 6300\cos(3\alpha) + 13356\cos(5\alpha)$$

$$-225\cos(7\alpha) - 1225\cos(9\alpha)\Big)/[1179648(1 - \cos(\alpha))],$$ (A.26)

$$\nu^2 = 2\Big(-3072 + 2730\cos(\alpha) - 35\cos(3\alpha) + 357\cos(5\alpha)$$

$$-15\cos(7\alpha) + 35\cos(9\alpha)\Big)/[3072(\cos(\alpha) - 1)].$$

VITA

Name: Throstur Thorsteinsson

Date: December 8, 2000

Education

B. S.: Geophysics, University of Iceland, 1995

Ph. D.: Geophysics, University of Washington, 2000

Dissertation Title

Ph. D.: ANISOTROPY OF ICE I_h: DEVELOPMENT OF FABRIC AND EFFECTS OF ANISOTROPY ON DEFORMATION

Publications

Throstur Thorsteinsson, E. D. Waddington, K. C. Taylor, R. B. Alley and D. D. Blankenship. Strain-rate enhancement at Dye 3, Greenland. *Journal of Glaciology*, 45(150), p. 338-345, 1999.

Throstur Thorsteinsson and M. T. Gudmundsson. Gravity model studies of the volcanic island Surtsey, Iceland. *Jökull*, 47, p. 89-96, 1999.

Throstur Thorsteinsson and C. F. Raymond. Sliding versus till deformation in the fast motion of an ice stream over a viscous till. *Journal of Glaciology*, (in press), 2000.

Throstur Thorsteinsson. Deformation of strongly anisotropic materials. *Journal of Glaciology*, (submitted), 2000.

Throstur Thorsteinsson. Fabric development with nearest neighbor interaction and dynamic recrystallization. *Journal of Geophysical Research*, (submitted), 2000.